

**Aerosol profiling with lidar
in the Amazon Basin
during the wet and dry season 2008**

Von der Fakultät für Physik und Geowissenschaften
der Universität Leipzig
eingereichte

D I S S E R T A T I O N

zur Erlangung des akademischen Grades

DOCTOR RERUM NATURALIUM
Dr. rer. nat.

vorgelegt

von Diplom-Meteorologe Holger Baars

geboren am 16. Mai 1981 in Meerane

Leipzig, den 7. Dezember 2011

Bibliographische Beschreibung:

Baars, Holger

Aerosol profiling with lidar in the Amazon Basin during the wet and dry season 2008

Universität Leipzig, Dissertation

178 S., 188 Lit., 77 Abb., 8 Tab.

Referat:

Im Rahmen der vorliegenden Arbeit wurden die Eigenschaften von atmosphärischen Aerosolpartikeln im tropischen Regenwald des Amazonasgebietes bestimmt. Dazu wurden die Daten einer fast einjährigen Lidarmesskampagne ausgewertet und diskutiert. Die Messungen wurden mit einem automatischen Mehrwellenlängen-Polarisations-Raman-Lidar im zentralen Amazonasbecken nahe Manaus, Brasilien, im Zeitraum von Januar bis November 2008 durchgeführt. Somit konnten erstmalig optische und mikrophysikalische Aerosoleigenschaften im Amazonasgebiet während der Regenzeit (ca. Dezember–Mai) und Trockenzeit (ca. Juni–November) höhenaufgelöst charakterisiert werden.

Einleitend werden die meteorologischen Bedingungen im Amazonasgebiet erläutert und eine Literaturübersicht über Aerosolforschung in dieser Region gegeben. Das Messgerät sowie verschiedene Kalibrier- und Korrekturschemen, die zur Datenauswertung notwendig sind, werden vorgestellt. Auch Vergleiche mit anderen Messgeräten werden diskutiert. Diese zeigen, dass die aus den Lidarmessungen abgeleiteten Parameter von hoher Qualität sind. Anhand von Fallstudien werden mit Hilfe von Rückwärtstrajektorien und Satellitenmessungen typische Aerosolbedingungen am Messstandort diskutiert. Um die generellen Unterschiede zwischen Regen- und Trockenzeit zu quantifizieren, wird eine statistische Auswertung aller analysierten Lidarmessungen präsentiert.

Die Analyse der Lidardaten zeigt, dass während der Regenzeit im Amazonasgebiet in ca. der Hälfte aller Fälle sehr saubere Bedingungen mit einer Aerosol Optischen Dicke (AOD) von weniger als 0.05 (bei 532 nm) vorherrschen können. Allerdings wurde in ca. 30% aller analysierten Fälle im Zeitraum von Januar bis Mai auch afrikanisches Aerosol, vornehmlich Saharastaub und Biomasseverbrennungsaerosol (BBA), am Messstandort detektiert. Dabei dominierte meist BBA die Aerosolpopulation, wie die Depolarisationsmessungen zeigten. In der Trockenzeit ist die Atmosphäre im Amazonasbecken hauptsächlich mit BBA aus Südamerika belastet. Daher ist die AOD im Durchschnitt um einen Faktor drei größer als in der Regenzeit. BBA wurde zu dieser Jahreszeit regelmäßig bis zu einer Höhe von 4–6 km detektiert. Basierend auf den vorgestellten Langzeitmessungen werden erstmalig die optischen Eigenschaften von südamerikanischem BBA statistisch analysiert und diskutiert.

Contents

1	Introduction	1
2	Amazon rain forest: Meteorological conditions, fire activity, and previous aerosol research	7
2.1	Amazonian weather conditions	7
2.2	Fire activity in Amazonia	10
2.3	Aerosol transport mechanisms	14
2.4	Findings from previous experiments	17
2.4.1	Amazonian aerosol characteristics	17
2.4.2	Vertical aerosol distribution	24
3	Experiment: Location, instrumentation, and observations	27
3.1	Field site	27
3.2	Polly ^{XT}	29
3.3	Overview of observations	34
4	Lidar methodology	39
4.1	Lidar principle and equations	40
4.2	Lidar methods	42
4.2.1	Backscatter and extinction coefficient – Raman lidar method . .	42
4.2.2	Backscatter coefficient – Klett method	43
4.2.3	Ångström exponents	44
4.2.4	Aerosol optical depth	45
4.2.5	Vertical aerosol structure analysis	46
4.2.6	Depolarization ratio	49
4.2.7	Smoke-dust separation	51

4.2.8	Microphysical particle properties from optical particle properties by inversion	52
5	Instrument characterization and quality assurance	55
5.1	Overlap characteristics	56
5.2	Polarization characterization and correction	60
5.2.1	Transmission ratios and corresponding signal correction	60
5.2.2	Filter-dependent molecular depolarization	65
5.3	Data-analysis algorithm check	67
5.4	Lidar intercomparison during EARLI09	69
5.5	Comparison with sun photometer	74
6	Observations – Part I: Case studies	77
6.1	African aerosol in Amazonia	77
6.1.1	10 February 2008	78
6.1.2	Overview of dust and smoke advection towards Amazonia during the wet season 2008	84
6.2	Background conditions in Amazonia	90
6.2.1	23 April 2008	90
6.2.2	Further background cases	96
6.3	Dry season: Smoke aerosol observations	98
6.3.1	11 September 2008	98
6.3.2	15 August 2008	105
6.3.3	28 October 2008	109
7	Observations – Part II: Seasonal aerosol characteristics	117
7.1	Meteorological conditions	117
7.2	Overview of optical and geometrical properties	119
7.2.1	Time series	119
7.2.2	Overview of vertical aerosol profiles	121
7.3	Statistical analysis	124
7.3.1	AOD	124
7.3.2	Vertical aerosol structure	128
7.3.3	Aerosol properties	132
8	Summary, conclusion, and outlook	139

Appendix	145
A Optical properties of atmospheric molecules	145
B Dark measurement test	146
C Laser polarization characterization	147
D NMMB/BSC-Dust	149
Bibliography	153
List of Abbreviations	179

Chapter 1

Introduction

The Amazon Basin is the largest hydrological basin in the world draining an area as large as 6,900,000 square kilometers (*Barthem et al.*, 2004). It contains the largest extent of tropical rain forest on Earth – the Amazon rain forest. The tropical rain forest covers more than 5,000,000 square kilometers (*Nobre et al.*, 2004) and thus an area half as large as Europe or rather one third of South America. The Amazon rain forest represents over half of the planets remaining tropical rain forests (*UNEP*, 2008). Because of its size and its pronounced hydrological cycle, the Amazon Basin is a key region for the global climate (heat pump, water work, major carbon dioxide sink). However, Amazonia is under pressure. Not only global warming disturbs this unique ecosystem, but it also suffers dramatically from deforestation. Each year thousands of square kilometers of tropical rain forest are burned to acquire new farming land. About 15% of the original forest area were already lost in 2003 (*Soares-Filho et al.*, 2006). *Nepstad et al.* (2008) even estimated that 55% of the forest area will be damaged or cut down by 2030, if present global climate change and deforestation trends continue. The strong linkage between the terrestrial ecosystem and the hydrological cycle makes the Amazon Basin very vulnerable to land-use changes. *Soares-Filho et al.* (2006) stated that more than 70% of the original forest area are needed to maintain the forest-dependent rain-fall regime. As a consequence, Amazonia could reach a tipping point at which the rain forest dies back and vegetation changes to Savanna (*Lenton et al.*, 2008). Once the rain forest is gone, local climate will change significantly and irreversibly and this in turn will also affect the global climate.

The deforestation fires in Amazonia significantly influence the global climate already today. Because the Amazon rain forest stores a lot of carbon, huge amounts of carbon dioxide are emitted during these fires. On a global scale, deforestation fires alone

account for 19% of the global carbon dioxide emissions (*Bowman et al.*, 2009). Beside carbon dioxide, huge amounts of aerosol are emitted into the atmosphere by the vegetation fires. These aerosol particles can be carried over long distances and influence cloud microphysics and atmospheric radiative transfer on a regional and hemispheric scale.

The effects of aerosol on global climate have been discussed for several decades and generally one distinguishes between the aerosol direct and indirect effects (e.g., *IPCC*, 2007). The aerosol direct effect describes the influence of aerosols on the Earth's radiation balance by scattering and absorption of shortwave and longwave radiation. Changes in the thermodynamical stability of the atmosphere due to light-absorption of aerosols are denoted as the semi-direct aerosol effect. The aerosol indirect effect describes the influence of aerosol on clouds. The potential of aerosol to change the cloud droplet concentration and cloud droplet size, and thus the cloud radiative properties, is called the first indirect aerosol effect. The second indirect effect describes the change of the amount and the lifetime of clouds by aerosol particles acting as cloud condensation nuclei (CCN).

However, the quantification of these effects is subject to the highest uncertainties in future climate predictions (*IPCC*, 2007). One reason for the uncertainties is the high horizontal and vertical inhomogeneity of the optical and microphysical aerosol properties. A good knowledge of the aerosol conditions (aerosol type, vertical aerosol structure, horizontal distribution etc.) is thus a prerequisite for a reliable estimation of the aerosol effects in the climate system.

From field campaigns during the last three decades (e.g., *Martin et al.*, 2010a), it was deduced that Amazonia is at times very clean and free of anthropogenic influences in the wet season, while during the dry season smoke from vegetation fires heavily influences the atmospheric conditions. *Pöschl et al.* (2010) even state that aerosol conditions in Amazonia's wet season "approach to those of the pristine pre-industrial era". Because of this strong contrast between the wet and the dry season, the Amazon Basin is considered to be favorable to study the direct and indirect aerosol effect on climate.

Aerosol research in Amazonia was predominantly performed during the dry season with the focus on biomass-burning aerosol (BBA, e.g., *Kaufman et al.*, 1992; *Ward et al.*, 1992; *Kaufman et al.*, 1998a; *Andreae et al.*, 2004). During several field campaigns microphysical and optical properties of smoke aerosol were investigated mainly at ground with in-situ instrumentation (e.g., *Artaxo et al.*, 1994, 2002; *Guyon et al.*,

2003) and by means of a few airborne measurements (e.g., *Reid et al.*, 1998; *Reid and Hobbs*, 1998; *Chand et al.*, 2006). Based on such measurements of BBA, estimations of the direct aerosol effect were made (*Ross et al.*, 1998) and hypotheses were formulated concerning the aerosol semi-direct (*Koren et al.*, 2004) and indirect effect (*Reid et al.*, 1999; *Williams et al.*, 2002; *Andreae et al.*, 2004; *Koren et al.*, 2004, 2008; *Rosenfeld et al.*, 2008). However, most of these campaigns were performed in the direct vicinity of the vegetation fires and thus may not be representative for the entire Amazon Basin. Aerosol research in the wet season was less frequent and focused on natural aerosol from the rain forest. Biogenic aerosol (primary organic and secondary organic aerosol) from the forest was identified as the dominant aerosol species during that season (*Artaxo et al.*, 1988; *Martin et al.*, 2010b). Because the concentration of aerosol under such conditions is very low and comparable to marine background conditions (*Roberts et al.*, 2001), the Amazon Basin is denoted as green ocean (*Andreae et al.*, 2004) during the wet season. As a consequence of the low natural aerosol concentrations, the impact of anthropogenic aerosol on rainfall production (aerosol indirect effect) may have a greater importance in the Amazon Basin than in other continental regimes (*Roberts et al.*, 2001; *Artaxo et al.*, 1990). Events of Saharan dust advection occasionally take place during the wet season and can significantly change the atmospheric aerosol conditions over the Amazon rain forest during that time (*Talbot et al.*, 1990; *Swap et al.*, 1992; *Formenti et al.*, 2001). *Reichholf* (1986) and *Bristow et al.* (2010) showed the need for Saharan dust intrusions into the Amazon Basin to maintain nutrient balance in Amazonian soils. Without this transport of nutrients from Africa, the growth of the Amazon rain forest would be limited. Beside Saharan dust, also BBA from African fires reaches the Amazon Basin as was first pointed out by *Kaufman et al.* (2005). Before this study, the transport of African smoke towards Amazonia was not recognized, and the potential of BBA to act as nutrient for the Amazon rain forest was not yet considered. Also the impact of such aerosol on weather and climate in Amazonia remained unknown because no information on the vertical aerosol distribution existed. For instance, *Remer* (2009) pointed out that BBA located above clouds has a significant heating effect on the atmosphere. Hence, the knowledge of the vertical aerosol structure, and thus the information if aerosol is above or below a potential cloud layer, is essential to estimate the aerosol effects on climate. Consequently, there is a clear need for more, especially height-resolved, aerosol observations in the Amazon Basin. However, measurements in this large, inaccessible area are difficult. Neither long-term in-situ measurements of the aerosol conditions nor continuous measurements of the

vertical aerosol structure have been performed so far. Measurements with ground-based and satellite passive remote-sensing instruments suffer from the high fractional cloud cover which usually exists during daytime in the Amazon Basin and are unable to resolve the layering of the aerosol as a function of height. Thus, most of the effects of Amazonian natural and anthropogenic aerosol on climate (direct and indirect effect) as previously discussed (e.g., *Ross et al.*, 1998; *Reid et al.*, 1998; *Koren et al.*, 2004; *Andreae et al.*, 2004; *Oliveira et al.*, 2007; *Prenni et al.*, 2009) were based on a few short, snapshot-like aerosol measurements and are not representative on a regional or even global scale.

To account for the role of the Amazon rain forest in the Earth's climate system, the following key questions with respect to aerosol need to be answered:

- How frequently do clean aerosol condition, i.e., free of anthropogenic influences, prevail? What are the aerosol characteristics (e.g., aerosol optical depth) of these natural aerosol conditions?
- What aerosol species do occur in the Amazon Basin throughout the year?
- How often does advection of Saharan dust and/or African BBA occur in the Amazon Basin and how much do these species contribute to the total aerosol load?
- How dominant is BBA from South American vegetation fires in entire Amazonia?
- What are the height-resolved optical and microphysical aerosol properties under ambient conditions during both the dry and the wet season?
- How is the vertical distribution of the aerosol? Are passive remote sensing and ground-based in-situ measurements sufficient for investigating the direct and indirect aerosol effect in Amazonia?

To address these questions, it is essential to perform long-term measurements in Amazonia gathering also information on the vertical aerosol distribution. Lidar is an appropriate tool to monitor the vertical aerosol structure. A lidar is an active remote-sensing instrument that makes use of the effects of atmospheric (molecular and particle) scattering and extinction of light to gain information on the state and composition of the atmosphere. Lidar is the acronym for **light detection and ranging**. The emission and detection of light at different wavelengths and information on the polarization state of the scattered light allows one to derive vertically resolved optical and microphysical aerosol properties and to differentiate aerosol species. High clouds, which disturb pas-

sive aerosol observations (e.g., with sun photometer and MODIS¹), do not hinder the lidar measurements, and aerosol information below the clouds are usually obtainable. Recent developments of small, compact lidars (e.g., *Althausen et al.*, 2009) make it possible to perform unattended, automatic lidar measurements at even remote locations. Consequently, long-term measurements of the vertical aerosol structure are now possible.

For the first time in Amazonia, continuous measurements of the vertical aerosol structure were carried out in the framework of EUCAARI (European Integrated Project on Aerosol, Cloud, Climate, Air Quality Interactions, *Kulmala et al.*, 2009, 2011) and AMAZE-08 (Amazonian Aerosol Characterization Experiment, *Martin et al.*, 2010b). The measurements were performed with the automated multiwavelength-Raman-polarization lidar Polly^{XT} (*Althausen et al.*, 2009) of the Leibniz Institute for Tropospheric Research (IfT), Leipzig, Germany. Lidar measurements were conducted from January to November 2008 near Manaus, Brazil, in the central northern part of the Amazon Basin. Pristine tropical rain forest covers the area around the lidar site for several hundred kilometers (except Manaus metropolitan area). In this dissertation, these lidar measurements are intensively discussed in terms of instrumentation, data analysis, and observed aerosol properties.

After the introduction, Chapter 2 gives an overview of the meteorological conditions and the fire activity in the Amazon Basin. Furthermore, a review concerning the knowledge on aerosols in Amazonia gathered from research activities before 2008 is given. In Chapter 3, the lidar experiment in Amazonia is described. The field site and the lidar Polly^{XT} are introduced. In Chapter 4, the lidar principle and the analysis methods to determine aerosol characteristics are outlined. Because Polly^{XT} was newly developed for the EUCAARI project, characterization and quality-assurance tests for the lidar are presented in Chapter 5. These tests and the corresponding corrections were essential to obtain high-quality aerosol information. The results of the long-term lidar observations in the Amazon rain forest covering the wet and the dry season of 2008 are presented in two chapters. In Chapter 6, several case studies are discussed, while in Chapter 7 the statistical analysis of the aerosol characteristics in the different seasons is presented. A summary and concluding remarks are given in Chapter 8.

¹Moderate Resolution Imaging Spectroradiometer

Chapter 2

Amazon rain forest: Meteorological conditions, fire activity, and previous aerosol research

In this Chapter, the general weather conditions in the region of the lidar measurements are discussed. A brief description of the vertical transport processes in the Amazon Basin and an introduction into the topic of biomass burning in the Amazon rain forest are given. Finally, an overview of knowledge on aerosol conditions in Amazonia gathered from previous field campaigns is presented.

2.1 Amazonian weather conditions

In general, the hot and humid climate in Amazonia is controlled by the migration of the Intertropical Convergence Zone (ITCZ) and thus by the trade-wind (Hadley) circulation. But also the El Niño/La Niña Southern Oscillation (*Rasmusson and Wallace, 1983*) affects the Amazonian climate (e.g., rainfall patterns, *Nobre et al., 2004*). Figure 2.1 shows the global position of the ITCZ in January and July based on a climatological average (*Lutgens and Tarbuck, 2010*). In contrast to Africa and Asia, the inter-annual migration of the ITCZ is rather limited. As a consequence, two dry and two wet seasons occur in tropical Africa, while only one dry and one wet season appear in South America. In addition to the location of the ITCZ, the evolution of the Bolivian High Pressure System has a significant effect on the meteorological conditions in the west and south of Amazonia (*Procopio et al., 2003*).

Typical for tropical climate in lowlands, mean temperatures have no significant annual

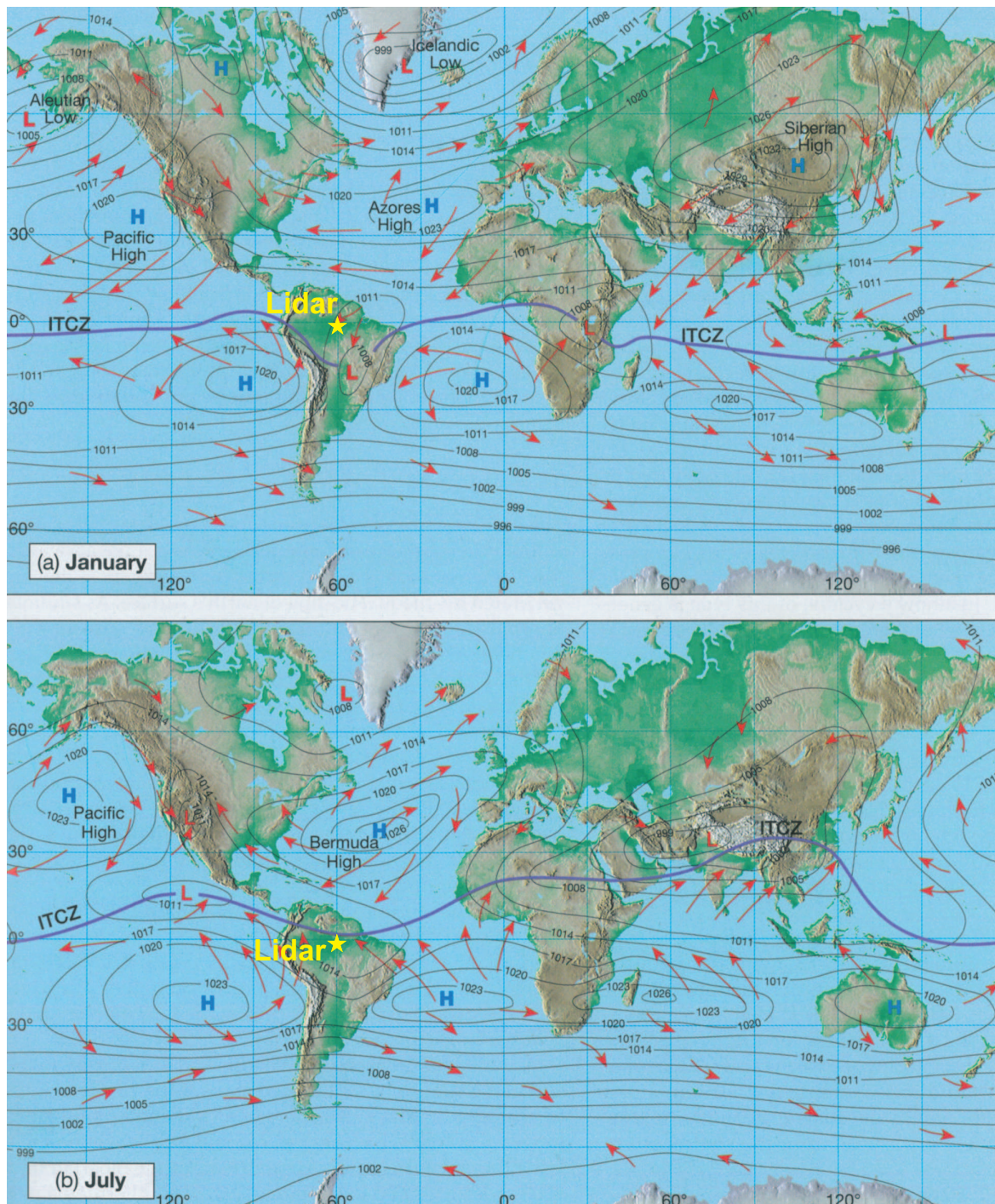


Figure 2.1: Global climatological conditions in January (wet season in Amazonia) and July (dry season). Mean values of the sea-surface-level pressure and the resulting wind fields are shown (*Lutgens and Tarbuck, 2010*). The thick purple line indicates the location of the ITCZ during the different seasons. The lidar field site is indicated by a yellow star.

cycle and are above 25 °C throughout the year. The wet season is characterized by heavy and long-lasting rain falls. In the dry season, precipitation is less and mainly caused by singular convective systems. The daily maximum surface temperatures are usually higher in the dry season than in the wet season. Due to the local surface forcings, the maximum of the mainly convectively driven precipitation in both seasons is observed in the afternoon and during the night (*Araújo et al.*, 2002). However, caused by the evolution of a river-and-land-breeze circulation, meteorological conditions can differ significantly from inland conditions near big rivers (*Oliveira and Fitzjarrald*, 1993). Due to its large size and the migration of the ITCZ, the dry season begins in different months in Amazonia (*Procopio et al.*, 2003). Depending on the region, the dry season peaks between August and November in most parts of the Amazon Basin. During this time, a high anthropogenic fire activity usually occurs (see Sec. 2.2).

The climate chart¹ for Manaus (3° 08' S, 60° 0.1' W), which is located about 60 km south of the lidar field site in the central northern part of the Amazon Basin, is shown in Fig. 2.2. The wet season in Manaus usually covers the months from December to May with monthly precipitation rates of 230–300 mm. The dry season begins end of June and lasts until November. Average monthly precipitation rates in Manaus are between 50 and 120 mm during this time. Monthly mean temperatures vary only slightly throughout the year. The day-night amplitude is largest (almost 10 °C) during the dry season. Usually, minimum temperatures are not below 23 °C. Dominant wind directions (not shown) in Manaus are north-east (wet season) to south-east (dry season) due to the trade-wind circulation.

¹The data was originally gathered for the World Meteorological Organization (WMO), then processed by the National Climatic Data Center (NCDC), and finally provided by the National Oceanic and Atmospheric Administration (NOAA) via NOAA Global Climate Normals 1961-1990. Source: <http://www.climate-charts.com>

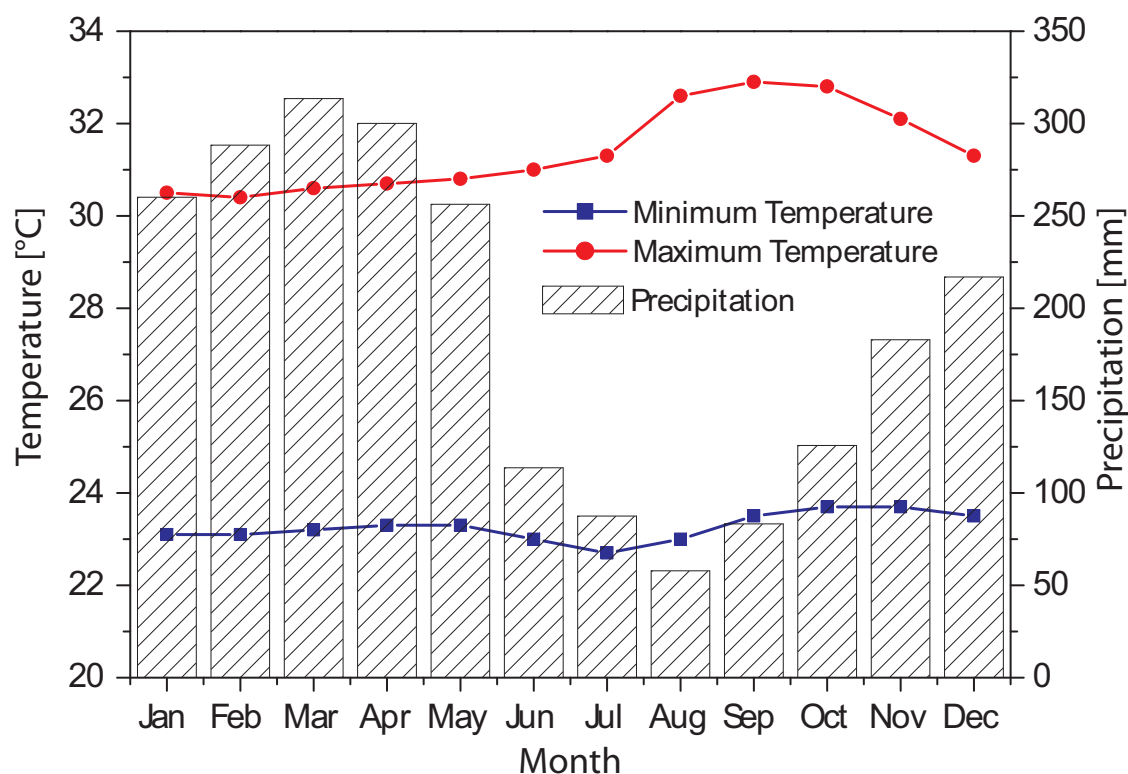


Figure 2.2: Monthly mean temperatures and precipitation rates for Manaus ($3^{\circ} 08' S$, $60^{\circ} 0.1' W$ at 72 m asl, Station: BZ83331).

2.2 Fire activity in Amazonia

A high anthropogenic fire activity is observed during the dry season in Amazonia (*Andreae*, 1991). As a consequence, large amounts of smoke are emitted into the atmosphere. According to *Longo et al.* (2009), the anthropogenic vegetation fires can be divided into three major fire types:

- primary deforestation fires: for new pasture or agriculture land,
- pasture maintenance fires: the most common type (every 2–3 years),
- savanna (cerrado) fires: burned to improve grazing (every 1–3 years).

Most fires in forested regions in Amazonia occur along rivers and near recently constructed roads and settlements (*Prins et al.*, 1998). The fire activity in Amazonia has a strong diurnal cycle and peaks in the middle of the afternoon (*Kaufman et al.*, 1998a; *Prins et al.*, 1998).

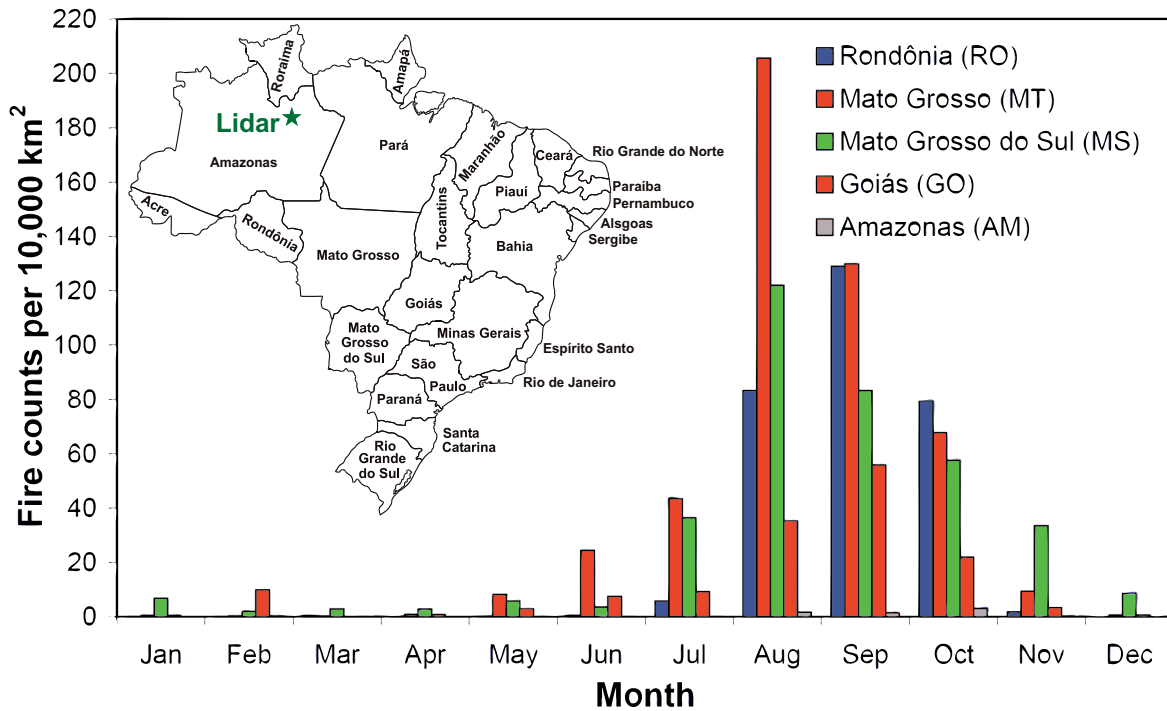


Figure 2.3: Monthly fire activity over the Amazon Basin for the states Rondônia, Mato Grosso, Mato Grosso do Sul, Goiás, and Amazonas in 1999 (*Guyon et al.*, 2003). The total number of fire pixels per 10000 km² detected by AVHRR is presented. The lidar location and the federal states of Brazil are shown for orientation in addition (Source: Instituto Brasileiro de Geografia e Estatística).

Figure 2.3 shows the frequency of fires in five different states in Brazil for 1999 determined with AVHRR² aboard the NOAA-12 satellite (*Guyon et al.*, 2003). The lidar station in the Brazilian state of Amazonas is indicated. The highest fire activity of the five analyzed states was observed in the state of Mato Grosso. Agriculture and cattle farming play the dominant economical role in this state. As a consequence, fire counts rise up to 210 per 10000 km² in August. In comparison to the other four analyzed Brazilian states, the fire activity in 1999 in the state of Amazonas seems negligible low. The highest fire activity in Amazonas state was observed in October and thus later than in the four other analyzed states.

Freitas et al. (2007) reported that most fire areas in Amazonia are smaller than 5 ha and only 3% of the fires are larger than 50 ha. Most of the small fires cannot be detected with satellite instruments. As a consequence, e.g., MODIS detects 25% of the total number of fires, but 60%–85% of the total fire radiative thermal energy. Thus, the

²Advanced Very High Resolution Radiometer

large fires which produce most of the BBA are detected by MODIS (*Kaufman et al.*, 1998b). Aerosol emissions from these fires are estimated by using emission factors, the size of the burned area, and fire counts from satellites (*Freitas et al.*, 2007).

Figure 2.4 shows fires detected by the MODIS rapid response system (*Justice et al.*, 2002; *Giglio et al.*, 2003; *Davies et al.*, 2009) in South America for the twelve months of the lidar observational period in 2008. A clear annual cycle is obvious. Between January and April 2008, fires predominantly occurred in the extreme northern part of South America in Venezuela and Colombia. At this time of the year, the ITCZ is located south of the equator causing the dry season in these northern regions (see Fig. 2.1). Sporadic fires were also detected in the south-east of Brazil. The fire activity in the whole Amazon Basin was lowest in the transition months May and June. An increasing number of fires was detected from July to September south and east of the lidar location. The maximum burning activity (most detected fires) in the south-eastern part of Brazil took place in the months of September and October. The burning activity east of the lidar site peaks in October/November.

Almost no fires were detected throughout 2008 in the interior part of the Amazon Basin which is covered with dense rain forest. The majority of the fires detected in 2008 occurred in the southern and south-eastern edges of the rain forest, where most of the pasture and agriculture (and thus also deforestation) takes place.

Because fire activity is strongly linked to deforestation, the yearly deforestation rate in Amazonia can be used to analyze 2008's fire activity with respect to other years. Figure 2.5 shows the yearly deforestation rate for the Brazilian Amazon rain forest from 1988 until 2009. The average deforestation rate in the 1990s was about 17000 km² per year. In 2004, the deforestation rate peaked with 27000 km² per year. It is obvious that since 2004 the forest clearing is significantly decreasing. The deforestation in 2007 (about 9000 km²) was only about one third of the deforestation in 2004 (27000 km²). However, the deforestation in 2008 (12000 km²), the year of the observations, was slightly higher than in 2007 and 2009. Consequently, 2008 seemed to be a year of increased fire activity but representative for the 2006–2009 period.

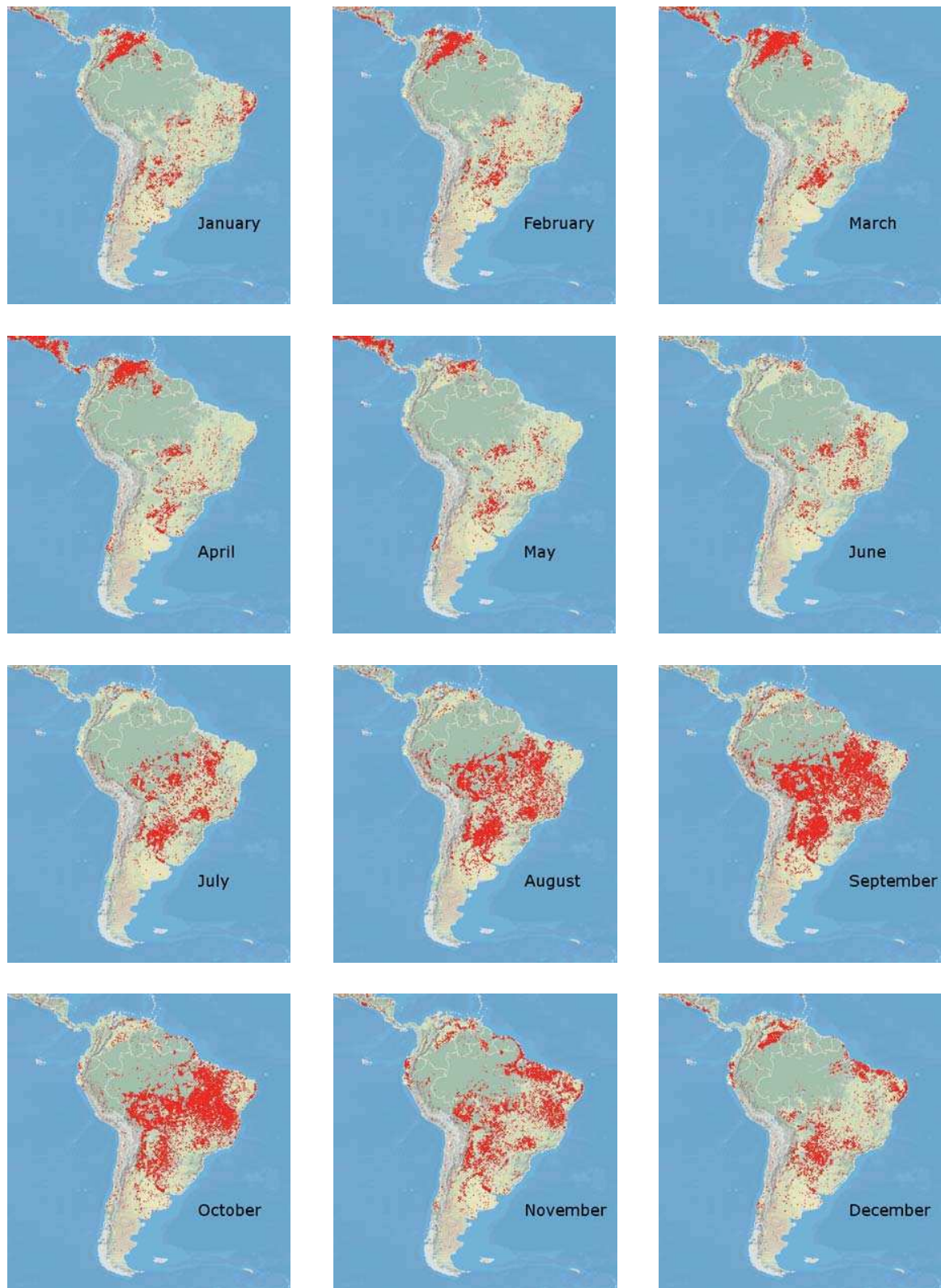


Figure 2.4: Monthly MODIS fire counts for January to December 2008.

Source: <http://rapidfire.sci.gsfc.nasa.gov>

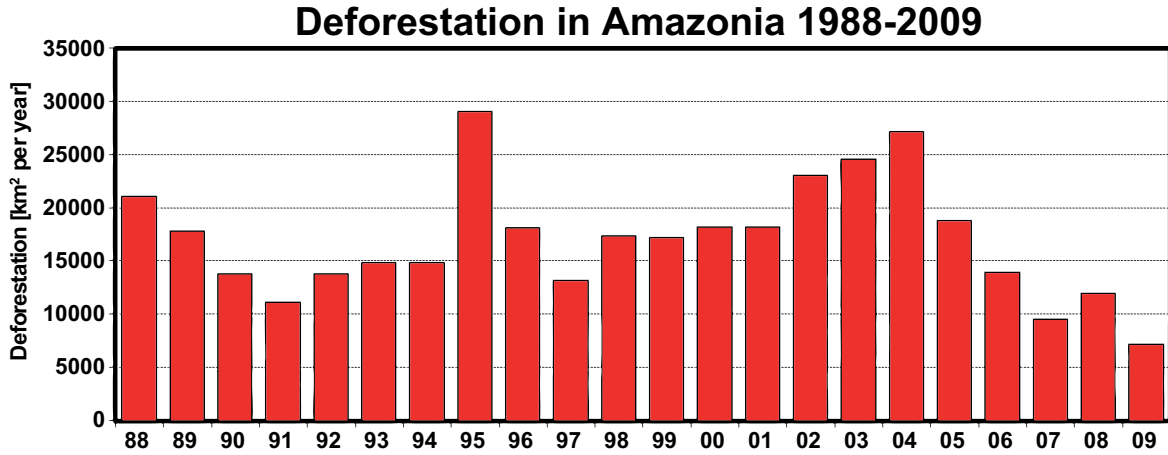


Figure 2.5: Yearly deforestation rate for the Brazilian Amazon rain forest. Source: *Artaxo et al.* (2010), data from INPE (Brazilian National Institute for Space Research).

2.3 Aerosol transport mechanisms

The diurnal cycle of the convective mixing layer (ML) in combination with shallow to deep convection controls the vertical transport of pollutants in the Amazon Basin. In areas with fires activity, pyroconvection plays an important role, too (*Freitas et al.*, 2006). The diurnal cycle of the ML is controlled by heat fluxes and thermodynamical stability of the lower atmosphere. Due to the humid environment, the latent heat flux is typically three times higher than the sensible heat flux (*Freitas et al.*, 2007) and limits ML development. As a consequence, the height of the ML top over rain forest in the Amazon Basin typically ranges from 1500–1800³ m only (*Nobre et al.*, 1996; *Guyon et al.*, 2005; *Fisch et al.*, 2004).

Figure 2.6 shows the frequency of occurrence of the daily maximum ML top height at the lidar site in 2008 as derived from ECMWF (European Centre for Medium-Range Weather Forecasts) model data⁴. More details on the determination of the ML top from ECMWF model data are given in Sec. 4.2.5. In most cases (more than 80%) of that year, the ML was not deeper than 1500 m at the tropical lidar location. During the dry season, a slightly broader distribution with higher values for the daily maximum ML top height is given. But only on 5% of the days, the ML exceeded a depth of 2000 m.

A sketch illustrating the aerosol distribution, vertical transport, and formation pro-

³In this work all altitudes are given as height above ground level (agl) if not otherwise stated.

⁴ML-top data kindly provided by the Finish Meteorological Institute (FMI, Contact: Mika Kompula (Mika.Kompula@fmi.fi)).

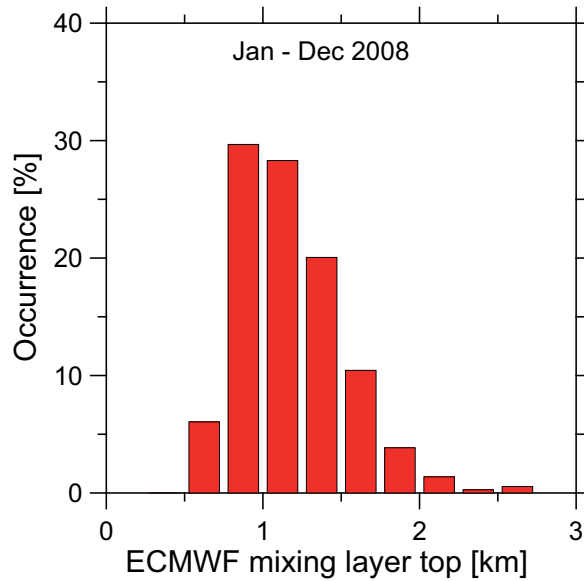


Figure 2.6: Frequency distribution of the daily maximum ML top height as derived from ECMWF (more information see Sec. 4.2.5) for the year of 2008.

cesses of aerosol in a smoky Amazonian environment is presented in Fig. 2.7 (modified composite from *Krejci et al.*, 2003 and *Reid et al.*, 1998). Shallow and non-precipitating convective systems develop typically in the upper part of the moist, but also polluted ML and cause the transport of gases and particles into the lower free troposphere, the so-called cloud convective layer (CCL, *Longo et al.*, 2010). This layer is above the ML but still below the trade-wind inversion (TWI) which usually occurs at altitudes of 3–4 km over Amazonia. The CCL in Amazonia is much more significant for the vertical transport of aerosol than in other regions of the Earth. Deep and moist convection are also important transport mechanisms and can carry aerosol into the clean free troposphere (FT) to altitudes up to the tropopause (*Andreae et al.*, 2001). During their transport by these convective systems, the particles can undergo several in-cloud processes and thus the optical and microphysical properties may change. In the out-flow region of cumulonimbus clouds (also indicated in Fig. 2.7), new particle formation has been observed (*Krejci et al.*, 2003).

Another important transport mechanism is pyroconvection in association with fires. Air parcels are released with a very high temperature compared to the surrounding air temperature. These air parcels can easily rise to high altitudes due to buoyancy and are not trapped within the local ML. As a consequence, a large amount of smoke particles reach the free troposphere and can be transported over large distances. Addi-

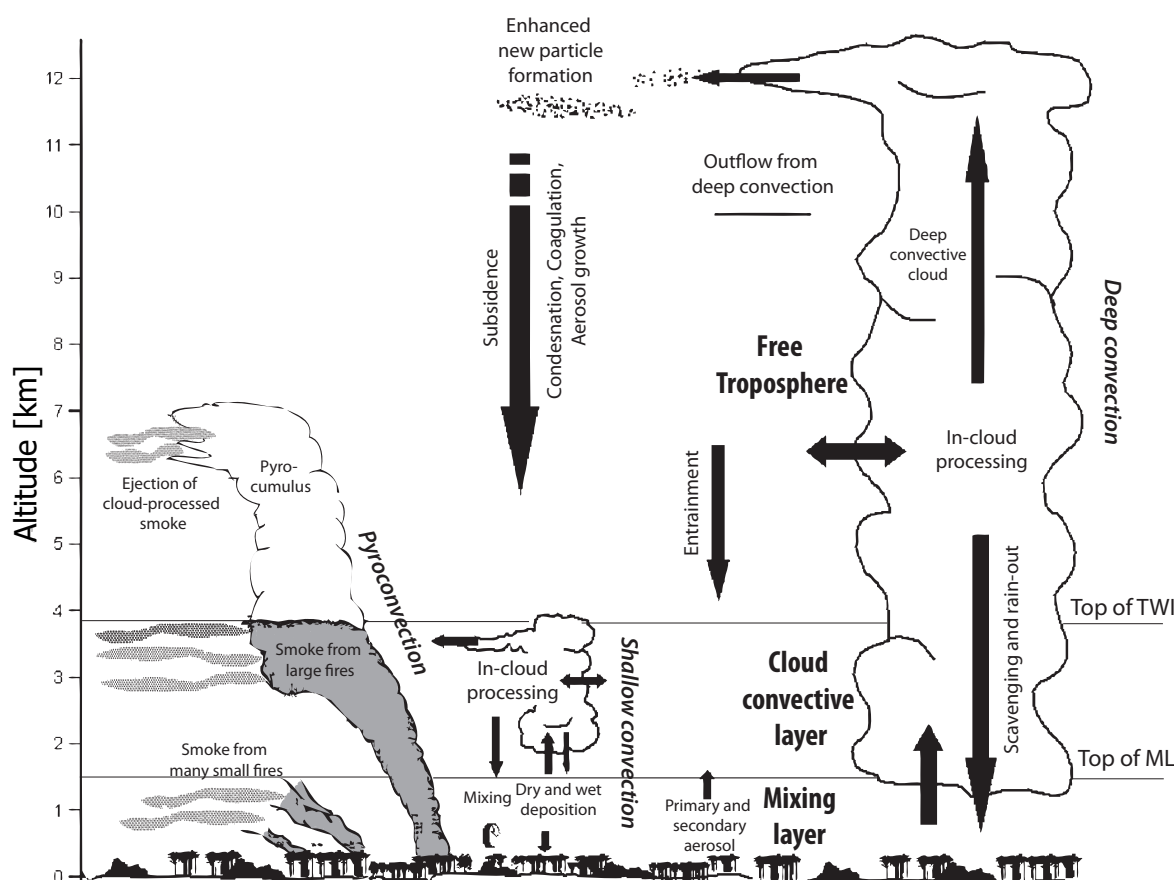


Figure 2.7: Schematic overview of the aerosol distribution and respective transport and transition processes in Amazonia under conditions with high fire activity (modified composite from *Krejci et al.*, 2003 and *Reid et al.*, 1998).

tionally, condensation processes within the smoke plumes favor the updraft of particles and pyro-clouds develop (*Andreae et al.*, 2004).

The horizontal transport of aerosol towards and within Amazonia is determined by the persistent trade winds. Once the aerosol has reached higher altitudes, the strong trade winds can transport the particles over long distances. A schematic overview of aerosol advection towards central Amazonia is shown in Fig. 2.8. During the wet season, the ITCZ is located in southern Amazonia (see Fig. 2.1) and thus north-easterly winds prevail. At this time, advection of marine aerosol, Saharan dust, and African BBA towards Amazonia is possible (e.g., *Artaxo and Orsini*, 1987; *Talbot et al.*, 1990). During the dry season, when the ITCZ is north of the equator (see Fig. 2.1), BBA from fires within South America can be transported to the Amazon Basin (*Artaxo et al.*, 1994).

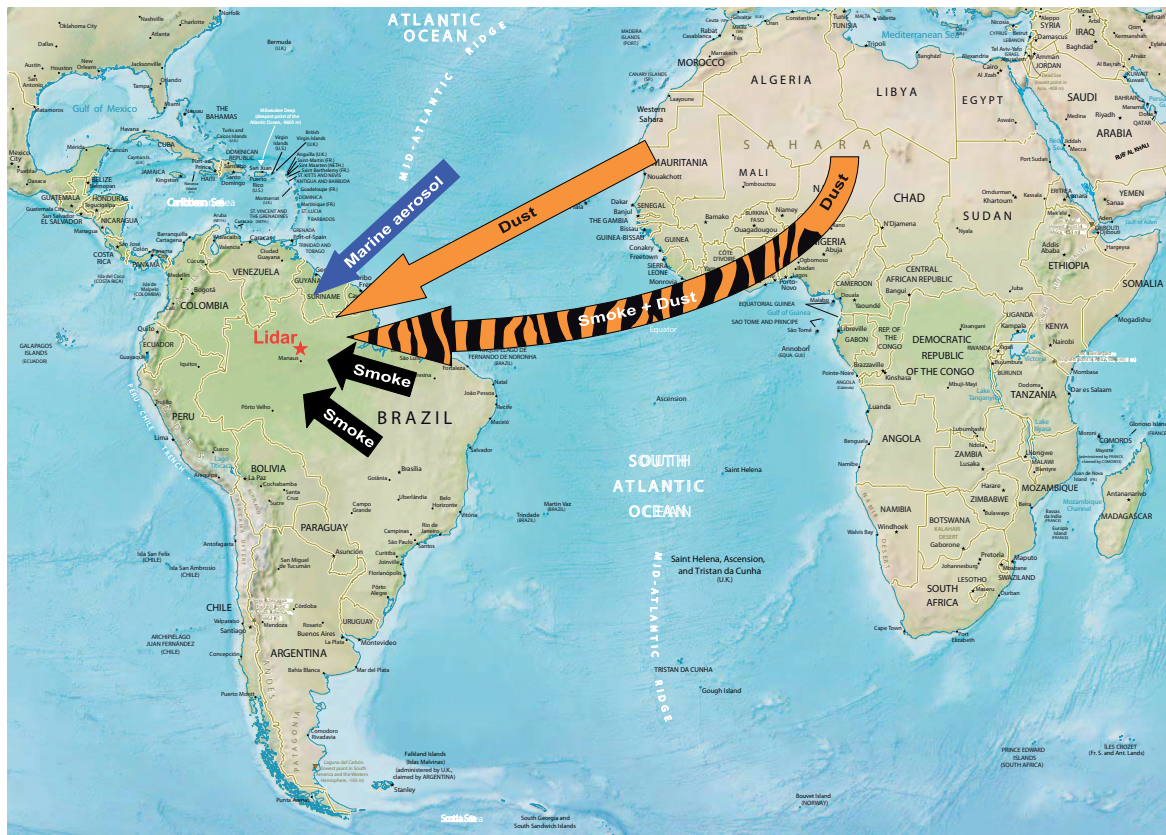


Figure 2.8: Schematic overview of aerosol advection towards the central Amazon Basin.

2.4 Findings from previous experiments

Several field studies have been conducted in the last decades to investigate aerosol conditions in the Amazon Basin. Table 2.1 lists these measurement campaigns together with the respective focus of research and the main reference. In the following, the findings from these field studies and other aerosol research activities relevant for the lidar results discussed in this work are reviewed.

2.4.1 Amazonian aerosol characteristics

Amazonian aerosol is a complex composition of internally and externally mixed aerosol particles. Biogenic aerosol (primary organic and secondary organic aerosols), BBA, urban aerosol, mineral dust, and marine aerosol were observed in the Amazon Basin during the field campaigns listed in Table 2.1. Figure 2.9 summarizes the main aerosol types and their source regions as observed in these previous campaigns. A discrimination between In-Basin and Out-of-Basin sources is made.

#	Campaign	Period	Focus, topic	Reference
1	ABLE 2 a & b (The Amazon Boundary Layer Experiment)	July – August 1985 April – May 1987	Ground-based and airborne observations of trace gases and aerosols	<i>Harriss et al.</i> (1988) <i>Harriss et al.</i> (1990)
2	BASE–A & B (Biomass Burning Airborne and Spaceborne Experiment –Amazonas & –Brazil)	August – September 1989 & 1990	Ground-based, airborne, and satellite observations of trace gases and aerosols	<i>Kaufman et al.</i> (1992) <i>Ward et al.</i> (1992)
3	TRACE–A (Transport and Atmospheric Chemistry near the Equator – Atlantic)	September 1992 (Brazil only)	Airborne observations and satellite remote sensing of trace gases and aerosols in tropical regions of the Earth (Amazonia included)	<i>Fishman et al.</i> (1996)
4	SCAR–B (Smoke, Clouds, Radiation – Brazil)	August – September 1995	Ground-based and airborne observation of biomass burning aerosol	<i>Kaufman et al.</i> (1998a)
5	CLAIRE–98 (Cooperative LBA Airborne Regional Experiment)	March 1998	Ground-based and airborne measurements of biomass burning in the northern hemisphere	<i>Krejci et al.</i> (2003)
6	LBA–EUSTACH 1 & 2 (European Studies on Trace Gas Emissions and Atmospheric Chemistry)	April – May 1999 September – October 1999	Ground-based measurements of background and smoke aerosol	<i>Andreae et al.</i> (2002)
7	LBA–SMOCC (Smoke, Aerosols, Clouds, Rainfall and Climate)	September – November 2003	Airborne and ground-based measurements of biomass burning aerosol	<i>Andreae et al.</i> (2004)
8	AMAZE–08 (The Amazonian Aerosol Characterization Experiment)	February – March 2008	Ground-based in-situ and lidar observations of natural aerosol during the wet season	<i>Martin et al.</i> (2010b)
9	EUCAARI (European Integrated project on Aerosol Cloud Climate and Air Quality Interactions)	2008 – 2009	Ground-based in-situ and lidar measurements of aerosols throughout the year to cover wet and dry seasons	<i>Kulmala et al.</i> (2009, 2011)

Table 2.1: Overview of field campaigns focusing on aerosols in Amazonia since 1985. LBA=Large-Scale Biosphere-Atmosphere Experiment in Amazonia.

In-Basin sources	Out-of-Basin sources
<p>Natural Amazonian aerosol Primary and secondary organic aerosol from the biosphere 1,6,8,9</p>	<p>Saharan dust Mineral dust transported over the Atlantic 1,5,8,9</p>
<p>Amazonian smoke Biomass-burning aerosol from Amazonian fires 1,2,4,5,6,7,9</p>	<p>Sea salt Marine particles from the Atlantic 1,5,8</p>
<p>Urban/industrial pollution Anthropogenic aerosol from cities or industrial areas 5,9</p>	<p>Smoke from Africa Biomass-burning aerosol originating from fires in Central Africa 1,(8),9</p>

Figure 2.9: Overview of the different aerosol types that can be found in the Amazon Basin. A separation between in-Basin and out-of-Basin sources is made. The campaigns (number in the first column of Tab. 2.1) that provide observations of this specific aerosol type are given in addition (lower right corner of each box).

In-Basin aerosols are dominated by natural and anthropogenic emissions from the biosphere (primary and secondary organic aerosols, BBA, *Martin et al.*, 2010a). Urban pollution plays a minor role for aerosol conditions in the Amazon, except downwind of Manaus (the so-called Manaus plume, *Kuhn et al.*, 2010) and other major cities and industrial areas. Intrusions of Saharan dust were frequently reported from observations in the wet season (e.g., *Talbot et al.*, 1990; *Swap et al.*, 1992). Other out-of-Basin sources are BBA from Africa (*Ansmann et al.*, 2009; *Kaufman et al.*, 2005; *Ben-Ami et al.*, 2010) and marine aerosol which are often mixed with Saharan dust (e.g., *Artaxo et al.*, 1990; *Formenti et al.*, 2001). The aerosol particles undergo several transitions processes (e.g., coagulation, condensation, photochemical processes, cloud interaction etc.) during their lifetime and thus the characteristics of aged aerosol may deviate considerably from the properties of fresh or undisturbed aerosol (pure marine, pure dust, pure smoke). In general, the aerosol conditions in Amazonia are very different between the wet season and the dry season.

Wet season

The wet season is characterized by a high frequency of low-level clouds, strong convection, and precipitation. Hence, wet deposition is highest in this season and particles are removed quickly from the atmosphere. Because biomass burning within the Amazon Basin is rare during the wet season (*Artaxo et al.*, 1990), biogenic emissions from the forest are the dominant aerosol source (*Artaxo et al.*, 1988). Since these emissions are comparably low, very clean aerosol conditions with dominance of natural aerosol can be observed. Aerosol number concentration at ground level can then be rather low with average values between 200 and 600 cm^{-3} (*Zhou et al.*, 2002; *Gunthe et al.*, 2009). *Martin et al.* (2010a) hypothesizes by analyzing ground-based in-situ measurements that the Amazon Basin is the only region in the world where it is possible to find at some time aerosol conditions free of anthropogenic influence. *Pöschl et al.* (2010) even state that aerosol conditions in Amazonia's wet season "approach to those of the pristine pre-industrial era." *Schafer et al.* (2008) reported minimum monthly mean values of 0.1 ± 0.06 for the aerosol optical depth (AOD) at 440 nm for such background conditions. *Roberts et al.* (2001) investigated cloud condensation nuclei during the wet season at Balbina (50 km north of the EUCAARI field site) and concluded that aerosol conditions in Amazonia are more "marine" than "continental."

Generally, a low rate of new particle formation was observed (e.g., *Ahlm et al.*, 2009). This implies that the majority of the aerosol populations consist of aged aerosol (possibly a result of long-range transport). *Artaxo and Hansson* (1995) analyzed aerosol samplings from different height levels of a 45 m high tower in a natural reserve near Manaus. The authors found that concentrations of soil dust are lower at the ground than above the canopy and concluded that the tropical rain forest is not a source of soil dust.

Out-of-Basin sources of aerosol in the wet season are Saharan mineral dust (*Swap et al.*, 1992), sea salt (*Artaxo et al.*, 1990), and BBA from Africa (*Kaufman et al.*, 2005). Due to the low natural aerosol load in Amazonia during the wet season, these particles may have an important impact on the radiation budget (direct aerosol effect) and on cloud processes (indirect effect). Saharan dust is the major source of aeolian soil dust in the Amazon Basin. In 1981, *Prospero et al.* (1981), reported for the first time that Saharan dust was observed at the coast of South America. In 1990, *Talbot et al.* (1990), *Artaxo et al.* (1990), and *Artaxo and Maenhaut* (1990) presented results from aerosol measurements made in central Amazonia during the ABLE experiment in 1987 and hypothesized that Saharan dust could even have reached the central part

of the Amazon Basin. *Reichholf* (1986) and *Bristow et al.* (2010) showed that without this transport of nutrients from Africa, the growth of the Amazonian rain forest would be limited. Since the first report of Saharan dust transport towards the Amazon Basin, this phenomenon has been a major topic in Amazonian atmospheric research resulting in many publications (e.g., *Swap et al.*, 1992; *Artaxo et al.*, 1994; *Artaxo and Hansson*, 1995; *Formenti et al.*, 2001; *Koren et al.*, 2006; *Schafer et al.*, 2008; *Prenni et al.*, 2009; *Ben-Ami et al.*, 2010). These investigations are mainly based on aerosol sampling at ground and satellite observations. Thus, almost no information on the vertical distribution and the dust mixing ratio is available. Only *Formenti et al.* (2001) reported extent and height of such dust plumes (see Sec. 2.4.2) from airborne measurements over Suriname (northern Amazonia). Due to new technical possibilities, e.g., the space-borne lidar CALIOP (Cloud-Aerosol Lidar with Orthogonal Polarization),⁵ information on the vertical aerosol structure are now available. For instance, *Ben-Ami et al.* (2010) analyzed the vertical structure of a dust plume moving over the Atlantic Ocean towards Amazonia. Unfortunately, CALIOP measurements over the Amazon Basin are strongly disturbed by enhanced radiation noise, because the Amazon Basin lies in the South Atlantic Anomaly region, where the inner Van Allen radiation belts make their closest approach to the Earth's surface (*Powell et al.*, 2009; *Hunt et al.*, 2009). In addition to the increased radiation noise, high cloud cover over the Amazon Basin prohibits in many cases the retrieval of aerosol profiles in the troposphere from CALIOP data. Thus, long-term ground-based remote sensing in the Amazon Basin is of great importance for aerosol monitoring (i.e., also Saharan dust).

The importance of African BBA for Amazonia, however, remained unknown. One of the first hints regarding smoke transport to South America was given by *Talbot et al.* (1990): “Aerosol chemistry in the wet season is strongly influenced by long-range transport from Saharan dust, marine aerosol, and possibly biomass-burning aerosol from Africa.” *Kaufman et al.* (2005) quantified for the first time the BBA transport from Africa towards Amazonia by using MODIS observations. The authors found that the smoke contribution to the AOD in the mixed BBA/Saharan-dust plumes over the Atlantic Ocean can be as high as almost 50% during the main burning period in Central Africa (January–March). The fact that BBA from Africa clearly influences the aerosol conditions in the Amazon Basin during the wet season is one major finding of this work and will be intensively discussed in Sec. 6.1. Although research showed that BBA is rich in specific elemental nutrients (e.g., *Artaxo et al.*, 1993), the possibility

⁵aboard satellite CALIPSO (Cloud-Aerosol Lidar and Infrared Pathfinder Satellite Observations)

that BBA from Africa also acts as nutrient matter for the Amazon rain forest has not been considered in the literature yet.

Dry season

In the dry season, there is less convection and precipitation than in the wet season and thus the removal of aerosols from the atmosphere is less effective. Hence, locally produced aerosol can be distributed on a regional scale. Due to the high fire activity in Amazonia's dry season (see Sec. 2.2), the aerosol conditions are strongly influenced by BBA from the Amazon Basin and surrounding areas (e.g. *Artaxo et al.*, 1994; *Guyon et al.*, 2003). Particle number concentrations at ground can then reach values up to 40000 cm^{-3} (*Artaxo et al.*, 2002). Mean values for the particle number concentration of 4000 cm^{-3} at surface level were reported during the burning season for the Brazilian state Rondônia (*Guyon et al.*, 2003, for orientation see Fig. 2.3). These values are one or two orders of magnitude larger than the aerosol number concentration in the wet season. Due to the meteorological conditions in the dry season, haze layers which extend over several 100 km can form and persist for several days. For example, *Prins et al.* (1998) reported a smoke pall covering about 7.9 million km^2 in South America in 1995 during SCAR-B as observed from space. This smoke heavily influences the chemical and optical characteristics of the atmosphere in Amazonia (*Andreae et al.*, 1988). As a consequence, clouds need to grow to higher altitudes before precipitation is possible (*Andreae et al.*, 2004; *Freud et al.*, 2008).

The influence of BBA can differ significantly in the various regions in the Amazon Basin. The western and central part (lidar site) of Amazonia are usually assumed to be less affected by anthropogenic fire activity. *Holben et al.* (1996a) analyzed sun photometer measurements at eight different locations in Amazonia and reported a high variability in AOD depending on the region of the measurement. The highest BBA influence was observed in the southern Amazon Basin, where most of the fire activity takes place. *Holben et al.* (1996a) reported monthly averages of the AOD at 440 nm of 1.5 for sites in the southern part of the Amazon Basin during this season. The authors concluded that the observed smoke was usually aged by more than one day. However, they also observed an increased AOD in regions of no or little burning activity during the dry season. Thus, advection of aged smoke towards these sites is important.

BBA can show very different optical and microphysical properties depending on, e.g., the fire type (*Ferek et al.*, 1998) and the age of the particles. Flaming fires are linked to higher burning temperatures than smoldering fires. As a consequence, smaller and

more highly absorbing particles are generated by flaming fires in comparison to smoldering fires (*Müller et al.*, 2005). Coagulation and condensation of gases on the surface of the particles cause a shift in the size distribution towards larger particle radii with time (age). *Reid and Hobbs* (1998) showed that the optical and physical properties can dramatically change during the first minutes after the emission. *Kaufman et al.* (1998a) reported that smoke particles increase their radius by as much as 60% in the first three days in the atmosphere due to condensation and coagulation, reaching a mass median radius of 0.13–0.17 μm . However, the authors found low variation in the particle size distribution of aged smoke. *Reid et al.* (1998) report volume mean diameter (VMD) of smoke particles for different burning types and aging stages in Amazonia. For example, VMD of 0.28 μm for young smoke (older than 4 minutes) from forest fires and of 0.35 μm for smoke hazes were observed. *Martins et al.* (1998) found that the spherical approximation (and therefore Mie theory) for smoke particles older than about 1 hour is reasonably valid for estimating the physical and optical properties of the particles. In general, a low humidification factor was observed for BBA in Amazonia (*Kotchenruther and Hobbs*, 1998).

The optical properties of BBA also show a wide variety due to the different fire types and aging processes. For example, Ångström exponents decrease with the age of the particle ensembles as a consequence of coagulation and condensation (*Müller et al.*, 2007a). *Eck et al.* (2003) analyzed and reported a wide range of Ångström exponents (440–870 nm) for BBA worldwide. Values between 1.1 and 2.1 during conditions with very high smoke aerosol loading ($\text{AOD} > 2$ at 500 nm) were observed.

Reported values of the single-scattering albedo (SSA) of BBA in the Amazon Basin show high variability. *Reid et al.* (1998) found SSA values at 550 nm of 0.79 for young smoke and 0.85 for aged smoke. *Eck et al.* (1998) reported SSA values between 0.81 and 0.94 and *Dubovik et al.* (1998) between 0.79 and 0.95 for BBA in Amazonia at 670 nm. SSA values for pure African smoke observed over the Cape Verde Islands range from 0.63 to 0.89 (*Tesche et al.*, 2011a).

However, radiative effects of a given aerosol layer depend not only on the optical properties of the aerosol layer but also on the presence of clouds (e.g., above a given aerosol layer) and the surface albedo (*Haywood and Shine*, 1997). *Ross et al.* (1998) performed radiative-transfer calculations and found that regional smoke haze over Amazonia lead to a negative radiative forcing in the short-wavelength range. The negative radiative forcing was found to be stronger over forest (dark surface) than over cerrado (less dark surface).

For improved radiative-forcing calculations a detailed knowledge of the aerosol properties in the vertical column over Amazonia on a statistical basis is necessary. The height-resolved observations presented in this work further contribute to this field of research.

2.4.2 Vertical aerosol distribution

Concerning the vertical aerosol layering over Amazonia most knowledge is based on a few snapshot-like airborne measurements performed during specific experiments. No long-term observations of the vertical aerosol structures have been conducted before 2008. In 2003, a micropulse lidar⁶ was operated in Rondônia during the dry season for two months. However, results were not published. In this section, the major findings from the airborne observations performed during the field campaigns listed in Table 2.1 are summarized.

Andreae et al. (1988) present airborne lidar and in-situ measurements made during ABLE 2a in northern Brazil near the Amazon river during the dry season in 1985. They found frequently smoke and haze layers between 1 and 5 km agl (above ground level). The pronounced haze layers had a vertical depth of about 100–300 m and extended over several hundred kilometers. Multiple layers of aerosol were frequently observed during 11 research flights. *Browell et al.* (1988) analyzed the same flights and found that under undisturbed conditions about two thirds of the aerosol loading are within the ML and that the aerosol distribution above the ML is very inhomogeneous. The airborne lidar used in this campaign was a DIAL (differential absorption lidar) which is designed for ozone observations. As a consequence, the authors only present the temporal evolution of aerosol backscatter intensity and thus no quantitative aerosol properties.

Airborne in-situ observations up to 4 km agl focusing on BBA were performed in the frame of TRACE-A in August/September 1992 (*Pereira et al.*, 1996). Six flights for vertical aerosol profiling were performed. It was found that the particle mass concentration in areas of high fire activity peaked at around 2500 m agl. A maximum particle number concentration of 16000 cm⁻³ was observed. Increased particle concentrations often coincided with temperature inversions and were generally found between 2000 and 3000 m for these six flights.

During the SCAR-B experiments (*Kaufman et al.*, 1998a), three different aircraft were available for airborne observations. Eleven flights were performed with a downward-

⁶The Micropulse Lidar Network: <http://mplnet.gsfc.nasa.gov>

looking standard backscatter lidar. Further 29 flights were conducted to characterize the optical and microphysical properties of young and aged smoke in the Amazon Basin by means of in-situ measurements (*Reid et al.*, 1998; *Reid and Hobbs*, 1998). However, most observations during this experiment with a focus on the dry season were performed in the southern cerrado regions and thus may not be representative for the Amazon rain forest. The research flights revealed that properties of aged smoke are significantly different from that of young smoke. Ångström exponents varied from 1.2 to 2.5 for different smoke layers. The flights showed also that above the ML top very often a second temperature inversion (i.e., TWI) was found below which the aerosol was trapped. The top height of this CCL (see Sec. 2.3) was found to be between 2.1 and 4.1 km. *King et al.* (1998) analyzed heavy smoke layers by airborne lidar measurements during the same experiment and found that aerosol was vertically confined on a large scale from the surface up to 3–5 km height.

Formenti et al. (2001) present results from airborne observations made during CLAIRE-98 in Suriname and Brazil in March 1998. Two cases with intrusions of Saharan dust and sea salt were observed. The dust extended from the ground up to a pressure level of 650 hPa (about 3500 m above sea level (asl)). On one day, the scattering maximum of the dust was close to the ground, on another day it was at around 750 hPa (about 2300 m asl). A sporadic enhanced carbon-monoxide concentration at 400 hPa (about 7400 m asl) was associated with smoke from vegetation fires in Central America and Venezuela. *Andreae et al.* (2001) analyzed the airborne measurements during this campaign and found increased concentrations of trace gases and aerosol above 10 km asl. After analyzing trajectories, *Andreae et al.* (2001) hypothesized that the aerosol found at these high altitudes originated from savanna fires at the edges of Amazonia. According to this hypothesis, the smoke was transported to interior regions of the Amazon Basin by the trade winds and there it was lifted by deep convection to high altitudes. Then the BBA was transported by the high-altitude circulation back to the edge regions of Amazonia where the measurements took place. It was speculated that 80%–95% of the accumulation-mode particles had been removed – most probably by wet deposition during the deep convective transport to the upper troposphere. Measurements of the particle size distributions also implied that new particle formation occurs at the edges of cumulonimbus clouds at high altitudes (*Krejci et al.*, 2003).

During LBA-SMOCC, several research flights with in-situ instrumentation were performed in Rondônia (south-west Amazonia, mostly cerrado) during September–

November 2002. *Chand et al.* (2006) discussed the optical and physical properties of smoke within and above the ML from these airborne and ground-based in-situ measurements. They found that scattering of aerosols increased from the surface to the FT by 2–10 times due to aging (coagulation and condensation). The authors concluded that aging plays a major role for the optical and microphysical properties of Amazonian smoke aerosol. *Guyon et al.* (2005) analyzed airborne temperature profiles during the same campaign and found that the afternoon ML top height is between 1350 and 1900 m agl over the mostly cerrado-covered area. The authors also found that vertical transport of smoke from the ML to the cloud convective layer and the FT above is a very common phenomenon, and that the reduction of the particle number concentration during this transport is of the order of 20% only. Thus, they conclude that non-precipitating clouds play an important role regarding the lifting of aerosol particles above the ML. *Guyon et al.* (2005) also observed that smoke particles above the ML were larger than particles unprocessed by clouds.

Despite these airborne and ground-based measurement activities conducted during the field campaigns listed in Table 2.1, a representative picture of the aerosol conditions over the Amazon rain forest including the vertical transport, mixing and aging processes was not available. As a next step of research, long-term observational studies were proposed. Thus, in the framework of EUCAARI, the first long-term study with an advanced aerosol lidar was performed in the Amazon Basin.

Chapter 3

Experiment: Location, instrumentation, and observations

Measurements of aerosol properties were performed in the Amazon rain forest in Brazil from 2008 to 2009 in the framework of the European Integrated Project on Aerosol, Cloud, Climate, Air Quality Interactions (EUCAARI, *Kulmala et al.*, 2009, 2011). Besides several ground-based in-situ aerosol observations, the Leibniz Institute for Tropospheric Research, Leipzig, Germany performed lidar observations with the automated multiwavelength-Raman-polarization lidar Polly^{XT} from January to November 2008. In this Chapter, information about the field site is given followed by a detailed description of the technical setup of Polly^{XT}. Last but not least, an overview of the lidar measurements taken in Amazonia is provided.

3.1 Field site

The location of the lidar field site is shown in Fig. 3.1 (left). The polarization-Raman lidar Polly^{XT} (Sec. 3.2) was situated at 2° 35.9' S and 60° 2.3' W at 83 m asl in the central northern part of the Amazon Basin. Local time is UTC – 4 hours. Figure 3.1 (right) shows a detailed view of the measurement area. The observations were performed 60 km north of downtown Manaus and the Amazon river at the Silvicultura research site of the National Institute for Amazonia Research (INPA). About 17 km west of the lidar location, the EUCAARI in-situ measurements were performed using several research towers. Because the main wind direction is east to north-east, advection of pollution from the two-million-inhabitants city Manaus (the so-called Manaus plume) is not expected at the field site (e.g., *Kuhn et al.*, 2010). Regular radiosonde

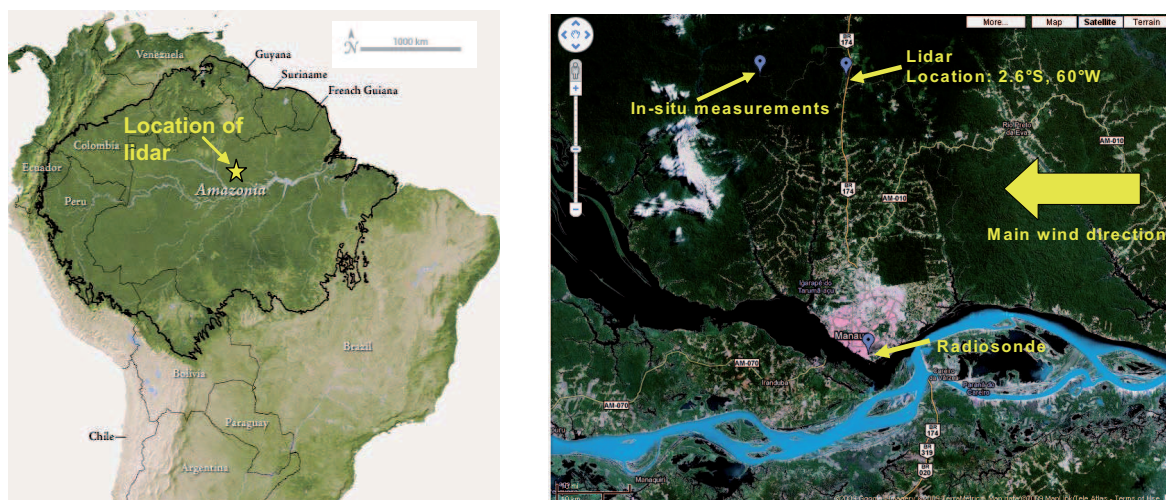


Figure 3.1: Left: Map of northern South America showing the location of the measurements (yellow star). Map source: <http://earthobservatory.nasa.gov>. Right: Satellite image of the experimental area. Lidar site, in-situ field sites, and location of radiosonde launches are indicated. Source: Google maps.

launches have been performed every 12 hours (0000 UTC and 1200 UTC) at the military airport of Manaus in the south of the city.

Figure 3.2 shows a photograph of the field site. The lidar was placed on a glade surrounded by pristine tropical rain forest. Polly^{XT} is on the right side in the photograph behind a tent for the operators. The satellite dish in the middle of the picture was used to maintain Polly^{XT} remotely via internet connection. An AERONET (Aerosol Robotic Network, *Holben et al.*, 2001) sun photometer was placed next to the lidar on a 15 m high tower (left in Fig. 3.2). This sun photometer was operated by the Institute of Physics of the University of São Paulo and analyzed data is available at the AERONET web site¹ (site name: Manaus).

In parallel to EUCAARI, the Amazonian Aerosol Characterization Experiment (AMAZE-08, *Martin et al.*, 2010b) took place at the same locations in February and March 2008. Additional instruments for aerosol and gas investigations were operated during that time.

¹<http://aeronet.gsfc.nasa.gov/>

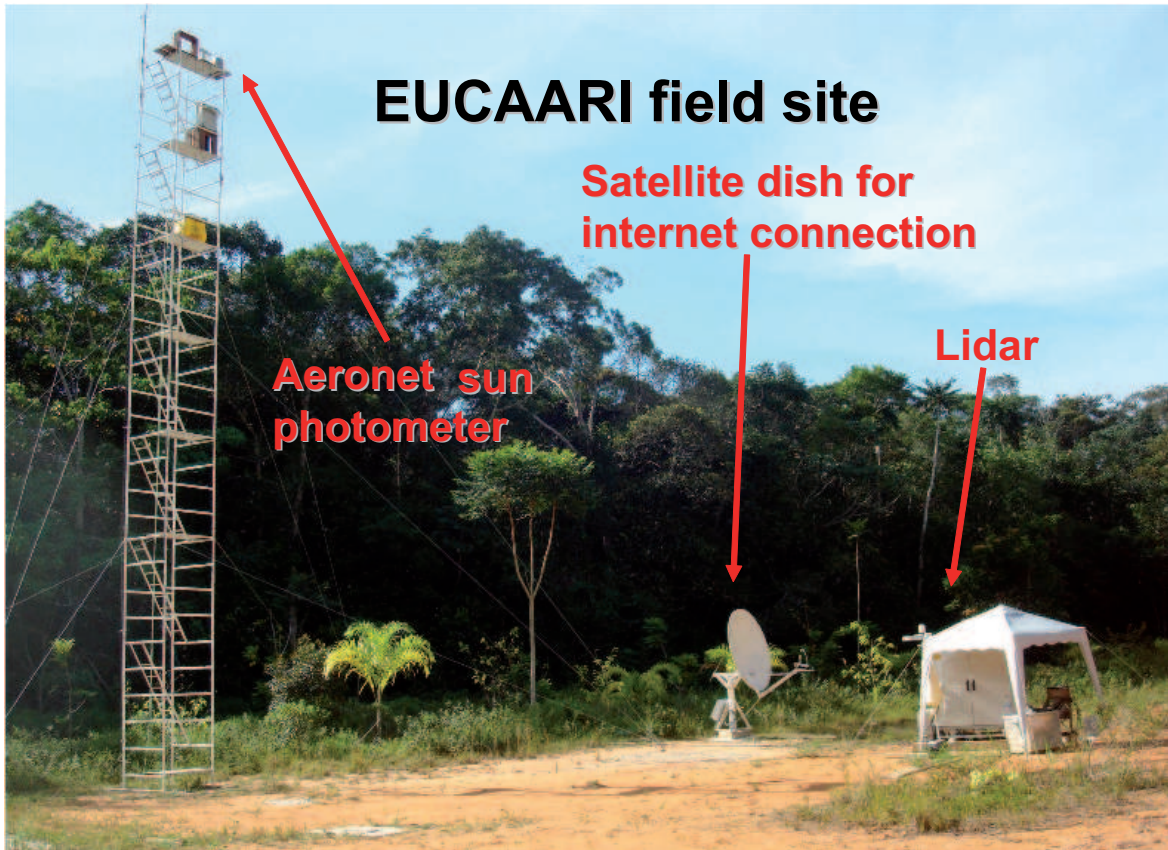


Figure 3.2: Lidar field site in the Amazon rain forest: The lidar (right), the satellite dish for the internet connection (middle), and the AERONET sun photometer on the top of a tower (left) can be seen.

3.2 Polly^{XT}

Polly^{XT} (**P**ortable lidar system **eXT**ended) is a compact automated multiwavelength-polarization-Raman lidar. An overview of the main features of this lidar is presented in Table 3.1. The lidar emits light at three wavelengths and has seven detection channels. This lidar is a so-called 3+2+1 system which means that the backscatter coefficient is determined at three wavelengths, the extinction coefficient at two wavelengths, and the depolarization ratio at one wavelength. Such systems are state of the art in lidar research but mostly not automated. In addition to these standard detection schemes, one fast analog channel is installed in the lidar. For the independent determination of backscatter and extinction coefficients, the Raman lidar method (*Ansmann et al.*, 1992) is applied. At daytime, when the Raman channels cannot be used, backscatter coefficients are retrieved with the Fernald-Klett algorithm (*Klett*,

Emitter					
Laser type			Nd:YAG Continuum Inlite III		
Simultaneously emitted @ 20 Hz			180 mJ/pulse (1064 nm) 110 mJ/pulse (532 nm) 60 mJ/pulse (355 nm)		
Beam expansion for all wavelengths			1:7.5 (beam diameter from 6 to 45 mm)		
Divergence after beam expansion			<0.2 mrad		
Receiver					
Newtonian telescope					
Diameter of main mirror			30 cm		
Focal length			90 cm		
Receiver field of view			1 mrad		
Signal detection					
Channel notation	Detected backscatter signal	Detection mode	Central wavelength (nm)	Max. filter transmission (%)	Filter bandwidth (FWHM, nm)
355	elastic	photon counting	354.68	72	0.94
355s	cross-polarized elastic	photon counting	354.68	72	0.94
387	N ₂ Raman	photon counting	386.73	68	0.34
532pc	elastic	photon counting	532.06	70	1.12
532a	elastic	analog	532.06	70	1.12
607	N ₂ Raman	photon counting	607.4	82	0.31
1064	elastic	photon counting	1064.09	79	1.15
Detection mode		Temporal resolution		Spatial resolution	
photon counting		30 sec		30 m	
analog		5 sec		7.5 m	

Table 3.1: Overview of main Polly^{XT} specifications.

1981; *Fernald*, 1984). From these measured extensive quantities, intensive particle properties like the lidar ratio (ratio of extinction to backscatter coefficient) and the Ångström exponents can be calculated. The volume and particle depolarization ratio is determined with the linear-polarization lidar method (*Murayama et al.*, 1999). Furthermore, microphysical properties, e.g., effective radius, can be retrieved via inversion (*Müller et al.*, 1999a). A full description of the lidar data analysis and the resulting products is provided in Chapter 4. However, for the understanding of the data analysis, an introduction into the technical setup of Polly^{XT} is essential and is given in the following.

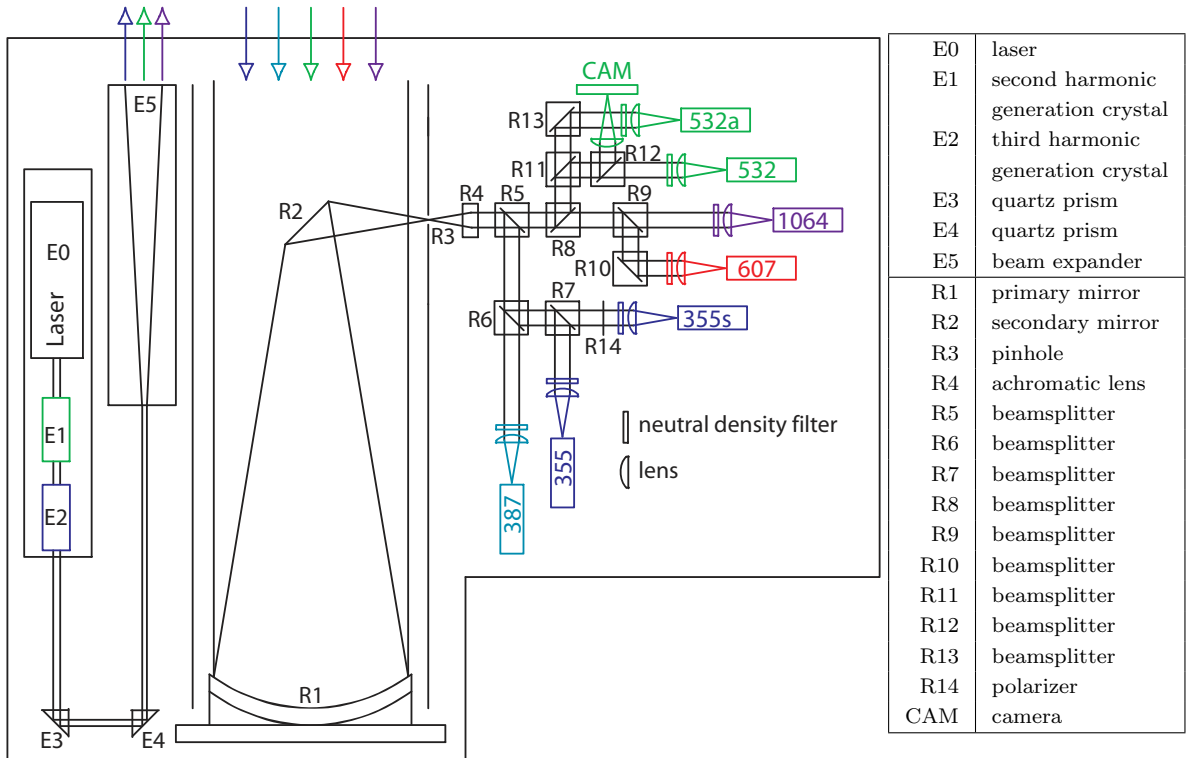


Figure 3.3: Optical set-up of Polly^{XT}. Details are explained in the text.

A full description of Polly^{XT} is presented in *Althausen et al.* (2009), from which the following information is extracted without explicit citing.

A schematic sketch of the optical setup of Polly^{XT} is shown in Fig. 3.3. The emitter and receiver optical parts are indicated with 'E' and 'R', respectively. As light source a Nd:YAG laser of type Inlite III from Continuum (E0 in Fig. 3.3) is used. This laser emits light pulses at 1064 nm with a repetition rate of 20 Hz (see Table 3.1). The total energy per laser pulse is about 450 mJ. The divergence of the emitted laser beam before beam expansion is less than 1.5 mrad. By using second-harmonic-generation (E1) and third harmonic generation (E2) crystals, parts of the light are transformed to light pulses at 532 and 355 nm, respectively. Thus, light at 355, 532, and 1064 nm is emitted simultaneously. The resulting energy of the emitted light pulses is approximately 180 mJ at 1064 nm, 110 mJ at 532 nm, and 60 mJ at 355 nm. The emitted radiation is linearly polarized at 355 and 532 nm. With two quartz prisms (E3 and E4), the beam is directed into the achromatic beam expander (E5), where the beam diameter is enlarged from about 6 mm to about

45 mm (a factor of 7.5). This leads to a divergence of the beam of less than 0.2 mrad. The beam is then transmitted into the atmosphere.

Backscattered light from the atmosphere is collected with a Newtonian telescope (R1 and R2). Technical details of the telescope are listed in Table 3.1. The pinhole (R3) defines the receiver field of view of 1 mrad. Behind the pinhole an achromatic lens (R4; focal length = 60 mm) collimates and transmits the light to the seven detection channels and a camera (CAM). Dichroic beamsplitters (R5, R6, R8, and R9) separate the light according to its wavelengths. The beamsplitter R7 transmits 70% of the light intensity at 355 nm to the channel that is used for detecting the cross-polarized backscattered light and reflects 30% of the intensity to the channel that is used for detecting the unpolarized backscattered light at 355 nm. The beamsplitters R11 and R12 have a transmission of 50% and a reflectivity of 50% reflection at 532 nm. The beamsplitters R13 (532 nm) and R10 (607 nm) are used to head the light into the pertinent detectors. R14 is a polarizer which ensures only the transmission of cross-polarized light at 355 nm. An overview of the seven detection channels regarding detected light and detection mode as well as the optical specifications of the used interference filters is given in Table 3.1. Planoconvex lenses are used in front of all detectors to focus the received light on the photocathode of the photo multiplier tubes (PMT). Absorptive neutral-density filters are installed in front of each detection channel to attenuate the received light to proper count rates. The filter strength for each channel can change during the operation of the system due to different atmospheric conditions, alternating laser power, etc. The maximum count rate of the PMTs is kept below 10 Mcps to avoid dead-time effects (*Donovan et al.*, 1993; *Wandinger*, 2005a). The signals of the photon-counting PMTs are adapted to the data acquisition (DAQ) cards by preamplifiers. The data are acquired with three 2-channel photon-counting cards. These cards have a 400 MHz count rate capability and 200 ns bin width. A temporal and spatial resolution of the detected signal of 30 s and 30 m, respectively, is used. The analog detected signals have a spatial and temporal resolution of 7.5 m and 5 s, respectively. The DAQ is triggered by a fast photodiode which responds to the laser pulse. All data are stored in Network Common Data Form (NetCDF). The CAM is used for the adjustment of the laser beam to the field of view of the telescope.

Fig. 3.4 shows Polly^{XT} with opened doors. All optical and electronic devices are mounted in a weather-proof, thermally insulated cabinet. The dimensions are approximately 1.8 m height, 1.44 m width, and 0.8 m depth. Two quartz plates



Figure 3.4: Cabinet with open doors showing the major parts of Polly^{XT}. 1: roof cover, 2: sensors for outdoor temperature, air pressure, and rain, 3: air condition, 4: uninterruptible power supply, 5: computer with data acquisition, 6: laser power supply, 7: laser head, 8: beam expander, 9: receiver telescope, and 10: receiver with seven channels.

are installed as windows at the roof of the cabinet to guarantee no air exchange with the environment but the undisturbed penetration of the emitted and received light. These quartz plates can be protected with an automatic roof cover (1 in Fig. 3.4). Furthermore, a precipitation sensor (2) is installed on the roof of the cabinet and is connected to the roof cover (1) and the main computer (5). When the sensor detects precipitation, the roof cover is closed and a signal is sent to the data acquisition software which in turn shuts down the laser and ends the measurement. Air temperature and pressure are recorded continuously at about 2 m height above the ground (2). The inverter air condition system (3) consists of an inner and an outer part and is needed to maintain a stable temperature within the cabinet. Inside

the cabinet, an uninterruptible power supply (4) is installed to ensure a proper power supply and to bypass short power failures. The main computer (5) and the laser power supply (6) are connected to the uninterruptible power supply. The optical board with the laser (7), the beam expander (8), the receiver telescope (9), and the 7-channel receiver unit (10) is mounted in such a way that all measurements are made at an off-zenith angle of 5° .

The measurements are performed automatically controlled by a computer. According to the measuring schedule, the DAQ software opens the roof, starts the laser, monitors the system status, starts data acquisition, and records the data. During the measurement, the temperature inside the cabinet is monitored with two temperature sensors and the laser power is monitored with an external power meter.

The automated, continuous measurements in Brazil were controlled remotely via internet. This allowed the control of the system and, e.g., the change of the measurement schedule. Local scientists assisted in maintaining the lidar (e.g., cleaning of the quartz window), and performed small reparations.

3.3 Overview of observations

The lidar observations at the EUCAARI site in Brazil started on 22 January 2008 and lasted until 11 November 2008. An overview of days at which measurements were performed is given in Fig. 3.5. This timetable is available on the webpage polly.tropos.de, where all data are collected. The temporal developments of the lidar measurements (height-time displays of the range-corrected signal, see, e.g., Chapter 6) are accessible for each observation day at this public domain. During the 10-months observational period, lidar measurements could be performed on 211 days resulting in more than 2500 hours of tropospheric aerosol and cloud profile observations. Thus a very high coverage in terms of observation days could be achieved (Fig. 3.6). A severe laser malfunction, however, interrupted the measurements in June/July for six weeks. For the rest of the observation period, only minor interruptions occurred due to, e.g., air-condition problems or power failures. Consequently both the wet and the dry season were sufficiently covered with lidar observations. Short-term interruptions were sometimes caused by insects which were attracted by the laser beam (see Fig. 3.7, upper right picture). These insects flew through the rain sensor and apparent rain fall was detected. In such cases, the measurements were automatically interrupted for 30 to 120 seconds only. Fortunately, these short-term interruptions occurred not very fre-

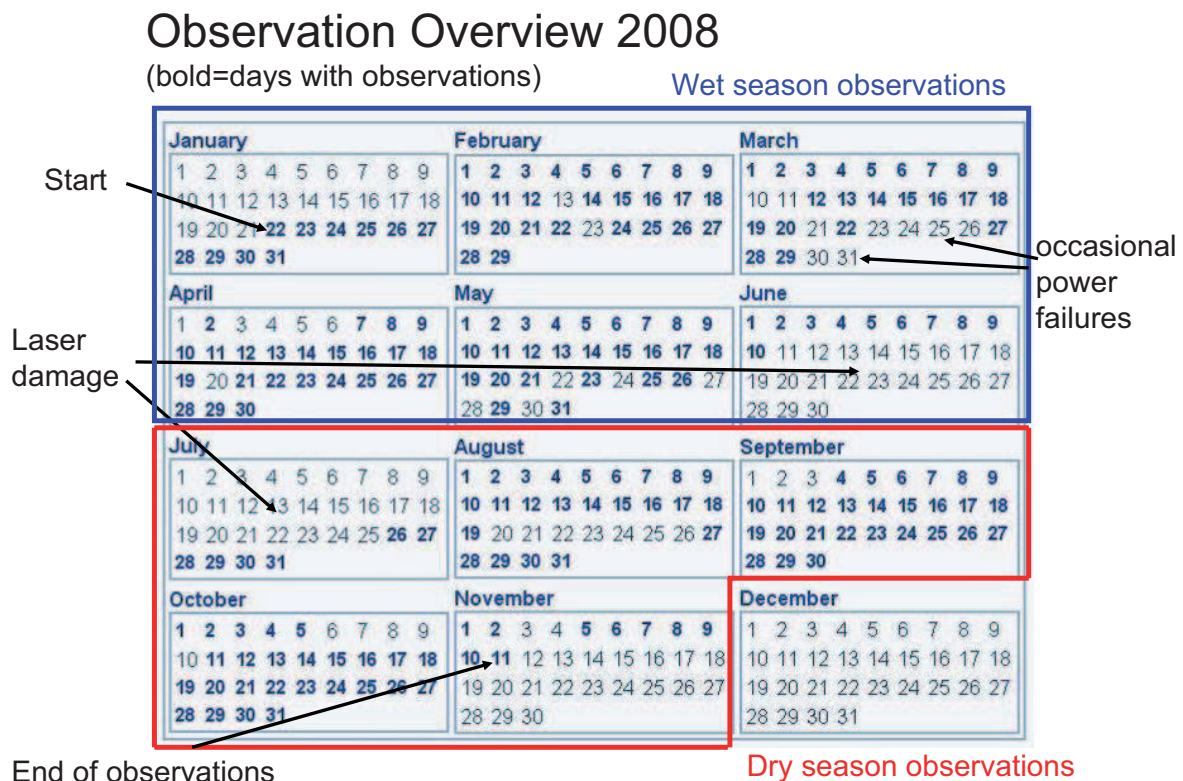


Figure 3.5: Overview of observations with Polly^{XT} in Brazil. Image taken from polly.tropos.de. Bold days are days with measurements. A large measurement gap due to a laser damage occurred in June–July.

quently and, hence, did not significantly disturb the data analysis.

All the different aerosol conditions which can be found in the Amazon rain forest were measured during the 10-months observational period. Nevertheless, fog development during night time at the canopy level (see Fig. 3.7, lower left picture) prohibited a detailed analysis of many wet-season observations. During daytime, the high frequency of low-level clouds and rain (Fig. 3.7, the two lowermost right pictures) often prevented the determination of vertical aerosol profiles. Fog, low-level clouds, and rain disturbed the lidar observations also during the dry season. However, the frequency of occurrence of such events was much lower than during the wet season.

Instrumental problems (e.g., air-condition problems, overlap problems, wrong adjustment of trigger levels and not working PMT's) occurred several times and caused that data from certain channels could not be used for analysis. Thus, not all data products are available for every observation case.

The results presented in this work are finally based on 60 wet-season and 55 dry-season

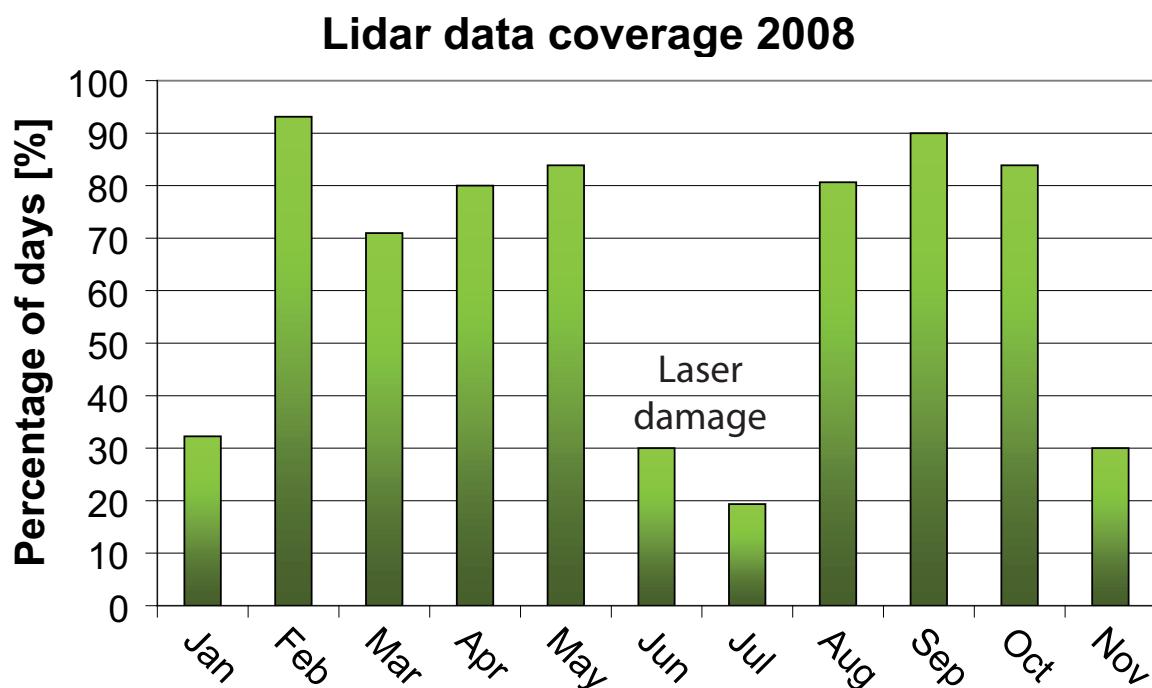


Figure 3.6: Lidar data coverage for the Amazonian measurements in 2008. The ratio of observation days to the total days per month is shown. Measurements began on 22 January and were terminated on 11 November, thus 100% coverage was not possible for these months. A severe laser crash caused the low data coverage in June and July.

observation cases. However, for most of the wet-season cases, a too low signal-to-noise ratio and problems with the overlap of the receiver field of view and the laser beam prohibited the independent evaluation of the extinction coefficient from the Raman channels (Sec. 4.2.1). Thus, for most wet-season cases, the AOD is retrieved from the elastic channel by assuming a constant extinction-to-backscatter ratio (see Sec. 4.2.4). For the dry-season cases, mostly all products of Polly^{XT} were available. Further impressions from the field campaign, also showing some “biological disturbances”, are presented in Fig. 3.7. The lidar observations are presented and discussed in form of representative case studies (Chapter 6) and in form of statistical results based on the entire set of measurements (Chapter 7).

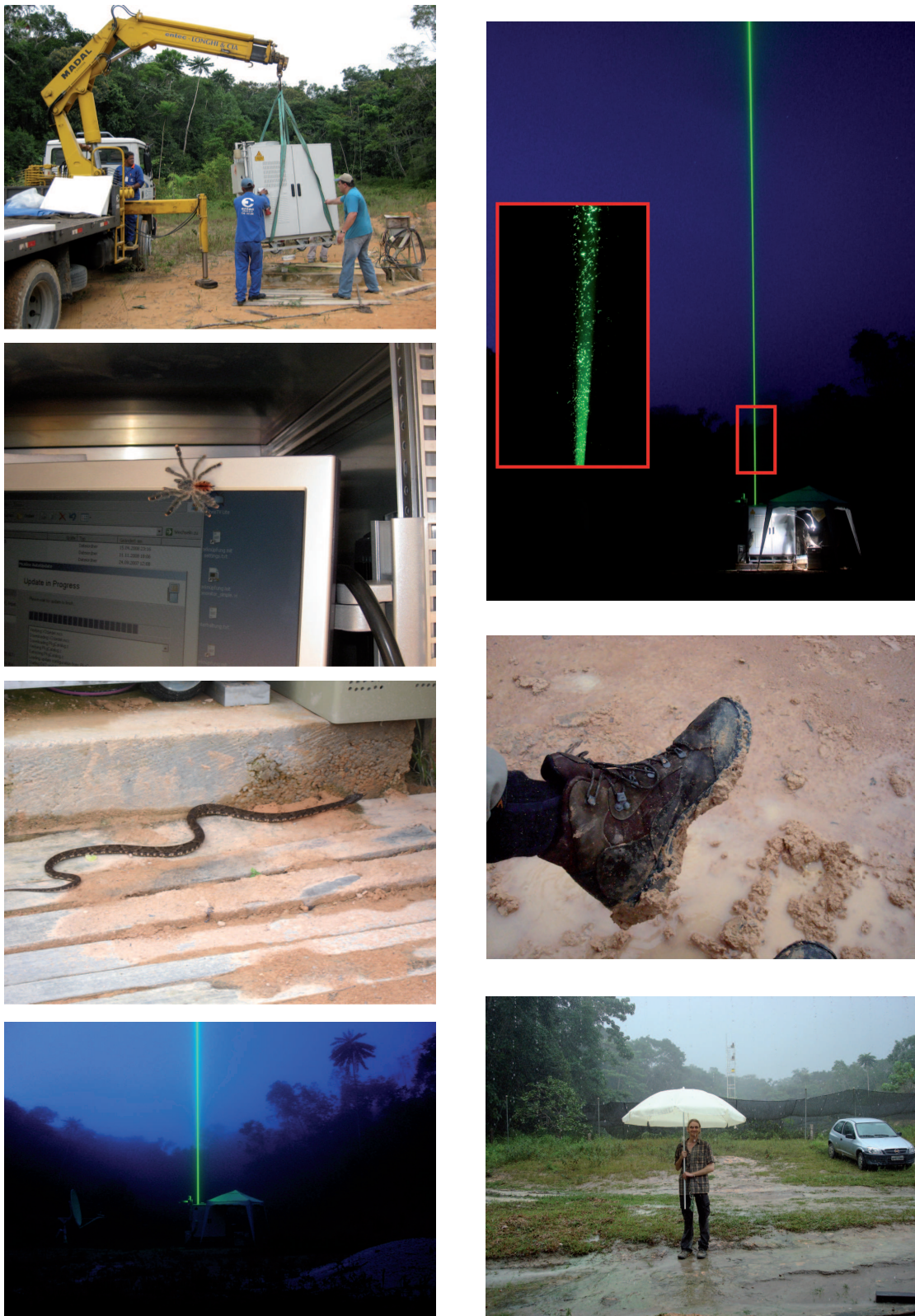


Figure 3.7: Impressions from the EUCAARI lidar campaign in Amazonia in 2008.

Chapter 4

Lidar methodology

Table 4.1 gives an overview of the possible aerosol products derived from Polly^{XT} measurements. In this Chapter, an introduction into the basic lidar theory and the lidar retrieval methods applied in this work is given. Some parts of the lidar theory and the lidar algorithms have been already discussed in *Baars* (2007) and are adopted without explicit citing.

Parameter	Symbol	Remarks
Backscatter coefficient	β^{par}	@ 355, 532, 1064 nm
Extinction coefficient	α^{par}	@ 355, 532 nm
Linear depolarization ratio	δ^{par}	@ 355 nm
Lidar ratio	$S_{\text{par}} = \frac{\alpha^{\text{par}}}{\beta^{\text{par}}}$	@ 355, 532 nm
Ångström exponent	\AA	α and β related
Volume size distribution		via inversion
Effective radius	r_{eff}	via inversion
Number, surface, and volume conc.		via inversion
Complex refractive index		via inversion
Single scattering albedo (SSA)		via inversion and Mie code

Table 4.1: Overview of particle optical and microphysical properties that can be derived from the multi-wavelength lidar observations with Polly^{XT}.

4.1 Lidar principle and equations

Lidar is the acronym for **l**ight **d**etection and **r**anging. A laser pulse is emitted into the atmosphere and the signal backscattered by molecules and particles is detected with the receiver unit with a high temporal resolution. The distance z between the lidar and the scattering volume in the atmosphere can be calculated with the speed of light c and the time t between the emission of the laser pulse and the detection of the returned light:

$$z = \frac{tc}{2}. \quad (4.1)$$

The received power due to elastic backscattering at the emission wavelength λ can be described with the lidar equation (e.g., *Wandinger, 2005b*):

$$P_{\lambda_0}(z) = P_0 \frac{O(z)}{z^2} C_s(\lambda_0) \beta_{\lambda_0}(z) \exp \left[-2 \int_0^z \alpha_{\lambda_0}(\zeta) d\zeta \right]. \quad (4.2)$$

The power P_{λ_0} received from the range z depends on the emitted power P_0 at wavelength λ_0 , the overlap function $O(z)$, a height-independent system constant $C_s(\lambda_0)$, the volume backscatter coefficient $\beta_{\lambda_0}(z)$ of the backscattering volume, and the volume extinction coefficient $\alpha_{\lambda_0}(z)$ between the backscattering volume and the lidar.

$O(z)$ describes the overlap between the laser beam and the field of view of the receiver (see Sec. 5.1). Close to the lidar there is no overlap and thus $O(z) = 0$. The distance at which a complete overlap is achieved ($O(z) = 1$) depends on the individual lidar system (transmitter-receiver configuration). Values vary between a few tens of meters and several thousand meters for this distance. $C_s(\lambda_0)$ represents the wavelength-dependent system efficiency. It contains all information about the performance of the individual system components (size of the telescope area, transmission of the optics at λ_0 , efficiency of detectors, etc). $\beta_{\lambda_0}(z)$ is the volume scattering coefficient for the scattering angle of 180° and has the dimension of $\text{m}^{-1}\text{sr}^{-1}$. The exponential term (transmission term) describes the attenuation of light by scattering and absorption on its way through the atmosphere. According to the Lambert–Beer–Bouguer law, the transmission depends on the volume extinction coefficient $\alpha_{\lambda_0}(z)$ and the length of the light path, which is in case of lidar twice the distance between the instrument and the backscattering volume. $\alpha_{\lambda_0}(z)$ is given in m^{-1} . The lidar equation (Eq. 4.2) is the basic equation for the retrieval of particle properties when using an elastic backscatter lidar (see methods in Sec. 4.2.2).

In the case of a Raman lidar, the inelastically backscattered light caused by Raman scattering from atmospheric molecules (e.g., nitrogen) is measured in addition to the

elastically backscattered light (see method in Sec. 4.2.1). The received power due to inelastic scattering at the Raman wavelength λ_{Ra} is described by

$$P_{\lambda_{\text{Ra}}}(z) = P_0 \frac{O(z)}{z^2} C_s(\lambda_{\text{Ra}}) \beta_{\lambda_{\text{Ra}}}(z) \exp \left[- \int_0^z \alpha_{\lambda_0}(\zeta) + \alpha_{\lambda_{\text{Ra}}}(\zeta) d\zeta \right], \quad (4.3)$$

with the molecular backscatter coefficient for vibrational-rotational scattering $\beta_{\lambda_{\text{Ra}}}(z)$ at the shifted wavelength λ_{Ra} . The transmission term considers light extinction on the way to the backscattering volume at λ_0 and on the way back to the lidar at the shifted wavelength λ_{Ra} .

The atmospheric volume backscatter and extinction coefficients consist of molecular (superscript mol) and particle (superscript par) contributions and are defined as:

$$\alpha(z) = \alpha^{\text{mol}}(z) + \alpha^{\text{par}}(z) \quad (4.4)$$

and

$$\beta(z) = \beta^{\text{mol}}(z) + \beta^{\text{par}}(z). \quad (4.5)$$

The relationship between the extinction and the backscatter coefficient defines the lidar ratio for the atmospheric particles and molecules:

$$S^{\text{par}}(z) = \frac{\alpha^{\text{par}}(z)}{\beta^{\text{par}}(z)} \quad (4.6)$$

and

$$S^{\text{mol}}(z) = \frac{\alpha^{\text{mol}}(z)}{\beta^{\text{mol}}(z)}. \quad (4.7)$$

The polarization state of the received light can be used to gain information on the sphericity of the particles. This is possible since the emitted laser light is linearly polarized. In order to retrieve the volume and particle depolarization ratio, the backscattered light vertically polarized (superscript \perp) with respect to the polarization plane of the emitted laser light is detected in addition to the unpolarized (no superscript) and/or the parallel-polarized (superscript \parallel) backscattered light component (more details in Sec. 4.2.6):

$${}^{\perp}P_{\lambda_0}(z) = P_0 \frac{O(z)}{z^2} {}^{\perp}C_s(\lambda_0) {}^{\perp}\beta_{\lambda_0}(z) \exp \left[-2 \int_0^z \alpha_{\lambda_0}(\zeta) d\zeta \right] \quad (4.8)$$

and

$${}^{\parallel}P_{\lambda_0}(z) = P_0 \frac{O(z)}{z^2} {}^{\parallel}C_s(\lambda_0) {}^{\parallel}\beta_{\lambda_0}(z) \exp \left[-2 \int_0^z \alpha_{\lambda_0}(\zeta) d\zeta \right]. \quad (4.9)$$

The received signals ${}^{\parallel,\perp}P_{\lambda_0}$ for parallel and cross-polarized light depend on the corresponding backscatter coefficient ${}^{\parallel,\perp}\beta_{\lambda_0}$ and the polarization-plane-dependent system efficiency ${}^{\parallel,\perp}C_s(\lambda_0)$. The emitted power P_0 and the transmission term are identical for Eq. 4.8 and 4.9. Also the overlap function $O(z)$ is assumed to be equal for both channels when the system is well designed and aligned.

4.2 Lidar methods

In this section, the evaluation methods for particle parameter as listed in Table 4.1 are briefly summarized. First, the retrieval of the particle backscatter and extinction coefficients with the Raman (*Ansmann et al.*, 1990; *Ansmann et al.*, 1992) and Fernald/Klett (*Fernald*, 1984; *Klett*, 1981) methods is described. The various Ångström exponents are introduced before the methodology for the AOD retrieval and the vertical structure analysis is presented. The calculation of the particle linear depolarization ratio (*Murayama et al.*, 1999; *Freudenthaler et al.*, 2009) is explained next. The smoke-dust separation by means of the particle depolarization ratio is described afterwards. Last but not least, a short overview over the determination of microphysical particle properties via inversion (*Müller et al.*, 1999a) is presented.

In the first step of the lidar data analysis, the raw signals are preconditioned by background subtraction and by temporal averaging to reduce the statistical error to a tolerable level. Statistical errors are computed by means of the Gaussian law of error propagation as, e.g., outlined by *Tesche* (2011). After temporal averaging, an overlap correction is applied (*Wandinger and Ansmann* (2002), see Sec. 5.1).

4.2.1 Backscatter and extinction coefficient – Raman lidar method

For the independent determination of the particle extinction and backscatter coefficients the Raman lidar method is applied. For this method, two independent measurements are performed to obtain the elastically backscattered lidar signal $P_{\lambda_0}(z)$ (Eq. 4.2) and the inelastically backscattered lidar signal $P_{\lambda_{\text{Ra}}}(z)$ (Eq. 4.3, in case of Polly^{XT} from atmospheric nitrogen molecules). The use of these two independently measured signals leads to profiles of the particle extinction coefficient (*Ansmann et al.*,

1990)

$$\alpha_{\lambda_0}^{\text{par}}(z) = \frac{\frac{d}{dz} \ln \frac{N_{\text{Ra}}(z)}{z^2 P_{\lambda_{\text{Ra}}}(z)/O(z)} - \alpha_{\lambda_0}^{\text{mol}}(z) - \alpha_{\lambda_{\text{Ra}}}^{\text{mol}}(z)}{1 + \left(\frac{\lambda_0}{\lambda_{\text{Ra}}}\right)^{\mathring{a}_\alpha}} \quad (4.10)$$

and the particle backscatter coefficient (*Ansmann et al.*, 1992)

$$\begin{aligned} \beta_{\lambda_0}^{\text{par}}(z) &= [\beta_{\lambda_0}^{\text{par}}(z_0) + \beta_{\lambda_0}^{\text{mol}}(z_0)] \frac{P_{\lambda_0}(z) P_{\lambda_{\text{Ra}}}(z_0) N_{\text{Ra}}(z)}{P_{\lambda_{\text{Ra}}}(z) P_{\lambda_0}(z_0) N_{\text{Ra}}(z_0)} \\ &\times \frac{\exp \left[- \int_{z_0}^z \alpha_{\lambda_{\text{Ra}}}^{\text{par}}(\zeta) + \alpha_{\lambda_{\text{Ra}}}^{\text{mol}}(\zeta) d\zeta \right]}{\exp \left[- \int_{z_0}^z \alpha_{\lambda_0}^{\text{par}}(\zeta) + \alpha_{\lambda_0}^{\text{mol}}(\zeta) d\zeta \right]} - \beta_{\lambda_0}^{\text{mol}}(z). \end{aligned} \quad (4.11)$$

N_{Ra} is the number density of nitrogen molecules and \mathring{a}_α is the wavelength dependence of the particle extinction coefficient (Ångström exponent, see Eq. 4.18). The overlap function $O(z)$ has a crucial influence on the determination of the particle extinction coefficient only, if one again assumes that $O(z)$ is identical in the two channels from which the signals for the retrieval of the backscatter coefficient are taken. This assumption is generally valid for a well designed Raman lidar system. z_0 in Eq. 4.11 is the reference height at which clear, i.e., ideally particle-free air conditions exist. $N_{\text{Ra}}(z)$ and the molecular parts of the backscatter and extinction coefficients are calculated from temperature and pressure profiles of the temporally closest radiosonde launch (Manaus military airport) after *Bucholtz* (1995). Calculation details are provided in Appendix A. The reference height z_0 and the particle backscatter coefficient $\beta_{\lambda_0}^{\text{par}}(z_0)$ at this height have to be estimated *a priori*.

If not otherwise stated, a vertical smoothing window of 3 height bins (90 m) and of 9 height bins (270 m) was applied in this work for the retrieval of the particle backscatter coefficient and of backscatter-related products (e.g., AL top and backscatter-related Ångström exponent), respectively. For the extinction coefficient and related products (e.g., lidar ratio and extinction-related Ångström exponent) a vertical smoothing window of 25 height bins (750 m) was applied.

4.2.2 Backscatter coefficient – Klett method

During daytime, only the elastically backscattered light can be used. The high level of sky background light prohibits the detection of Raman signals with sufficiently low signal noise. The Fernald/Klett method (*Fernald*, 1984; *Klett*, 1981) must be employed

in this case. The particle backscatter coefficient is then obtained as

$$\beta_{\lambda_0}^{\text{par}}(z) = -\beta_{\lambda_0}^{\text{mol}}(z) + \frac{A(z_0, z, \lambda_0)}{B(z_0, \lambda_0) - 2S_{\lambda_0}^{\text{par}} \int_{z_0}^z A(z_0, \zeta, \lambda_0) d\zeta}, \quad (4.12)$$

with

$$A(z_0, x, \lambda_0) = x^2 P_{\lambda_0}(x) \exp \left[-2 (S_{\lambda_0}^{\text{par}} - S^{\text{mol}}) \int_{z_0}^x \beta_{\lambda_0}^{\text{mol}}(\zeta) d\zeta \right] \quad (4.13)$$

and

$$B(z_0, \lambda_0) = \frac{z_0^2 P_{\lambda_0}(z_0)}{\beta_{\lambda_0}^{\text{par}}(z_0) + \beta_{\lambda_0}^{\text{mol}}(z_0)}. \quad (4.14)$$

Here, contrary to the Raman method, the particle lidar ratio S^{par} (Eq. 4.6) has to be assumed in addition to the reference height z_0 and the particle backscatter coefficient at this height $\beta_{\lambda_0}^{\text{par}}(z_0)$. Thus, with this method the particle backscatter coefficient is obtained — and the particle extinction coefficient is derived from it — by means of an estimated particle lidar ratio $S_{\lambda_0}^{\text{par}}$.

4.2.3 Ångström exponents

The spectral dependence of the aerosol optical properties is described by the Ångström exponent (Ångström, 1964; Ansmann and Müller, 2005). From measurements with the multi-wavelength lidar Polly- XT , Ångström exponents are calculated from the three particle backscatter coefficients, the two particle extinction coefficients and the two particle lidar ratios.

The backscatter-related Ångström exponent is computed from the particle backscatter coefficients at 355 and 532 nm, and at 532 and 1064 nm, respectively:

$$\mathring{a}_{\beta_{355/532}}(z) = -\frac{\ln[\beta_{532}^{\text{par}}(z)/\beta_{355}^{\text{par}}(z)]}{\ln(532/355)} \quad (4.15)$$

and

$$\mathring{a}_{\beta_{532/1064}}(z) = -\frac{\ln[\beta_{1064}^{\text{par}}(z)/\beta_{532}^{\text{par}}(z)]}{\ln(1064/532)}. \quad (4.16)$$

The relationship between the particle lidar ratio at 355 and 532 nm is determined by

$$\mathring{a}_{S_{355/532}}(z) = -\frac{\ln[S_{532}^{\text{par}}(z)/S_{355}^{\text{par}}(z)]}{\ln(532/355)}. \quad (4.17)$$

The respective spectral behavior of the particle extinction coefficient is gathered by

$$\mathring{a}_{\alpha_{355/532}}(z) = -\frac{\ln[\alpha_{532}^{\text{par}}(z)/\alpha_{355}^{\text{par}}(z)]}{\ln(532/355)} \quad (4.18)$$

and via the relationship (Ansmann *et al.*, 2002)

$$\mathring{a}_{\alpha_{355/532}}(z) = \mathring{a}_{\beta_{355/532}}(z) + \mathring{a}_{S_{355/532}}(z). \quad (4.19)$$

4.2.4 Aerosol optical depth

The aerosol optical depth (AOD) for a certain wavelength λ is determined with the lidar by integrating the extinction profile from the surface up to the maximum possible measurement height z_{\max} (e.g., the tropopause or in case of clouds the cloud base height):

$$\tau_{\lambda} = \int_0^{z_{\max}} \alpha_{\lambda}^{\text{par}}(z) dz. \quad (4.20)$$

Because of the incomplete overlap between the laser beam and the field of view of the telescope (see Sec. 5.1), the particle extinction coefficient cannot be determined near the surface. For the AOD calculation, a well-mixed atmosphere with height-independent extinction is therefore assumed for the lowermost part of the atmosphere for which no lidar measurements are available.

The extinction coefficient is usually determined with the Raman lidar method (see Sec. 4.2). However, for some night-time measurements in the wet season and for all daytime measurements, the vertical profile of the particle extinction coefficient cannot be retrieved via the Raman lidar method due to a too low signal-to-noise ratio (caused by, e.g., a very low AOD, detector problems, or high light-background level). In these cases, the extinction coefficient is calculated as follows: The backscatter coefficient is calculated with the Raman lidar method (night time) or the Klett method (daytime). In contrast to the retrieval of the particle extinction coefficient, the calculation of the particle backscatter coefficient at times with a low signal-to-noise ratio in the Raman channels is possible because the method is less sensitive to signal noise. The minimum height of the vertical profile of the particle backscatter coefficient depends on the method used for the calculation. It is about 300 m with the Raman lidar method and about 800 m with the Klett method depending on the specific overlap characteristics (see Sec. 5.1). Finally, a constant lidar ratio is multiplied to the profile of the particle backscatter coefficient to obtain the vertical profile of the particle extinction coefficient. The AOD is then calculated by using Eq. 4.20 as follows:

$$\tau_{\lambda} = S_{\lambda}^{\text{par}} \int_0^{z_{\max}} \beta_{\lambda}^{\text{par}}(z) dz. \quad (4.21)$$

It is obvious that the estimation of the particle lidar ratio is crucial for the AOD computation with this method. The resulting uncertainties are estimated by varying the particle lidar ratio from 40 to 80 sr. For the results presented in this work, $\tau_{\lambda}(S^{\text{par}} = 60 \text{ sr})$ is shown together with error bars obtained from the calculation of $\tau_{\lambda}(S^{\text{par}} = 40 \text{ sr})$ and $\tau_{\lambda}(S^{\text{par}} = 80 \text{ sr})$.

4.2.5 Vertical aerosol structure analysis

Aerosol layering in the tropics can be very complex (see Sec. 2.3). Sources at the surface as well as local and meso-scale aerosol transport processes influence aerosol layering and the vertical extent of the aerosol column. At daytime, low-level clouds frequently develop so that a CCL exists above the ML as it was illustrated in Fig. 2.7. The CCL usually extends up to the TWI but is already a part of the FT. At night time, the vertical structure in the Amazon Basin can be even more complex than at daytime as discussed by *Browell et al.* (1988). Aerosol layering is, however, often not well correlated to these thermodynamical layering caused by cloud-formation and convective processes. Usually no clear aerosol gradient was found between the ML, the CCL, and the clear troposphere above. Therefore, the classical approaches for the determination of the ML top height by lidar as possible at mid-latitudes (*Baars et al.*, 2008) cannot be applied to lidar profiles in the tropics. Thus, analysis of the aerosol layer structure from the lidar observations in Amazonia (Sec. 7.2) is performed by applying several different approaches: The top height of the aerosol layer (AL), the aerosol scale height, and the ML top from a forecast model are used. These parameter are discussed in the following.

Aerosol layer top height

The AL top height represents the height at which the atmospheric aerosol load reaches clean FT conditions. To quantify the aerosol load at different heights and to identify the top of the AL, the particle backscatter coefficient at 1064 nm is used. Backscattering at 1064 nm is very sensitive to particles because molecular scattering (i.e., Rayleigh scattering) is proportional to λ^{-4} . Thus, the contribution of molecular scattering to the total backscatter is much lower at 1064 nm than at, e.g., 355 nm (about two orders of magnitude).

As suggested in *Vaughan et al.* (2005), aerosol layers can be defined as “any extended and contiguous region of enhanced backscatter signal that rises significantly above the expected clear air value”. In this work, the height of the AL top (z_{AL}) is defined by means of a threshold as follows:

$$\begin{aligned} \beta_{1064}^{\text{par}} &\geq 0.02 \text{ Mm}^{-1}\text{sr}^{-1} \text{ for } 0 \leq z \leq z_{AL}, \\ \beta_{1064}^{\text{par}} &< 0.02 \text{ Mm}^{-1}\text{sr}^{-1} \text{ for } z = z_{AL} + \Delta z. \end{aligned} \quad (4.22)$$

This means, $\beta_{1064}^{\text{par}}$ is always higher or equal to $0.02 \text{ Mm}^{-1}\text{sr}^{-1}$ below and at the AL top. Directly above the AL top ($z_{AL} + \Delta z$), $\beta_{1064}^{\text{par}}$ must be less than $0.02 \text{ Mm}^{-1}\text{sr}^{-1}$. Δz is

the vertical resolution of the lidar. However, an increase of $\beta_{1064}^{\text{par}}$ at higher altitudes, e.g., due to clouds or lofted, separated aerosol layers, does not influence the AL top height determination. Consequently, within the AL (from the ground up to the AL top), aerosol is continuously present above free-tropospheric-background-aerosol levels (particle backscatter coefficient above the expected clear air value). The AL top is thus an absolute criterion for the analysis of the vertical aerosol structure.

Typically the threshold value of $\beta_{1064}^{\text{par}} = 0.02 \text{ Mm}^{-1}\text{sr}^{-1}$ at, e.g., 4 km agl corresponds to a backscatter ratio (total/molecular) of about 1.3 ($\beta_{1064}^{\text{mol}}(4 \text{ km}) \approx 0.06 \text{ Mm}^{-1}\text{sr}^{-1}$). Thus, if the particle backscatter coefficients are well below the corresponding $\beta_{1064}^{\text{mol}}(4 \text{ km}) \approx 0.06 \text{ Mm}^{-1}\text{sr}^{-1}$, the free troposphere is assumed to be clean. The threshold value of $\beta_{1064}^{\text{par}} = 0.02 \text{ Mm}^{-1}\text{sr}^{-1}$ is sufficiently high to be insensitive to noise in the vertical profile of the particle backscatter coefficient. Consequently, one can expect that the AL top height retrieval is robust and works well. In addition, the retrieved AL tops have been inspected by eye to ensure a proper detection of the top of the aerosol layer. An example of a particle backscatter coefficient profile and the resulting AL top is shown in Fig. 4.1. The AL top for this example is at 4.61 km and can be seen as the height agl up to which aerosol can be found continuously above the surface.

Aerosol scale height

For a simple description of the vertical extent of the aerosol layers the scale height H_{aer} of aerosols (*Turner et al.*, 2001) is introduced. The scale height is defined as the height at which the AOD reaches the 63% level (with respect to the total AOD, 100%), i.e., 37% (1/e) of the entire AOD is caused by the particles above H_{aer} :

$$\frac{1}{e}\tau_{\lambda} = \int_{z=H_{\text{aer}}}^{z_{\text{max}}} \alpha(z)dz. \quad (4.23)$$

Although the extinction profile does not follow an exponential decay, the scale height of aerosols is often used as a good approximation of the vertical extent of aerosols by the modeling and satellite remote-sensing community (*Léon et al.*, 2009). In contrast to the AL top, H_{aer} is a relative criterion for the analysis of the vertical aerosol structure depending on the overall aerosol load in the troposphere. The scale height in this work is always determined from the particle extinction coefficient profile at 532 nm. This profile is either directly derived from the N₂ Raman channels (Eq. 4.10) or by using the particle backscatter coefficient (Eq. 4.11 or Eq. 4.12) multiplied with a constant particle lidar ratio. However, in contrast to the AOD computation by Eq. 4.21, the

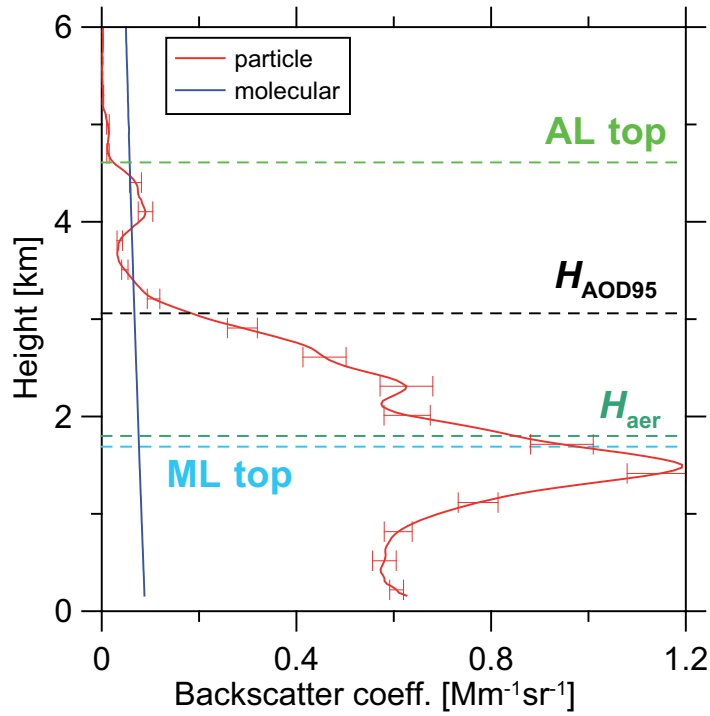


Figure 4.1: Vertical profile of particle backscatter coefficient at 1064 nm on 08 September 2008. AL top, scale height H_{aer} , the height H_{AOD95} , and ECMWF ML top height are shown.

assumption of the particle lidar ratio does not influence the vertical distribution of the particle extinction and thus has no influence on the scale height determination.

Figure 4.1 shows an example profile of the particle backscatter coefficient at 1064 nm. A very complex aerosol structure was observed. The corresponding AOD at 532 nm (determined with the Raman method) is about 0.28. The scale height H_{aer} is at 1.86 km agl. It is obvious that H_{aer} does not give any information about the real layering and can only be regarded as a very rough information on the vertical aerosol distribution. In this example, H_{aer} is very close to the strongest gradient in the particle backscatter coefficient profile. However, this was not observed in other lidar measurements and must be seen as a coincidence, because the 63% threshold has no relation to mixing-layer processes.

Because H_{aer} is not sufficient for aerosol structure analysis in the tropics, another height H_{AOD95} is introduced. At this height, the AOD reaches the 95% level (with respect to the total AOD, 100%), so that only 5% of the entire AOD are caused by particles above H_{AOD95} . For the example case shown in Fig. 4.1, H_{AOD95} is 3.06 km and thus represents well the top of the major aerosol plume.

Mixing-layer top height

The determination of ML top height by lidar was not possible for the measurements presented here, because of the very complex vertical aerosol structure typical in the tropics (as discussed already in the beginning of this section). Therefore, the ML top as derived from the global simulation of ECMWF¹ is used in this work. The retrieval of the ML top by the model² is based on the analysis of the vertical profiles of meteorological stability parameter (e.g., *Baars et al.*, 2008) which are computed from thermodynamic quantities like temperature and wind. The ML top height was provided in the frame of EUCAARI for the Brazilian site by the Finish Meteorological Institute.³ The ML-top value used for the lidar site was interpolated from the four closest grid points. Even if this modeled quantity will not perfectly reflect the reality, it gives a very good impression about up to which height surface-forced mixing can be expected at this tropical rain forest site. The maximum daytime ML top height from the day before the measurement is used as representative for the night-time lidar measurements. Consequently, one has to assume that the maximum daytime ML top is the height up to which aerosol was mixed upwards. Deposition of aerosol has to be neglected for the time between the collapse of the convective ML and the time of the lidar measurement.

The ECMWF ML top height is as well indicated in Fig. 4.1 in light blue. The strongest gradient in aerosol backscatter is in the same height range as the ML top height. Assuming the height region with the strong gradient to be the real top of the ML on the day before, one can conclude that the ECMWF ML top height is a good indicator for the strength of mixing at the Amazonian lidar site. However, a clear gradient in the vertical backscatter profile like in this case is very rare for most lidar observations. Hence, the ML top height as derived from ECMWF is used in the following when referring to the ML top. Then, always the maximum ML top height from the day before the measurement is used.

4.2.6 Depolarization ratio

With Polly^{XT}, the volume and the particle linear depolarization ratio at 355 nm can be determined by using Eq. 4.2 and Eq. 4.8 with the polarization lidar method (*Murayama et al.*, 1999; *Cairo et al.*, 1999; *Freudenthaler et al.*, 2009). In this work, the

¹more information: <http://www.ecmwf.int/about/forecasts.html>

²more information: <http://www.ecmwf.int/research/ifsdocs/CY31r1/index.html>

³Contact: Mika Komppula (Mika.Komppula@fmi.fi)

term depolarization ratio always refers to the depolarization with respect to linearly polarized emitted light. Therefore, in the following, the terms volume depolarization ratio and particle depolarization ratio are used without explicitly stating “linearly”. The volume depolarization ratio is defined as:

$$\delta_{\lambda}^{\text{vol}}(z) = \frac{\perp\beta_{\lambda}(z)}{\|\beta_{\lambda}(z)} = \frac{\perp\beta_{\lambda}^{\text{mol}}(z) + \perp\beta_{\lambda}^{\text{par}}(z)}{\|\beta_{\lambda}^{\text{mol}}(z) + \|\beta_{\lambda}^{\text{par}}(z)}. \quad (4.24)$$

The superscripts \parallel and \perp denote the parallel and orthogonal polarization plane of the received light with respect to the plane of polarization of the linear-polarized emitted laser light, respectively. The particle depolarization ratio is defined analogously:

$$\delta_{\lambda}^{\text{par}}(z) = \frac{\perp\beta_{\lambda}^{\text{par}}(z)}{\|\beta_{\lambda}^{\text{par}}(z)}, \quad (4.25)$$

as well as the molecular depolarization ratio:

$$\delta_{\lambda}^{\text{mol}}(z) = \frac{\perp\beta_{\lambda}^{\text{mol}}(z)}{\|\beta_{\lambda}^{\text{mol}}(z)}. \quad (4.26)$$

With Polly^{XT}, the unpolarized backscattered light (no superscript) and the cross-polarized backscattered light (superscript \perp) at 355 nm is measured and used for the determination of the depolarization ratio. The volume depolarization ratio is calculated by

$$\delta_{\lambda}^{\text{vol}}(z) = \frac{C_{\lambda}^{\delta} - \frac{\perp P_{\lambda}(z)}{P_{\lambda}(z)}}{D_{\lambda} \frac{\perp P_{\lambda}(z)}{P_{\lambda}(z)} - \perp D_{\lambda} C_{\lambda}^{\delta}}, \quad (4.27)$$

where C_{λ}^{δ} is a calibration constant which is determined for measurements in particle-free atmospheric regions (*Grein, 2006*). $\perp P_{\lambda}(z)$ and $P_{\lambda}(z)$ are the signals received from cross-polarized and unpolarized backscattered light, respectively. D_{λ} and $\perp D_{\lambda}$ are the corresponding transmission ratios which describe the ratio of the transmission efficiencies of cross-polarized and parallel light for each detection channel. The determination of the transmission ratio for Polly^{XT} is described in Sec. 5.2.1. With the assumption of only molecular scattering (i.e., $\delta_{\lambda}^{\text{vol}}(z_0) = \delta_{\lambda}^{\text{mol}}(z_0)$) at the height z_0 , the calibration constant can be calculated using

$$C_{\lambda}^{\delta} = \frac{\frac{\perp P_{\lambda}(z_0)}{P_{\lambda}(z_0)} [1 + \delta_{\lambda}^{\text{mol}}(z_0) D_{\lambda}]}{1 + \perp D_{\lambda} \delta_{\lambda}^{\text{mol}}(z_0)}. \quad (4.28)$$

The calculation of the molecular depolarization ratio $\delta_{\lambda}^{\text{mol}}$ for Polly^{XT} is described in Sec. 5.2.2. After the determination of the volume depolarization ratio, the particle

depolarization ratio can be obtained by using the particle and molecular backscatter coefficients (*Mattis, 2002*):

$$\delta_{\lambda}^{\text{par}}(z) = [\delta_{\lambda}^{\text{vol}}(z) + 1] \left(\frac{\beta_{\lambda}^{\text{mol}}(z) [\delta_{\lambda}^{\text{mol}}(z) - \delta_{\lambda}^{\text{vol}}(z)]}{\beta_{\lambda}^{\text{par}}(z) [1 + \delta_{\lambda}^{\text{mol}}(z)]} + 1 \right)^{-1} - 1. \quad (4.29)$$

4.2.7 Smoke-dust separation

Lidar observations of smoke and dust in Brazil are discussed in Sec. 6.1. One method for analyzing mixed dust-smoke plumes with lidar measurements is described by *Tesche et al.* (2009). In this approach, the method for the separation of dust and smoke particles by means of lidar depolarization measurements is presented. According to the retrieval, the dust fraction in terms of the particle backscatter coefficient at 532 nm is given by

$$\frac{\beta_{\text{dust}}^{\text{par}}}{\beta_{\text{meas.}}^{\text{par}}}(z) = \frac{[\delta_{\text{meas.}}^{\text{par}}(z) - \delta_{\text{smoke}}^{\text{par}}](1 + \delta_{\text{dust}}^{\text{par}})}{(\delta_{\text{dust}}^{\text{par}} - \delta_{\text{smoke}}^{\text{par}})[1 + \delta_{\text{meas.}}^{\text{par}}(z)]}. \quad (4.30)$$

$\beta_{\text{dust}}^{\text{par}}/\beta_{\text{meas.}}^{\text{par}}(z)$ is the dust fraction defined as the ratio of the dust-related and measured particle backscatter coefficient, respectively. $\delta_{\text{meas.}}^{\text{par}}(z)$ is the measured particle depolarization ratio profile, and $\delta_{\text{dust}}^{\text{par}}$ and $\delta_{\text{smoke}}^{\text{par}}$ are the respective particle depolarization ratio values for dust and smoke.

In the case of Polly^{XT}, the particle depolarization ratio is measured at 355 nm. Thus, the corresponding depolarization values for dust and smoke at this wavelength need to be known. According to *Groß et al.* (2011), the particle depolarization ratio at 355 nm for dust is $\delta_{\text{dust}}^{\text{par}} = 0.25 \pm 0.03$. For the particle depolarization ratio of pure smoke, no consistent values are given in the literature. *Heese and Wiegner* (2008) report from measurements in the African Savanna that the particle depolarization ratio of BBA is less than 0.1. *Butler et al.* (2003) reported a particle depolarization ratio of 0.035 for Alaskan wildfire smoke observed with airborne lidar. *Murayama et al.* (2004) published values of 0.05–0.08 for aged Siberian forest-fire smoke observed over Tokio, Japan. In contrast, *Müller et al.* (2005) reported particle depolarization ratios close to the Rayleigh value (less than 0.03) for aged Siberian forest-fire smoke observed over Leipzig, Germany. Observations with Polly^{XT} during the dry season in Amazonia showed that aged BBA does not significantly depolarize the backscattered light. The particle depolarization ratio was always less than 5% (including uncertainty). Hence, $\delta_{\text{smoke}}^{\text{par}} = 0.03 \pm 0.02$ was assumed for the smoke-dust separation.

The result of the dust-fraction estimation at 355 nm by means of Eq. 4.30 is shown in Fig. 4.2. As can be seen, a measured particle depolarization ratio of $\delta_{\text{meas.}}^{\text{par}} > 0.2$

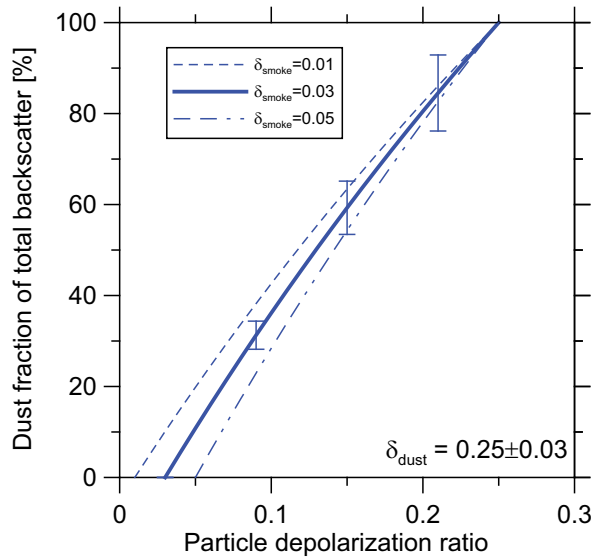


Figure 4.2: Dust fraction in dependence of the particle depolarization ratio measured at 355 nm assuming a dust-smoke mixture. The dust fraction is plotted for a particle depolarization ratio of aged smoke of $\delta_{\text{smoke}}^{\text{par}} = 0.01, 0.03$ (thick blue line), and 0.05. Vertical error bars indicate the uncertainty due to the assumed particle depolarization ratio of dust and are plotted for $\delta_{\text{smoke}}^{\text{par}} = 0.03$ only.

indicates a very high dust fraction ($>80\% \pm 11\%$). On the other hand, particle depolarization ratios of $\delta_{\text{meas}}^{\text{par}} < 0.1$ correspond to a dust fractions less than $30\% \pm 11\%$. The absolute uncertainty of the dust fraction caused by the uncertainty of the used particle depolarization ratios for dust and smoke is about 11% for all measured particle depolarization ratios.

4.2.8 Microphysical particle properties from optical particle properties by inversion

Vertical profiles of microphysical particle properties can be determined from measurements with state-of-the-art 3+2 lidars by “inversion with regularization with constraints” (Ansmann and Müller, 2005). A data inversion algorithm (Müller *et al.*, 1999a,b, 2001; Veselovskii *et al.*, 2002, 2004) was applied to derive the microphysical particle properties from backscatter coefficients measured at three wavelengths (355, 532, and 1064 nm) and extinction coefficients measured at two wavelengths (355 and 532 nm). The inversion code provides approximations of (volume) size distributions. These size distributions are subsequently used to calculate particle effective radius,

volume concentration, surface-area concentration, and the complex refractive index. In the following, a short description of the inversion concept is given. Details are discussed in *Ansmann and Müller (2005)*.

Atmospheric particle size distributions (PSD) are described in the inversion code as a combination of one or more logarithmic-normal distributions (*Hinds, 1999*)

$$dn(r) = \frac{n_t}{\sqrt{2\pi} \ln \sigma} \exp \left[-\frac{(\ln r - \ln r_{\text{mod}})^2}{2 (\ln \sigma)^2} \right] d \ln r, \quad (4.31)$$

where $dn(r)$ denotes the number concentration of particles in the radius interval $[\ln r; \ln r + d \ln r]$, n_t the total number concentration, r_{mod} the mode radius, and σ the mode width (geometric standard deviation). The surface-area and volume concentrations are retrieved from Eq. 4.31 by multiplication with $4\pi r^2$ and $4\pi r^3/3$, respectively. The relationship between the optical input parameter and the microphysical properties is described by a set of Fredholm integral equations,

$$g_i = \int_{r_{\text{min}}}^{r_{\text{max}}} K_i(r, m, \lambda_i, s) v(r) dr + \epsilon_i^{\text{exp}}, \quad (4.32)$$

which cannot be solved analytically. g_i denotes the optical input data (particle backscatter coefficient or particle extinction coefficient) at a certain wavelength. The kernel efficiency (function) K_i depends on particle radius r , the complex refractive index m , the wavelength of the interacting light λ_i , and the shape s of the particles. K_i is weighted with the volume-concentration PSD function $v(r)$. ϵ_i^{exp} accounts for the measurement error in the optical input data set. The integration of Eq. 4.32 is performed for a certain size range of the PSD from r_{min} to r_{max} (e.g., in the case of the Brazilian observations from 100 nm to 10 μm). For spherical particles with the geometric cross-section πr^2 , the kernel function K_i can be calculated with the respective backscatter or extinction efficiencies $Q_i(r, m, \lambda_i)$ (*Bohren and Huffman, 1983*):

$$K_i(r, m, \lambda_i) = \frac{3}{4r} Q_i(r, m, \lambda_i). \quad (4.33)$$

Equation 4.32 represents an ill-posed, non-linear problem that must be solved numerically. Since the problem is ill-posed, the mathematically correct solutions do not necessarily need to be physically useful. Due to the non-linearity of these integral equations, the solutions of the problem are very sensitive to changes in the input data and numerical instability can occur. The instability of the solutions can only be controlled by introducing meaningful boundary conditions. To minimize the number of *a priori* assumptions in the retrieval, $n(r)$ is described as a combination of weighted

triangular base functions (*Müller et al.*, 1999a). The number of base functions depends on the PSD. Three base functions are sufficient to reproduce one particle mode. If the number of base functions is too large, the inversion procedure might become unstable. In the version of the algorithm applied here, eight base functions are used.

Because the use of the base functions may still lead to unstable or physically meaningless solutions, regularization is used to reduce the number of solutions. Regularization sorts out solutions of the inversion algorithm which are mathematically possible but physically meaningless, e.g., only positive solutions of $n(r)$ are allowed. Despite this regularization, only a fraction of the solutions of the inversion algorithm represents trustworthy, physically useful results for a given input data set. Thus, a further manual careful analysis of the inversion output is necessary. For example, solutions with a very high number of small particles (radius less than, e.g., 50 nm) are neglected. Finally, out of thousands of mathematical inversion results only several hundred trustworthy solutions remain. These solutions are averaged and further properties, e.g., the mean particle number concentration or the mean complex refractive index, are obtained. The surface-area weighted mean, or effective, radius is defined as

$$r_{\text{eff}} = \frac{\int n(r)r^3 dr}{\int n(r)r^2 dr} \quad (4.34)$$

and used as a measure of mean particle size. The surface-area concentration a and the volume concentration v are calculated to

$$a = 4\pi \int n(r)r^2 dr \quad (4.35)$$

and

$$v = \frac{4}{3}\pi \int n(r)r^3 dr, \quad (4.36)$$

respectively. Thus, the effective radius is

$$r_{\text{eff}} = \frac{3v}{a}. \quad (4.37)$$

Finally, the retrieved results in terms of the volume size distribution and complex refractive index are used to calculate the particle SSA at 532 nm wavelength with a Mie-scattering code (*Bohren and Huffman*, 1983).

Chapter 5

Instrument characterization and quality assurance

The design and construction of Polly^{XT} lasted until mid of 2007. The construction was completed just a few weeks before the shipment of the system to Brazil. Thus, results presented here are the first ones made with this new lidar. Performance tests of the system are essential to assure a good data quality. Hence, several hardware and software tests were made and resulting corrections were applied. These tests are explained in the following. Some of them were made in Brazil during the campaign, some were made after the arrival of the system back home in Germany.

First of all, the overlap between the laser beam and the field of view of the telescope is discussed. The determination of the overlap function for Polly^{XT} and resulting errors are explained. Secondly, the polarization characteristics of Polly^{XT} are presented. The problem of polarization cross-talk within the system and the applied correction is described. Next, the data retrieval software, which was specifically developed for Polly^{XT} in the framework of this thesis, was tested according to EARLINET (European Aerosol Research Lidar NETwork) standards. Finally, a comparison with other lidars during the EARLI09 campaign in Leipzig (*Freudenthaler et al., 2010*) and a direct comparison to AERONET measurements in Brazil are presented. Correct photon counting was also a major issue during the measurements in Brazil. The corresponding dark-measurement test is presented in Appendix B.

5.1 Overlap characteristics

The adjustment of the so-called overlap is a crucial feature when performing lidar measurements. The overlap function $O(z)$, which describes the fraction of the laser beam within the receiver field of view over height, influences directly the measured signals (see Sec. 4.1, in particular Eq. 4.2 and Eq. 4.3). Theoretical calculations prior to the construction of Polly^{XT} led to the result that the full overlap ($O(z) = 1$) is reached at 1500 m above the lidar. In Polly^{XT}, the laser beam is adjusted to the receiver field of view by small, motor-controlled changes in the position of the beam expander with the help of a camera (see Sec. 3.2). This overlap adjustment has to be done, e.g., after each maintenance of the laser head. But also temperature changes within the lidar can lead to maladjustments of the laser beam due to thermal effects on the opto-mechanical mountings. Therefore, many different overlap functions were obtained for different measurement periods in Brazil. These overlap functions were calculated from the respective Raman signals at 355 and 532 nm using the method described by *Wandinger and Ansmann (2002)*. For the 1064-nm channel no overlap function can be calculated, because no corresponding Raman signal is available at this wavelength.

An overview of all experimentally derived overlap functions of the Brazilian measurements is shown in Fig. 5.1. $O(z)$ for 355 and 532 nm is presented. The overlap function derived in Leipzig under very clean conditions for a well-aligned Polly^{XT} setup is drawn in addition (thick red line) and can be regarded as the ideal overlap function. Obviously, $O(z)$ is different for 355 and 532 nm, so that the overlap characteristics for the different wavelengths are not unique. In general, the overlap is complete ($O(z) = 1$) at 1500 m as calculated theoretically. However, the shape of the overlap functions differs slightly during the measurement period which is mainly caused by temperature fluctuations inside the lidar. In one case of a maladjusted overlap (the dark green line in Fig. 5.1), the full overlap is reached only at 2300 m.

Using a wrong overlap function can lead to large errors in the retrieval of the particle extinction coefficient with the Raman method and the particle backscatter coefficient with the Klett method. The estimation of the resulting error for the particle extinction coefficient is shown in the following. Reformulation of Eq. 4.10

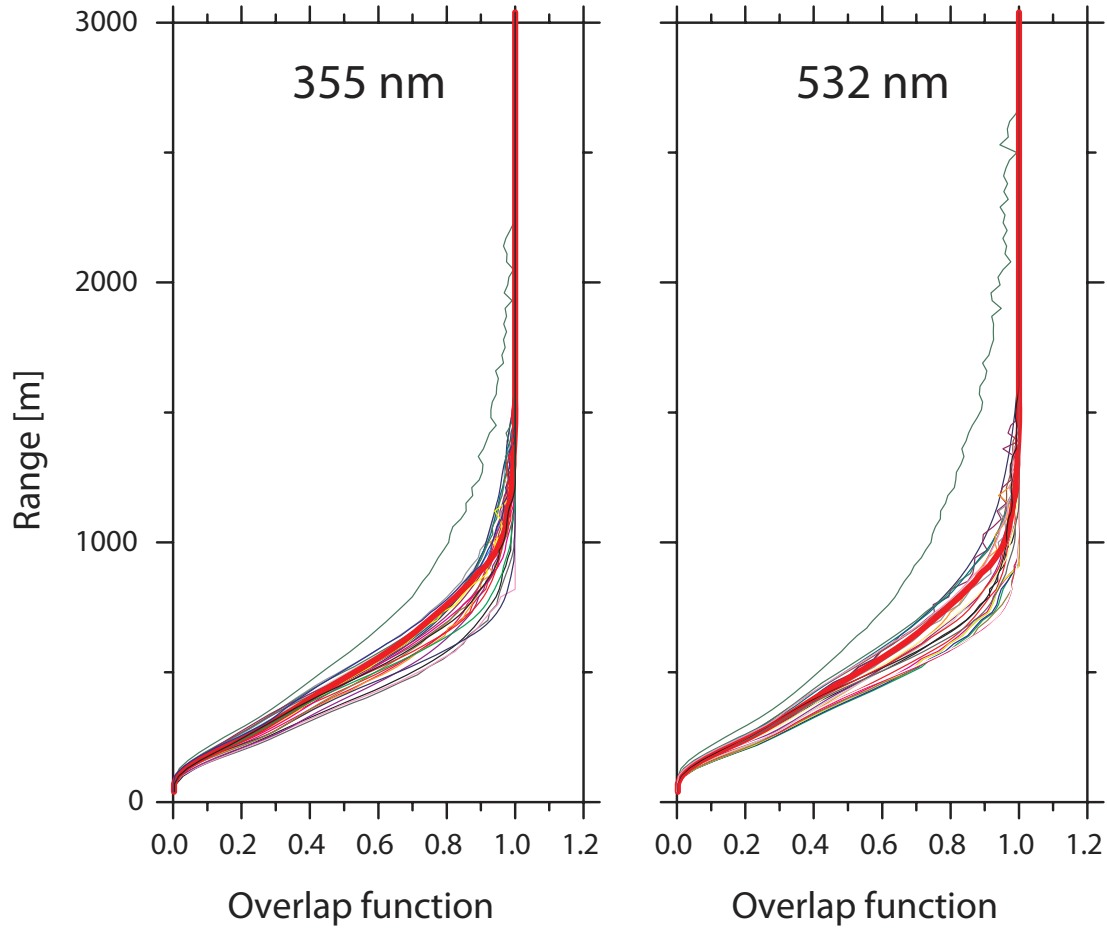


Figure 5.1: All determined overlap functions for the measurement period in Brazil for 355 nm (left) and 532 nm (right). The thick red line shows the overlap function measured in Leipzig under very clean conditions on 13 January 2009 (this is the reference).

leads to

$$\alpha_{\lambda_0}^{\text{par}} = \frac{\frac{d}{dz} \ln N(z) + \frac{d}{dz} \ln O(z) - \frac{d}{dz} (2 \ln z) - \frac{d}{dz} \ln P_{\text{Ra}}(z) - \alpha_{\lambda_0}^{\text{mol}} - \alpha_{\lambda_{\text{Ra}}}^{\text{mol}}}{1 + \left(\frac{\lambda_0}{\lambda_{\text{Ra}}}\right)^{\hat{a}_\alpha}}. \quad (5.1)$$

To estimate the effect of the overlap function $O(z)$ on the extinction coefficient retrieval, one has to analyze the term

$$\frac{\frac{d}{dz} \ln O(z)}{1 + \left(\frac{\lambda_0}{\lambda_{\text{Ra}}}\right)^{\hat{a}_\alpha}}. \quad (5.2)$$

This term was calculated for all overlap functions shown in Fig. 5.1 with $\hat{a}_\alpha = 1$. The mean effect, i.e., the absolute contribution of Term 5.2 (and thus of $O(z)$) to

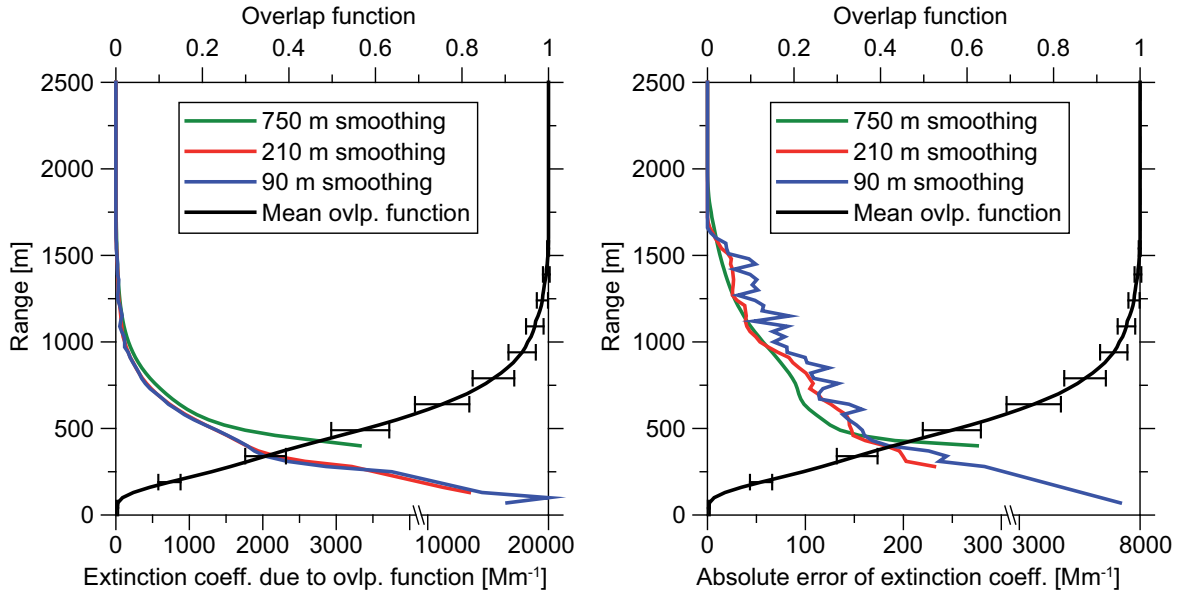


Figure 5.2: Left: Absolute contribution of the mean overlap function to the particle extinction coefficient at 532 nm for different vertical smoothing lengths. Right: Absolute error introduced by $O(z)$ to the particle extinction coefficient at 532 nm determined for different smoothing lengths. The mean overlap function with the corresponding standard deviation (black line) is shown in addition in both graphs.

the particle extinction coefficient at 532 nm is shown in Fig. 5.2, left. Different vertical smoothing lengths are applied. In addition, the mean overlap function and the corresponding standard deviation is shown. For the typical smoothing length of 750 m (green line) for the particle extinction coefficient, an artificial contribution of more than 3000 Mm^{-1} is introduced to the lowermost part of the lidar profile. At 1000 m, the contribution of $O(z)$ to the particle extinction coefficient is about 170 Mm^{-1} . For this smoothing length, the overlap correction affects the extinction profile up to 1920 m. In contrast, if the extinction coefficient is determined with a vertical resolution of 90 m only (blue line in Fig. 5.2), a maximum contribution due to $O(z)$ of 20000 Mm^{-1} was found for the lowermost height at 100 m. For this smoothing length, the particle extinction coefficient is affected by $O(z)$ only up to 1600 m.

To estimate the error which is introduced by the overlap correction to the particle extinction coefficient, the standard deviation of the solutions of Term 5.2 for all overlap functions is shown in Fig. 5.2, right. The standard deviation of Term 5.2 is assumed to be a good estimation of the standard error introduced by the overlap

correction, since it reflects the variability of $O(z)$ for Polly^{XT}. For 750 m vertical smoothing, an error of more than 250 Mm^{-1} is calculated at the lowermost height at 400 m. At 1000 m, the error is still of the order of 50 Mm^{-1} . At 1500 m, the error is comparably low with about 10 Mm^{-1} . For 90 m vertical smoothing, a maximum absolute error for the lowermost height at 100 m of about 7500 Mm^{-1} is calculated. At 400 m, the error is about 180 Mm^{-1} and thus lower than for a vertical smoothing of 750 m. At 1000 m, an error of about 70 Mm^{-1} is determined which is higher than the one for 750 m vertical smoothing. Thus, vertical smoothing has to be applied under consideration of the overlap correction effect.

However, the overlap determination was done carefully for every measurement period after changes within the Polly^{XT}. This means, after every setup change a new overlap function was calculated. Thus, the real error of the extinction coefficient is assumed to be much lower than the error presented here. However, a more realistic error estimation for the overlap correction is not possible, because the actual overlap function for a single measurement is usually unknown. Consequently, one has to be very careful when using extinction-coefficient-related data below 1000 m.

Another approach to test the overlap characteristics of a lidar is the so-called telecover test (*Freudenthaler, 2008*). This test was performed in Leipzig after the EUCAARI campaign. For this test, only one quarter of the telescope (quadrant) is used for receiving the backscatter signals. This is repeated four times for all quadrants until the whole telescope is characterized. The full overlap is reached at the height at which all quadrants receive equal signal. The results of the performed test show that the full overlap is reached at different heights for the UV channels¹ (full overlap at 2.0 km) and the VIS channels² (full overlap at 1.5 km). This finding is in agreement with the overlap functions calculated for the Brazil campaign and shows that different overlap functions have to be used for the correction of the UV and VIS channels. Nevertheless, this test also revealed a good performance for all tested channels, i.e., no further optical problems could be detected.

¹355, 355s, 387

²532, 607

5.2 Polarization characterization and correction

Important products of Polly^{XT} are the vertical profiles of the volume and particle depolarization ratios. For the proper determination of these profiles, a high-quality characterization of the instrument concerning polarization effects is necessary. The characterization tests of the receiver optics of Polly^{XT} concerning polarization effects following *Mattis et al.* (2009) and the applied correction schemes are described in Sec. 5.2.1. In addition, the proper calculation of the atmospheric molecular depolarization ratio is discussed in Sec. 5.2.2. This value is dependent on the bandwidth of the used interference filter and wrong assumptions can lead to large errors in the particle depolarization ratio. The purity in terms of linear polarization of the emitted laser light was also tested and is presented in Appendix C. In this Section, the receiving channels are denoted as presented in Table 3.1, i.e., channels receiving unpolarized light have no addition and channels receiving perpendicular polarized light have the channel addition “s”. For example, the channel receiving unpolarized light at 355 nm is denoted with 355 whereas the channel receiving only cross-polarized light is denoted as 355s.

5.2.1 Transmission ratios and corresponding signal correction

Systematic errors occur in the presence of depolarizing scatterers for the determination of the particle backscatter coefficient, the particle extinction coefficient, and the depolarization ratio due to polarization-dependent receiver transmission. To correct these effects and to determine the depolarization ratio, the transmission ratio D for each detection channel needs to be known (see Sec. 4.2.6). The transmission ratio is defined as the ratio of the transmission efficiency η of parallel-polarized (superscript \parallel) and perpendicular-polarized (superscript \perp) light with respect to the plane of polarization of the emitted laser light (*Mattis*, 2002; *Mattis et al.*, 2009):

$$D = \frac{\perp\eta}{\parallel\eta}. \quad (5.3)$$

To determine D for each channel of the receiver unit of Polly^{XT}, a polarization test was performed. The experimental setup of this test is shown in Fig. 5.3. Unpolarized light from a combined deuterium and halogen light source (getLight-DHS by Sentronic GmbH, Germany) was directed via an optical fiber through a polarization filter onto the main mirror of Polly^{XT}. From the main mirror the white light was reflected into

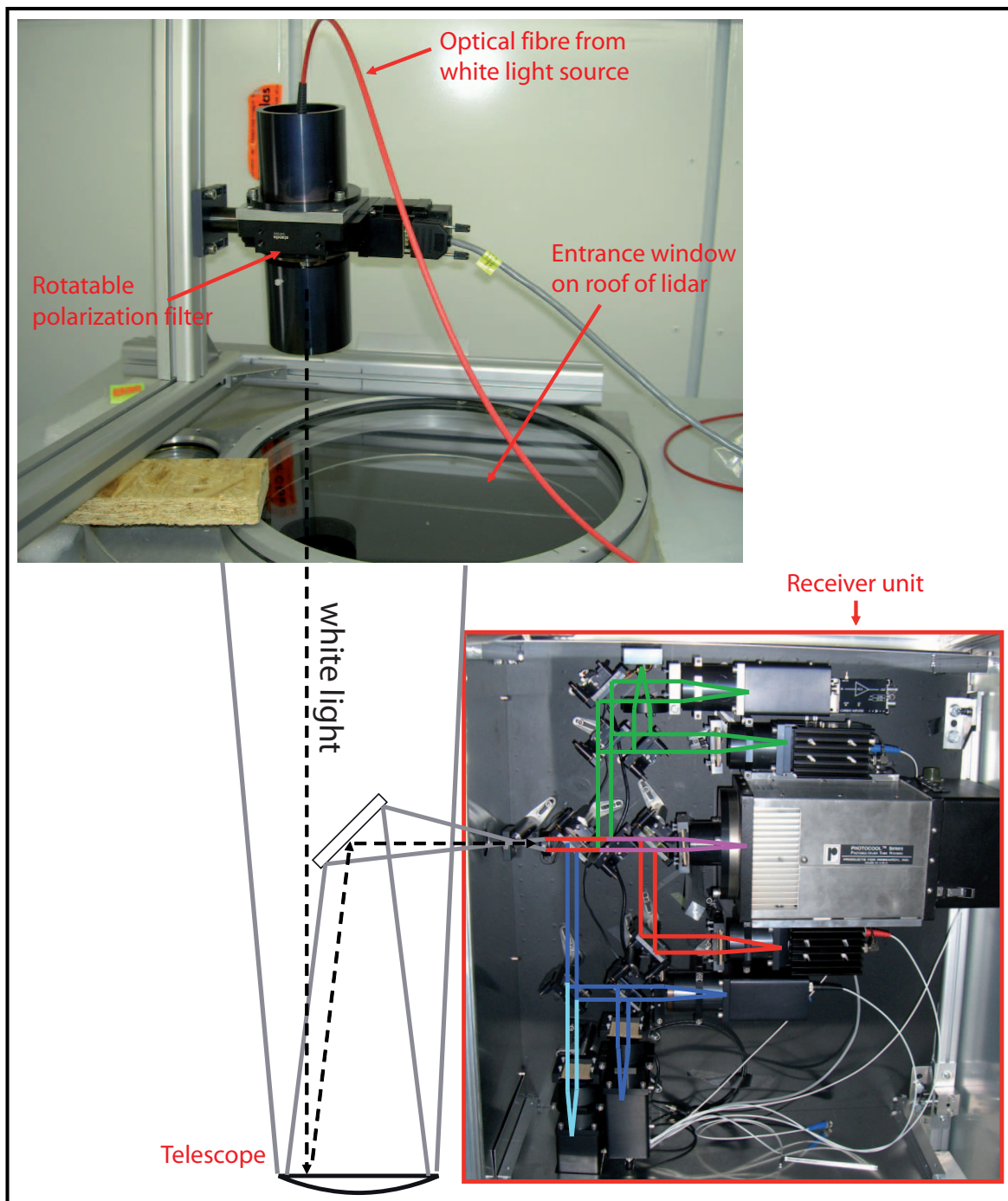


Figure 5.3: Experimental setup for the determination of the transmission ratios. The measurement apparatus was installed on the roof of Polly^{XT}. Via an optical fiber (red) light is directed through a motorized polarization filter (black tube). The linear-polarized light is then directed onto the main mirror of the telescope and signals are detected by the DAQ. The optical paths are indicated by overlaid colored lines (see Sec. 3.2).

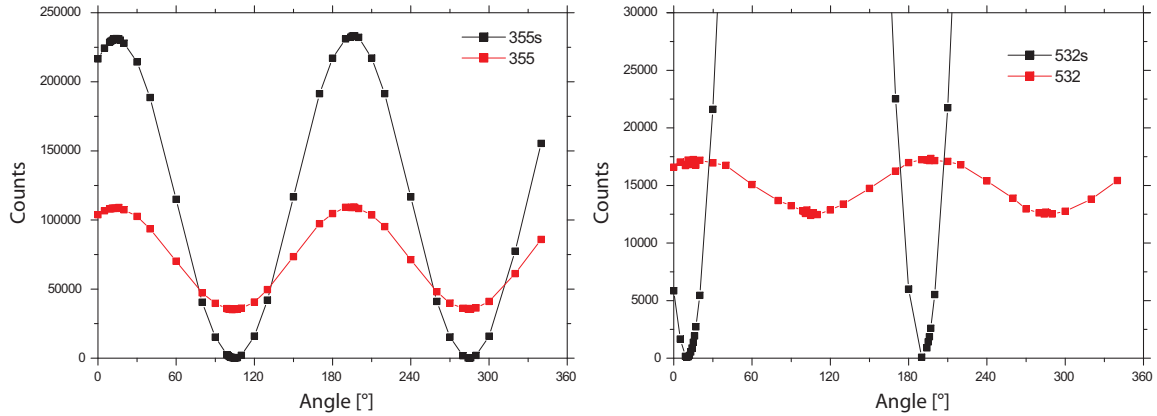


Figure 5.4: Results from the transmission efficiencies test for several detection channels (355, 355s, 532, 532s) as a function of the polarization plane angle. Counts were summed up over 3000 shots. The polarization filter plane angle must not agree with optical axis of Polly^{XT}.

the receiver optics, where it is spectrally separated by the beamsplitters and interference filters and directed to the detection channels. Photons were counted by the PMTs and data recorded by the DAQ as during usual measurements. The rotatable polarization filter was housed in a stable apparatus. The transmission efficiencies for parallel or cross-polarized light were retrieved for each tested channel by changing the polarization state of the incoming light by rotating the polarization filter. The rotation was performed with a remotely controlled motor which leads to exact and reproducible results. The test was carried out for several polarization angles from 0° to 350°. To obtain a good signal-to-noise ratio for each polarization plane during the experiment, photons counts were summed up over 3000 simulated shots and over all range bins (16384).

The results are shown in Fig. 5.4 for the 355, 355s, 532, and 532s channels. The 532s channel was not installed during the Brazil campaign but at the time of the depolarization test. Note that the polarization plane of the polarization filter in the 0°-position is not parallel to the polarization plane of the emitted laser light due to difficulties in the experimental setup. Thus, the minima and maxima of the curves appear at arbitrary absolute angles. The frequency doubling and tripling of the emitted light causes a polarization plane difference between 355 and 532 nm of 90°. Therefore, the orientation of the depolarization filters in the lidar receiver is different and an angular shift of exactly 90° is observed for the depolarization channels (355s and 532s) in Fig. 5.4.

A clear dependence on the polarization state of the light is obvious for the 355s and 532s channels. But also effects in dependence of the polarization plane were observed for the 355 and 532 channels. For an ideal system, a high contrast (i.e., high ratio of counts in the maxima and minima) should be observed for the depolarization channels and no dependence on the polarization state should be measured for the channels receiving unpolarized light.

To determine the transmission ratio for each detection channel, a sinusoidal fit $y(x) = A + B \sin(\frac{x-xc}{w})$ (with A =offset, B =amplitude, xc =angle offset, w = period, y =counts, x =measurement angle) was applied to the measured counts for the different polarization angles in each channel. The transmission ratio for each channel can then be calculated with the amplitude and the offset to $D_\lambda = \frac{A+B}{A-B}$ and thus independent of the angular parameter xc and w . This yields for the tested channels to:

D_{355}	${}^\perp D_{355}$	D_{387}	D_{532}	${}^\perp D_{532}$	${}^{\text{tot}} D_{607}$	D_{1064}
3.07 ± 0.01	1495 ± 670	0.965 ± 0.002	0.734 ± 0.005	570 ± 275	1.05 ± 0.04	0.95 ± 0.03

The emitted laser light at 1064 nm is circular polarized, thus the value of this channel - which was characterized in an earlier measurement in Leipzig in 2009 - is not important for the data analysis but shown for completeness. The relative high errors for the transmission ratio of the 355s and 532s channels are the result of the strong noise influence during measurements at a very low count rate (e.g., for 355s at about 100°). However, independent calibration of the volume depolarization ratio to cirrus clouds, for which $0.3 < \delta^{\text{vol}} < 0.7$ is expected (*Sassen and Benson, 2001*), has shown that ${}^\perp D_{355} = 200$ has to be used to achieve the expected volume depolarization ratio. The reason for this disagreement could be that the emitted laser light is not 100% linearly polarized. According to Eq. 4.27, one can account for such impurity by decreasing ${}^\perp D_{355}$. Tests of the purity of the emitted laser light in terms of linear polarization (see Appendix C) have shown that the purity is better than 95%. However, measurement errors did not allow the determination of the purity in terms of linear polarization more precisely. Thus, the calibration to cirrus is the most robust method for the determination of a realistic ${}^\perp D_{355}$. As a consequence of the difficulties and the resulting measurement uncertainties in the determination of ${}^\perp D_{355}$, Polly^{XT} was redesigned in 2011 and an additionally possibility to calibrate the volume depolarization ratio was installed ($\pm 45^\circ$ -method after *Freudenthaler et al., 2009*). First test measurements with this new and independent calibration method showed that the volume depolarization ratio profiles retrieved with ${}^\perp D_{355} = 200$ by Eq. 4.27 are equal to the profiles determined with the $\pm 45^\circ$ -method. Thus, the usage of this value leads to trustworthy

volume depolarization ratio profiles.

As mentioned above, for an ideal system the transmission ratio for channels receiving unpolarized light is one and for the channels receiving polarized light it should be as high as possible. This ideal behavior was observed for the 355s, 387, 532s, 607, and 1064 channels. However, the 355 and 532 channels show a clear dependence on the polarization plane of the incoming light. If the transmission ratio is not equal to 1, errors in the retrieved backscatter signals occur when depolarizing aerosol is present. According to *Mattis et al.* (2009), the error is higher than 5% when the transmission ratio is below 0.85 or higher than 1.15. Thus, a correction has to be applied to the lidar signals for the 355 and 532 channels ($D_{355} > 1.15$ and $D_{532} < 0.85$), when depolarizing scatterers are present. The correction scheme is different for the 355 channel and the 532 channel, because depolarization was measured only at 355 nm during the Brazil campaign. The correction at $\lambda = 355$ nm is done by calculating a height-dependent correction factor (*Grein, 2006; Mattis et al., 2009*)

$$\chi(z) = \frac{1 + D_{355}\delta_{355}^{\text{vol}}(z)}{1 + \delta_{355}^{\text{vol}}(z)} = \frac{P_{355}^{\text{meas.}}(z)}{P_{355}^{\text{corr.}}(z)} \quad (5.4)$$

from the volume depolarization ratio $\delta_{\lambda}^{\text{mol}}(z)$ and the transmission ratio D_{λ} . The measured signal $P_{\lambda}^{\text{meas.}}(z)$ is then corrected with

$$P_{355}^{\text{corr.}}(z) = \frac{P_{355}^{\text{meas.}}(z)}{\chi(z)}. \quad (5.5)$$

For the correction of the measured signal at 532 nm, the volume depolarization ratio at 532 nm is necessary. With the assumption of a wavelength-independent particle depolarization ratio ($\delta_{355}^{\text{par}}(z) = \delta_{532}^{\text{par}}(z)$) the volume depolarization ratio is calculated to (*Tesche et al., 2009*)

$$\delta_{532}^{\text{vol}}(z) = \frac{\beta_{532}^{\text{mol}}(z)\delta_{532}^{\text{mol}}(z)[\delta_{532}^{\text{par}}(z) + 1] + \beta_{532}^{\text{par}}(z)\delta_{532}^{\text{par}}(z)[\delta_{532}^{\text{mol}}(z) + 1]}{\beta_{532}^{\text{mol}}(z)[(\delta_{532}^{\text{par}}(z) + 1)] + \beta_{532}^{\text{par}}(z)[\delta_{532}^{\text{mol}}(z) + 1]}. \quad (5.6)$$

For $\beta_{532}^{\text{par}}(z)$, a “first guess” profile with the uncorrected signal is used. After applying the correction (Eq. 5.5) to the signal, the particle backscatter coefficient is calculated again. With this new profile the volume depolarization ratio at 532 nm and hence the correction factor is recalculated and again applied to the signal. This iterative process is done until no significant change in the backscatter profile is observed anymore.

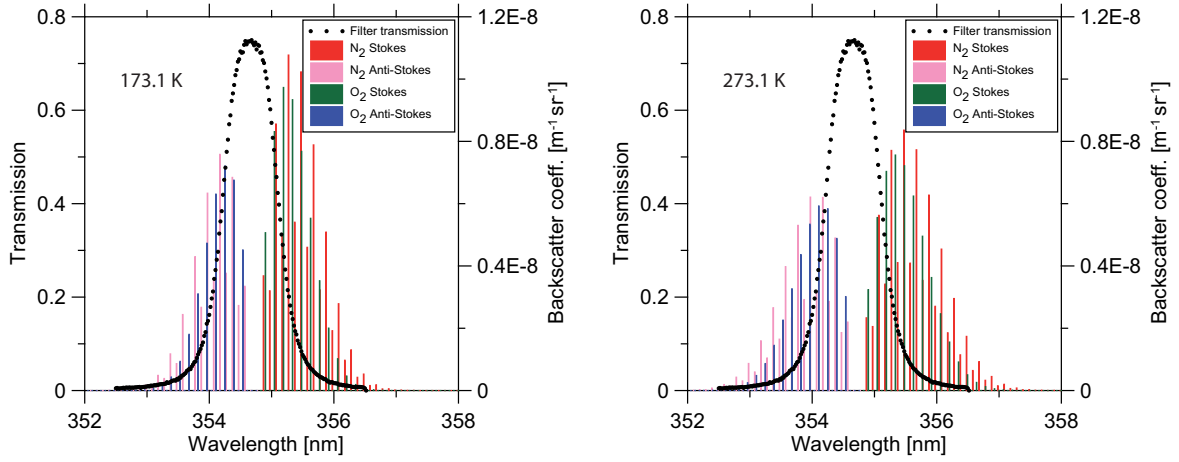


Figure 5.5: Filter transmission (black dots) for one UV filter as used in Polly^{XT} and rotational Raman backscatter coefficients for 173.1 K (left) and 273.1 K (right).

5.2.2 Filter-dependent molecular depolarization

The molecular depolarization ratio of air $\delta_{\lambda}^{\text{mol}}$ that is measured depends on the band widths of the interference filters used in the lidar (e.g., *Behrendt and Nakamura, 2002*). The lidar receives both backscatter signal of the Cabannes line and the rotational Raman lines of the molecules. The Cabannes line contributes with 97.3% to the received total molecular backscattered light whereas the rotational Raman lines contribute only with 2.7%. However, the Cabannes and rotational Raman lines cause a very different polarization. Whereas the Cabannes line induces a depolarization ratio of 0.00395, the rotational Raman lines have a depolarization ratio of 0.75. Hence, when considering depolarization, the rotational Raman lines cannot be neglected. The spectral distribution of these lines depends on the air temperature. If the filter band width in the receiver is smaller than a certain value, not all of the rotational Raman lines are detected. Thus, when using narrow-band filters also the detected molecular depolarization ratio is temperature-dependent. The temperature dependence of the molecular depolarization ratio can be calculated, if the filter transmission curve is known (see *Wandinger, 2005a*). The filter transmission curves for each individual filter of Polly^{XT} were provided by the manufacturer BARR Associates, Inc. (Westford, USA). For Polly^{XT}, a filter band width of 1.0 nm in the UV channels is used (cf. Table 3.1). Figure 5.5 shows the transmission curve of such a filter at 355 nm and the rotational

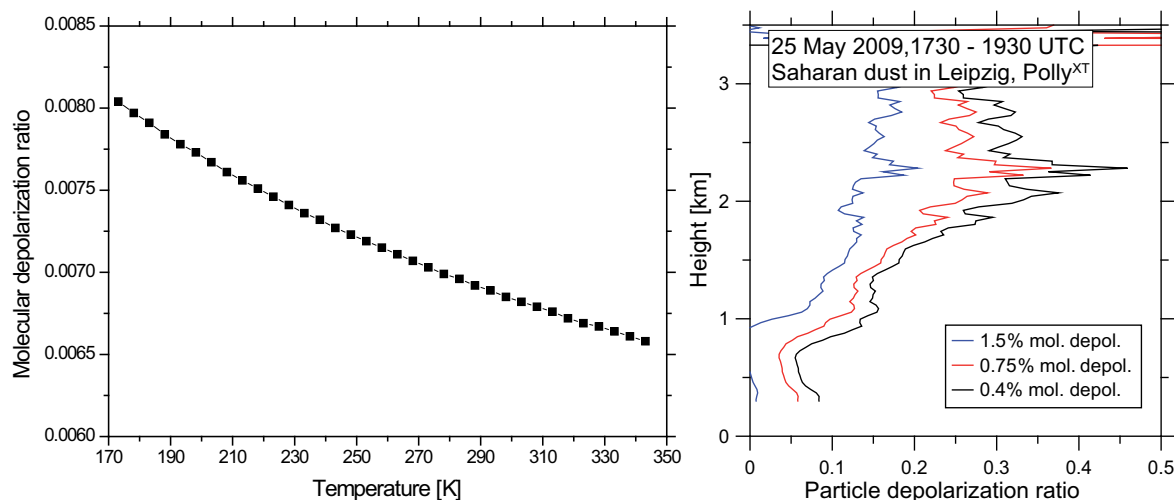


Figure 5.6: Left: Temperature dependent molecular depolarization ratio as calculated for the filter settings in Polly^{XT} at 355 nm. Right: Profile of the particle depolarization ratio at 355 nm as calculated from equal particle backscatter coefficient and volume depolarization ratio profiles but different molecular depolarization ratio. An example measurement from 25 May 2009 in Leipzig is shown.

Raman backscatter spectra of nitrogen and oxygen for two different air temperatures.³ It is obvious that rotational Raman lines partly contribute to the received signal at 355 nm and thus influence molecular depolarization for this filter type. Consequently, the molecular depolarization ratio as observed with Polly^{XT} is a function of air temperature.

Figure 5.6, left, shows the calculated molecular depolarization ratio for Polly^{XT} at 355 nm in dependence of the temperature. A slight temperature dependence could be obtained. Values for the measured molecular depolarization ratio for this filter type (1.0 nm band width) range from 0.008 at 173 K to 0.007 at 273 K. The molecular depolarization ratio measured with Polly^{XT} is consequently only about half the value of the depolarization ratio measured with a broad-band filter transmitting the entire rotational Raman spectrum (depolarization ratio of 0.0155).

The use of the molecular depolarization ratio is especially critical for the calculation of the particle depolarization ratio (Eq. 4.29). A wrong molecular depolarization ratio can lead to significant deviations in the particle depolarization ratio as shown for an example case in Fig. 5.6, right. Here, the particle depolarization ratio in depen-

³calculated with a Fortran code provided by Ulla Wandinger, IfT, Germany (E-mail: ulla@tropos.de)

dence on three different molecular depolarization ratios for fixed profiles of volume depolarization ratio and particle backscatter coefficient is shown. It is obvious that the particle depolarization ratio depends significantly on the molecular depolarization ratio. Hence, the usage of the correct value is essential for the retrieval of the particle depolarization ratio.

5.3 Data-analysis algorithm check

The data retrieval software for Polly^{XT} was newly developed in the framework of Baars (2007) and this PhD thesis. To ensure a proper data analysis the performance of the software package had to be tested independently. Therefore, a test with artificial lidar profiles developed in the framework of EARLINET was made (Pappalardo *et al.*, 2004; Böckmann *et al.*, 2004; Böckmann and Pappalardo, 2007). For this test, the profiles of the particle backscatter coefficient and the particle extinction coefficient had to be calculated from the raw data without *a priori* knowledge of the aerosol type and the vertical aerosol distribution. The Polly^{XT} algorithm and the algorithms from 13 other groups participated in several comparison stages. The results were administrated by independent referees. Figure 5.7 shows the result of the intercomparison for the particle backscatter and extinction coefficients at 355 and 532 nm determined with the Raman method at stage III (temperature and pressure profiles were given). The Polly^{XT} algorithm is marked as **A5** (deep blue line – the results from the other groups were handled anonymously). The Polly^{XT} algorithm performed well for the Raman method and is close to the real solution (input) for the particle backscatter coefficient and the particle extinction coefficient at both wavelengths. No overlap correction was performed at this stage, thus extinction coefficient values below 1 km differ significantly from the real solution. In reference to official EARLINET criteria, one can conclude that the newly designed algorithm software is of high quality and performs excellent for the retrieval of optical properties from Polly^{XT} measurements.

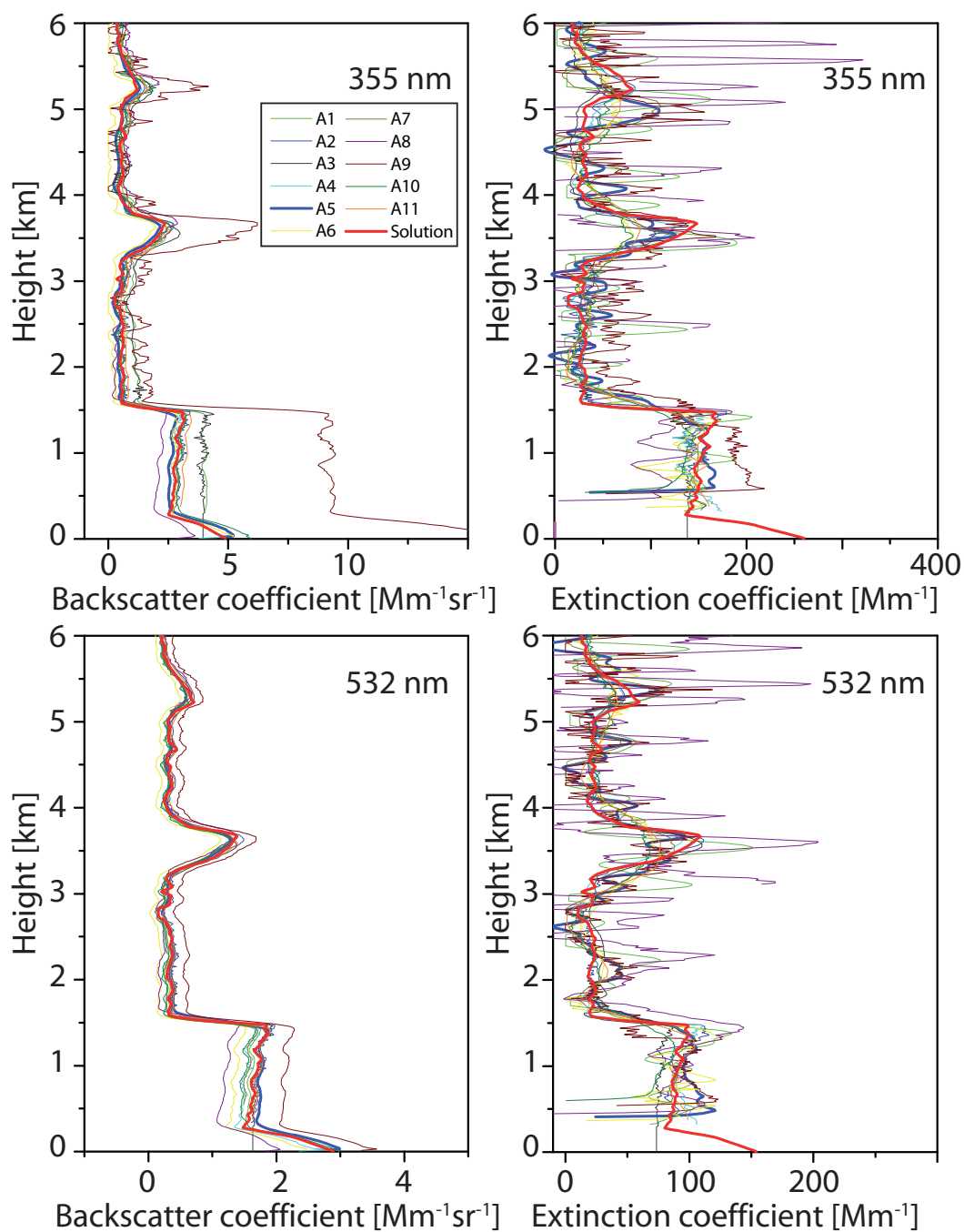


Figure 5.7: Comparison of different data analysis algorithms for multiwavelength lidars in the frame of EARLINET (*Böckmann and Pappalardo, 2007*). The algorithm for Polly^{XT} is marked as A5 (deep blue line).

5.4 Lidar intercomparison during EARLI09

In May 2009 the EARLI09 (EARlinet Reference Lidar Intercomparison 2009) campaign took place in Leipzig in the framework of EARLINET. For this campaign, 13 lidars from all over Europe were installed at IFT and intercomparison measurements for more than four weeks were performed. The results from the intercomparison campaign are presented by *Freudenthaler et al.* (2010). Polly^{XT} took also part in this campaign. After its transport from Brazil back to Leipzig, no changes in the lidar system were made. Thus, measurements during EARLI09 could be performed with the same system setup as during the observations in the Amazon Basin. To assure an independent comparison, Polly^{XT} measurements are not compared to measurements of IFT's EARLINET lidar MARTHA but to two lidars of the University of Munich. Comparisons of Polly^{XT} with POLIS (Raman and polarization lidar at 355 nm, *Heese et al.*, 2002; *Groß et al.*, 2008) and MULIS (3+2 Raman lidar at 355, 532, 1064 nm, *Freudenthaler et al.*, 2009) are shown. These two lidars are EARLINET certified and have been used already in several field campaigns (e.g., AMMA⁴ and SAMUM⁵ 1 and 2). The data of the two Munich lidars were independently analyzed at the University of Munich with own software.⁶ In contrast, Polly^{XT} data was analyzed as for the Amazonian measurements according to the methods described in Chapter 4 and the correction schemes introduced previously in this Chapter. Thus, independent intercomparison of the lidars is given.

The comparison of the vertical aerosol profiles of the three lidars was performed for 25 May 2009. On that day, Saharan dust was observed over Leipzig. The temporal development of the range-corrected signal between 1200 and 2400 UTC is shown in Fig. 5.8. A complex vertical aerosol layer structure up to 6 km was present on that day. After 2000 UTC, cirrus occurred above 11 km. The vertical aerosol structure was not stable over the whole period, hence, short intervals for the data analysis had to be chosen. For the comparison of the particle backscatter coefficient and the particle extinction coefficient, data from MULIS were used. Both MULIS and Polly^{XT} profiles are determined with the Raman method (Sec. 4.2.1). For the depolarization comparison, measurements with Munich's depolarization lidar POLIS are presented. To achieve a temporal overlap of the measurements, depolarization profiles are

⁴African Monsoon Multidisciplinary Analyses (*Redelsperger et al.*, 2006)

⁵Saharan Mineral Dust Experiment (*Heintzenberg*, 2009)

⁶data provided by Silke Groß and Volker Freudenthaler, Meteorological Institute of the University of Munich (E-mail: volker.freudenthaler@physik.uni-muenchen.de)

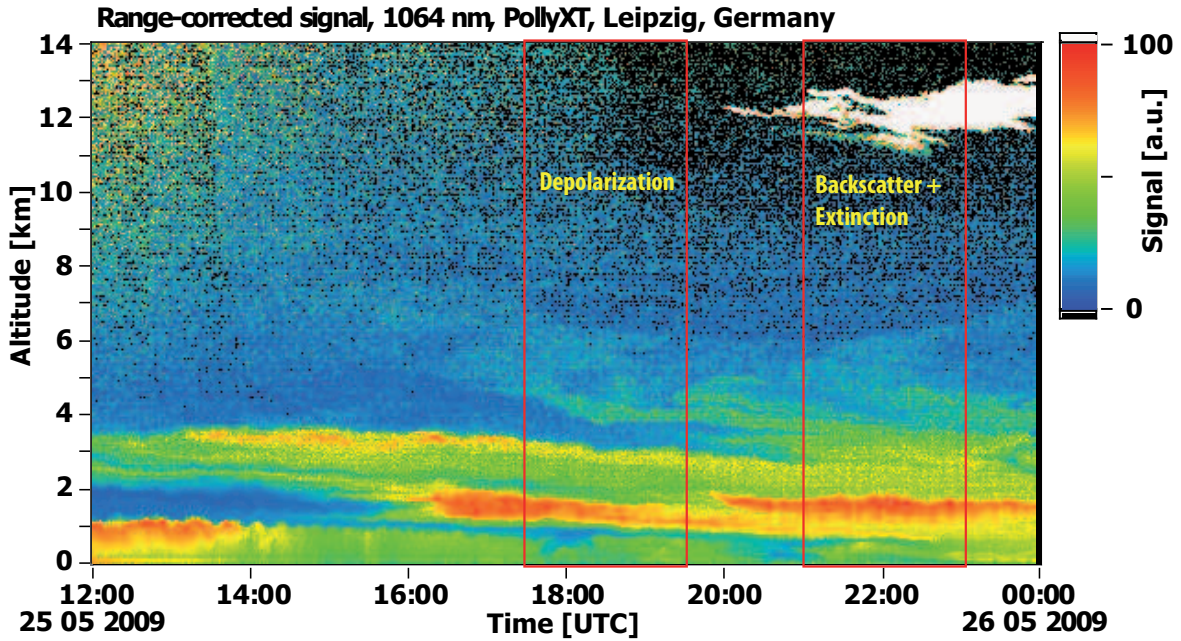


Figure 5.8: Temporal development of the range-corrected signal of Polly^{XT} at 1064 nm between 1200 UTC and 2400 UTC on 25 May 2009. The red rectangles show the inter-comparison periods.

compared for the time period between 1730 and 1930 UTC while particle backscatter coefficient and particle extinction coefficient profiles are compared between 2100 and 2300 UTC. An overlap correction was applied to profiles of Polly^{XT}. Compared to Polly^{XT}, the overlap of POLIS and MULIS is complete ($O(z) = 1$) at a much lower height. Thus, no overlap correction had to be applied for the Munich lidar profiles. Figure 5.9 shows the particle backscatter coefficient profiles at 355, 532, and 1064 nm for Polly^{XT} and MULIS. In addition, the particle backscatter coefficient at 355 nm from Polly^{XT} as derived without depolarization correction is presented. Concerning the vertical profiles of the particle backscatter coefficient derived with the Raman method, a reasonable agreement between the two instruments was achieved. All particle backscatter coefficient profiles show the same relative profile shape and thus measure the same aerosol structure. Absolute values differ depending on the wavelength and the height. A good agreement was found for the particle backscatter coefficient at 532 nm. At 355 nm, the depolarization-corrected particle backscatter coefficient agrees well with the MULIS particle backscatter coefficient below 3 km, where most of the aerosol was trapped. Above 3 km, slight differences were obtained. The particle backscatter coefficient without depolarization correction is clearly

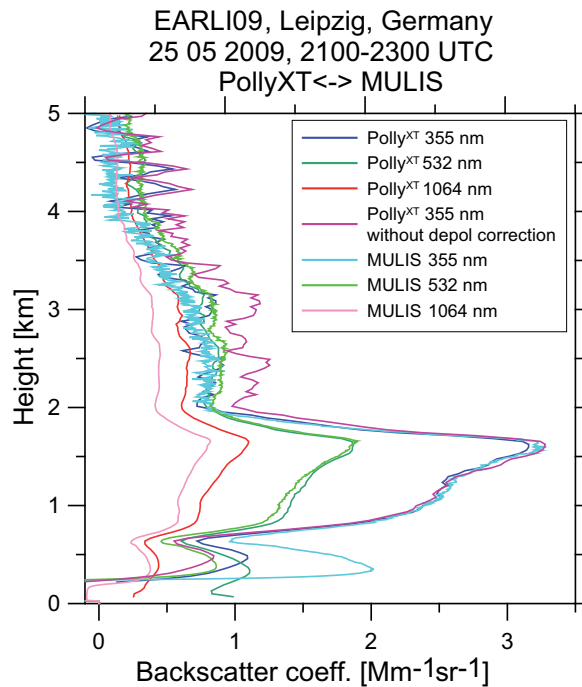


Figure 5.9: Comparison of the particle backscatter coefficient between Polly^{XT} and MULIS (University of Munich) on 25 May 2009 during EARLI09. A vertical smoothing of 90 m and 30 m was applied for Polly^{XT} and MULIS, respectively.

too high in regions of Saharan dust (2–4 km). This shows the importance of the depolarization correction when depolarizing aerosol is present. On the other hand, it also shows that the depolarization correction works very well, since the particle backscatter coefficient of the affected channels (355 and 532 nm) fit very well to measurements of MULIS. At 1064 nm, a relatively large discrepancy was observed. However, one has to keep in mind that the particle backscatter coefficient at 1064 nm is very sensitive to the chosen reference value. When altering the reference value for the Polly^{XT} profile, a perfect agreement with the Munich measurements can be achieved. However, the particle backscatter coefficients of Polly^{XT} were calibrated within a cirrus cloud at 11–13 km. Inside the cirrus, a wavelength-independent particle backscatter coefficient is assumed. This calibration is the most robust method for the retrieval of the particle backscatter coefficient at 1064 nm. Therefore, the resulting profile of Polly^{XT} with this calibration method is shown here and may explain the large deviation of the absolute values. Below 600 m, a large discrepancy between the two lidars was observed for all wavelengths, which is caused by the different overlap functions.

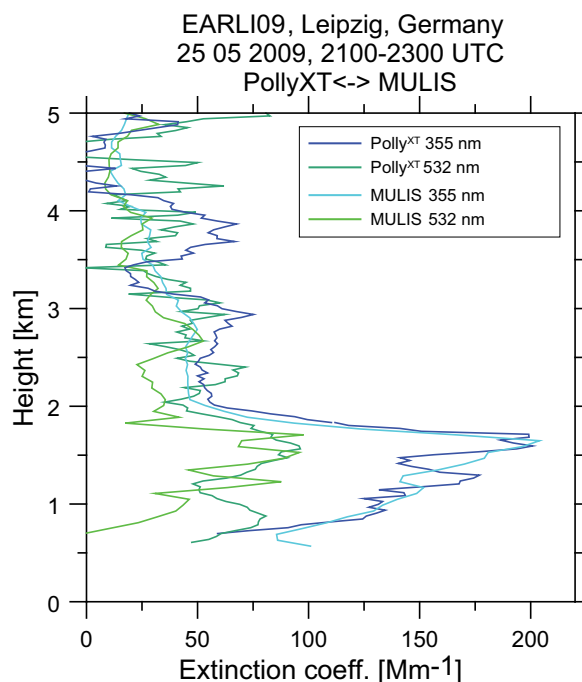


Figure 5.10: Comparison of the particle extinction coefficient of Polly^{XT} and MULIS (University of Munich) on 25 May 2009 during EARLI09. A vertical smoothing of 270 m and 82.5 m was applied for Polly^{XT} and MULIS, respectively.

The comparison of the extinction coefficient (Fig. 5.10) shows also very promising results. The vertical profile shape is the same for both lidars at both wavelengths. The retrieved profile of the particle extinction coefficient of Polly^{XT} at 355 nm is much noisier than the one of MULIS while at 532 nm it is the other way around. Nevertheless, a very satisfying agreement was observed for the particle extinction coefficient at 355 nm below 2 km. Almost identical absolute values were measured. This also shows that the overlap correction as described before works very well for measurements with Polly^{XT}. Below 600 m, an overlap correction for Polly^{XT} is not possible anymore and thus no comparison could be made. Above 2000 m, Polly^{XT} measured higher values than MULIS. The reason for this behavior is unclear, but could be due to the higher noise level. At 532 nm, the agreement of the two lidars is very good in the major aerosol layer between 1000 and 2000 m. Below 1000 m, discrepancies occur which are most obviously caused by the overlap problem. Above the major aerosol layer (>2 km), the agreement between the two lidars is acceptable, since due to the high noise level of MULIS a comparison is rather difficult.

The results of the comparison of the depolarization ratios at 355 nm between

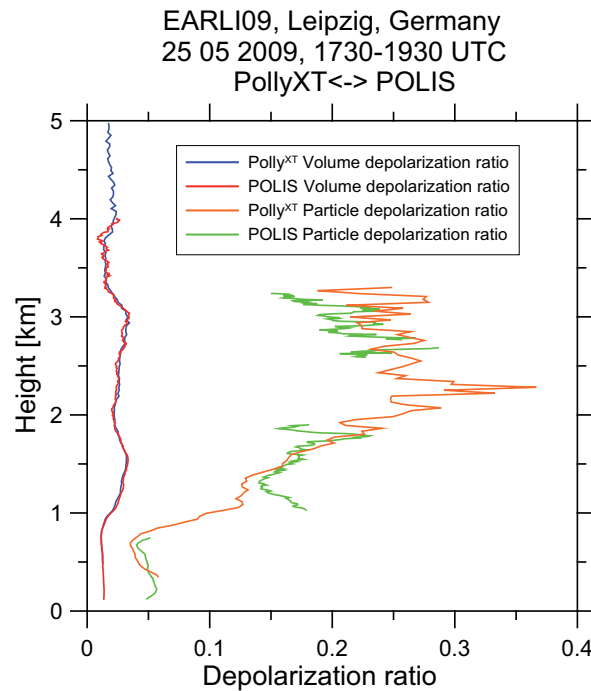


Figure 5.11: Comparison of the volume and particle depolarization ratios between Polly^{XT} and POLIS (University of Munich) on 25 May 2009 during EARLI09. A vertical smoothing of 90 m and 82.5 m was applied for Polly^{XT} and POLIS, respectively.

Polly^{XT} and POLIS are shown in Fig. 5.11. Different calibration methods have been used to retrieve the volume depolarization ratio from POLIS (calibration after *Freudenthaler et al., 2009*) and Polly^{XT} (calibration as described in Sec. 4.2.6 and Sec. 5.2). However, a very good agreement for the volume depolarization ratio was achieved. Obviously, both calibration methods work well and can be applied for lidar depolarization measurements. The comparison of the particle depolarization ratio profile shows also a reasonable agreement between POLIS and Polly^{XT}. Both profiles are noisy due to the input of two separately determined profiles (particle backscatter coefficient as derived with the Klett method and volume depolarization ratio). To high errors for the determination of the particle depolarization ratio with POLIS are the reason for data gaps between 0.8–1.1 km and 2–2.6 km. Nevertheless, the profile shape is the same for the both independently determined particle depolarization ratios and also the absolute values are nearly equal.

Finally, one can conclude that Polly^{XT} has a good performance. The retrieved quantities of particle backscatter coefficient, particle extinction coefficient, and

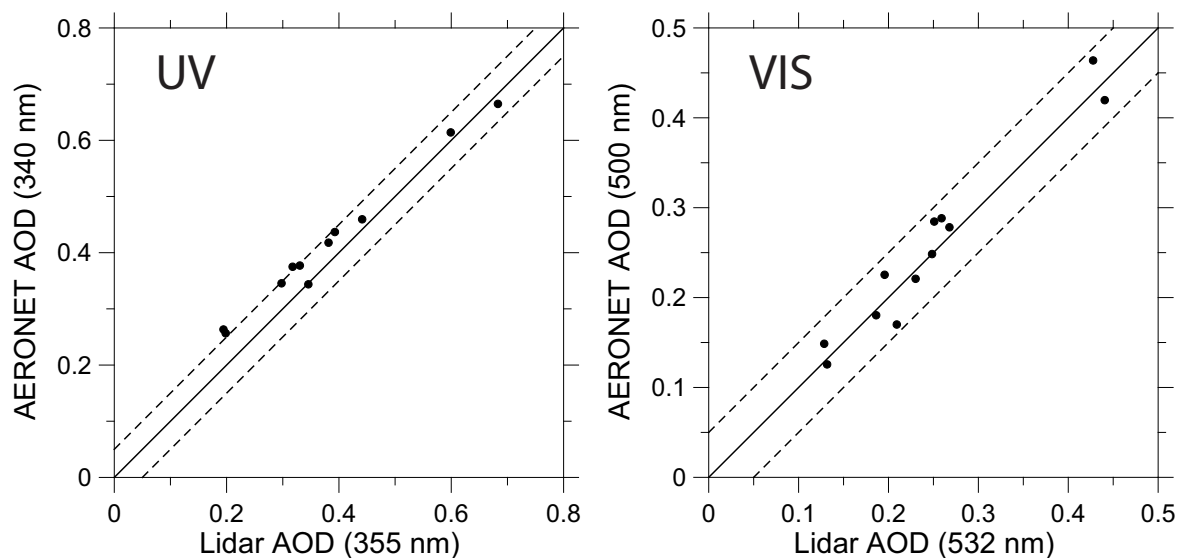


Figure 5.12: Comparison of AOD as measured with lidar and AERONET sun photometer. The 1:1 line is shown in addition (black thin line). Dotted lines indicate a deviation of 0.05.

particle depolarization ratios are trustworthy when all corrections as presented in this Chapter are applied.

5.5 Comparison with sun photometer

The determination of the AOD with Polly^{XT} is based on the assumption of a well-mixed planetary boundary layer with a constant particle extinction coefficient in the lowermost part of the lidar profile. To quantify the errors resulting from this assumption, a comparison to AERONET sun photometer measurements performed at the lidar field site⁷ is presented in Fig. 5.12. Unfortunately, AERONET sun photometer measurements were only sporadically available from July to October 2008 (cf. AERONET website, level 2.0 data). Because sun photometer measurements are carried out at daytime and Raman lidar observations are available at night time only, one has to assure equal atmospheric conditions for the comparison between the instruments. Consequently, only measurements performed during temporally close intervals with a low temporal aerosol variability were used for the comparison. As a result of these requirements, only 12 days (11 days) could be used to compare the lidar-derived AOD at 532 nm (355 nm) with the sun photometer AOD at 500 nm (340 nm).

⁷official site name on the AERONET website: Manaus

The result of the comparison is shown in Fig. 5.12. A good agreement between the two instruments was found for the UV (340 nm–355 nm) and the visible wavelength range (VIS, 500 nm–532 nm). Deviations were always less than 0.05 (indicated by the dashed lines) in the visible wavelength range and less than 0.06 in the UV wavelength range. The corresponding relative deviation between the AOD measured with the lidar and the sun photometer was less than 5%–15% at both wavelength ranges. Thus, the assumption of a well-mixed atmosphere in the lowermost part of the lidar profiles does not lead to significant errors in the AOD determination with lidar. These findings also indicate that the extinction profiles retrieved from the Raman lidar measurements are trustworthy and of good quality.

Chapter 6

Observations – Part I: Case studies

In this Chapter, the lidar observations made in 2008 are presented and discussed in form of representative case studies. The different cases provide an overview over the aerosol conditions which can be observed throughout the year in Amazonia. Some results presented in Sec. 6.1.1, 6.1.2, 6.2.2, and 6.3.2 have already been published in *Baars et al.* (2009), *Ansmann et al.* (2009), *Althausen et al.* (2009), and *Baars et al.* (2011). In the following, text passages and figures are taken from these publications without explicit citing. The seasonal analysis based on the entire set of measurements in 2008 is discussed in Chapter 7.

6.1 African aerosol in Amazonia

As outlined in Sec. 2.4, advection of Saharan dust towards Amazonia during the wet season has been reported several times (*Talbot et al.*, 1990; *Swap et al.*, 1992; *Formenti et al.*, 2001). In 2005, a MODIS-based study revealed that also African BBA is regularly transported together with Saharan dust towards South America and possibly even reaches the Amazon Basin (*Kaufman et al.*, 2005). The lidar observations performed in the framework of EUCAARI provide further evidence of smoke long-range transport towards Amazonia and also give information on the vertical aerosol structure during such smoke-transport events. In addition, the contribution of the dust and smoke fractions to the total aerosol optical properties was measured for the first time. In the following, the observation case of 10 February 2008 is discussed with focus on the advection of African aerosol towards Amazonia. Afterwards, further periods with African dust/smoke advection towards the lidar site during the wet season 2008 are presented and analyzed.

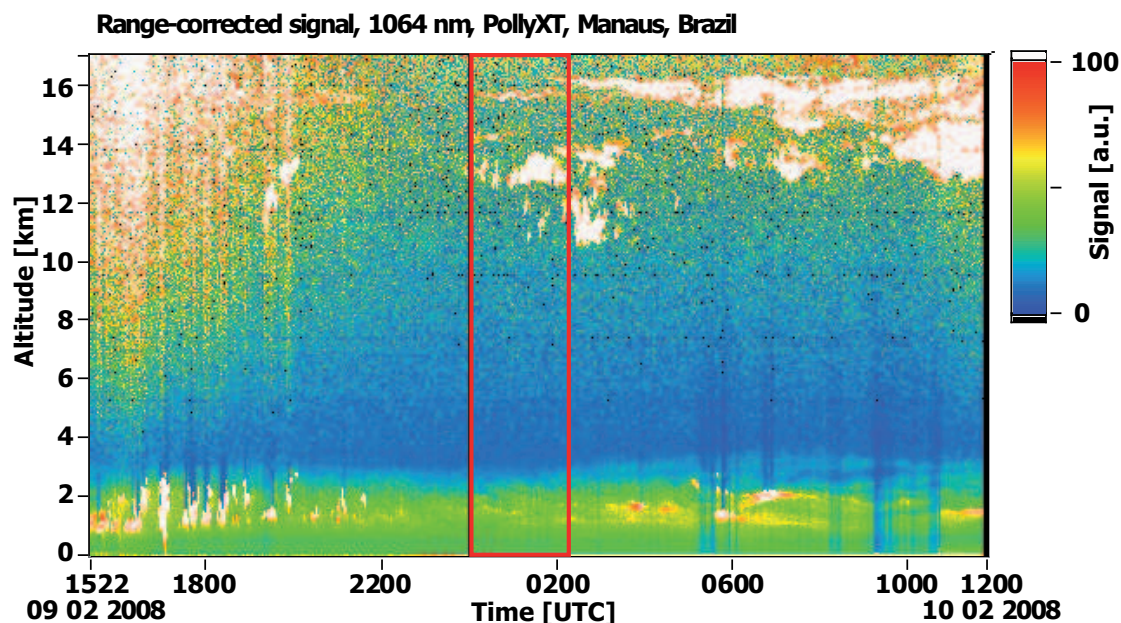


Figure 6.1: Range-corrected signal at 1064 nm between 9 February 2008, 1522 UTC and 10 February 2008, 1200 UTC. The red rectangle indicates the period for the analysis of the optical properties. Local time is UTC–4 hours.

6.1.1 10 February 2008

Figure 6.1 shows the temporal development of the range-corrected signal at 1064 nm between 9 February 2008, 1522 UTC (1122 lt), and 10 February 2008, 1200 UTC (0800 lt). Obviously, a temporally stable, approximately 3.5 km deep aerosol layer was present during the whole measurement period. This layer was not significantly disturbed by ML-related cloud formation processes which occurred before 2200 UTC. The cloud base of these ML cumuli was between 1 and 1.5 km and thus within the aerosol layer. Between 2200 and 0500 UTC, no low-level clouds occurred. Afterwards, increased backscattering due to hygroscopic particle growth and cloud formation within the aerosol layer was observed from time to time. Occasionally, fog developed during the measurement period (e.g., at around 0500 UTC). Extended cirrus fields were observed between 10 and 17 km all the time.

The aerosol layer observed at the lidar site probably originated from Africa as indicated by the 8-day composite image of MODIS AOD (550 nm) from 2–10 February 2008 shown in Fig. 6.2. A high aerosol load (AOD >0.9) over Central Africa was observed by the satellite. The aerosol plume obviously propagated westwards towards

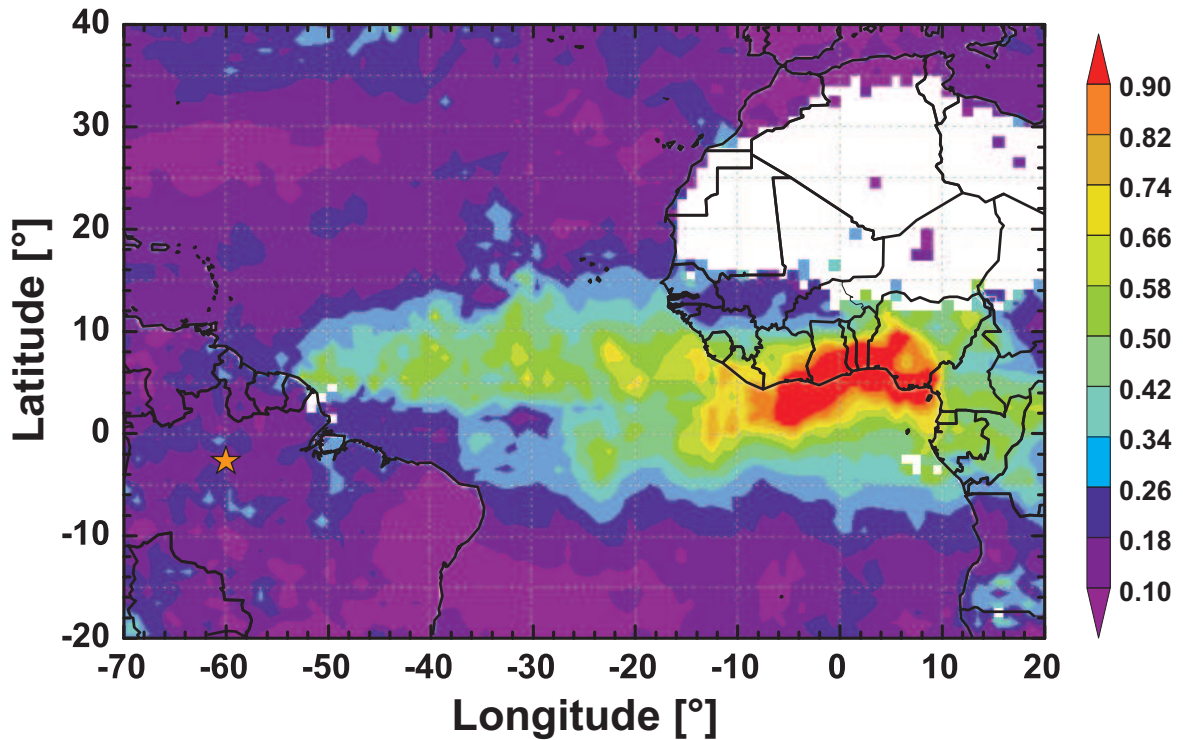


Figure 6.2: Mean AOD (550 nm) observed with MODIS from 2–10 February 2008 (<http://disc.sci.gsfc.nasa.gov/giovanni/>).

the Amazon Basin as indicated by HYSPLIT¹ backward trajectories (Fig. 6.3, left, *Draxler and Hess, 1998; Draxler et al., 2009; Draxler and Rolph, 2011*). As a result, AOD values up to 0.6 were observed over the Atlantic Ocean. In contrast, the AOD measured at the lidar site was relatively low with AOD values of about 0.15. However, local Amazonian sources of aerosol cause an AOD less than 0.05 as discussed below in Sec. 6.2, so that even weak contributions of out-of-Basin aerosol can significantly influence the aerosol conditions in Amazonia.

The high AOD over Central Africa and the Atlantic was partly caused by fires in Africa as MODIS fire counts (*Giglio et al., 2003*) in Fig. 6.3, left, indicate. A pronounced fire activity was observed between 5°N and 15°N in Africa from 2–10 February 2008. Consequently, large amounts of BBA were produced and partly transported across the Atlantic Ocean.

However, also Saharan dust was advected towards South America as model calcu-

¹Hybrid Single Particle Lagrangian Integrated Trajectory Model. Meteorological fields from the archived model assimilation data sets of GDAS (NCEP Global Data Assimilation System) were used.

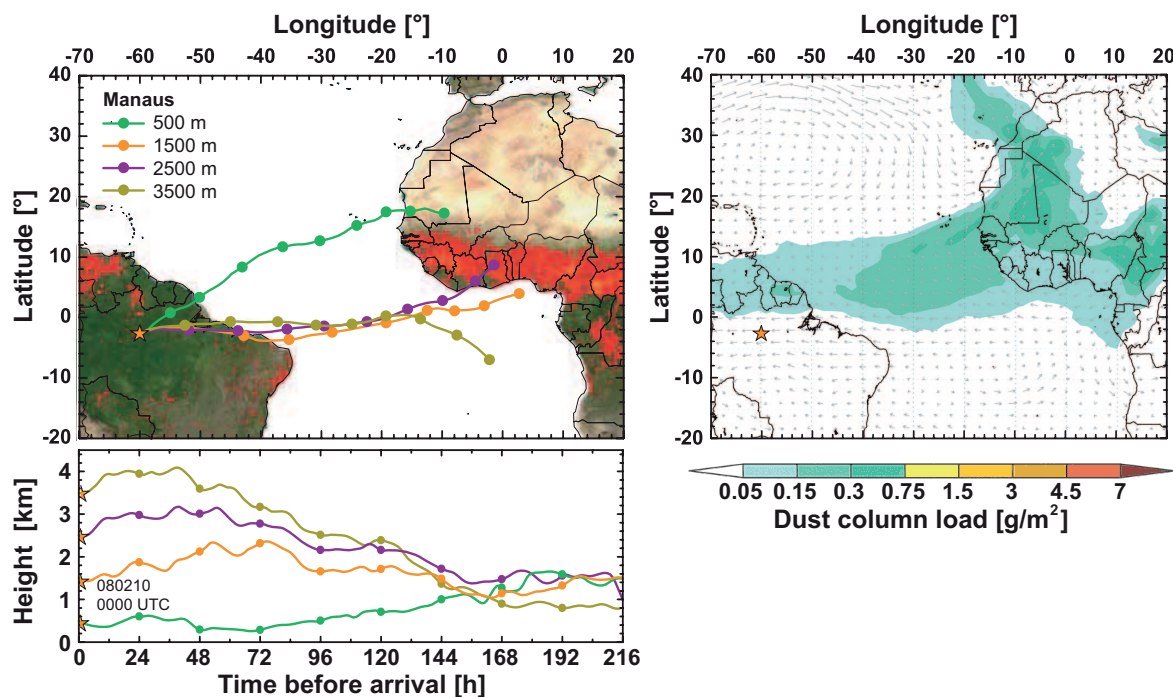


Figure 6.3: Left: 9-day HYSPLIT backward trajectories ending at Manaus, Brazil, on 10 February 2008, 0000 UTC. The underlying fire map derived from MODIS observations shows all fires (red spots) detected during 21–30 January 2008 (<http://www.arl.noaa.gov/ready/hysplit4.html> and <http://rapidfire.sci.gsfc.nasa.gov>). Right: Column dust load and 700 hPa wind direction as computed with NMMB/BSC-Dust for 10 February 2008, 0000 UTC.

lations of NMMB/BSC-Dust² indicate (Fig. 6.3, right, *Pérez et al.*, 2011; *Haustein et al.*, 2011, more information is given in Appendix D). According to the simulation for 10 February 2008, 0000 UTC (Fig. 6.3, right), Saharan dust arrived in Amazonia mainly north of the lidar site. At the lidar site, dust concentrations below $0.05 \frac{\text{g}}{\text{m}^2}$ (and thus not displayed in Fig. 6.3) were computed. The computations of NMMB/BSC-Dust thus indicate the possibility that both Saharan dust and African BBA were transported towards Amazonia on this particular day.

From findings of the DABEX,³ AMMA, and SAMUM-2 experiments it was shown (*Haywood et al.*, 2008; *Ansmann et al.*, 2011) that smoke is injected and mixed into the Saharan dust plume when the air masses cross the fire regions in Central

²data kindly provided by Karsten Haustein, Barcelona Supercomputing Center, Spain (Email: karsten.haustein@bsc.es)

³Dust And Biomass-burning EXperiment

Africa on their way from the Saharan desert to the Atlantic Ocean. The resulting dust/smoke mixture is transported further towards the Atlantic Ocean and can reach South America. The transport from Africa to Amazonia in the trade-wind-controlled region takes 8–10 days according to HYSPLIT backward trajectories (Fig. 6.3, left). An intensive analysis of the vertical profiles of the optical and microphysical aerosol properties observed on 10 February 2008, 0030–0230 UTC, was performed to quantify the influence of Saharan dust and African BBA on Amazonia’s aerosol population. Figure 6.4 presents the corresponding vertical profiles of particle backscatter coefficient, particle extinction coefficient, particle lidar ratio, Ångström exponent, particle depolarization ratio, and effective radius. According to the vertical structure analysis discussed in Sec. 4.2.5, the scale height H_{aer} was 1.7 km, the height H_{AOD95} was 3.5 km, and the AL top height was 4.3 km. The maximum ML top height was computed to be 1 km and, hence, lower than the height with the maximum particle backscatter coefficient (at 1.5 km). Above 1.5 km, the particle backscatter coefficient was slightly decreasing. The different values of the AL top and H_{AOD95} reveal that the majority of the aerosol load was below 3.5 km but that aerosol was also present up to 4.3 km. Maximum extinction coefficients of 60 Mm^{-1} occurred around 1.5 km. Integration of the extinction profile leads to an AOD of 0.15 for 355 and 532 nm. Extinction and backscatter-related Ångström exponents of around 0 and 0.8, respectively, were observed in the aerosol plume above 1 km height. Lidar ratios at 355 nm are considerably smaller (40–50 sr) than at 532 nm (60–70 sr) as a consequence of the high backscatter-related Ångström exponents and the low extinction-related Ångström exponents. The particle depolarization ratio does not exceed 5%. The inversion calculations (Sec. 4.2.8) reveal almost constant, large effective particle radii from 0.32 to 0.37 μm for the fine-mode fraction (radius $< 1 \mu\text{m}$) of the smoke aerosol. These specific optical and microphysical aerosol properties are an unique and clearly indication for the presence of aged biomass-burning smoke after long-range transport of more than one week (*Müller et al.*, 2005; *Ansmann et al.*, 2009). According to the discussion of *Müller et al.* (2007a) concerning the long-range transport of BBA, particle growth occurs during the transport in the atmosphere and levels off after 10–15 days only. This is corroborated by the comparably large effective radii ($> 0.3 \mu\text{m}$). According to *Fiebig et al.* (2003), the particles grow by condensation the first two days after the emission while afterwards the particle growth is dominated by coagulation. According to the low particle depolarization ratio observed by the lidar, it is obvious

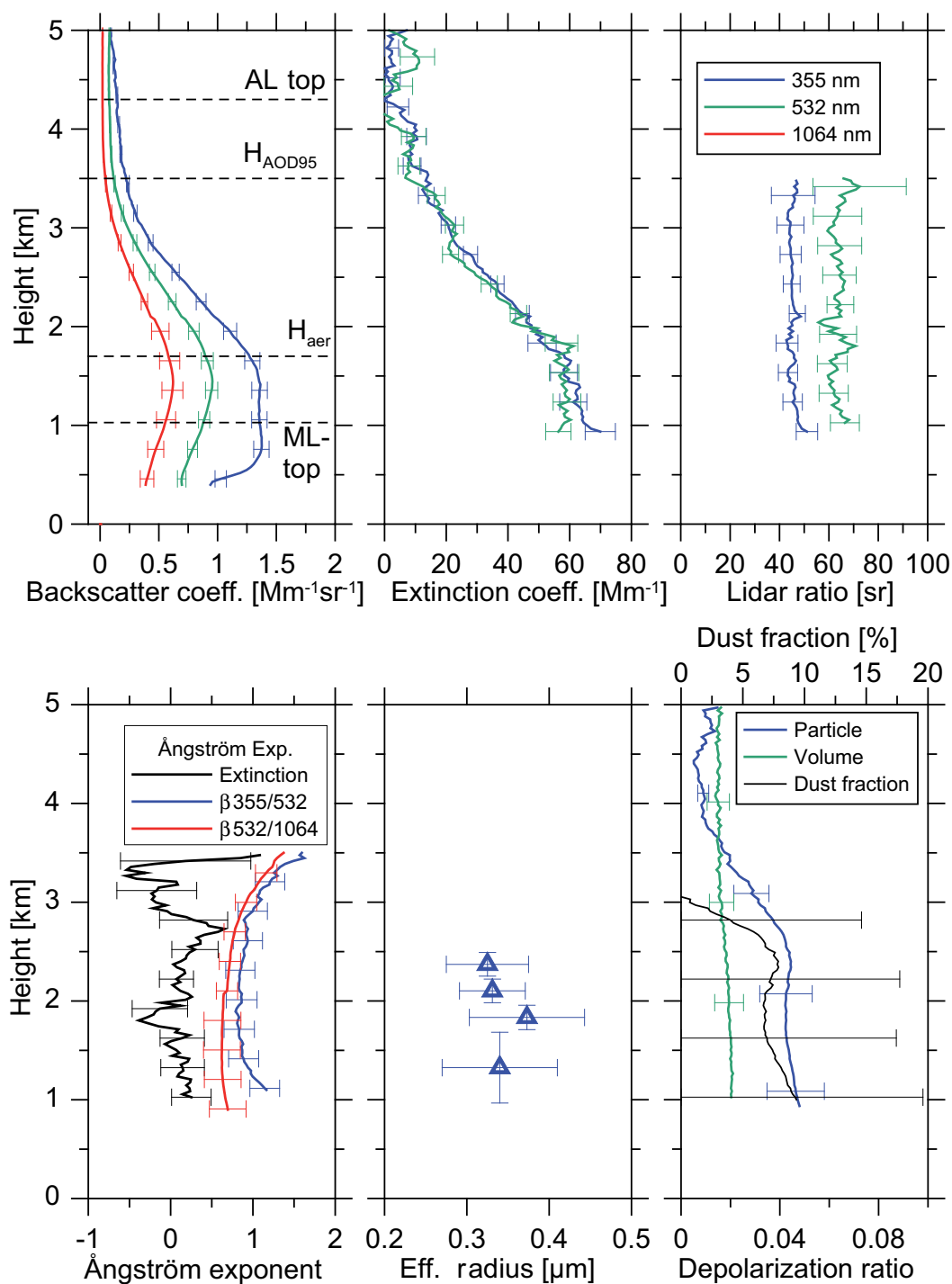


Figure 6.4: Vertical profiles of the particle backscatter coefficient, particle extinction coefficient, particle lidar ratio, Ångström exponents, volume and particle depolarization ratio, and effective radius measured on 10 February 2008, 0030–0230 UTC. The dust fraction is plotted in addition. A vertical smoothing of 750 m was applied.

that the dust fraction in this African plume was low. The dust-smoke separation (see Sec. 4.2.7) revealed that the dust fraction was less than 12% in the aerosol layer (Fig. 6.4, lower right panel). To quantify the contribution of dust and smoke particles to the aerosol conditions in Amazonia, the dust-related and smoke-related AOD was computed by means of the vertical profiles of the dust fraction and the particle backscatter coefficient. An AOD of 0.03 (background AOD in Amazonia, see next section) was subtracted from the smoke-related AOD to account for the local impact. A dust-related AOD of only 0.011 ± 0.01 was computed. In contrast, the smoke-related AOD was 0.11 ± 0.01 , and thus contributed 72% to the total AOD.

NMMB/BSC-Dust calculations for the lidar location for 10 February 2008, 0000 UTC, support these findings. The NMMB/BSC-Dust column dust load is rather low for the lidar site (interpolated from the closest grid points) with 8.25 mg m^{-2} . The resulting modeled dust optical depth at 550 nm is 0.0097. This value is in good agreement with the lidar-derived dust AOD of 0.011.

Thus, one must conclude that aged BBA from Africa dominated the aerosol optical properties at the lidar site on 10 February 2008. The influence of smoke produced in South America during that time is less plausible. No fires were detected in South America along the air-mass travel path (Fig. 6.3) which is well defined due to the trade-wind circulation. The enhanced fire activity which can be seen in Fig. 6.3 ca. 700 km north of the lidar site occurred between 2 and 5 February 2008 (individual analysis by FIRMS web fire mapper⁴) and hence should not have affected the measurements near Manaus (consider also the computed air-mass travel path). These considerations are consistent with ground-based in-situ measurements made at the same time during the AMAZE-08 campaign (see *Chen et al.*, 2009). No markers of fresh BBA were found in the particle-phase mass spectra, but sometimes clear indications for the presence of out-of-Basin aerosol (e.g., Saharan dust and aged BBA).

⁴Fire Information for Resource Management System, <http://firefly.geog.umd.edu/firemap/>

6.1.2 Overview of dust and smoke advection towards Amazonia during the wet season 2008

Advection of smoke and dust was observed several times during the wet season 2008. Such advection events were characterized by an AOD above background levels (i.e., >0.05 , see Sec. 6.2) and by an enhanced particle depolarization which is indicative for the presence of Saharan dust. An AOD >0.05 together with an enhanced particle depolarization ratio was observed for 17 lidar measurements in the wet season 2008 (about one third of all wet-season observations). For these 17 periods with enhanced particle depolarization ratio, the dust fraction was calculated as described in Sec. 4.2.7. The vertical profiles of the dust fraction and the corresponding particle extinction coefficient at 532 nm are shown in Fig. 6.5 and are grouped into four different plots corresponding to date of occurrence. It is interesting to note that the occurrence of enhanced depolarization in the lidar profiles lasted usually for several days and three major episodes of African aerosol advection towards Amazonia could be identified. The first period lasted from 8–15 February 2008, a second pronounced period occurred from 25 February–1 March 2008 (consistent with the dust and smoke transport over the Atlantic Ocean discussed by *Ben-Ami et al.*, 2010), and the third one was recorded from 8–11 May 2008. Rarely, advection of African aerosol for one day only was observed (30 January, 15–16 March, and 8 April).

The dust fraction was found to roughly increase with time from values below 35% for the 8–15 February period to values between 20% and 50% for the second episode (25 February–1 March) and the observations mid of March and April. In mid May, dust fractions up to 100% could finally be observed as a result of significantly decreasing fire activity at the beginning of the wet season in Central Africa. The non-dust fraction during such events may be partly influenced by marine particles and local pollution events, but is mainly related to African smoke as indicated by the clear aged-smoke signature in the spectral dependence of the particle backscatter and extinction coefficients (see Sec. 6.1.1).

These findings from the lidar observations are consistent with ground-based mass spectral characterization of sub-micron particles at the same location in February and March 2008 (*Chen et al.*, 2009). The authors state that aerosol from outside the Amazon Basin occasionally influences the aerosol population. Marine aerosol and African smoke are suggested to be good candidates for that out-of-Basin aerosol. The advection of marine aerosol cannot be ruled out. However, the analyzed optical properties for the 17 lidar cases do not indicate a significant influence of marine

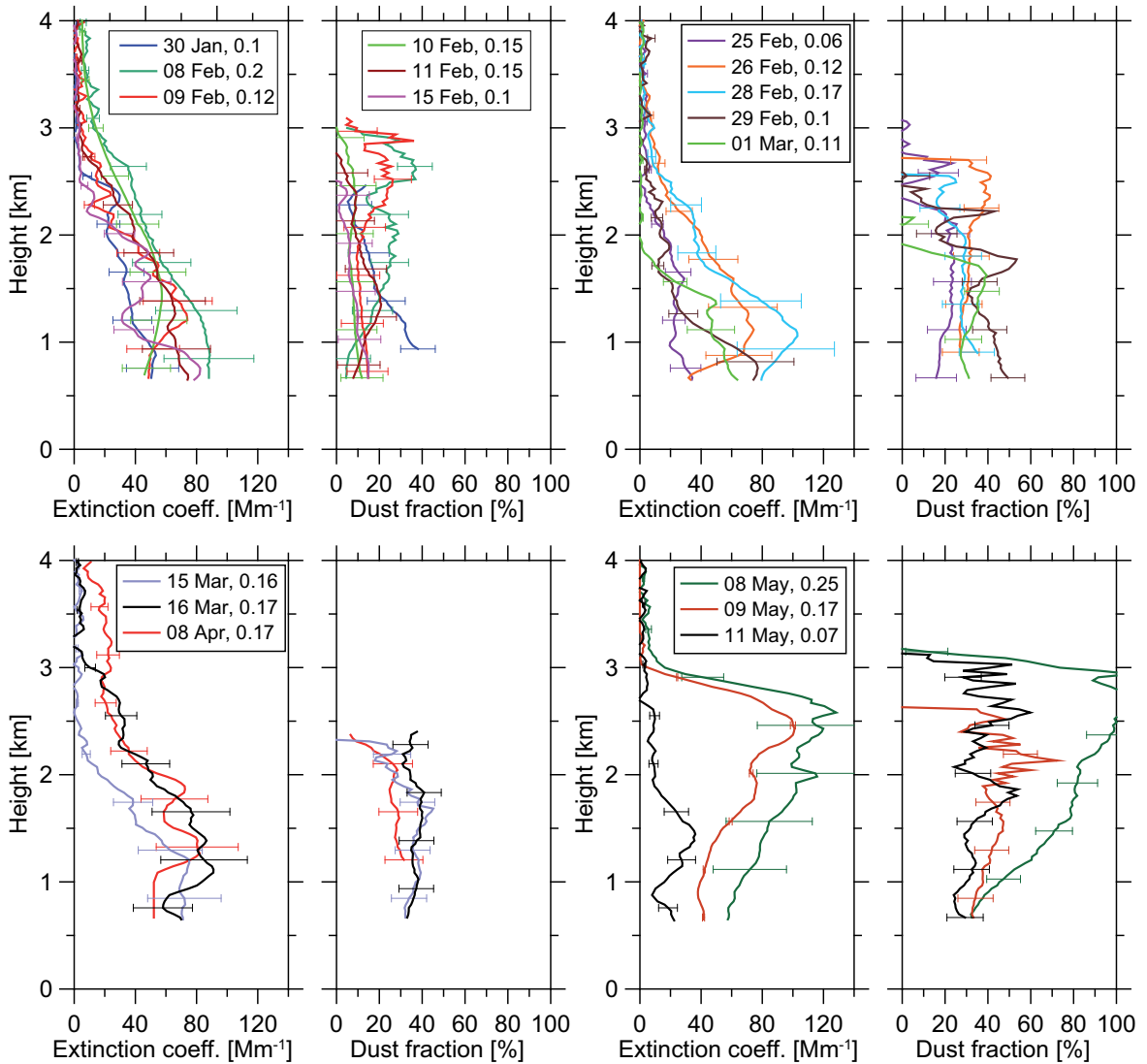


Figure 6.5: Vertical profiles of the particle extinction coefficient at 532 nm and the corresponding dust fraction (355 nm) for observations with enhanced depolarization measured in 2008. A vertical smoothing of 270 m was applied. The legend indicates the date of the observation in 2008 and the measured AOD at 532 nm.

aerosol to the total optical properties. Particles of marine origin have lidar ratios well below 30 sr (*Groß et al.*, 2011). Such low lidar ratios were never observed during the wet season 2008.

One general finding from the analyzed cases is that the Saharan dust and the African BBA were trapped in the lowermost 3–3.5 km at the lidar site. *Ben-Ami et al.* (2010) discussed the transport of two mixed smoke-dust plumes from Africa over the Atlantic Ocean from 17 February–1 March 2008 and showed that the aerosol plume extended up to 3.3 km along the Brazilian coastline on 24 February 2008. Consequently, the mixed aerosol plume did not significantly change its vertical extent during the 48-hour transport from the Brazilian coast over the continent towards the lidar site (compare 26 February in Fig. 6.5).

However, the vertical layering of the mixed dust/smoke plumes arriving in Amazonia was different to the vertical distribution of smoke and dust in Central Africa, measured close to the source regions. Lidar observations of Saharan dust and BBA in the Sahel region (Africa) during AMMA and DABEX (*Heese and Wiegner*, 2008; *Johnson et al.*, 2008) showed that the aerosol is typically lifted up to 3–5 km height. Different aerosol layers were frequently observed during the measurements. Pure Saharan dust was found in the lowermost part of the troposphere (<2 km) and a mixture of dust and smoke above (2–5 km). Similar aerosol layering was observed near the African continent at Cape Verde during SAMUM-2 (*Tesche et al.*, 2011b). Consequently, sedimentation and scavenging processes during the 6–8 days of transport across the Atlantic Ocean may have led to the mixing of the different aerosol layers and to a slight decrease in the vertical extent of the aerosol plume when arriving at the South American continent.

In Fig. 6.6, the dust-related and smoke-related AOD (computed from the vertical profiles of the dust fraction and the particle extinction coefficient) is shown for the 17 cases of long-range transport. One can see that the AOD at 532 nm was between 0.05 and 0.15 for African BBA particles during the period of 8–15 February. The BBA contribution to the AOD was up to 0.1 for the period end of February and between 0.06–0.09 for the period in mid of March. A strong Saharan dust event with a dust-related AOD value up to 0.18 was observed only on one day (8 May 2008). The observation of this dust event is rather interesting, because usually no aerosol transport from Africa towards Amazonia is expected in May. The location of the ITCZ is north of the Equator at this time, so that African aerosol is usually transported towards the Caribbean. Dust concentrations as derived from the dust transport

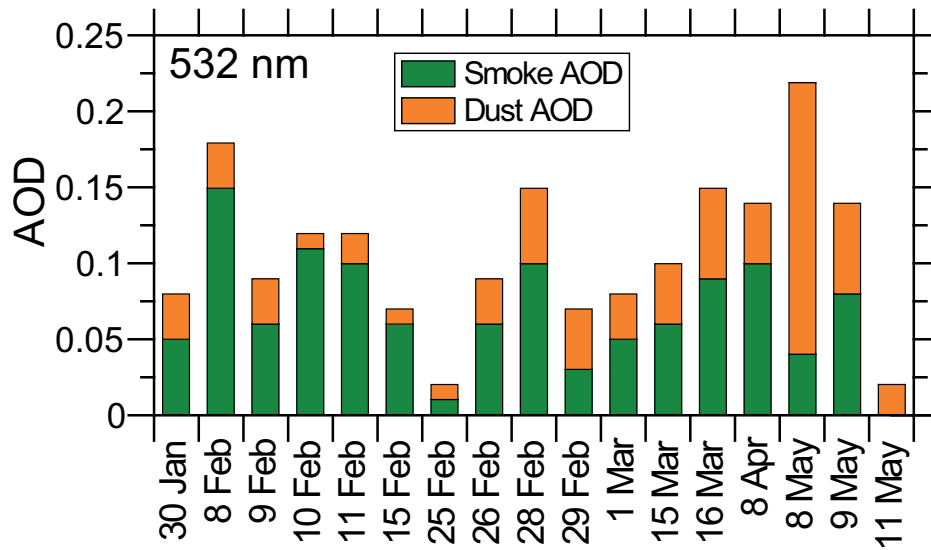


Figure 6.6: Smoke and dust related AOD for the 17 observation cases in 2008 indicating the advection of African aerosol towards Amazonia. The measured total particle optical depth is obtained by adding 0.03 to the shown AOD (full green-orange bar).

model NMMB/BSC-Dust corroborate the finding of the pronounced dust intrusion on 8 May 2008. Simulated maps of the columnar dust load (Fig. 6.7) show that Saharan dust advection occurred from 8–11 May 2008 towards the northern part of Amazonia and the Caribbean. In accordance with the predictions from NMMB/BSC-Dust, high dust concentrations were also measured at Ragged Point, Barbados, Caribbean on 8 May 2008. There, Saharan dust concentrations up to $80 \mu\text{g}/\text{cm}^3$ were observed at surface-level (*Prospero*, 2011). A dust AOD (500 nm) of only 0.04 was modeled for the lidar location for 8 May 2008, which is much lower than the measured value (0.18 at 532 nm). The discrepancy between the measured and simulated dust AOD seems to be large. However, the simulation of Saharan dust transport over a distance of more than 7000 km covering very different regions (desert, savanna, ocean, and tropical rain forest) is very difficult. For example, *Pérez et al.* (2011) discussed the effects upon modeled dust concentration due to the sensitivity of dust removal by stratiform and convective rain to the prescribed dust solubility in the model. Consequently, a high uncertainty can be expected in the quantification of the Saharan dust amount in Amazonia. With regard to the high dust concentration in northern South America (compare Fig. 6.7) one may conclude that the Saharan dust plume extended much more to the interior of the Amazon Basin than simulated by NMMB/BSC-Dust.

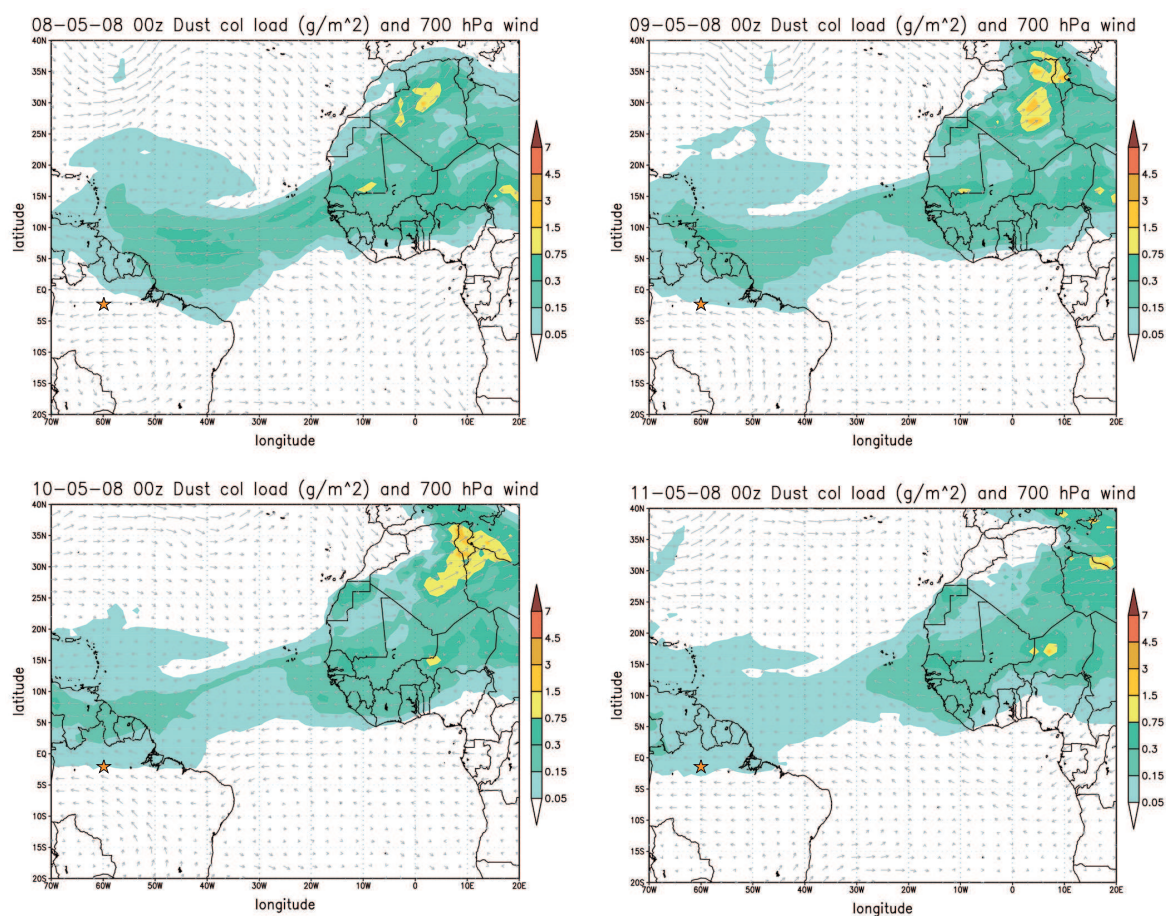


Figure 6.7: Dust column load and 700 hPa wind direction as derived from NMMB/BSC-Dust for 8–11 May 2008.

Kaufman et al. (2005) analyzed long-term MODIS data and concluded that the anthropogenic influence in the dust/smoke plumes traveling over the Atlantic Ocean is highest in February. The authors state, that the mixed plumes contain about 45% of smoke close to the source at this time of the year. Further away of the source (0°–5° N, 20°–30° W) it was found that the dust fraction is reduced to 10% probably due to sedimentation, and that marine particles contributed about 25% and BBA about 65% to the total AOD in February. When the burning activity in Central Africa was decreasing (e.g., in March and April), an increasing dust fraction was reported by *Kaufman et al.* (2005). These findings are in good agreement with our observations (compare Fig. 6.6). Consequently, BBA from Africa cannot be neglected when considering intercontinental transport of aerosol towards Amazonia.

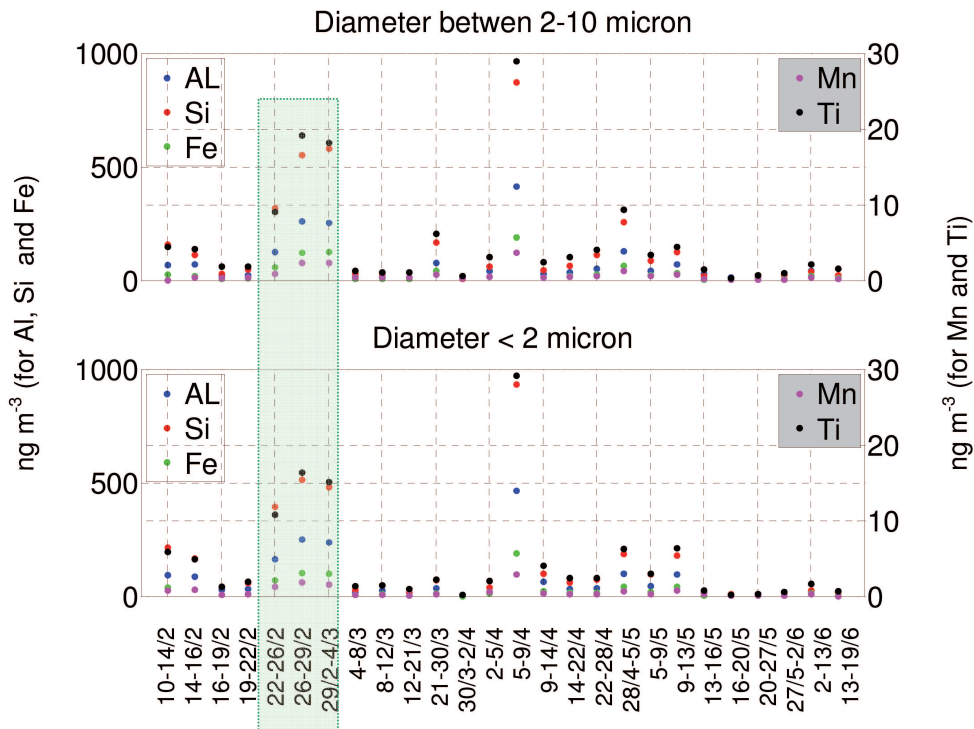


Figure 6.8: Elemental composition (mass concentration) of aerosol collected during February and June 2008 at the EUCAARI site in Amazonia. Top: fine mode (radius $<1 \mu\text{m}$), bottom: coarse mode (1 to $5 \mu\text{m}$). The area in the green rectangle marks the dates for which crustal elements were enhanced. Plot taken from *Ben-Ami et al.* (2010).

African aerosol was also detected by in-situ measurements at ground during EUCAARI and AMAZE-08. For example, Fig. 6.8 (taken from *Ben-Ami et al.*, 2010) shows the PIXE (Particle-Induced X-ray Emission, *Artaxo and Orsini*, 1987) filter analysis of fine and coarse-mode particles from February to June 2008 at the EUCAARI site in Amazonia for five elemental components: aluminum, silicon, iron, manganese, and titanium. The concentration of these specific elemental components is strongly related to mineral dust. One can clearly see that two periods of enhanced concentration of the five elemental components were observed at surface level. The period from end of February to beginning of March is in good agreement with the observation of enhanced particle depolarization with lidar (compare Fig. 6.5). For the second period beginning of April 2008, unfortunately no lidar data is available. The dust period observed by lidar in May 2008 is only slightly reflected in the PIXE analysis. This may indicate that the Saharan dust was mainly advected within lofted layers above the ML.

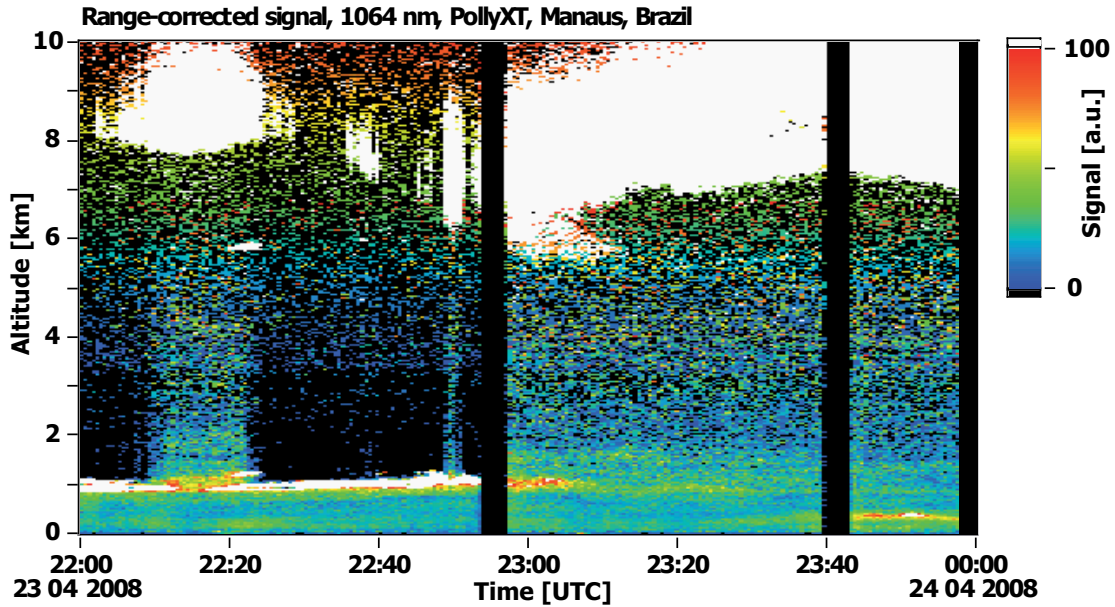


Figure 6.9: Temporal evolution of the range-corrected signal at 1064 nm on 23 April 2008, 2200–2400 UTC. Local time is UTC–4 hours.

6.2 Background conditions in Amazonia

The wet season in the Amazon Basin is assumed to be very clean in terms of aerosols and almost free of anthropogenic influence (*Martin et al.*, 2010a). *Pöschl et al.* (2010) even state that aerosol conditions “approach to those of the pristine pre-industrial era”. However, aerosol advection towards Amazonia can dominate the local aerosol population as shown in Sec. 6.1. Therefore, it is interesting to know what the natural background conditions in Amazonia are and how the aerosol is vertically distributed under such background conditions. In the following, a case study representing background conditions is presented, followed by an overview and related statistical results of all background observations during the wet season 2008.

6.2.1 23 April 2008

As one example for very clean conditions, the lidar observations on 23 April 2008 are discussed. Figure 6.9 shows the temporal evolution of the range-corrected signal of Polly^{XT} between 23 April 2008, 2200 UTC and 24 April 2008, 0000 UTC. No rain was observed during the whole observation period. In the beginning of the observation, low-level clouds were present at around 1 km agl which prohibited the penetration of the laser beam to higher altitudes. At about 2300 UTC (1900 local time), the low-level

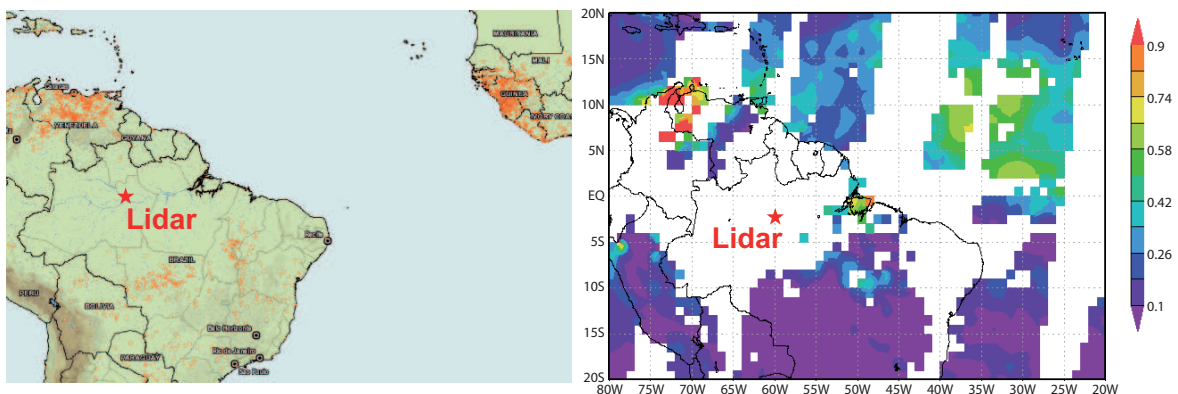


Figure 6.10: Left: MODIS fire counts between 17 and 23 April 2008 (<http://maps.geog.umd.edu/firms/>). Right: MODIS AOD for 23 April 2008, 1345–1525 UTC (<http://daac.gsfc.nasa.gov/giovanni/>).

clouds dissolved and the vertical extent of the aerosol layer of 2 km could be measured. Mid-level clouds were then observed at altitudes above 6 km. No MODIS AOD was available on 23 and 24 April 2008 for the whole Amazon Basin (Fig. 6.10, right) due to the high cloud cover. Figure 6.10, left, shows the fire counts for 17–23 April 2008 derived from MODIS. A high fire activity in South America was observed only in the northernmost part of the continent in Venezuela and Colombia. Sporadic fires were detected at the south-eastern edges of the Amazon Basin. However, no fires occurred close to the lidar site and along the air-mass transport path (Fig. 6.11) in Amazonia. Consequently, South American BBA is not expected at the field site during the analyzed period.

HYSPLIT ensemble backward trajectories were calculated for three different arrival heights (Fig. 6.11). The backward-trajectory ensemble calculation for 500 and 1000 m arrival height shows a relatively high but acceptable scatter. A low scatter is obtained for the backward trajectory ensemble at 2000 m arrival height. The air flow close to the surface (500 m and 1000 m arrival height) came from easterly to north-easterly direction, while the backward trajectories at 2000 m arrival height indicate transport from easterly directions. Thus, the air flow during that period was strongly dominated by the trade-wind circulation. An influence of African aerosol as discussed in Sec 6.1 cannot be ruled out. A high fire activity in Central Africa was also observed during that time (Fig. 6.10, left), and smoke from these fires and possibly Saharan dust were obviously transported westward over the Atlantic Ocean. As a result, an enhanced AOD (>0.5) was observed on 23 April over the Atlantic Ocean (Fig. 6.10, right).

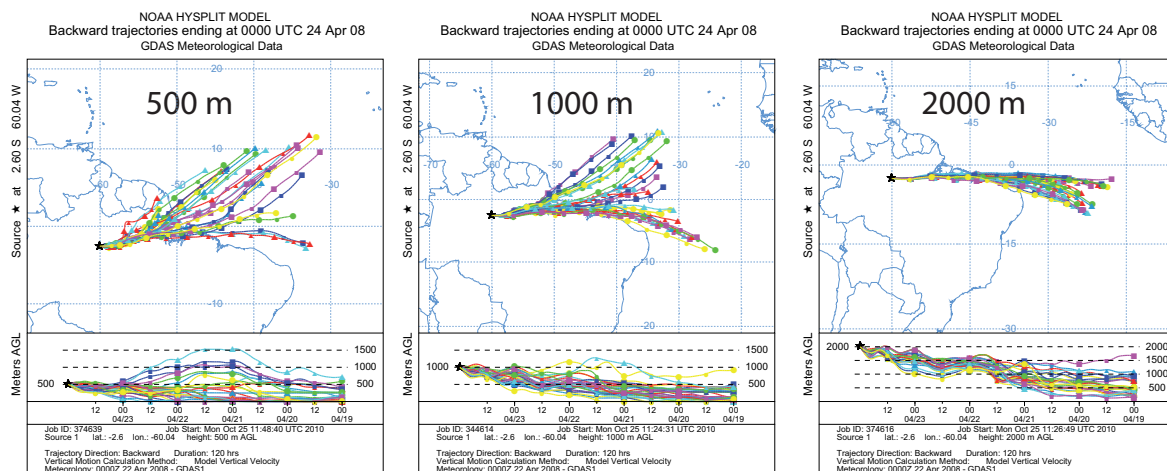


Figure 6.11: HYSPLIT ensemble backward trajectories for 500, 1000, and 2000 m agl arrival height on 24 April 2008, 0000 UTC.

These air masses of high AOD may have been also transported towards the Amazon Basin. However, the backward-trajectory calculations for all three altitudes (Fig. 6.11) show that the air masses needed about 48 hours to travel from the coast to the lidar site in central Amazonia. During this transport time, potential out-of-Basin aerosol was most probably removed by strong tropical precipitation events as can be seen in Fig 6.12. Here, the accumulated precipitation as derived from NMMB/BSC-Dust for 23 April 2008 is shown. The computation of the precipitation rate is based on NCEP reanalysis data which contain precipitation observations. The precipitation rate from NMMB/BSC-Dust is thus an objective parameter to estimate the wet deposition efficiency. Fig 6.12 shows a high precipitation rate (up to 5–10 mm in 3 h) at the lidar site and in the north-east of the lidar site from 0300 until 1500 UTC. These strong rain events may have contributed to the cleaning of the air from out-of-Basin aerosol upwind of the measurement site.

The vertical profiles of the particle backscatter coefficient at 532 and 1064 nm and the respective Ångström exponent for the period without low-level clouds between 2330 and 0000 UTC are shown in Fig. 6.13. One aerosol layer near to the surface and a second aerosol layer at around 1 km were observed. The second layer may be interpreted as the residual of the cloud that was observed at the same height before (Fig. 6.13). The corresponding Ångström exponents for the observed particle backscatter coefficients (Fig. 6.13) were between 1 and 1.5 which indicates the presence of a well-developed accumulation mode in the particle size distribution (PSD). Because of instrumental problems, no information from the UV channels was available.

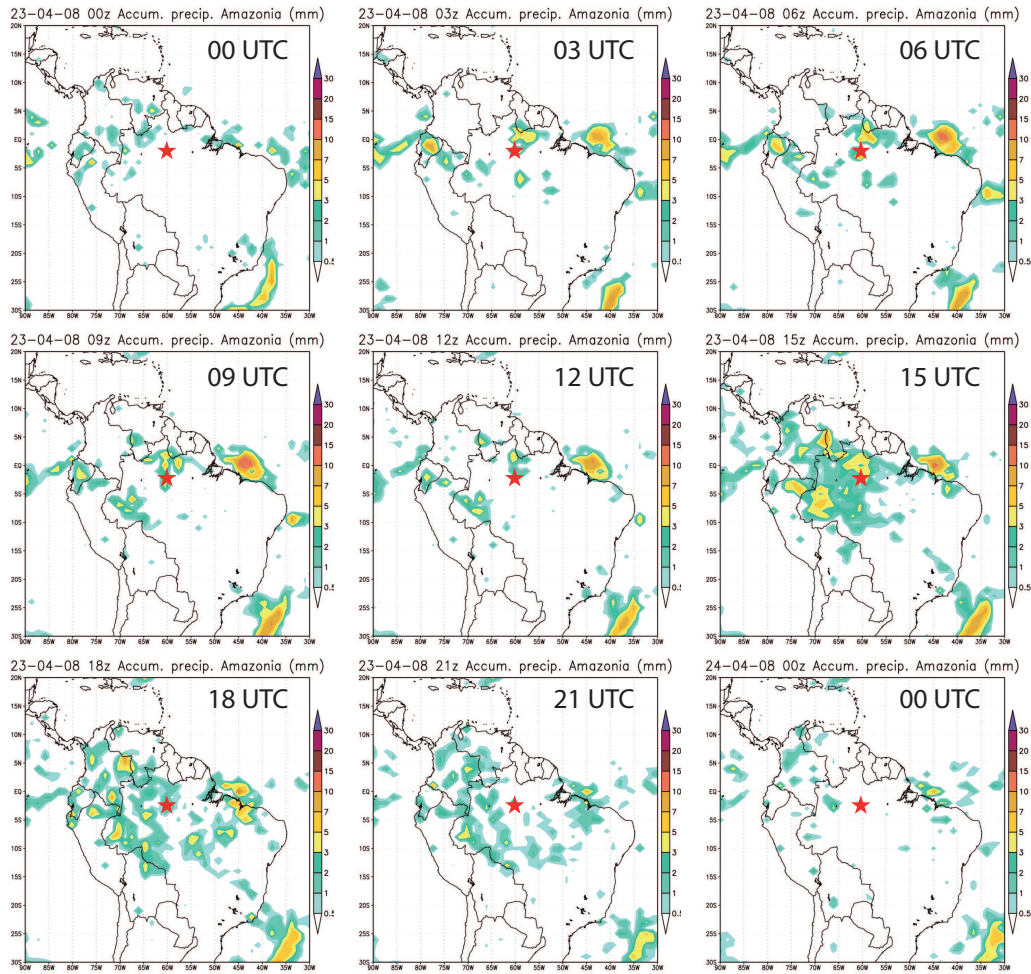


Figure 6.12: 3-h accumulated precipitation for 23–24 April 2008 from NMMB/BSC-Dust on the basis of the NCEP reanalysis. The red star indicates the lidar location.

According to the particle backscatter coefficient profile extrapolated to the surface and assuming a constant lidar ratio of 60 ± 20 sr (see Sec. 4.2.4), the lidar AOD at 532 nm on that day was only 0.019 ± 0.008 . This value is lower than the average AOD over clean marine sites (*Smirnov et al.*, 2009). Table 6.1 summarizes some observations of very low AOD (500–532 nm) measured at marine and continental sites. According to these values, the AOD of 0.019 is one of the lowest values ever measured on a continent and even lower than for usual clean marine conditions. Only measurements above the marine ML and near Antarctica showed similar low AOD values.

The analysis of the vertical aerosol structure as introduced in Sec. 4.2.5 revealed that the maximum ML top on that day was 760 m. Thus, it was slightly higher than the observed top of the first aerosol layer. The scale height H_{aer} was calculated to be

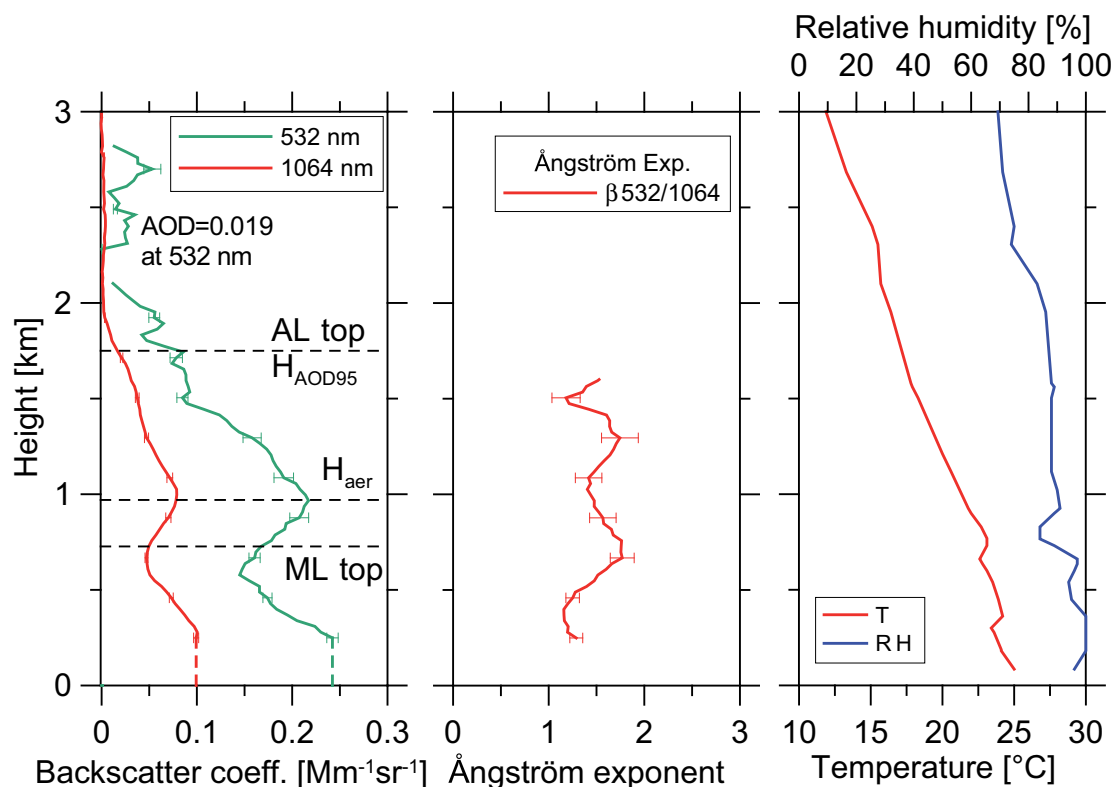


Figure 6.13: Vertical profiles of the particle backscatter coefficient and the corresponding Ångström exponent between 2330 UTC and 0000 UTC. A vertical smoothing of 510 m was applied. Temperature and relative humidity (RH) profile from the radiosonde launch on 24 April 2008, 0000 UTC at Manaus are shown in addition. $AOD(532\text{ nm}) = 0.019 \pm 0.008$.

960 m. The AL top and the height H_{AOD95} coincide at 1750 m. Hence, the AL top and H_{AOD95} are suitable to identify the uppermost aerosol layer on that day while H_{aer} is useless for the identification of the aerosol layers in this case.

The vertical profiles of temperature and relative humidity (RH) on 24 April 2008, 0000 UTC are shown in Fig. 6.13, right. From the temperature profile one can identify three different inversion layers. The first one is located at around 400 m, the second one at 800 m, and the third one at around 2000 m. The second and the third temperature inversion at 800 and 2000 m, respectively, fit very well to the observed aerosol profile. The second inversion coincides with the top of the lowest aerosol layer and the third one is close to the AL top. Therefore, one can conclude that the radiosonde launch performed 60 km to the south is representative for the meteorological conditions at the field site on this day. The RH profile derived from the radiosonde shows values up to 100% in the lowest 1000 m which is in good agreement with fog observation later during

Air-mass origin	Minimum AOD	Location, time period, and further notes	Reference
marine	0.05	Portugal, 1999	<i>Ansmann et al. (2001)</i>
above marine ML	0.013	5-year mean (1994–1999) for August at Mauna Loa (3.4 km agl), Hawaii	<i>Holben et al. (2001)</i>
marine at low wind speed	0.05	Atlantic Ocean, RV Polarstern transects	<i>Kanitz (2011)</i>
arctic, marine	0.02–0.03	near the coastline of Antarctica	<i>Smirnov et al. (2009)</i>
marine	0.04–0.08	southern Atlantic, October–December 2004	<i>Smirnov et al. (2006)</i>
marine	0.01	Mean value for July at Cape Grim, Tasmania for 1986–1999. Pinatubo affected periods have been removed.	<i>Wilson and Forgan (2002)</i>
continental	0.05	Beijing, January 2005	<i>Tesche et al. (2007)</i>
continental	0.011	Amazon rain forest, wet season 2008	this study
continental	0.06	5-year mean (1994–1999) for December–January at the CART Site, Oklahoma, USA	<i>Holben et al. (2001)</i>

Table 6.1: Observations of minimum AOD at several locations (wavelength range: 500–532 nm). The lowest AOD of a certain campaign or lowest monthly-mean AOD of an AERONET site are given.

the observation period (after 0000 UTC). The RH decreases to values between 60% and 80% at higher altitudes. The observation of an AOD < 0.02 is very surprising under conditions of RH close to 100% because one would expect increased light attenuation due to hygroscopic growth of the particles. Either the aerosol concentration was so low that hygroscopic growth effects did not significantly amplify the light scattering or hygroscopic growth is weak for the natural aerosol particles in Amazonia as, e.g., outlined by *Zhou et al. (2002)* and *Rissler et al. (2004)*. The authors classified the majority of the particles under clean background conditions in Amazonia as “less hygroscopic”. In summary, one can conclude that the observed aerosol conditions on 23 April 2008 with an AOD of 0.02 represents background or natural aerosol conditions over the Amazon rain forest.

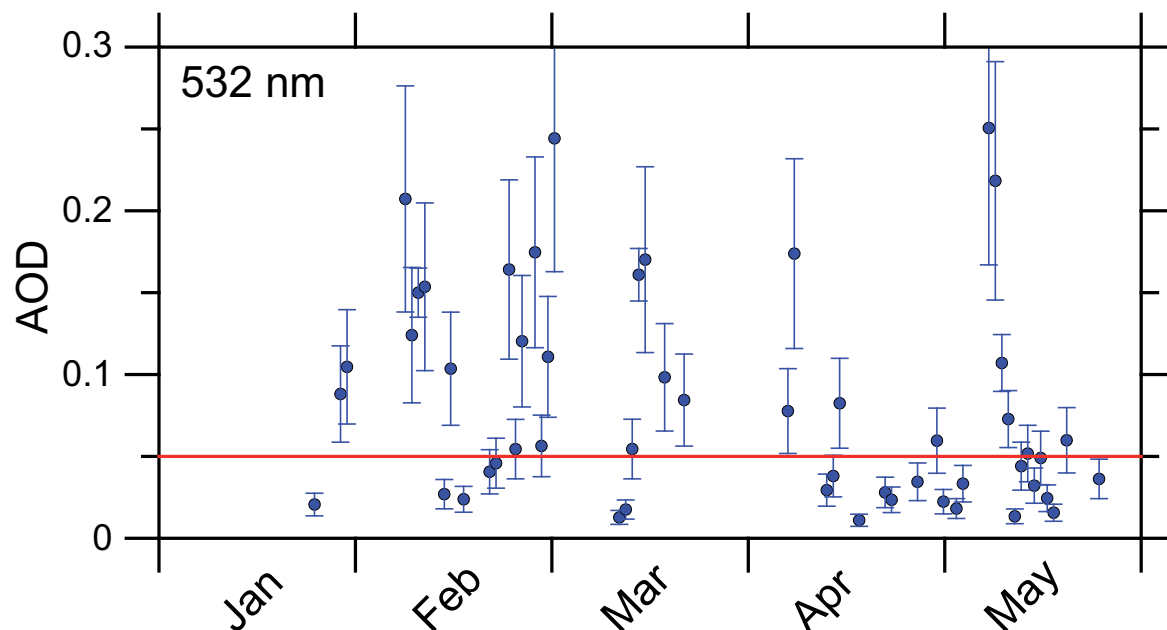


Figure 6.14: Temporal evolution of the AOD at 532 nm during the wet season 2008. Error bars indicate the uncertainty due to the assumption of the lidar ratio. AOD values below the red line indicate background aerosol conditions.

6.2.2 Further background cases

In total, vertical profiles of the particle backscatter coefficient at 532 nm could be obtained for 53 lidar observation days from January to May 2008. The aerosol optical depth (AOD) at 532 nm for these 53 observations is shown in Fig. 6.14. Very clean conditions with an AOD well below 0.05 were frequently found (in about half of these 53 observation). A mean AOD of 0.03 ± 0.02 was observed for such clean conditions. This mean AOD value can be used as a measure for background conditions over the tropical rain forest. Accordingly, this AOD level may be interpreted to be caused by primary aerosol emission and secondary aerosol formation of condensable precursor gases emitted by the tropical rain forest.

The minimum AOD of the entire campaign of 0.011 ± 0.004 was observed on 18 April. This is the lowest value the IfT has ever measured with its lidars over a continental site during the last 20 years. Our observations in central Amazonia are in good agreement with AOD observations for background conditions performed in Rondônia (*Guyon et al.*, 2003). A mean AOD (500 nm) of 0.048 ± 0.08 from 10 days of background conditions was measured.

Six cases in 2008 for which the AOD at 532 nm was below 0.05 are presented in

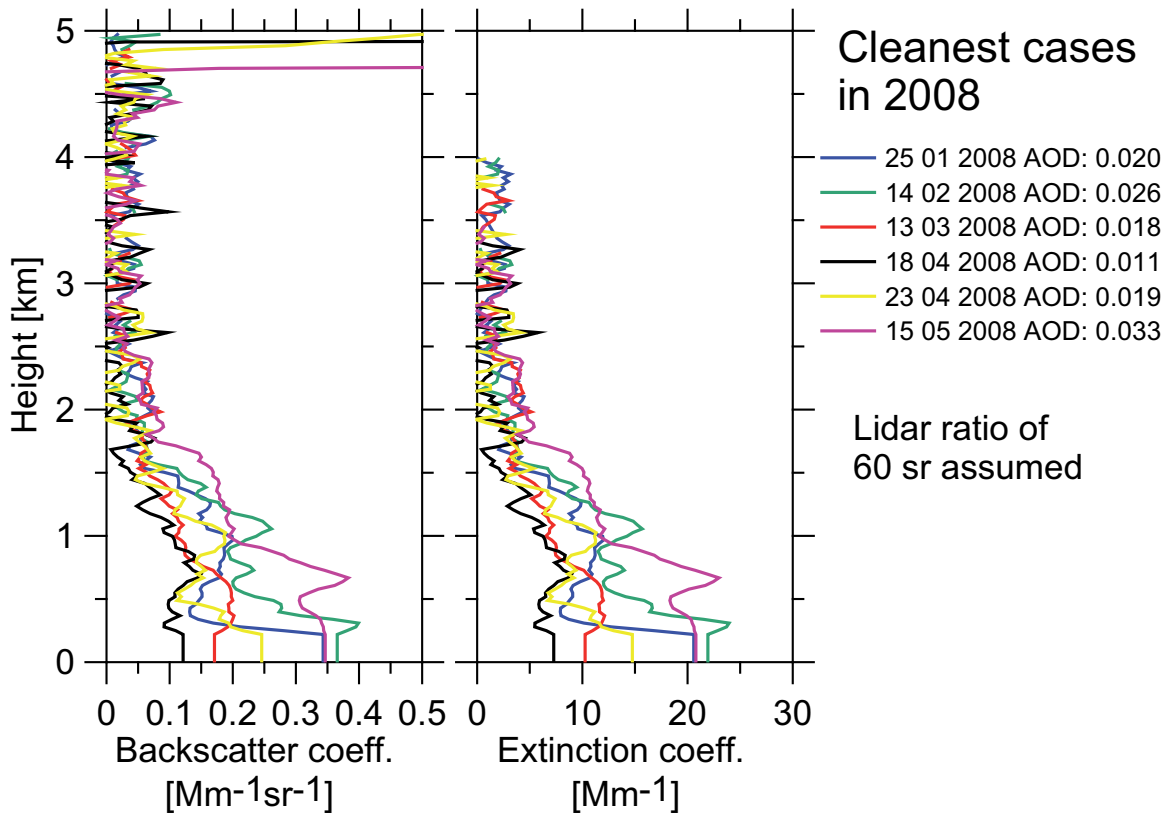


Figure 6.15: Backscatter and extinction coefficient profiles at 532 nm for very clean cases in 2008. Dates and the corresponding AOD at 532 nm are given in the legend.

Fig. 6.15. The AOD ranged from 0.011 to 0.037 and was thus below the marine and continental background values listed in Table 6.1. Backward-trajectory analysis for these cases shows the typical north-easterly to easterly air flow as observed for most observation cases in the wet season (see Sec. 7.1). According to the vertical profiles of particle backscatter coefficient and particle extinction coefficient (lidar ratio = 60 ± 20 sr) for these background cases, aerosol was absent at heights above 2 km. Thus, long-range transport of aerosols obviously did not contribute to the aerosol load on these days. Clouds were present above the AL top in all cases (not always visible in Fig. 6.15), so that rain events and thus wet deposition may have partly caused these clean conditions.

Maximum extinction coefficients for these background conditions reach up to about 25 Mm^{-1} at 532 nm. On average the particle extinction coefficients were close to 10 Mm^{-1} , which is an order of magnitude lower than the mean particle extinction coefficient at Leipzig, Germany.

Finally, one may conclude that background aerosol condition in the central Amazon Basin are characterized by an AOD (532 nm) of 0.03 ± 0.02 . Under these background conditions, the particle extinction coefficient is of the order of $10\text{--}20 \text{ Mm}^{-1}$ and the aerosol is trapped in the lowermost 1.5–2 km in the troposphere. Due to the findings discussed here, background conditions in this work are defined by an AOD (532 nm) below 0.05. This is a factor of two lower than the value suggested by *Holben et al.* (1996b) and much lower than the background AOD of 0.1–0.14 at 440 nm reported from AERONET observations in the northern Amazonian forest (*Schafer et al.*, 2008).

6.3 Dry season: Smoke aerosol observations

The aerosol characteristics in the dry season are dominated by BBA from vegetation fires in Amazonia. This was already documented in publications from many previous campaigns (see Sec. 2.2). However, a detailed vertical analysis of optical and microphysical smoke aerosol properties has not been presented in the literature up to now. Here, three cases of smoke observations are shown and intensively discussed. The first case deals with aged regional smoke layers and a high aerosol load. The second case deals also with smoke transported towards the lidar site, but the aerosol load was lower and optical and microphysical properties were different to the first case. A third case illuminates the hygroscopic growth of the smoke particles.

6.3.1 11 September 2008

The temporal development of the range-corrected signal at 1064 nm measured between 10 September 2008, 2130 UTC and 11 September 2008, 1500 UTC is shown in Fig. 6.16. For intervals drawn in black, no measurements were available. A dense and ca. 4.5 km deep aerosol layer was observed during the whole period as well as diverse cloud layers. Between 0000 UTC and 0030 UTC (2000 lt and 2030 lt), a decreased backscattering intensity was measured - most obviously as a result of fog development. Further fog formation was observed after 0600 UTC. The backscatter intensity between 2 and 3 km increased after 0700 UTC ending in sporadic cloud formation (indicated by the shadow above the cloud). The extent of the aerosol layer did not significantly change during the whole observation period. The AERONET sun photometer measured an AOD (500 nm) of 0.42 on 10 September 2008, 2105 UTC and of 0.61 on 11 September 2008, 1223 UTC. These values are quite high compared to AOD values

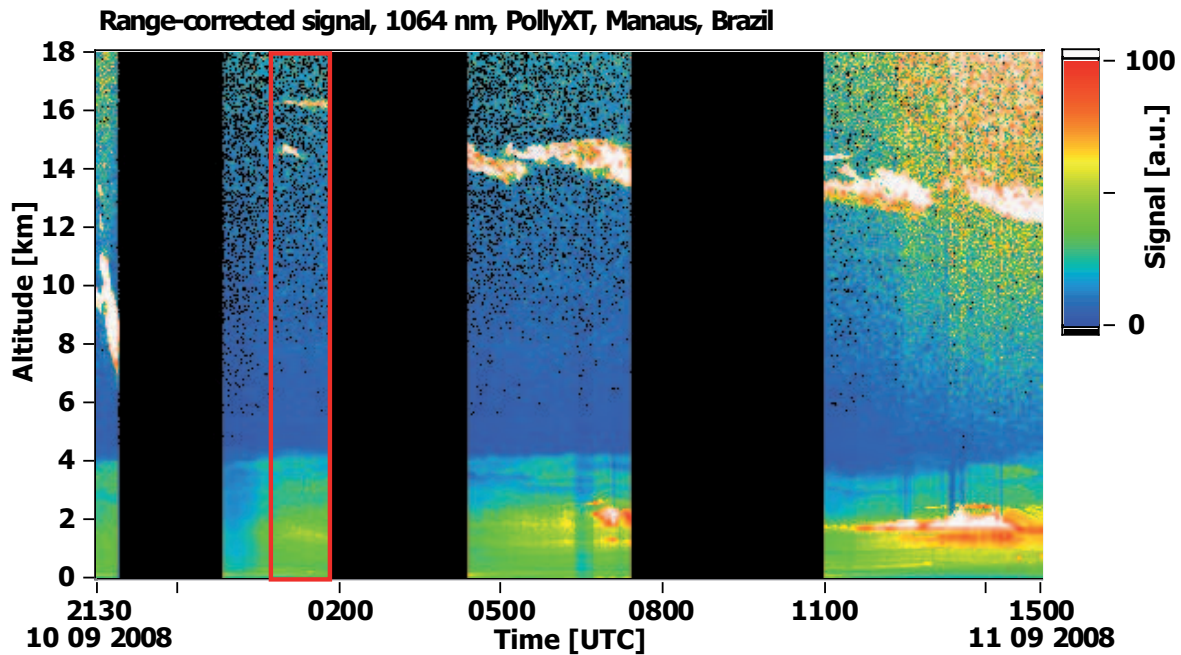


Figure 6.16: Range-corrected signal at 1064 nm between 10 September 2008, 2130 UTC and 11 September 2008, 1500 UTC. The red rectangle indicates the period for the analysis of the optical properties. Local time is UTC–4 hours.

usually measured during the dry season at the lidar location (see Chapter 7).

Fig. 6.17, left, shows the MODIS AOD (550 nm) for 10–11 September. According to these satellite measurements, an aerosol plume was located over central South America south-east of the lidar site. AOD (500 nm) values up to 0.74 were detected within this plume. Around the lidar site, the MODIS AOD was about 0.5. A very pronounced fire activity in the south, south-east, and east of the lidar site obviously caused this aerosol plume over Amazonia as can be seen in Fig. 6.17, right. The fire counts for 7–10 September 2008 as obtained by FIRMS from MODIS measurements and 3-day backward trajectories for the arrival heights of 1500, 3500, and 5000 m from HYSPLIT are shown. The backward trajectories indicate an air-mass flow from easterly directions. The air masses have crossed the fire-active regions in the east 1–2 days before the arrival at the lidar site. Thus, having the uncertainties of the backward trajectories in mind, smoke from these numerous fires had obviously reached the lidar site between 10 and 11 September 2008.

The vertical profiles of the optical and microphysical properties of smoke aerosol are presented in Fig. 6.18 for the observation period between 0100 and 0200 UTC (indicated by a red rectangle in Fig. 6.16). The particle backscatter and extinction

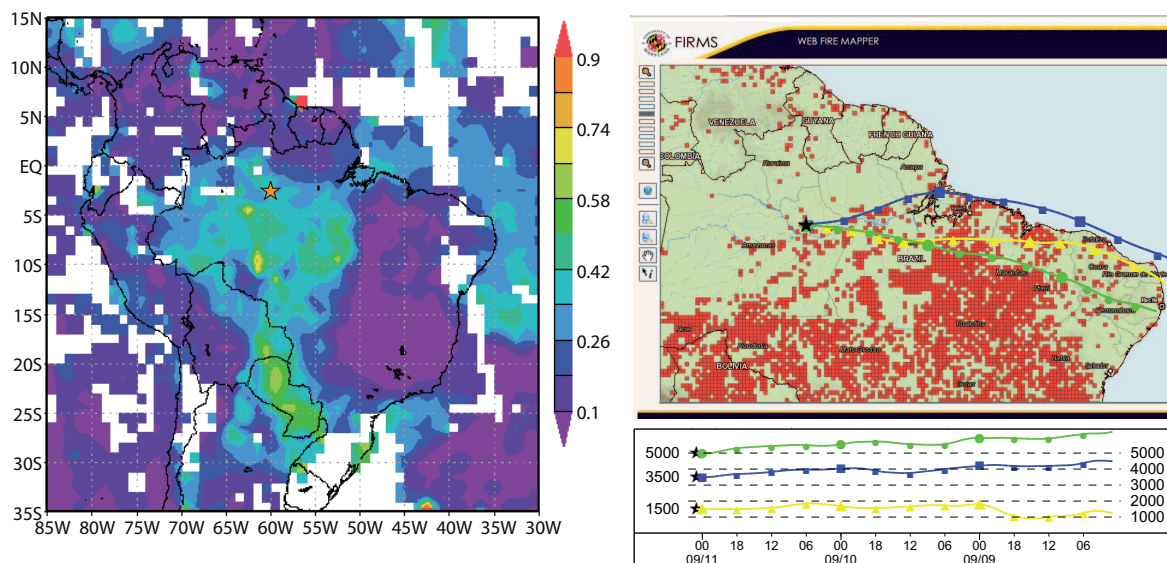


Figure 6.17: Left: MODIS AQUA AOD composite (550 nm) for 10–11 September. The star indicates the lidar location. Right: Fire counts as derived by FIRMS for 7–10 September 2008 and HYSPLIT backward trajectories in 6-h steps for the arrival heights of 1500 (yellow), 3500 (blue), and 5000 m agl (green) for 11 September 2008, 0100 UTC.

coefficients, particle lidar ratios, Ångström exponents, effective radii, and SSA values (532 nm) determined for this one-hour period are shown. The vertical profiles of RH and potential temperature derived from the radiosonde launch at Manaus military airport at 11 September 2008, 0000 UTC are given in addition. A complex vertical structure with multiple aerosol layers is visible. The analysis of the vertical aerosol structure as introduced in Sec. 4.2.5 revealed that the AL top (indicated in Fig. 6.18, upper left panel) is 4.52 km. The AL top coincides with a strong temperature inversion and a decrease of RH to values of about 20% (cf. Fig. 6.18, lower right panel). The $H_{\text{AOD}95}$ is slightly below the AL top at 3.89 km, while H_{aer} is at 2.1 km. This again shows that H_{aer} cannot be used to quantify layer boundaries and is a poor indicator for the vertical distribution of the aerosol. The maximum ML top on 10 September was calculated to be 1.57 km.

The maximum values of the particle backscatter and extinction coefficients at 532 nm of $1.8 \text{ Mm}^{-1}\text{sr}^{-1}$ and 150 Mm^{-1} , respectively, were observed at 1.6 km height and hence at the top of the ML. Because RH is highest (85%) at this height, hygroscopic growth had most obviously led to an increased scattering. Above the ML top, the backscatter and extinction coefficients slightly decreased with height up to 2.8 km as a consequence of the decreasing RH. Above 2.8 km, a third aerosol layer extending up

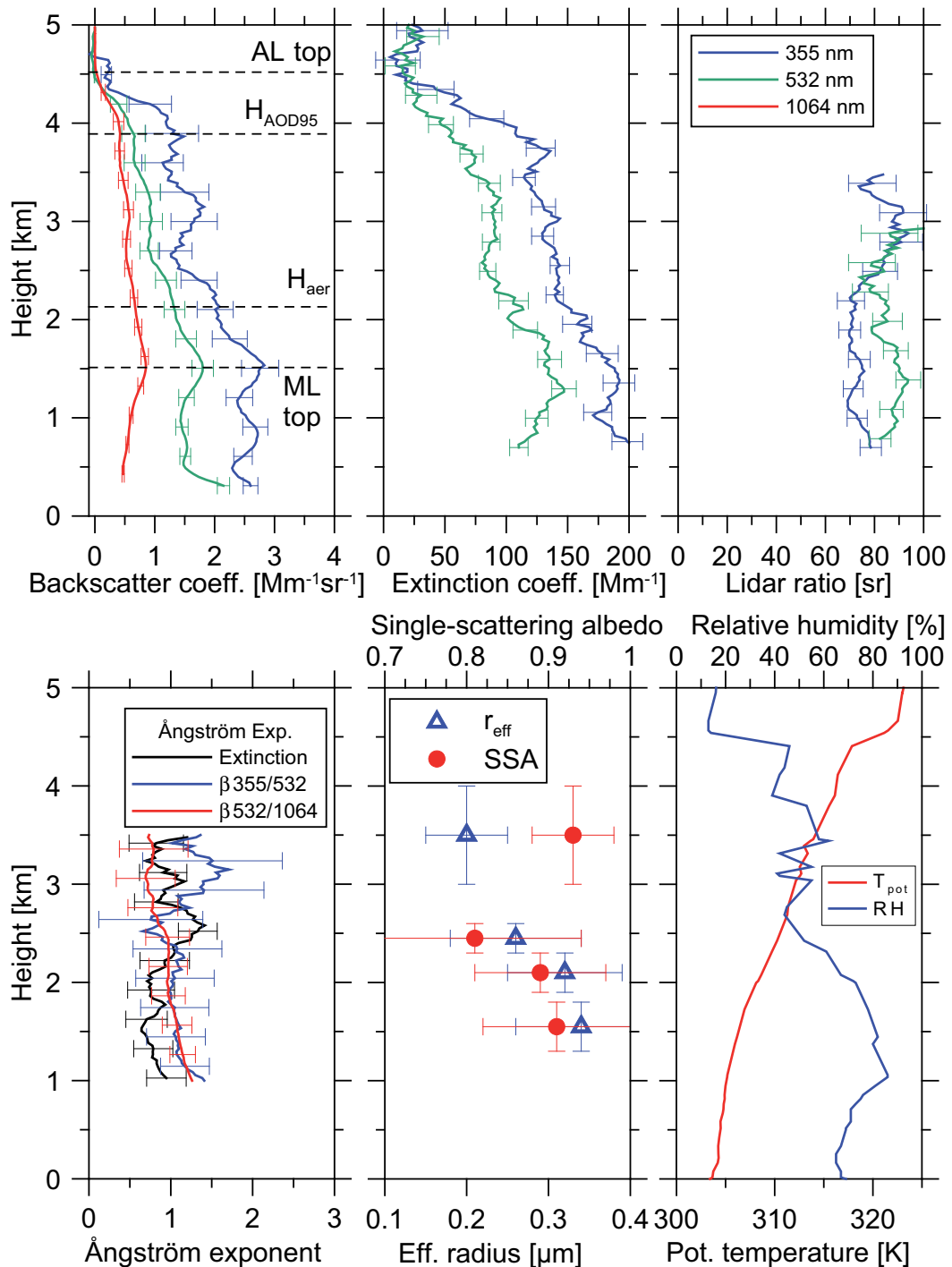


Figure 6.18: Vertical profiles of backscatter coefficient, extinction coefficient, lidar ratio, Ångström exponents, effective radius, and SSA on 11 September 2008, 0100 UTC–0200 UTC. AOD (532 nm) is 0.44. Potential-temperature (T_{pot}) and relative-humidity (RH) profiles from the Manaus radiosonde launch on 11 September 2008, 0000 UTC are shown in addition.

Layer	Height range [km]	r_{eff} [μm]	a [$\mu\text{m}^2/\text{cm}^3$]	SSA	VMD [μm]
1	1.3 – 1.8	0.34 ± 0.08	250 ± 30	0.91 ± 0.09	0.51
2	1.9 – 2.3	0.32 ± 0.07	220 ± 35	0.89 ± 0.08	0.48
3	2.3 – 2.6	0.26 ± 0.08	200 ± 50	0.81 ± 0.13	0.37
4	3.0 – 4.0	0.21 ± 0.05	170 ± 40	0.93 ± 0.05	0.35

Table 6.2: Microphysical properties as derived by inversion for different aerosol layers for 11 September 2008. Effective radius, surface-area concentration a , and SSA were computed. Volume mean diameter (VMD) was derived from effective radius as explained in the text.

to the AL top was present with mean values of about $0.9 \text{ Mm}^{-1}\text{sr}^{-1}$ for the particle backscatter coefficient at 532 nm. Stable and relative dry conditions ($\text{RH}\approx 50\%$) led to almost constant aerosol properties in this layer. Integration of the particle extinction coefficient results in an AOD (532 nm) of 0.44 for the 1-hour period. This is one of the highest values measured by the lidar during the entire campaign.

Relatively high particle lidar ratios were observed (see Fig. 6.18, upper right panel). Values of 70 sr at 355 nm and 80–90 sr at 532 nm in the lowermost 2.5 km and wavelength-independent values of 80–90 sr above 2.5 km were calculated. These values are in the same range as lidar ratio values of aged African smoke observed at the Cape Verde Islands in 2008 (*Tesche et al.*, 2011a). The Ångström exponents were about 1 for both particle backscattering and extinction (see Fig. 6.18, lower left panel). The Ångström exponents are almost constant over height. The particle depolarization ratio (not shown) was very low on that day ($\delta^{\text{par}} < 0.03$). This observation corroborates the assumption that aged BBA does not depolarize the backscattered light. This assumption was used for the smoke-dust separation (Sec. 4.2.7).

The inversion results for four different layers are presented in Fig. 6.18 (lower center panel) and Table 6.2. Effective radii between 0.26 and 0.32 μm were calculated in the humid aerosol plume below 2.8 km. The effective radius was highest in layer 1 which corresponds to the layer with the highest RH. The effective radii are slightly decreasing with height in accordance to the vertical profile of, e.g., the particle backscatter coefficient and the RH.

The SSA was relatively high with values from 0.81 to 0.91 and was decreasing with height in the humid aerosol plume (layer 1–3). For the dry aerosol plume (above

	Period	AOD
Lidar	11 September, 0100–0200 UTC	0.44
CATT-BRAMS (BBA only)	11 September, 0000 UTC	0.12
AERONET	10 September, 2105 UTC	0.42
AERONET	11 September, 1223 UTC	0.61

Table 6.3: AOD from lidar (532 nm), from CATT-BRAMS (500 nm), and from AERONET sun photometer (500 nm) around the lidar observation on 11 September 2008.

2.8 km, layer 4), the inversion shows that the effective radius was smaller than in the humid aerosol plume and the SSA was 0.93. These values, in accordance with the rather high effective radii in the four layers, are a clear indicator for smoke from forest fires that is several days old (*Müller et al.*, 2007a).

Reid et al. (1998) found SSA values, derived from measurements of dried aerosol, of 0.85 for aged smoke in south-east Amazonia. *Dubovik et al.* (2002) reported SSA values from columnar AERONET measurements between 0.9 and 0.94 for Amazon forest-fire smoke and between 0.86 and 0.92 for South American savanna smoke. The lidar-derived SSA values are thus within the range of these findings from previous experiments.

Reid et al. (1998) observed a volume mean diameter (VMD) of 0.35 μm in aged smoke hazes in southern Amazonia. By assuming a log-normal aerosol size distribution, the VMD can be estimated from the inversion results of the lidar observations on 11 September 2008. The resulting lidar VMD was 0.51, 0.48, 0.37, and 0.35 μm for layer 1,2,3, and 4 respectively (cf. Table 6.2). Consequently, a good agreement between the lidar observations and airborne measurements performed by *Reid et al.* (1998) was found for the dry aerosol plume (above 2.8 km, layer 4). Because aerosol was dried for the airborne measurements, one may speculate that hygroscopic-growth effects lead to higher VMD in layers with high RH (layer 1 and 2).

The AERONET sun photometer at the lidar site measured an AOD of 0.42 at 500 nm just before sunset and thus 4 hours before the lidar measurements (see Table 6.3). Hence, virtually no differences in the aerosol conditions could be observed between sunset and the intense analysis period between 0100 and 0200 UTC (lidar AOD of 0.44). In the morning after the lidar measurement (ca. 10 hours after the observation), the AERONET AOD increased to 0.62 (see Table 6.3). Consequently, the aerosol load had increased during the night of 10–11 September 2008 as already discussed in

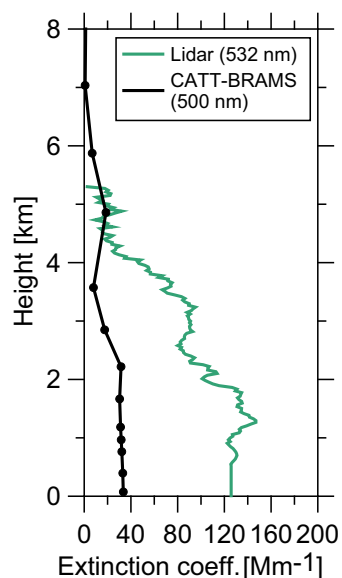


Figure 6.19: Comparison of the vertical profiles of extinction coefficient between lidar (green, at 532 nm) and CATT-BRAMS (black, at 500 nm). The CATT-BRAMS profile was computed from the model AOD and the vertical profile of model PM2.5 for BBA.

the analysis of the temporal evolution of the range-corrected signal (Fig. 6.16). The AERONET Ångström exponent was 1.46 on 11 September 2008, 2105 UTC and 1.08 on 11 September 2008, 1225 UTC and thus slightly higher than the values derived from the lidar observations.

A comparison of the lidar results to the respective simulation with the operational BBA forecast model CATT-BRAMS⁵ (Freitas *et al.*, 2009; Longo *et al.*, 2010) is shown in Fig. 6.19. The vertical profile of the lidar extinction coefficient and the derived model BBA extinction profile is shown. The output of CATT-BRAMS is the AOD at 500 nm and a vertical PM2.5⁶ profile every 3 hours. The extinction profile from the model was calculated by scaling the PM2.5 profile to the AOD. Since CATT-BRAMS computes BBA from burning events, the AOD and PM2.5 values are valid for BBA only. According to Fig. 6.19, the model clearly underestimated the smoke amount in the whole aerosol layer (below 4.3 km) at the lidar site.

This underestimation by the model can be also seen from the values listed in Table 6.3. The sun photometer AOD and the lidar AOD are almost equal with 0.42–0.44 and are

⁵Coupled Aerosol and Tracer Transport model to the Brazilian developments on the Regional Atmospheric Modeling System, data kindly provided by Karla Longo, CPTEC, INPE, E-mail: karla.longo@inpe.br.

⁶Mass concentration for particles with a diameter of 2.5 μm or less.

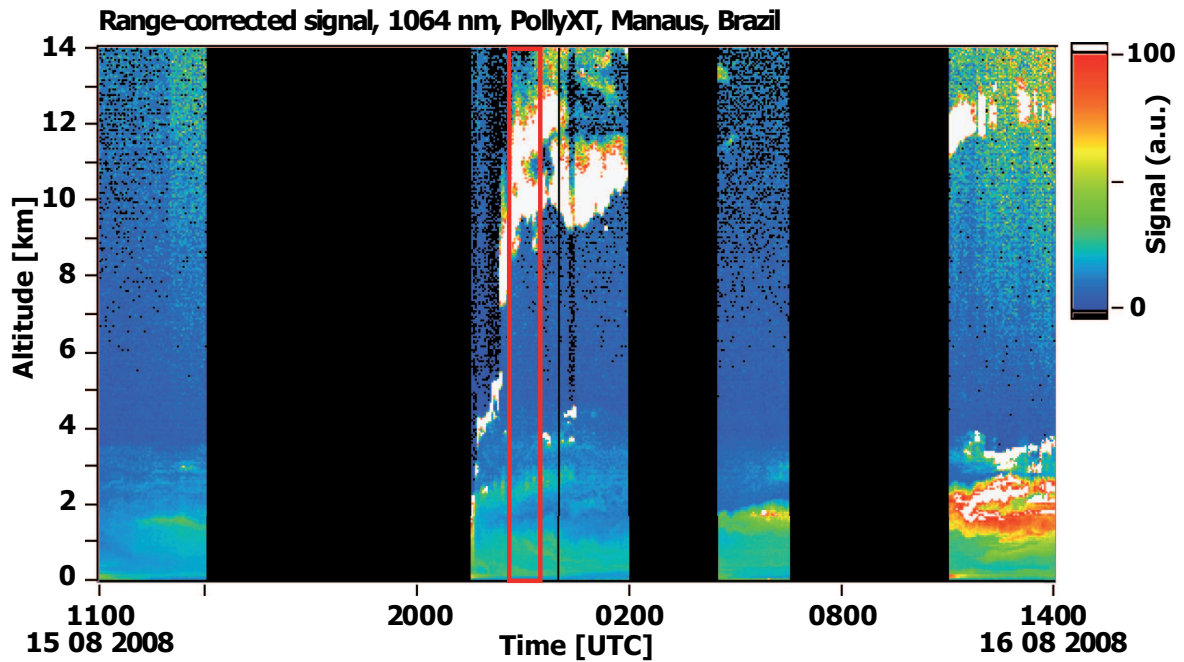


Figure 6.20: Temporal development of the range-corrected signal at 1064 nm between 15 August 2008, 1100 UTC and 16 August 2008, 1400 UTC. The red rectangle indicates the time period for the analysis of the optical aerosol properties. Black areas are measurement interruptions. Local time is UTC–4 hours.

consistent with the MODIS AOD observations (Fig. 6.17, left). In contrast, the model reproduces an AOD of 0.12 for BBA only. Because the background AOD at the lidar site is about 0.03 ± 0.02 (see Sec. 6.2), more than 0.38 of the lidar AOD can be attributed to smoke. Hence, the model underestimates the smoke AOD by more than 0.2. The reason for the underestimation remains unclear, but is most probably related to wrong assumptions concerning fire activity and smoke emissions.

6.3.2 15 August 2008

The temporal development of the range-corrected signal at 1064 nm from 15 August 2008, 1100 UTC to 16 August 2008, 1400 UTC is shown in Fig 6.20. For intervals drawn in black, no measurements were available. A highly variable, complex aerosol layering was observed during that period. No clouds and relatively low aerosol backscattering were observed between 1100 and 1400 UTC on 15 August 2008. After the restart of the measurements at 2000 UTC, rain events prohibited lidar observations for about one hour. Between 2100 and 0100 UTC, a two-layer aerosol

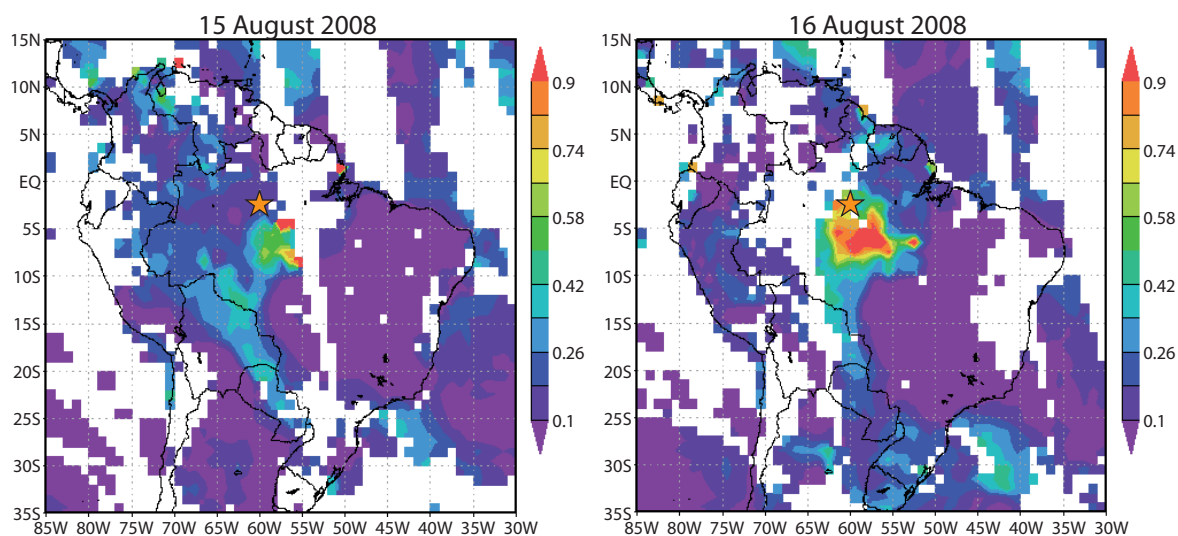


Figure 6.21: MODIS AQUA AOD composite (550 nm) for 15 August 2008 (1805 UTC) and 16 August 2008 (1710 UTC). The star indicates the lidar location.

structure was observed together with clouds at various height levels. Aerosol conditions changed after 0430 UTC, when a new, dense aerosol plume (centered at around 2 km) arrived at the lidar location. The backscatter intensity in this layer continuously increased until 1400 UTC. Cloud development between 3 and 4 km was observed from 1130 UTC. Several cirrus layers were frequently present during the whole observation period.

The MODIS AOD (550 nm) for 15 and 16 August 2008 is shown in Fig. 6.21. A high AOD (AOD >0.9) was observed in 600 km distance south-east of the lidar site on 15 August 2008, 1805 UTC. At the lidar site, an AOD of less than 0.2 was obtained at the same time. Unfortunately, no MODIS data are available for regions east of the lidar site. However, the MODIS AOD on 16 August 2008 shows that the aerosol plume detected on 15 August in the southeast of Manaus was obviously moving towards northwest and crossed the lidar site. An AOD of 0.5 around the lidar site was reported by MODIS at 1705 UTC on 16 August 2008. The increasing backscatter intensity as observed with the lidar (see Fig. 6.20, 1100–1400 UTC) was obviously caused by this aerosol plume.

In Fig. 6.22, active fires detected by NOAA-15 (polar orbiting satellite) and GOES (Geostationary Operations Environmental Satellite) are shown in addition to the MODIS fires spots (MODIS did not pass the area southeast of the lidar). Several fires were detected by GOES 600 km away from the lidar site close to the location of the

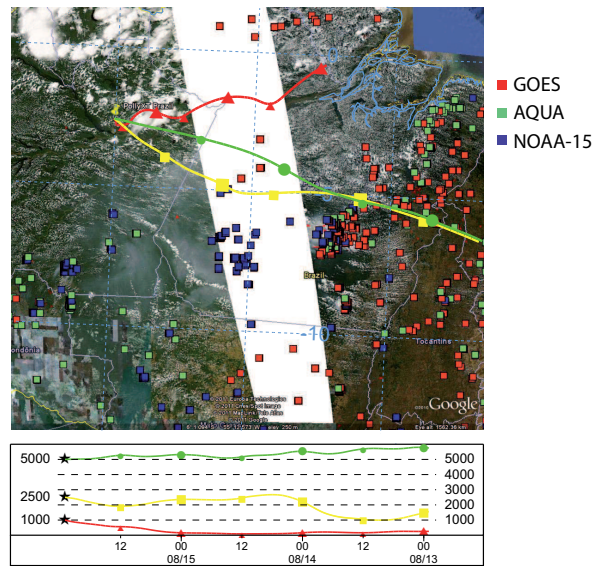


Figure 6.22: Fire spots as detected by various satellites (see legend) on 15 August 2008. Data were provided by CPTEC (Brazilian Center for Weather Forecasting and Climate Studies, <http://sigma.cptec.inpe.br/queimadas/>). HYSPLIT backward trajectories ending on 15 August 2008, 2300 UTC at 1000 (red), 2500 (yellow), and 5000 m (green) are overlaid. MODIS AQUA visible image from 15 August 2008 is underlaid.

maximum MODIS AOD. According to the MODIS visible images and the HYSPLIT backward trajectories (Fig. 6.22), the produced smoke was obviously transported towards the lidar site. According to the HYSPLIT backward trajectories, the travel time to the lidar site was approximately 24 hours.

Figure 6.23 shows the vertical profiles of particle backscatter and extinction coefficient, lidar ratio, and Ångström exponents at different wavelengths and the corresponding microphysical aerosol properties for the observation period from 2235–2335 UTC on 15 August 2008. The vertical profiles of temperature and RH from the radiosonde launch on 16 August 2008, 0000 UTC at Manaus military airport are shown in addition. The analyzed period from 2235–2335 UTC corresponds to the pronounced two-layer aerosol structure observed directly after the rain events at the lidar site (compare Fig. 6.20) and can be regarded as the arrival time of first smoke from the fires in the southeast.

During this observation, the lowermost aerosol layer extended up to ca. 1.6 km and coincides perfectly with the modeled daytime ML top (for methodology see Sec 4.2.5). A lofted aerosol layer centered at ca. 2.5 km was present during the whole analyzed

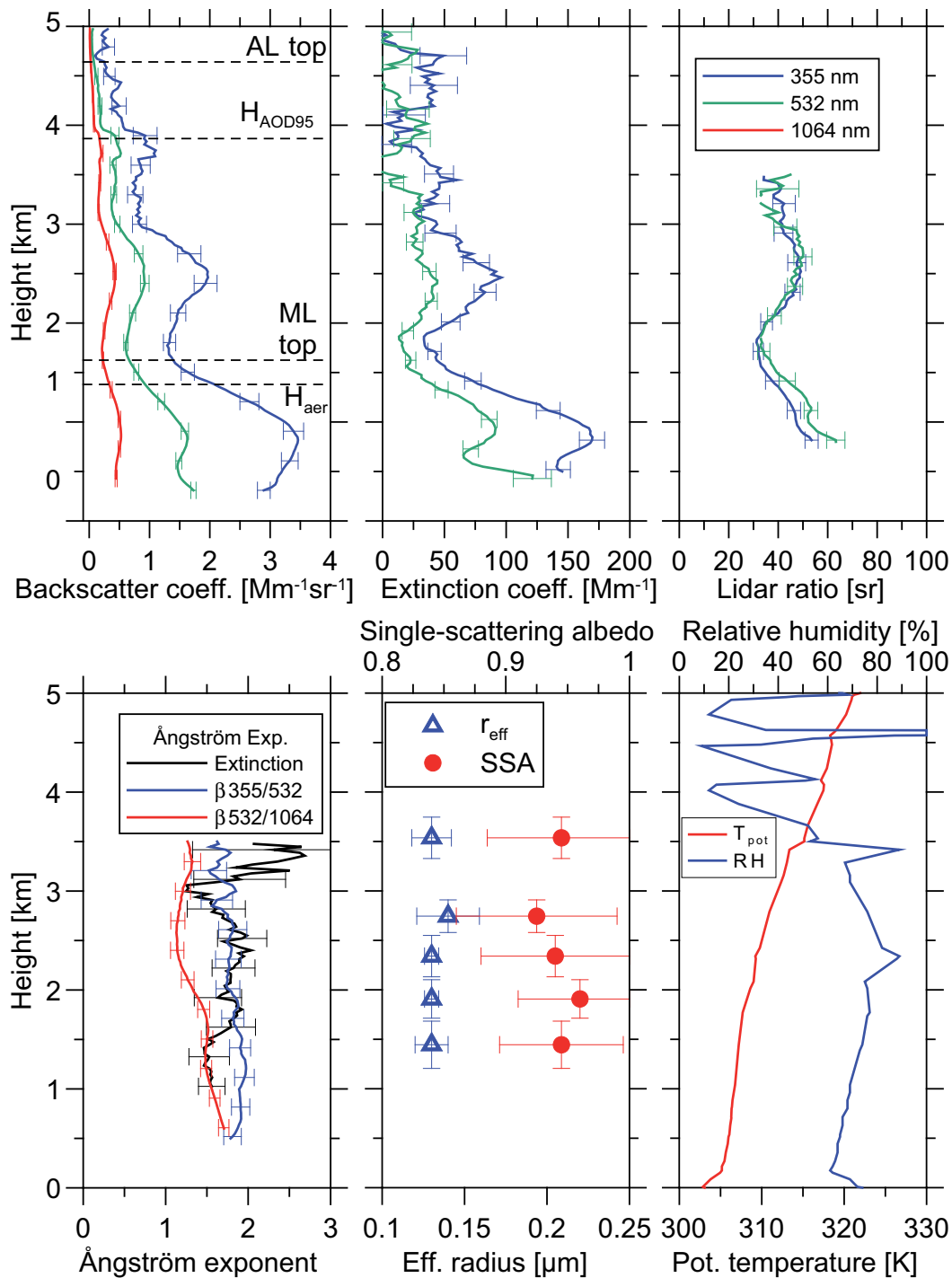


Figure 6.23: Vertical profiles of the particle backscatter coefficient, particle extinction coefficient, particle lidar ratio, Ångström exponents, effective radius, and SSA measured on 15 August 2008, 2235–2335 UTC. AOD (532 nm) = 0.15. Temperature (T) and relative humidity (RH) profiles from the radiosonde launch in Manaus on 16 August 2008, 0000 UTC are shown in addition.

period. Aerosol was observed up to 4.64 km (AL top). Integration of the extinction profile yields an AOD of about 0.3 and 0.15 for 355 and 532 nm, respectively, and was thus well above the background level. H_{aer} was 1.38 km and hence even lower than the ML top. H_{AOD95} was 3.9 km. Different clouds were observed above 9 km during the whole measurement (not shown in Fig. 6.23). The vertical profiles of backscatter and extinction coefficient show a strong spectral behavior. The respective Ångström exponents are high with values between 1.5 and 2 in the short-wavelength range. Particle extinction coefficients of 170 and 80 Mm^{-1} for 355 and 532 nm, respectively, were retrieved in the aerosol layer centered at around 1 km. Values up to 100 and 45 Mm^{-1} , respectively, were observed in the center of the lofted aerosol layer at 2.5 km, where the RH had its maximum with values close to 90%. Hygroscopic-growth effects may thus have been responsible for the increased scattering at 2.5 km agl. The lower limit of the lofted aerosol layer (2.1 km) coincided with a minor temperature inversion and a steep gradient in RH. A strong temperature inversion is visible at 3.4 km in the radiosonde temperature profile taken 60 km away from the lidar site. The height of the inversion was slightly higher than the top of the pronounced lofted aerosol layer. The vertical profiles of the lidar ratio for the two wavelengths indicate a weak wavelength dependence at lower heights and independence above 2 km height. Typical values of the particle lidar ratio for this case varied between 45 and 55 sr. In agreement with the high extinction-related Ångström exponents, rather low particle radii (0.13–0.14 μm) for both aerosol layers were obtained from the inversion calculations. The computed SSA is 0.945 ± 0.05 in the lowermost aerosol layer and between 0.92 and 0.94 in the center of the lofted aerosol layer. The particles were obviously only weakly absorbing.

The optical and microphysical properties of the smoke aerosol on 15 August were considerably different to the ones on 11 September 2008. Particles were much smaller and less absorbing on 15 August than on 11 September. The reason for those differences could be the shorter travel time to the lidar site (<24 h) or different aging processes (e.g., cloud/rain processing). But also different burning conditions (different location, different vegetation etc.) may have led to different smoke with different optical and microphysical properties.

6.3.3 28 October 2008

As already noticed in the foregoing case studies, smoke particles seem to be hygroscopic as indicated by the correlation of RH with the particle backscatter coefficient

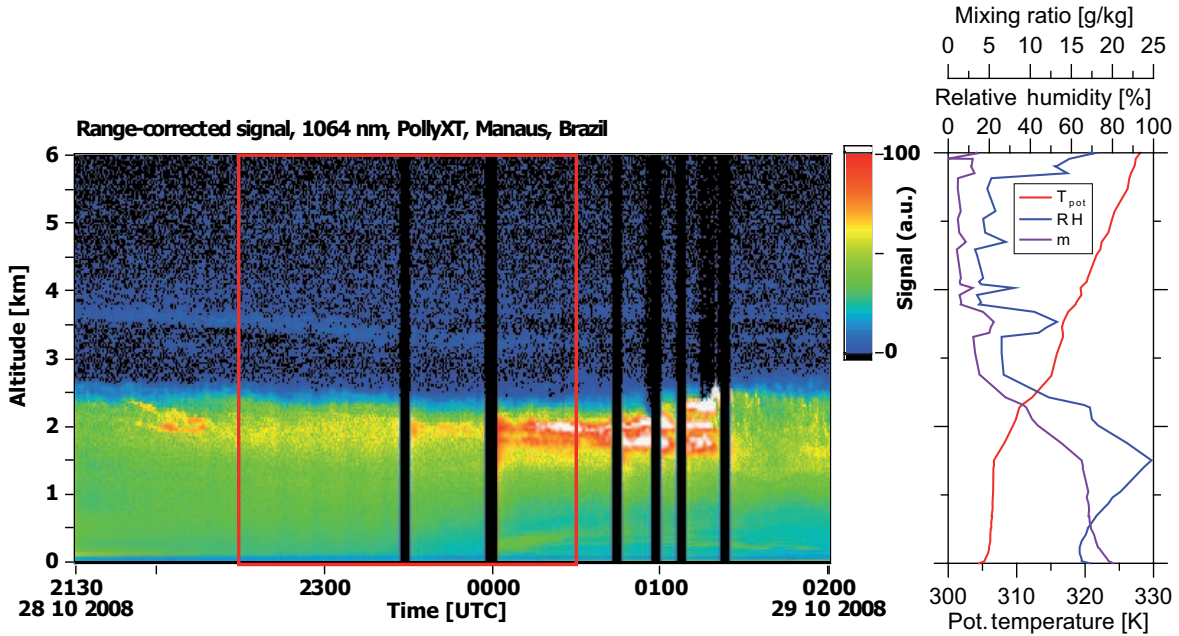


Figure 6.24: Temporal development of the range-corrected signal at 1064 nm on 28 October 2008. The red rectangle indicates the period for the detailed analysis. Potential temperature, RH, and mixing ratio m profiles from the radiosonde launch at Manaus military airport on 29 October 2008, 0000 UTC are shown in addition.

and the particle extinction coefficient. This aspect is illuminated in more detail in this Section, based on the lidar observation performed between 28 October 2008, 2230 UTC and 29 October 2008, 0200 UTC. The analysis of backward trajectories, MODIS fire counts, and MODIS AOD shows that again BBA was advected from the south-east towards the lidar site. As indicated by an AOD of 0.38, which is well above the background level, this BBA dominated the aerosol optical properties during the lidar measurement.

Figure 6.24 shows the temporal development of the range-corrected signal at 1064 nm for this time period. A pronounced aerosol layer up to about 2.7 km was present. Near the top of the aerosol layer, the backscatter intensity was partly strongly enhanced. Some cumulus clouds developed near the top of the AL between 0050 and 0120 UTC. Figure 6.24, right, shows the corresponding profile of the potential temperature, RH, and the water-vapor mixing ratio derived from the radiosonde launch at Manaus military airport on 29 October 2008, 0000 UTC. The RH was increasing with height up to 1.6 km. The maximum RH measured with the radiosonde was 98.3% and thus close to saturation. The water-vapor mixing ratio indicates a well-mixed boundary layer up

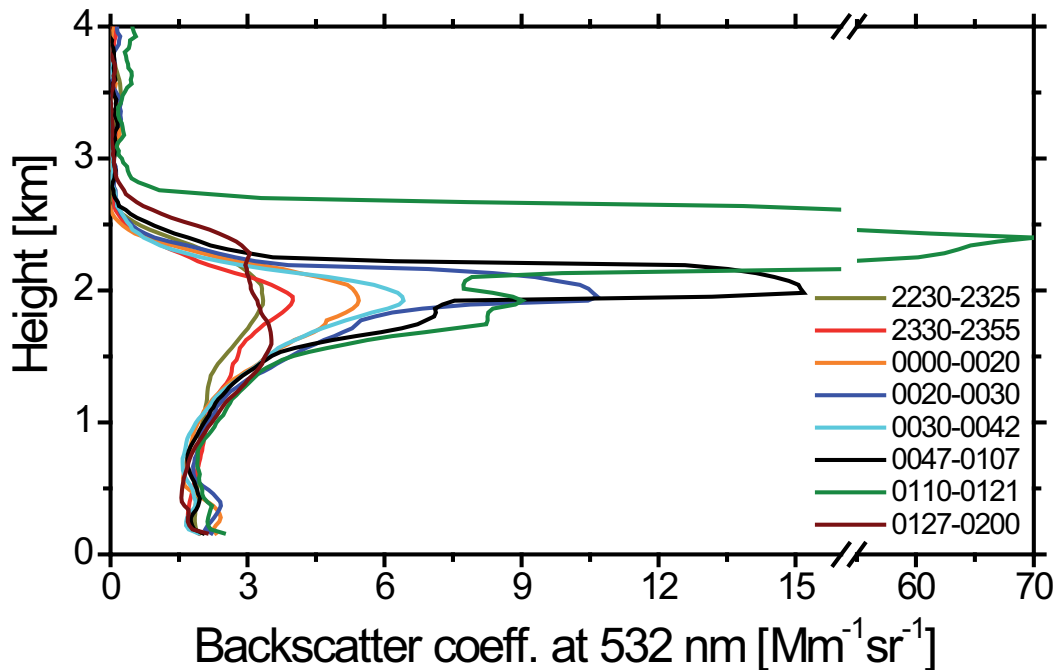


Figure 6.25: Temporal evolution of the particle backscatter coefficient at 532 nm on 28–29 October 2008 for several periods. A vertical smoothing of 90 m was applied. Times (UTC) are given in the legend.

to the height of the maximum RH.

The particle backscattering is obviously strongly correlated to the RH as the profiles in Fig. 6.25 indicate. Several consecutive short-term particle backscatter coefficient profiles are shown. Backscatter values at 750 m were almost constant (around $2 \text{ Mm}^{-1}\text{sr}^{-1}$) during the entire measurement period and seems to represent dry aerosol conditions (RH below 65%). Above 750 m height, the backscattering changed significantly for the different analyzed periods. The particle backscatter coefficient at ca. 1.9 km increased continuously from values of $3 \text{ Mm}^{-1}\text{sr}^{-1}$ to values of $15 \text{ Mm}^{-1}\text{sr}^{-1}$ between 2230 and 0107 UTC as a result of hygroscopic growth. Backscatter values of $15 \text{ Mm}^{-1}\text{sr}^{-1}$ (corresponding to particle extinction coefficients $<1000 \text{ Mm}^{-1}$) are still indicating aerosol scattering processes, but are a factor of 7.5 higher than under dry conditions. As a consequence of the steady hygroscopic growth, finally activation of cloud condensation nuclei occurred and clouds developed in the aerosol layer after 0107 UTC leading to a maximum backscatter coefficient of $70 \text{ Mm}^{-1}\text{sr}^{-1}$. The cloud base, however, was slightly higher than the location of the maximum aerosol backscattering before. After the cloud formation period (0127–0200 UTC), the parti-

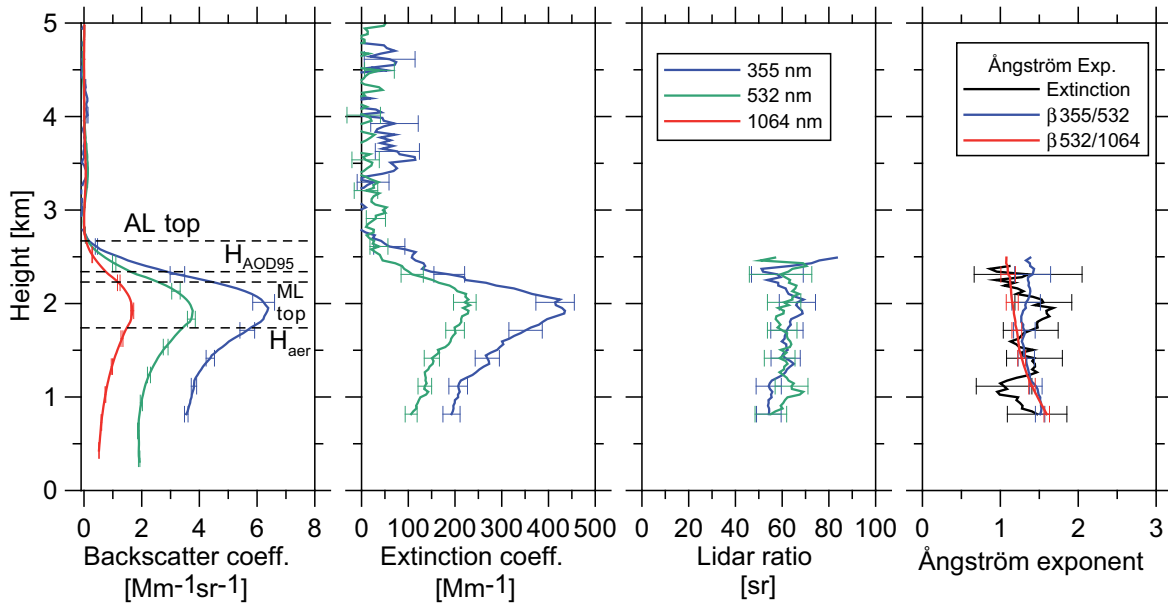


Figure 6.26: Vertical profiles of particle backscatter and extinction coefficient, lidar ratio, and Ångström exponent for 28 – 29 October 2008 between 2230 UTC and 0030 UTC.

cle backscatter coefficient suddenly dropped to values of about $3 \text{ Mm}^{-1}\text{sr}^{-1}$ as observed in the beginning of the measurement. The vertical profile then showed two maxima, one at 1.6 km and a second one at the former cloud peak at 2.4 km.

To study the humidification effect in more detail, the vertical profiles of particle backscatter coefficient, particle extinction coefficient, particle lidar ratio, and Ångström exponent for the period between 2230 and 0030 UTC (indicated by red lines in Fig. 6.24, 2-h period needed to determine the extinction coefficient from the weak Raman signals) are presented in Fig. 6.26. The profiles of the particle backscatter and extinction coefficients show a clear increase with height up to about 2 km for all wavelengths. Above this peak, a strong decrease of the backscatter and extinction coefficients was observed. The vertical structure analysis revealed an AL top of 2.7 km, an $H_{\text{AOD}95}$ of 2.37 km, and an H_{aer} of 1.7 km. The ML top was simulated to be 2.23 km. In contrast to the vertical gradient in the particle backscatter and extinction coefficients, the particle lidar ratios and the extinction-related Ångström exponent do not show any significant height dependence. Backscatter-related Ångström exponents were slightly decreasing with height. Depolarization is negligible on that day for the observed particles. The height-independent lidar ratios for both wavelengths indicate that both the particle backscatter and extinction coefficient increase by almost the same factor with increasing RH. The week dependence of the Ångström exponent on

RH is in agreement with measurements of ambient aerosol extinction of urban aerosol in Leipzig (*Skupin, 2011*). RH-independent Ångström exponents of urban aerosol were observed under conditions of high RH.

An attempt to analyze the hygroscopic growth behavior of the optical aerosol properties in more detail is presented in the following. A correlation between the vertical aerosol profiles and RH was performed to determine the humidification factor (*Kotchenruther and Hobbs, 1998*):

$$f(\text{RH}) = \frac{\xi^{meas}}{\xi^{dry}} = 1 + a \left(\frac{\text{RH}}{100\%} \right)^b. \quad (6.1)$$

The humidification factor $f(\text{RH})$ is the ratio of the measured optical quantity ξ^{meas} (particle backscatter coefficient or particle extinction coefficient) to the optical quantity under dry conditions ξ^{dry} . $f(\text{RH})$ can then be expressed by a simple model with the parameter a and b .

Fig. 6.27 shows the 532-nm particle backscatter and extinction coefficients as well as the corresponding RH profile in the lowermost 3 km – for which the correlation was performed. It is obvious that the height of the maximum RH in the radiosonde profile (at 1.6 km) is below the height of the maximum backscatter (and extinction) coefficient in the lidar observation (at 1.9 km). The radiosonde is launched 60 km away, in the south of Manaus close to the Amazon river. The 2-million inhabitant city Manaus (heat island effect, e.g., *Oke, 1973*) and also the Amazon river (sea-land-circulation observed, *Garstang et al., 1990*) may have a significant influence on the local meteorology. Thus, different meteorological conditions must be kept in mind when comparing lidar and radiosonde profiles. Nevertheless, an attempt to investigate the hygroscopic growth of the particles at the lidar site was made by shifting the RH profile of the radiosonde in such a way that the maximum (RH = 98.3%) coincides with the maxima in the lidar-derived optical data. Now, a strong correlation between RH and the particle backscatter and extinction coefficients is found (Fig. 6.27, right). Even if this procedure is critical, it is the best estimate for the investigation of hygroscopic growth of Amazonian aerosol by the lidar observations. No other humidity profiles than the radiosonde data from Manaus military airport were available.

The humidification factors for the particle backscatter and extinction coefficient are 2.21 and 2.15, respectively, after Eq. 6.1 for RH <65% (dry conditions) to RH = 98%. However, the extinction-related humidification factor of $f(98\%) = 2.15$ is a factor of 2 lower than the respective value observed for urban aerosol in Leipzig (*Skupin et al., 2010*). *Kotchenruther and Hobbs (1998)* measured a humidification factor between

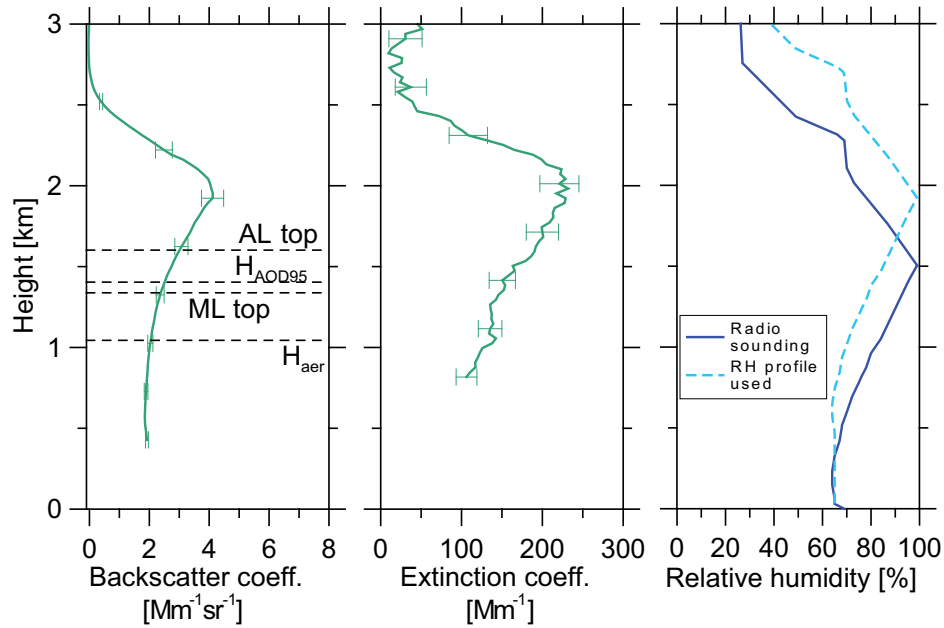


Figure 6.27: Vertical profiles of particle backscatter coefficient and particle extinction coefficient (532 nm). A vertical smoothing of 90 m was applied. The RH profile as derived from the radiosonde launch at 0000 UTC on 29 October 2008 and the used RH profile for the correlation is shown.

$RH = 65\%$ and $RH = 85\%$ of $f(85\%) = 1.24$ for BBA in Brazil, which is in fair agreement with the lidar observation that yields a humidification factor of $f(85\%) = 1.51$ in the respective RH range.

The corresponding fitting curves for the lidar data as derived from Eq. 6.1 are presented in Fig. 6.28. The derived parameter a is 1.31 and 1.47, and b is 5.05 and 6.71 for the particle extinction coefficient and the particle backscatter coefficient, respectively. The hygroscopic growth of the particles observed by lidar was thus stronger than the hygroscopic growth of BBA observed in the Brazilian cerrado for $30\% < RH < 90\%$ as reported by *Kotchenruther and Hobbs* (1998; two examples plotted in Fig. 6.28). The authors obtained $0.14 < a < 0.7$ and $3.2 < b < 6.1$. The fitting curve for the hygroscopic growth of urban aerosol observed in Leipzig, Germany (*Skupin*, 2011), is shown in addition in Fig. 6.28. The hygroscopic growth of urban aerosol is obviously more pronounced than the hygroscopic growth of Amazonian BBA. The growth behavior of the urban aerosol was modeled with $a = 3.67$ and $b = 7.04$.

An attempt to study the hygroscopic growth behavior of BBA by lidar was presented. However, the comparison to other published hygroscopic-growth measurements is difficult, since these measurements were performed at a different RH range and with

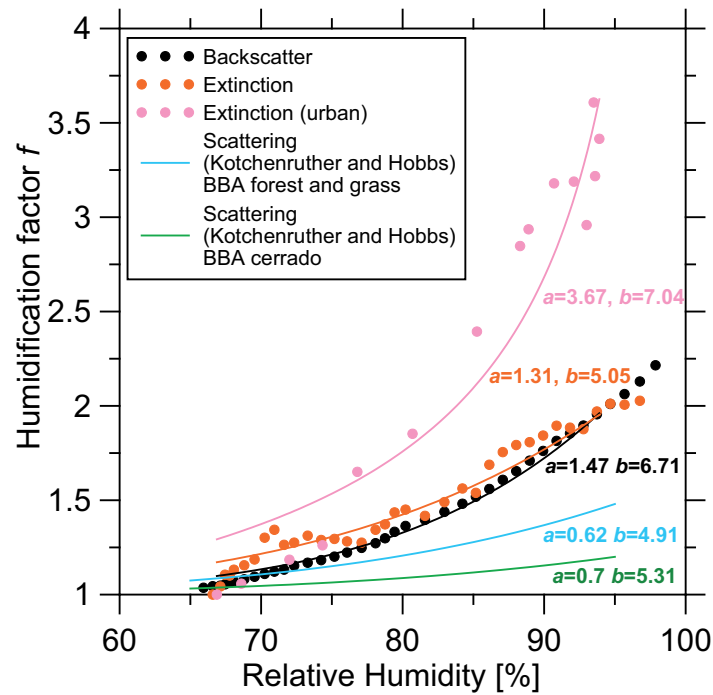


Figure 6.28: Correlation between RH and lidar optical properties at 532 nm on 28 October 2008. Hygroscopic-growth examples of BBA from scattering measurements in Brazil during SCAR-B (Kotchenruther and Hobbs, 1998) and of urban aerosol from extinction measurements in Leipzig (Skupin, 2011) are shown for comparison. The fitting curve and the respective parameter (see Eq. 6.1) are plotted in addition.

different instrumentation. Furthermore, the humidity profile used for the lidar study was not taken at the location of the measurements and thus is not ideal for the investigation of hygroscopic growth. However, it was shown that hygroscopic growth of BBA is not negligible. But due to the critical assumptions, which had to be made, a quantification of these effects is very uncertain and thus should be seen as a rough estimation.

Polly^{XT} was modified in 2011. It is now possible to measure the water-vapor mixing ratio with the Raman technique. This means that vertical profiles of aerosol and water vapor can be obtained simultaneously. It will be therefore possible to study the hygroscopic growth behavior of aerosol with much higher accuracy in future lidar campaigns.

Chapter 7

Observations – Part II: Seasonal aerosol characteristics

In Chapter 6, lidar measurements of the different aerosol conditions prevailing in Amazonia were presented in the form of case studies. However, the whole variability of vertical aerosol profiles cannot be covered with the analysis of these case studies. In this Chapter, statistical results from the measurement campaign in Amazonia in 2008 are presented and discussed with focus on the differences between the wet and dry season. First, the general wind patterns prevailing in 2008 are analyzed using HYSPLIT backward trajectories. Afterwards, an overview of the measured vertical aerosol profiles is given, and finally the statistical analysis of the lidar-retrieved aerosol properties is intensively discussed.

7.1 Meteorological conditions

The meteorological conditions at the tropical observation site in Brazil were rather similar within the wet season and within the dry season. No significant day-to-day variability was observed in both seasons. The wind-direction patterns in both seasons were analyzed by using HYSPLIT backward trajectories. A cluster analysis¹ (Fig. 7.1) based on backward trajectories arriving at 1500 m at 0000 and 1200 UTC was performed. This analysis revealed that air masses were transported from easterly directions to the field site during both seasons. Four clusters for each season were identified, but virtually no difference in the airflow occurred during 2008. These find-

¹The backward-trajectory cluster analysis was performed with the offline-version of HYSPLIT (version 4.9), which can be downloaded at <http://ready.arl.noaa.gov/HYSPLIT.php>.

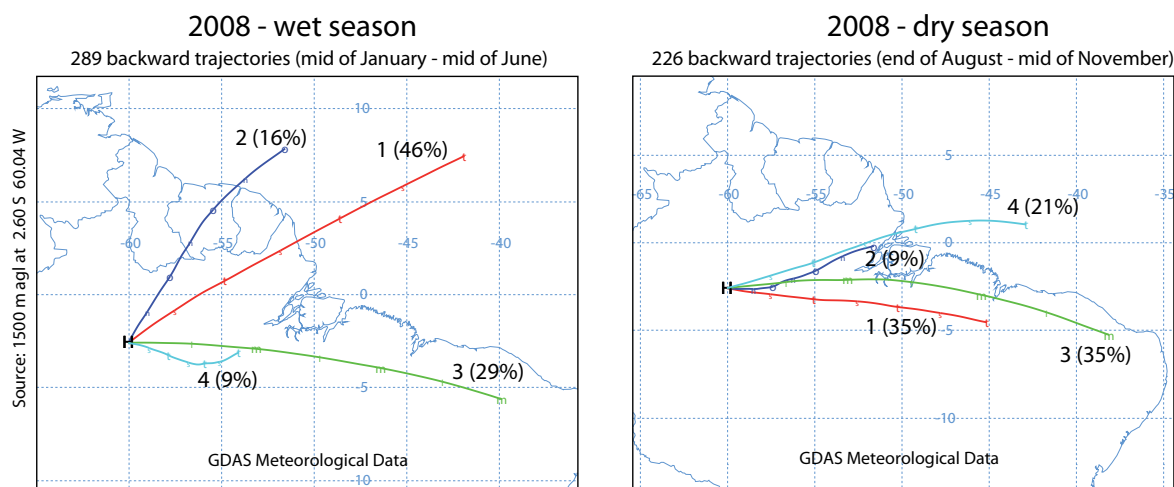


Figure 7.1: Cluster analysis for the wet and dry season based on daily 172-h backward trajectories at an arrival height of 1500 m agl. Four clusters for each season were identified. The frequency of occurrence of each of the clusters (1–4) is given in brackets.

ings reveal the dominance of the trade-wind circulation for the location as described in Chapter 2. The weighting of the trajectory clusters is slightly different between the two seasons. In the wet season, mostly a north-easterly flow prevails (in 62% of all cases, compare cluster 1 and 2 in Fig. 7.1, left), whereas the air masses came mainly from easterly direction in the dry season (all clusters in Fig. 7.1, right). However, with respect to the uncertainty of a single backward trajectory (see, e.g., Fig. 6.11) and the small difference between the clusters, one must conclude that the cluster analysis cannot be applied for correlating lidar-derived aerosol properties to the air mass origin.

The backward-trajectory analysis also indicates that the Manaus pollution plume did not affect the lidar observations in 2008 as already discussed in Sec. 3.1. Manaus is 60 km south of the EUCAARI site and thus generally not in the upwind region of the lidar observations. These findings corroborate the results presented by *Kuhn et al.* (2010). The authors showed that the Manaus pollution plume is usually transported from Manaus to south-westerly directions due to the strong trade winds. During this transport, the dispersion of the pollution plume was found to be low, so that only regions directly downwind of Manaus were affected. These trajectory-based findings are proven by ground-based wind-direction measurements at the EUCAARI site during 2008 (*Rizzo, 2010*). Winds from south-east at surface level were reported only a few times (<20 days). Consequently, our measurements can be regarded as

representative on a regional scale for central northern Amazonia. No other major point sources of urban/industrial aerosol are present in this region.

7.2 Overview of optical and geometrical properties

In this Section, the temporal development of the AOD and of the vertical aerosol structure is discussed. Furthermore, an overview of all derived vertical aerosol profiles during 2008 is given.

7.2.1 Time series

The temporal evolution of the AOD at 532 nm as measured with Polly^{XT} in 2008 is shown in Fig. 7.2, top. A clear contrast between the two seasons was found. During the wet season, AOD values were typically much lower than during the dry season. Frequently, clean background conditions with an AOD below 0.05 were observed during the wet season (see Sec. 6.2). AOD values above the background level (>0.05) caused by the intrusion of African aerosol (see Sec. 6.1) accumulate in February and March. The cleanest air conditions tend to occur from April to May. A strong dust intrusion event mid of May caused the only episode of increased AOD during that period. AOD values did not exceed 0.25 during that season. The mean wet-season AOD was found to be 0.08 and was thus three times smaller than the mean dry-season AOD of 0.26.

In the dry season, a high AOD variability was observed. AOD values ranged from 0.05 (10 August 2008) to 0.55 (11 September 2008). Interestingly, the day-to-day variability during this season was almost as high as the seasonal variability in 2008. Highest AOD values were observed in September and October, when the fire activity east and thus upwind of the lidar site was highest (see Sec. 2.2). Several lidar observations indicated that the removal of aerosol by short convective precipitation effects is ineffective. Virtually, no difference in terms of AOD could be observed before and after a shower event.

Figure 7.2, bottom, shows the temporal development of the AL top, H_{aer} , and H_{AOD95} in 2008. As defined in Sec. 4.2.5, the AL top defines the height at which the particle backscatter coefficient at 1064 nm falls below $0.02 \text{ Mm}^{-1}\text{sr}^{-1}$ and is thus an absolute criterion for the vertical aerosol distribution. H_{aer} and H_{AOD95} are relative criteria for the extent of the vertical aerosol column and are defined as the height at which the AOD reaches the 63% and 95% level, respectively, in regard to the total AOD (100%).

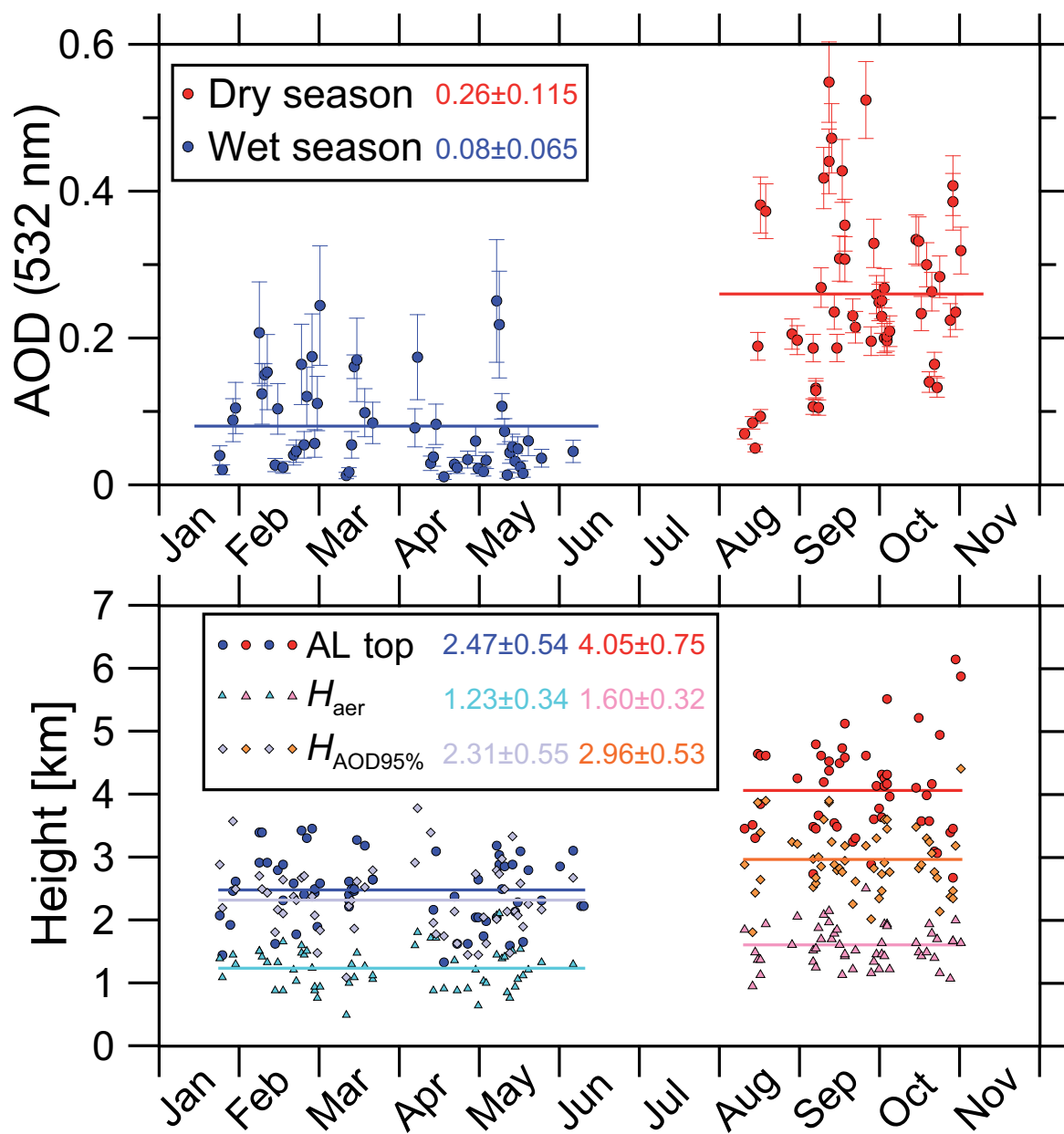


Figure 7.2: Top: Temporal development of the AOD at 532 nm in 2008. Bottom: Time series of the AL top, $H_{AOD95\%}$, and H_{aer} in 2008. The horizontal lines indicate the mean values for the respective season which are also given in the legend.

A clear difference in the vertical aerosol distribution is seen in Figure 7.2, bottom, between the two seasons. The vertical extent of the aerosol column (represented by the AL top, H_{aer} , and H_{AOD95}) was significantly lower in the wet season than in the dry season. However, H_{AOD95} shows less seasonal variability than the AL top height. On average, the AL top in the dry season was 1.5 km higher than in the wet season, while the mean H_{AOD95} differs by only 650 m between the two seasons. The seasonal variation of H_{aer} was found to be very low with a mean difference of 350 m. For the seasonal mean values in both seasons it was found that $\text{AL top} > H_{\text{AOD95}} > H_{\text{aer}}$. A high in-season variability was observed for the AL top and H_{AOD95} , while the day-to-day fluctuations of H_{aer} were rather weak. However, neither in the dry nor in the wet season a general temporal trend concerning the vertical aerosol distribution was found. Typically, the AL top and H_{AOD95} were much higher than H_{aer} during both seasons.

7.2.2 Overview of vertical aerosol profiles

Figure 7.3 shows all particle backscatter coefficient profiles (at 355, 532, and 1064 nm) that could be evaluated for the wet (top) and dry (bottom) season. The corresponding mean profile (red) plus standard deviation is presented in addition. All vertical aerosol profiles were cloud-screened. Due to detector problems, the particle backscatter coefficient at 355 nm could not be determined below 500 m.

A high in-season variability of the particle backscatter coefficient profiles is seen in Fig. 7.3. In most cases, the vertical distribution of the particle backscatter coefficient was very inhomogeneous. A strong contrast between the wet and dry season is again obvious. The profile shape and the magnitude of the particle backscatter coefficient profiles differ significantly for both seasons. During the dry season, frequently lofted layers of enhanced backscattering occurred. Hygroscopic growth as explained in Sec. 6.3.3 was the reason for the enhanced backscattering in these layers. Throughout the entire observation period, aerosol layers above 10 km were not detected.

The mean values of the dry-season particle backscatter coefficient within the ML were a factor of 2–3 larger than the respective mean values for the wet season. Above the ML (between 1500 and 2500 m), the dry-season mean values of the particle backscatter coefficient were even 3–4 times larger than the respective value of the wet season.

The absolute values of the particle backscatter coefficient (and thus aerosol load) varied significantly from case to case during the dry season. The magnitude of this in-season variation was as high as the seasonal variation. Absolute differences of the particle

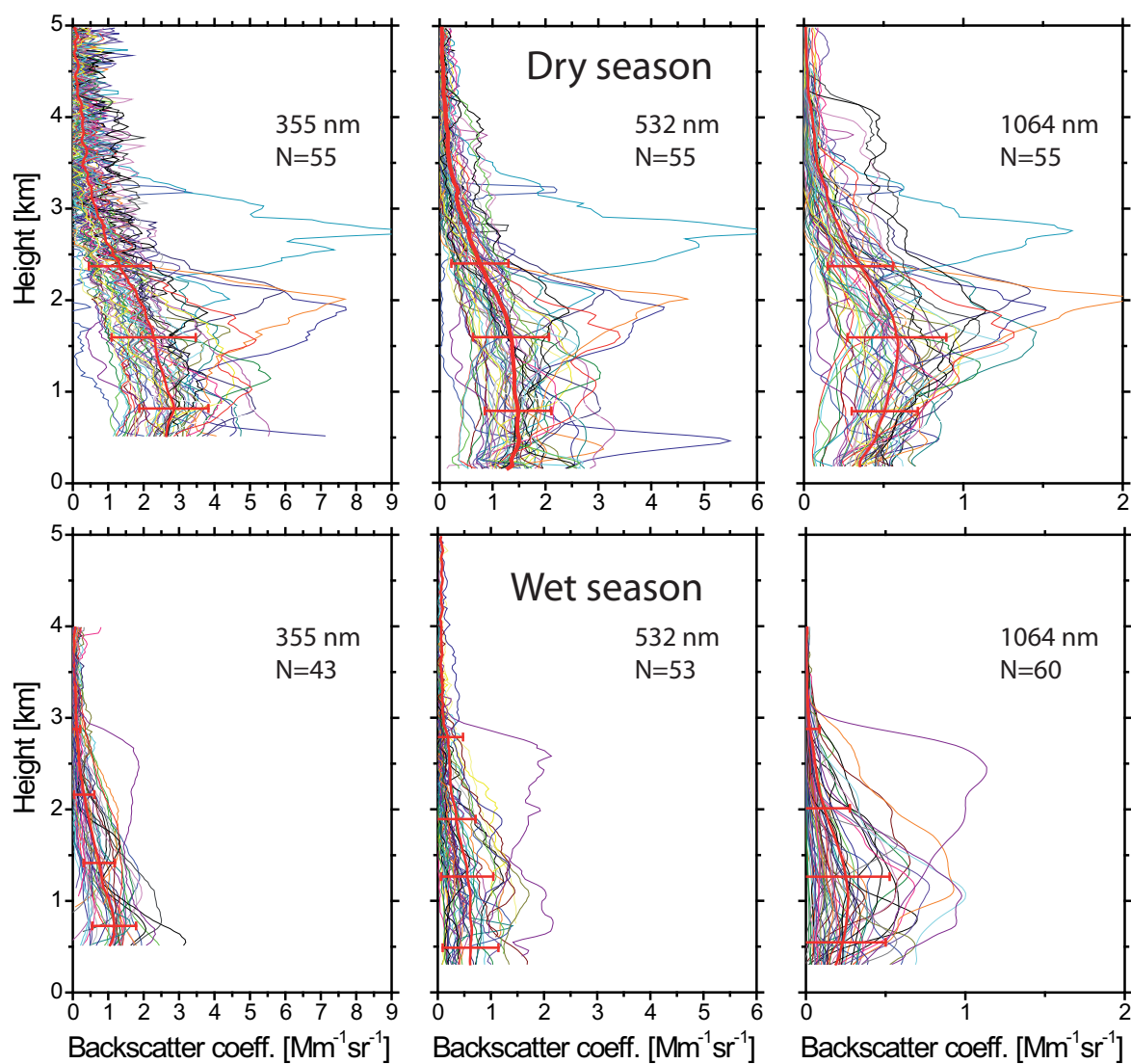


Figure 7.3: Composite of N vertical profiles of the particle backscatter coefficient during the dry (top) and wet (bottom) season at 355 (left), 532 (center), and 1064 nm (right). The red lines show the corresponding mean profiles with the respective standard deviations.

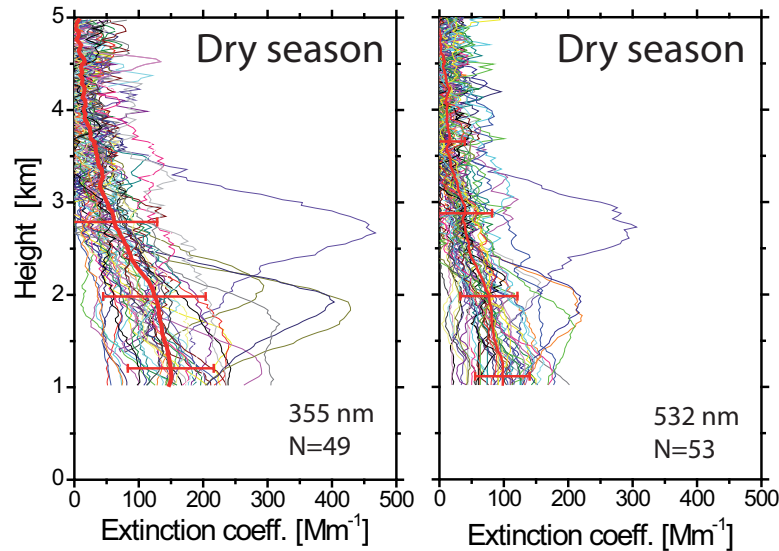


Figure 7.4: N vertical profiles of the particle extinction coefficient at 355 and 532 nm in the dry season 2008. The red lines show the corresponding mean profiles with the respective standard deviations.

backscatter coefficient up to a factor of 10 were observed in the ML. For instance, the particle backscatter coefficient at 532 nm at 1 km agl on 3 October 2008 was $0.28 \text{ Mm}^{-1}\text{sr}^{-1}$, while it was $2.95 \text{ Mm}^{-1}\text{sr}^{-1}$ on 12 September 2008. During the wet season, absolute differences were much lower and the profile shape was much less variable than during the dry season. Thus, in terms of profile shape the mean wet-season particle backscatter coefficient profile is more representative than the corresponding dry-season mean profile.

Absolute maximum values observed during the almost one-year period were $7.7 \text{ Mm}^{-1}\text{sr}^{-1}$ at 355 nm and $2 \text{ Mm}^{-1}\text{sr}^{-1}$ at 1064 nm. These values were observed on 28 October 2008 during the dry season. The maximum values observed in the wet season were $2.65 \text{ Mm}^{-1}\text{sr}^{-1}$ at 355 nm and $1 \text{ Mm}^{-1}\text{sr}^{-1}$ at 1064 nm observed on 9 May 2008 during an intrusion of African aerosol (see Sec. 6.1).

Figure 7.4 shows all particle extinction coefficient profiles of the dry season 2008 that could be independently evaluated with the Raman lidar technique (Eq. 4.10). The extinction coefficient retrieval is limited to values above 1 km due to the incomplete overlap between the laser beam and the field of view of the telescope (see Sec. 5.1). Cloud-contaminated data were removed in Fig. 7.4. Wet-season data cannot be presented because the high frequency of low-level clouds, rain, and fog prohibited temporal

averaging of the lidar signal for more than 1 hour which is necessary for the determination of the particle extinction coefficient.

A high in-season variability of the particle extinction coefficient profiles is visible in Fig. 7.4 in agreement with the findings for the particle backscatter coefficient profiles for the dry season. Absolute values of the particle extinction coefficient within the ML varied by a factor of about 10 between 20 Mm^{-1} and 190 Mm^{-1} at 532 nm. The mean dry-season value in the height range below 2000 m was $143 \pm 71 \text{ Mm}^{-1}$ at 355 nm and $88 \pm 44 \text{ Mm}^{-1}$ at 532 nm. Between 2000 and 2500 m, mean values of $103 \pm 64 \text{ Mm}^{-1}$ at 355 nm and of $60 \pm 39 \text{ Mm}^{-1}$ at 532 nm were recorded. Maximum particle extinction coefficient values of 450 Mm^{-1} and 300 Mm^{-1} at 355 and 532 nm, respectively, were observed.

The observed inter-seasonal and in-season behavior of the lidar-derived optical aerosol properties is in good agreement with findings from measurements of optical aerosol properties in Alta Floresta, Rondônia, southern Amazonia (*Guyon et al.*, 2003). There, also a high day-to-day variability during the dry season was observed as well as a strong contrast between the wet and the dry season. However, the magnitude of the observed variation of the optical aerosol properties was much lower at the lidar site. Thus, one may conclude that the lidar location is less affected by pollution (BBA) than regions in southern Amazonia.

7.3 Statistical analysis

In this Section, statistical results of the aerosol properties based on the entire set of measurements in the wet and dry season 2008 are shown. First, frequency distributions of the AOD and a comparison to different AERONET observations are discussed. Afterwards, statistics concerning the vertical aerosol structure are presented, and finally aerosol-specific (intensive) properties are discussed. As already mentioned above, the independent retrieval of the particle extinction coefficient profiles was possible only for the dry season. Thus, the statistical analysis of extinction-related aerosol properties is restricted to this season.

7.3.1 AOD

The frequency distribution of the lidar-derived AOD (532 nm) for the wet and dry season is shown in Fig. 7.5. A significant difference in the shape of the AOD frequency distribution was observed.

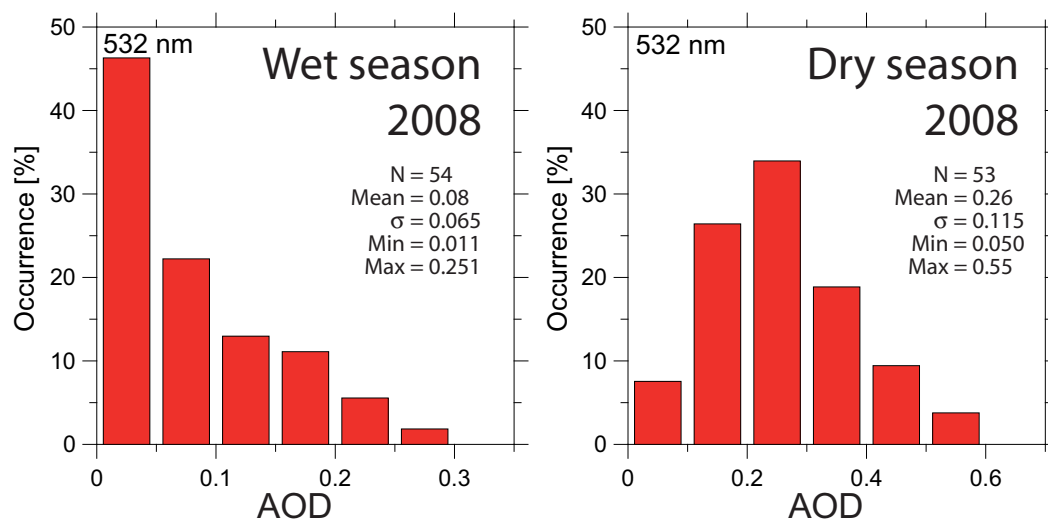


Figure 7.5: Frequency distribution of the lidar-derived AOD for the wet (left) and dry (right) season 2008. N observations were analyzed.

Typical AOD values in the dry season ranged from 0.1–0.4 while in the wet season the AOD was usually below 0.2. The maximum AOD was 0.55 measured on 11 September 2008. AOD values below 0.1 were observed in only 7% of all cases during the dry season. Background conditions (AOD < 0.05, cf. Sec. 6.2) were never measured during this season. In contrast to the dry season, the wet-season AOD was always below 0.26. In more than 46% of all cases, background conditions were prevailing. AOD values above 0.15 occurred in about 19% of all cases.

In the following, an intensive comparison between the lidar-derived AOD and AERONET sun photometer measurements made at different locations in the Amazon Basin before 2008 is presented. AERONET sun photometer observations were performed from 1999 to 2002 at Balbina, only ca. 100 km north-east of the lidar site. For comparison, the frequency distributions of the daily mean AOD at Balbina (AERONET Level 2.0 data)² are shown in Fig. 7.6. The daily AOD averages could be obtained from 123 wet-season and 435 dry-season days between 1999 and 2002. In general, a good agreement was found between the two measurement campaigns (compare lidar AOD frequency distribution in Fig. 7.5). Lidar-derived mean values at 532 nm are 0.26 ± 0.12 in the dry season and 0.08 ± 0.07 in the wet season, whereas the photometer-derived values at 500 nm are 0.24 ± 0.13 in the dry season and 0.11 ± 0.07 in the wet season. An AOD higher than 0.43 was never observed in the wet season

²downloaded from <http://aeronet.gsfc.nasa.gov>, site name: Balbina

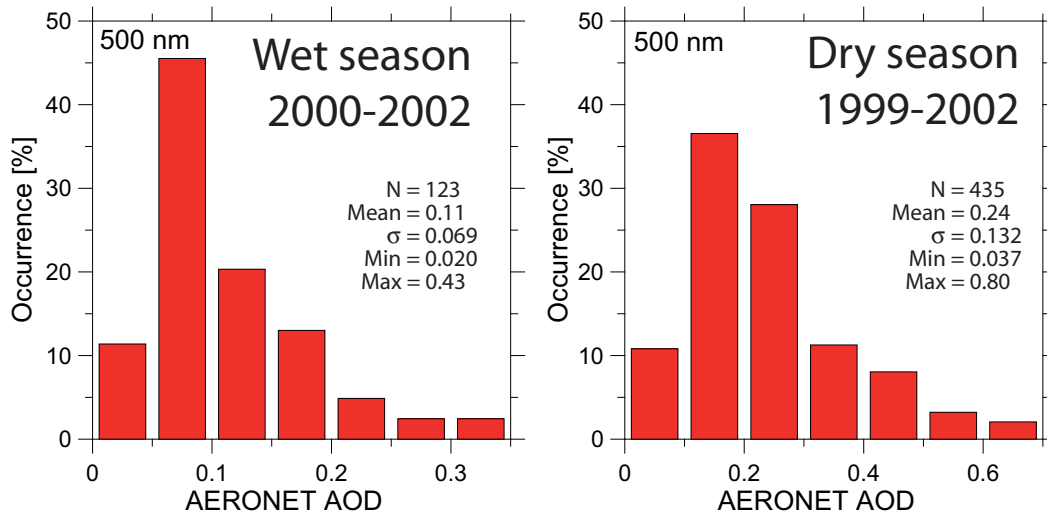


Figure 7.6: Frequency distribution of the AERONET AOD obtained from N daily mean values in the wet and dry season between 1999 and 2002 at Balbina (100 km north-east of the lidar site).

at Balbina, which is in agreement with the lidar AOD observations. The shape of the lidar AOD frequency distribution in the wet season is different to the AERONET one. In the case of the lidar observations, the AOD frequency distribution peaks between 0 and 0.05, whereas the AERONET distribution peaks between 0.05 and 0.1. This may partly be caused by the different measurement techniques. The sun photometer cannot determine the AOD under cloudy conditions. In addition, cases with subvisible thin cirrus may have introduced a positive bias. On the other hand, lidar allows the measurement of the AOD shortly after rainfall events when the AOD is rather low. This is usually not possible with sun photometer.

The dry-season AOD frequency distribution of AERONET is broader than the respective one for the wet season. Thus, highly variable aerosol conditions were observed in this region also between 1999–2002. The photometer-derived AOD frequency distribution is similar to the lidar-derived AOD frequency distribution in the dry season 2008 (Fig. 7.5, right). Only minor deviations can be seen, e.g., for the frequency of AOD between 0.2–0.3. One can thus conclude that the general aerosol conditions did not significantly change between 1999–2002 (AERONET observations) and 2008 (Polly^{XT} observations).

Schafer et al. (2008) analyzed several years of AERONET observations at 15 sites

	Jan	Feb	Mar	Apr	May	Jun	Jul	Aug	Sep	Oct	Nov	Dec
Lidar 2008	0.06	0.10	0.09	0.05	0.07	–	–	0.18	0.29	0.25	–	–
AERONET	0.14	0.11	0.12	0.09	0.10	0.08	0.10	0.18	0.26	0.37	0.36	0.33

Table 7.1: Monthly mean AOD values at 532 nm as derived by lidar in 2008 and from AERONET observations in the northern forest region as published by *Schafer et al.* (2008). The AERONET AOD was converted from 440 nm to 532 nm by using the published monthly mean Ångström exponent.

(including Balbina) in Amazonia between 1999 and 2006. Monthly mean AOD values at 440 nm were presented for the cerrado region, southern forest region, and the northern forest regions (the region of the EUCAARI lidar site). For comparison with the lidar, the AERONET AOD was converted from 440 to 532 nm by using the published monthly mean Ångström exponent. The final comparison at 532 nm is shown in Table 7.1. Monthly mean AOD values from the lidar measurements and the AERONET observations in the northern forest region are given.

For the dry-season months, a good agreement of the mean AOD was found between the lidar and the AERONET observations. *Schafer et al.* (2008) reported a moderate AOD of 0.175 (after conversion to 532 nm) in August, which is in perfect agreement with the monthly mean AOD of August 2008 obtained from the lidar observations. Also the mean values of the AERONET AOD for September of 0.29 was almost equal to the lidar-derived mean AOD value of 0.26. However, the monthly mean value of the AERONET AOD for October of 0.37 (532 nm) was considerable higher than the value measured by lidar at this time of the year. This discrepancy could be due to different locations, since the authors included also measurement sites east of the lidar site. These areas are more populated and a high fire activity is observed in October/November.

For the wet season, *Schafer et al.* (2008) reported AOD values between 0.1 and 0.14 (532 nm) in the northern forest region. This is much higher than observed with the lidar (0.05–0.1 at 532 nm). A stronger influence of African aerosol to the AERONET sites east of the lidar location as well as the different measurement methodology as discussed above could be the reason for that.

The study conducted by *Schafer et al.* (2008) also revealed that there are significant differences in the aerosol load (AOD) between different regions in the Amazon Basin (northern forest, southern forest, and cerrado) during the dry season. Most of the recent campaigns (e.g., SCAR-B, LBA-EUSTACH, LBA-SMOCC – compare

Table 2.1) were conducted in southern Amazonia, where a higher aerosol variability and a much higher burning activity than in the northern part was observed. In addition, the burning season peaks at different times in the southern and northern forest regions. This is the reason why at the lidar location the aerosol load is highest in October whereas in southern Amazonia, e.g., as reported by *Guyon et al.* (2003), it is in August. These regional differences must be kept in mind when comparing the results from the lidar campaign to findings from previous research activities in Amazonia.

7.3.2 Vertical aerosol structure

Figure 7.7 shows the frequency distribution of the AL top, H_{aer} , and H_{AOD95} derived from the lidar profiles in the wet and dry season 2008. A pronounced difference in the AL top frequency distribution of the dry and wet season was found. The AL top frequency distribution was narrower in the wet season compared to the dry season. Most frequently, the AL top was between 2 and 3 km in the wet season and between 3 and 5 km in the dry season. The AL top did not exceed 3.45 km in the wet season, while it reached up to 6.14 km in the dry season. According to the AL top, aerosol was always present up to at least 1.3 and 2.7 km in the wet and dry season, respectively. Compared to the AL top, the frequency distribution of H_{AOD95} shows only a weak difference between the wet and dry season. H_{AOD95} was most frequently observed between 2 and 3 km in the wet season and between 2.5 and 3.5 km in the dry season. Maximum values of H_{AOD95} were 3.8 and 4.4 km in the wet and dry season, respectively. Consequently, the majority of the aerosol load (95% of the AOD) was measured below 4 km in both seasons. With respect to the discrepancy to the observed AL tops, one may conclude that only thin layers of aerosol are above 4 km during the dry season.

For completeness, the frequency distributions of H_{aer} are also shown in Fig. 7.7. Only little seasonal differences can be seen for the frequency distribution of H_{aer} . A very narrow distribution was observed for both seasons. H_{aer} never exceeded 2.52 km, implying that two thirds of the AOD were always caused by aerosol below that height. Most frequently values of H_{aer} were between 0.5 and 1.5 km in the wet and between 1 and 2 km in the dry season. H_{aer} did not exceed 2.1 km during the wet season. Thus, one may conclude from the frequency distribution that two thirds of the AOD (see definition of H_{aer} in Sec. 4.2.5) are usually trapped in the lowermost 2 km.

It is interesting to know whether the vertical extent of the aerosol layer depends on the

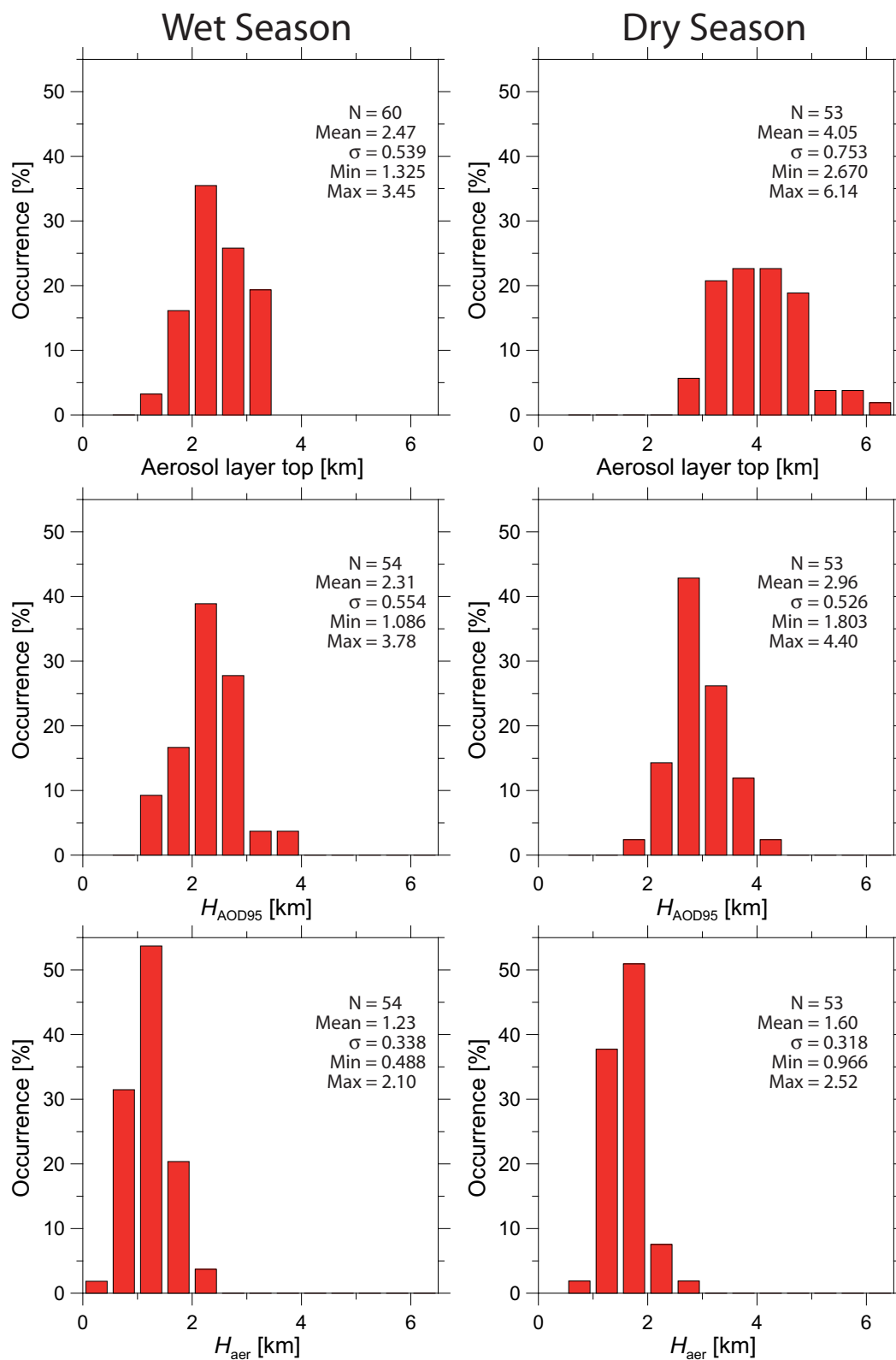


Figure 7.7: Frequency distribution of AL top, H_{AOD95} , and H_{aer} for the wet season (left) and dry season (right). The number of the used profiles (N) differs.

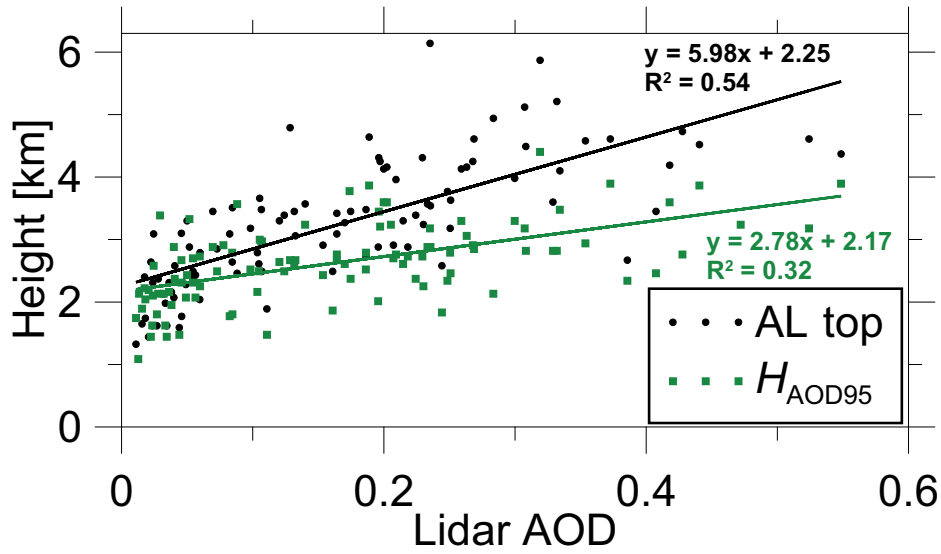


Figure 7.8: AL top height and H_{AOD95} as function of the AOD at 532 nm for the dry season 2008. The respective linear regression together with the corresponding formula and the correlation coefficient are drawn as well.

aerosol load. An attempt to study this relation is shown in Figure 7.8. The correlation between the measured AOD and the derived AL top and H_{AOD95} is presented. However, only a weak correlation was found between the AOD and the depth of the entire aerosol layer (correlation coefficient R^2 of 0.54 and 0.32 for the AL top and H_{AOD95} relationship, respectively). Thus, the aerosol layer depth is not a function of the AOD. This means, no conclusions about the vertical aerosol structure (distribution) in Amazonia can be drawn from column-integrated measurements (e.g., sun photometer observations). This finding of the lidar measurements agrees well with findings reported by *Browell et al.* (1988) from 11 observation flights made in the dry season 1985 in northern Brazil near the Amazon river. An airborne DIAL (Differential Absorption Lidar, *Browell et al.*, 1983) was used for vertically resolved ozone and aerosol profiling. It was found that significant amounts of aerosol were above the ML but its vertical distribution was very inhomogeneous.

An attempt to analyze the vertical aerosol distribution in more detail is discussed in the following. For this purpose, the AOD of the ML (AOD_{ML}) is compared to the AOD of the entire vertical column. The maximum height of the ML top as derived from ECMWF for the day before the measurement (see Sec. 4.2.5) was used to determine AOD_{ML} . The ratio of the AOD_{ML} to the total AOD (AOD ratio) is then used as a measure for the vertical aerosol distribution. An AOD ratio of 0.3 indicates that 30%

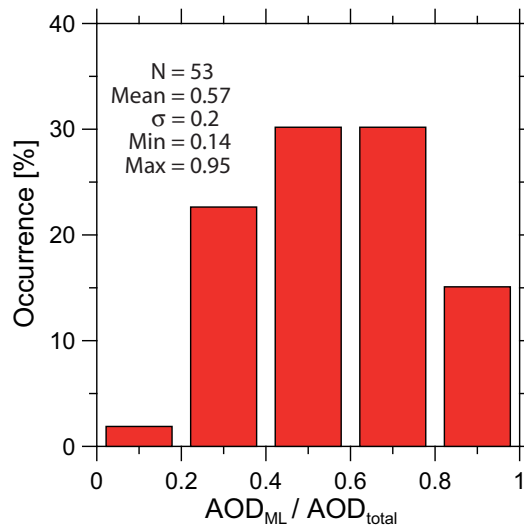


Figure 7.9: Frequency of occurrence of the AOD ratio (ratio between the AOD_{ML} and the total AOD) for the dry season 2008.

of the aerosol load are within the ML, while an AOD ratio of 1 means that 100% of the aerosol are within the ML.

Figure 7.9, shows the AOD ratio at 532 nm for the dry season in 2008. It is evident that in more than one half of the dry-season cases the contribution of aerosols above the ML to the total AOD is >40%. Only in about 15% of all cases, ML aerosol contributed more than 80% to the total AOD. In about one third of all dry-season measurements, the contribution of ML aerosol to the AOD was between 60% and 80%.

As can be seen in Fig. 7.10, left, a correlation of the modeled ML top with the measured AOD is not given. This means that the total aerosol load is independent of local mixing processes. However, the AOD ratio is well correlated with the height of the ML top (Fig. 7.10, right). The solid line in Fig. 7.10, right, is obtained in the ideal case of a height-independent particle extinction coefficient within the aerosol layer from the surface to the AL top. This means that in this ideal case no differences in terms of aerosol conditions exist below and above the ML top.

According to Fig. 7.10, right, one can conclude that the contribution of ML aerosol to the AOD is high when the ML top is high. Thus, the ideal case of a particle extinction coefficient profile independent of the ML top is nearly valid for the vertical aerosol distribution in Amazonia during the dry season. Therefore, one can conclude that the thermal stratification in the lower troposphere (i.e., the development of the ML) has only a small influence on the vertical spreading of BBA. Obviously, hot smoke plumes can easily be transported above the ML as a result of pyro-convection and

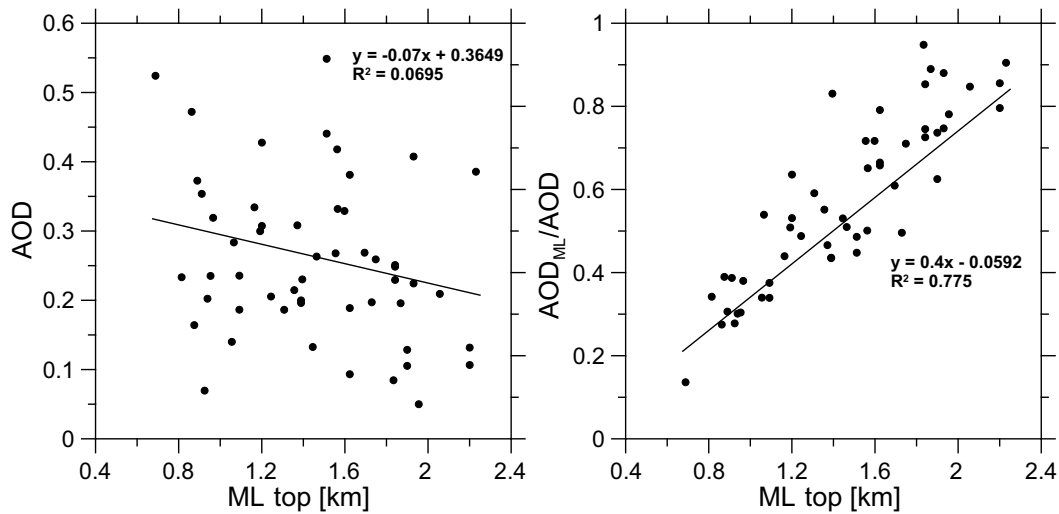


Figure 7.10: Left: AOD as a function of the ML top. Right: Correlation between the AOD ratio (ratio of AOD_{ML} to total AOD) and the ML top. Linear regression lines plus corresponding formulae with correlation coefficients are shown in addition.

shallow convection. As a consequence, a high aerosol load can be found above the ML top throughout the dry season. One may thus conclude that in contrast to mid-latitudes, the ML top in Amazonia is not a strong boundary for vertical transport processes. These findings corroborate results from airborne measurements during the dry season in Rondônia presented by *Guyon et al.* (2005). No differences in the aerosol characteristics within the ML and above the ML were found.

7.3.3 Aerosol properties

The frequency distribution of the maximum extinction coefficient of each single aerosol profile of the dry season is shown in Fig. 7.11. Typically, the maximum particle extinction coefficient was observed within the ML. In 28% of all cases, the maximum particle extinction coefficient was between 150 and 200 Mm^{-1} at 355 nm. In 13% of all cases, values above 300 Mm^{-1} could be observed. Regarding maximum values of particle extinction coefficient at 532 nm, most frequently values between 50 and 150 Mm^{-1} were measured.

Guyon et al. (2003) presented results from in-situ measurements performed above the canopy level in Alta Floresta, Rondônia, in 1999. Scattering and absorption coefficients (at 545 and 565 nm, respectively) for dried aerosol particles were measured. For the wet season, the authors reported extinction coefficients of 3–17 Mm^{-1} , while

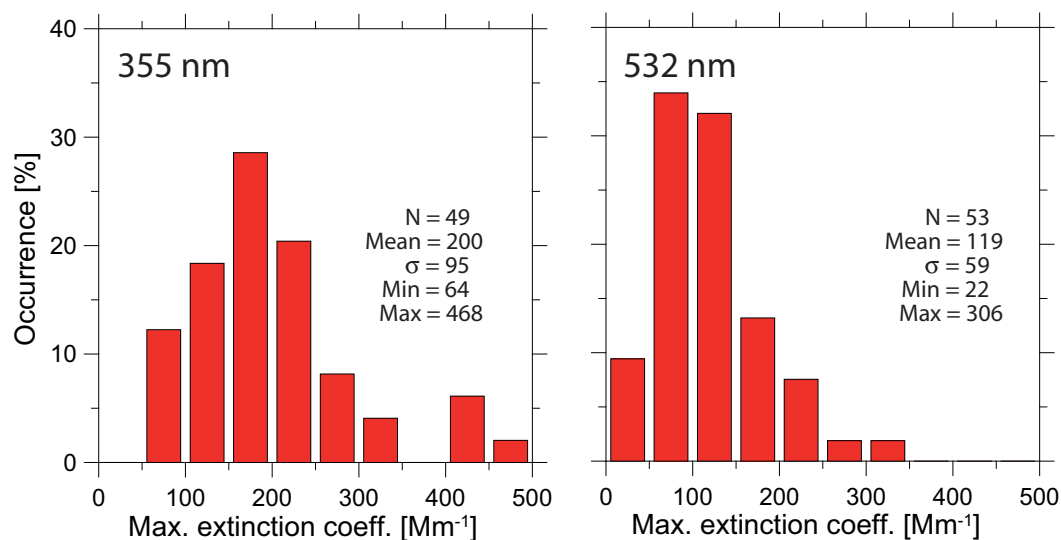


Figure 7.11: Frequency distribution of the maximum extinction coefficient of N individual aerosol profiles at 355 (left) and 532 nm (right) during the dry season 2008.

during the dry season, extinction coefficients up to 650 Mm^{-1} were observed. This is about 5 times higher than the mean maximum extinction coefficient measured with lidar at 532 nm under ambient conditions in 2008. These findings show again that Rondônia in southern Amazonia is under much higher BBA influence than the lidar site in the northern forest.

Fig. 7.12 shows the statistical analysis of the lidar ratio at 355 and 532 nm for the dry season 2008. Mean values for the height range from 1500–2500 m were analyzed. The presented values are thus independent of overlap corrections (see Sec. 5.1) and are representative for the aerosol layer characteristics in the dry season (AL top always above 2500 m, compare Fig. 7.7).

As can be seen in Fig. 7.12, lidar ratios between 20 and 80 sr at 355 nm and between 20 and 90 sr at 532 nm were observed. Most frequently, the values at 355 nm were between 50 and 70 sr (in 61% of all cases) and at 532 nm between 50 and 80 sr (in 71% of all cases). In about 42% of the cases, the lidar ratios at 532 nm exceeded 70 sr and thus indicate the presence of strongly absorbing smoke particles. In comparison to lidar-ratio frequency distributions of urban haze observed at Leipzig (mean value of 58 ± 12 sr at 355 nm and 53 ± 11 sr at 532 nm, *Mattis et al.*, 2004; *Müller et al.*, 2007b), the frequency distributions observed during the BBA-dominated dry season in Amazonia are shifted towards higher values (mean value of 62 ± 12 sr at 355 nm, 64 ± 15 sr at 532 nm). Because backscatter and extinction properties of

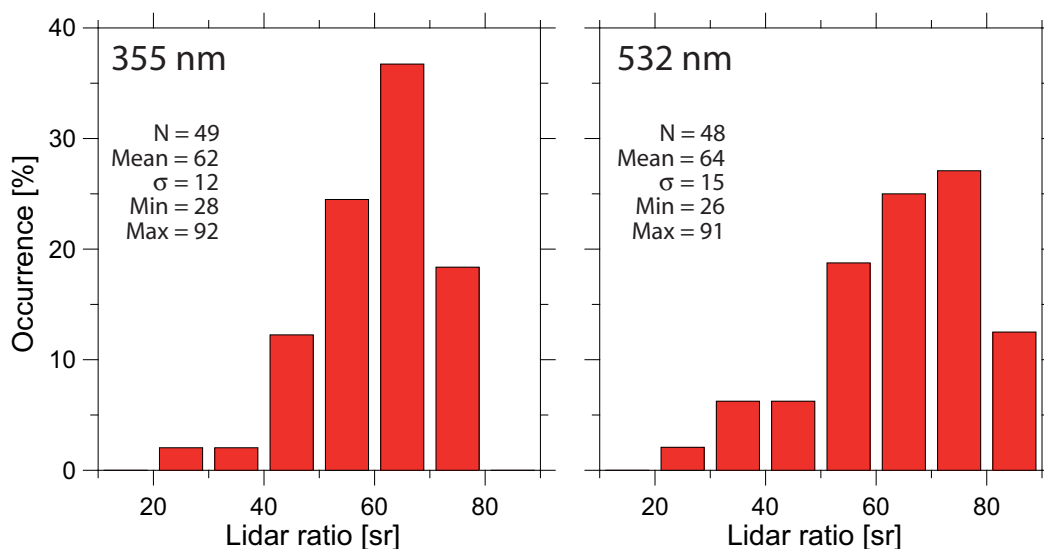


Figure 7.12: Frequency distributions of the lidar ratio at 355 (left) and 532 nm (right) at 1500–2500 m retrieved from N observations in the dry season.

particles sensitively depend on both absorption efficiency and particle size distribution characteristics, the higher mean lidar ratio in Amazonia may be related to smaller and stronger absorbing particles. However, the wide spread of lidar-ratio values from 20–90 sr reflects the influence of aging and in-cloud processes of the particles that can significantly alter the BBA optical properties. Different burning types (flaming and smoldering) and different fuels could also be a reason for the high variability in the lidar-ratio data set.

The observations of low lidar ratios (i.e., below 50 sr) always coincided with a low aerosol load as shown in Fig. 7.13. According to this figure, lidar ratios (532 nm) <50 sr were only observed when the average particle extinction coefficient between 1500 and 2500 m was below 50 Mm^{-1} . For these cases of low aerosol load, the BBA influence is weak and also other aerosol types determine the aerosol optical properties. Lidar-ratio values >50 sr do not show any correlation to the aerosol load, even though very high average particle extinction coefficients $>100 \text{ Mm}^{-1}$ were rare.

Figure 7.14 shows the frequency distribution of the lidar-derived Ångström exponents for the dry and wet season. In the wet season, only the analysis of the backscatter-related Ångström exponents was possible. In consistence with the lidar-ratio analysis, mean values for the height range between 1500 and 2500 m are presented.

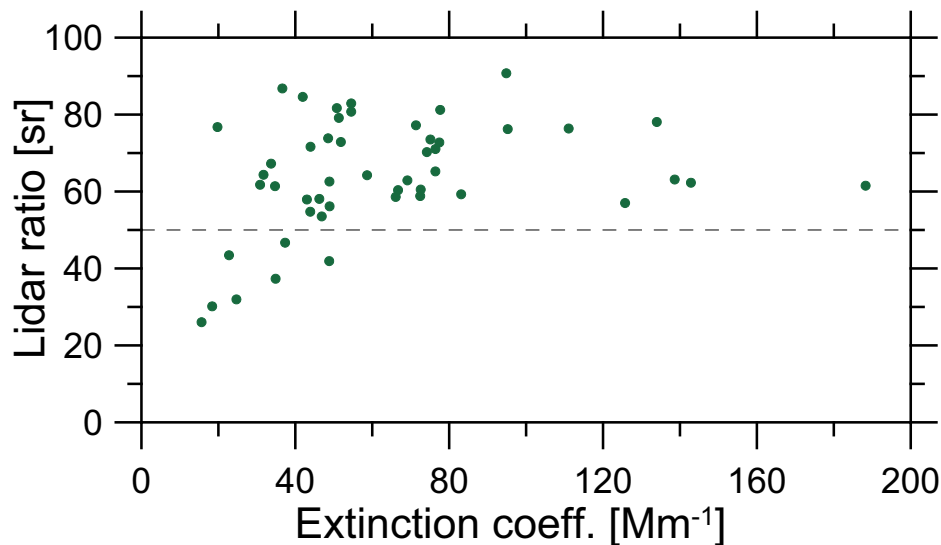


Figure 7.13: Lidar ratio at 532 nm as a function of the mean particle extinction coefficient at 532 nm between 1500 and 2500 m.

A clear seasonal difference concerning the frequency distribution of the backscatter-related Ångström exponent was observed. In the dry season, the frequency distribution of the backscatter-related Ångström exponent shows a sharp maximum between 1 and 1.5 (for about 60% of all cases). Observations of backscatter-related Ångström exponents below 0.5 or above 2 were rare in that season. In contrast, the frequency distribution of the backscatter-related Ångström exponent in the wet season is very broad. Obviously, very different aerosol types with different optical properties crossed the lidar site. As shown in Sec. 6.1 and Sec. 6.2, aged BBA from Africa, Saharan dust, and background aerosol were identified with Polly^{XT} in the wet season. On the other hand, BBA particles originating from fires on the South American continent were dominating during the dry season.

The frequency distribution of the extinction-related Ångström exponent during the dry season is shown in Fig. 7.14 (upper right panel). In most cases (more than 70%), an Ångström exponent between 0.5 and 1.5 was observed. Extinction-related Ångström exponents >1.5 were measured in 19% of all cases, whereas values <0.5 were only rarely found. Similar values were observed by *Schafer et al.* (2008) for the northern forest regions from AERONET observations. In the southern forest and cerrado regions, however, the authors report a frequent occurrence of Ångström exponents above 1.5 during the dry season. *Guyon et al.* (2003) even reported Ångström exponents above 2 over Alta Floresta, southern Amazonia. Because the

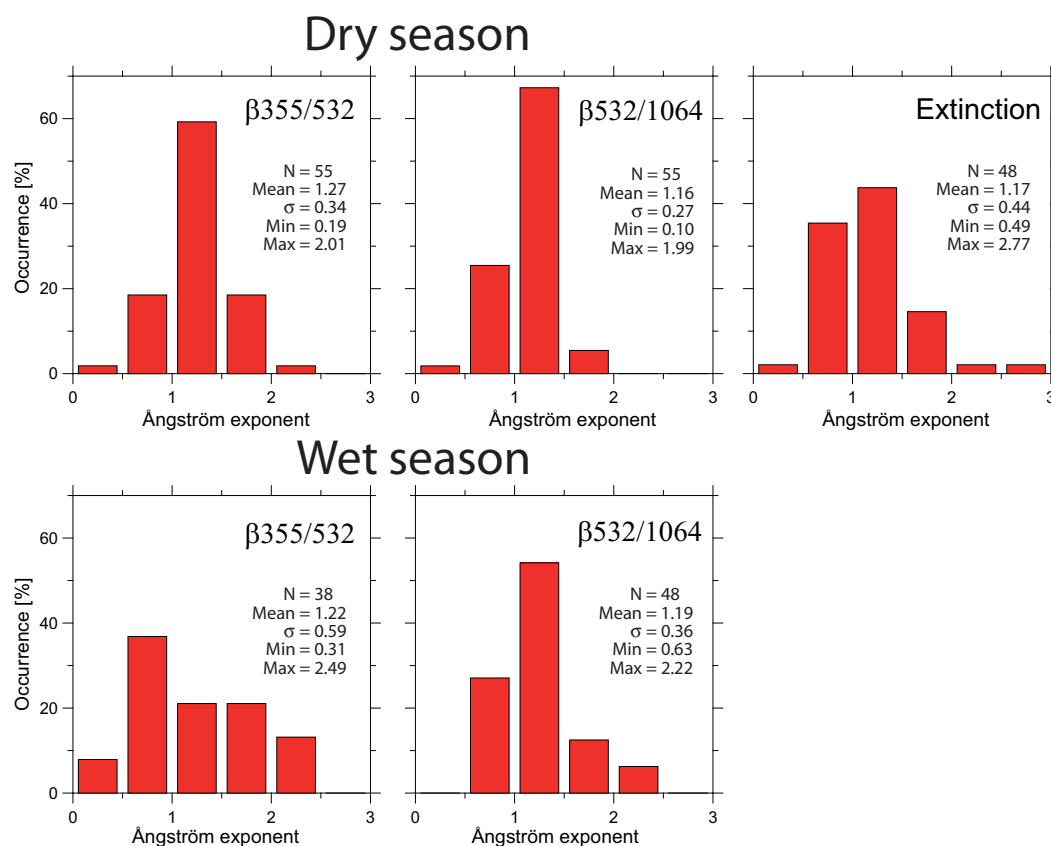


Figure 7.14: Frequency distributions of the mean Ångström exponents derived from N observation cases. Values of the Ångström exponent related to the backscatter coefficient at 355 and 532 nm (left), to the backscatter coefficients at 532 and 1064 nm (center), and to the extinction coefficients at 355 and 532 nm (right) between 1500 and 2500 m agl for the dry (top) and wet (bottom) season are shown.

Ångström exponent is sensible to the particle size distribution, these high values indicate the dominance of small particles. Most obviously, different or younger smoke prevails in southern Amazonia compared to northern Amazonia as a result of the high fire activity related to deforestation and pasture maintenance.

The frequency distribution of the daily mean Ångström exponent derived at Balbina from AERONET observations between 1999 and 2002 is shown in Fig. 7.15. A good agreement between the lidar measurements in 2008 (compare Fig. 7.14) and these sun photometer measurements is found. During the dry season at Balbina, an Ångström exponent between 1 and 1.5 could be observed in more than 60% of all observations. Extinction-related Ångström exponents within this range were observed with Polly^{XT} in 44% of all cases during the dry season 2008.

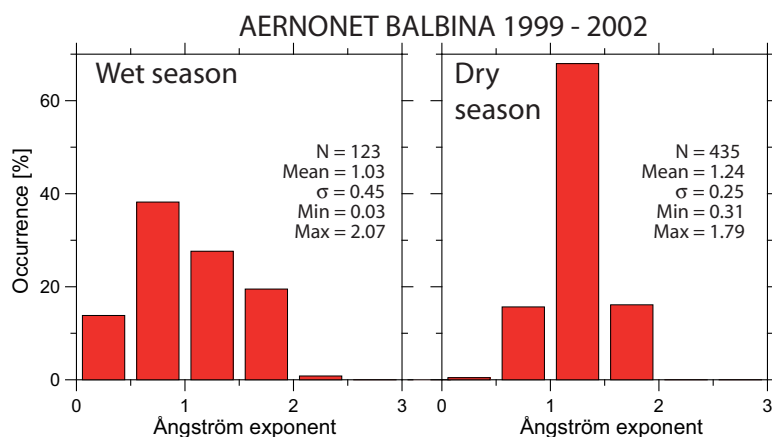


Figure 7.15: Frequency distribution of the Ångström exponent of the AOD at 380 and 500 nm from three years of AERONET observations at Balbina. N daily mean values in the wet and dry season were used.

In the wet season, a broad distribution of the Ångström exponent with values from 0 up to 2.5 was detected at the AERONET site. This supports our and previous findings that the aerosol regimes are completely different in northern central Amazonia during the two seasons. Whereas the dry season is dominated by one aerosol species (BBA), during the wet season various aerosol mixtures (different types, i.e., background, smoke, dust) can be observed.

Finally, a summarizing overview of the lidar observations during the wet and dry season 2008 is presented in Table 7.2. Mean values and respective standard deviations for the aerosol properties discussed in this Chapter are given. Values are presented for the entire vertical column, for the mixing layer, and for the lofted layer between 1500 and 2500 m.

Quantity	Dry Season	Wet season
Total vertical profile		
AOD (355 nm)	0.383 ± 0.167	0.129 ± 0.059
AOD (532 nm)	0.256 ± 0.115	0.080 ± 0.065
AL top	4.05 ± 0.75 km	2.47 ± 0.54 km
H_{aer}	1.60 ± 0.32 km	1.23 ± 0.34 km
H_{AOD95}	2.96 ± 0.53 km	2.31 ± 0.55 km
ML top	1.46 ± 0.42 km	1.10 ± 0.29 km
Max. α (355 nm)	200 ± 95 Mm ⁻¹	-
Max. α (532 nm)	119 ± 59 Mm ⁻¹	-
Max. β (355 nm)	3.54 ± 1.60 Mm ⁻¹ sr ⁻¹	1.21 ± 0.57 Mm ⁻¹ sr ⁻¹
Max. β (532 nm)	2.17 ± 1.12 Mm ⁻¹ sr ⁻¹	0.71 ± 0.52 Mm ⁻¹ sr ⁻¹
Max. β (1064 nm)	0.79 ± 0.37 Mm ⁻¹ sr ⁻¹	0.32 ± 0.26 Mm ⁻¹ sr ⁻¹
Mixing layer		
β (355 nm)	2.63 ± 0.99 Mm ⁻¹ sr ⁻¹	1.18 ± 0.52 Mm ⁻¹ sr ⁻¹
β (532 nm)	1.44 ± 0.69 Mm ⁻¹ sr ⁻¹	0.62 ± 0.50 Mm ⁻¹ sr ⁻¹
β (1064 nm)	0.50 ± 0.21 Mm ⁻¹ sr ⁻¹	0.24 ± 0.26 Mm ⁻¹ sr ⁻¹
1500–2500 m		
α (355 nm)	118 ± 64 Mm ⁻¹	-
α (532 nm)	70 ± 38 Mm ⁻¹	-
β (355 nm)	1.83 ± 1.15 Mm ⁻¹ sr ⁻¹	0.41 ± 0.33 Mm ⁻¹ sr ⁻¹
β (532 nm)	1.09 ± 0.67 Mm ⁻¹ sr ⁻¹	0.30 ± 0.35 Mm ⁻¹ sr ⁻¹
β (1064 nm)	0.48 ± 0.20 Mm ⁻¹ sr ⁻¹	0.13 ± 0.18 Mm ⁻¹ sr ⁻¹
Lidar ratio (355 nm)	62 ± 12 sr	-
Lidar ratio (532 nm)	64 ± 15 sr	-
$\mathring{a}_{\alpha_{355/532}}$	1.17 ± 0.44	-
$\mathring{a}_{\beta_{355/532}}$	1.27 ± 0.34	1.22 ± 0.59
$\mathring{a}_{\beta_{532/1064}}$	1.16 ± 0.27	1.19 ± 0.36

Table 7.2: Mean value and standard deviation of the lidar quantities derived in the dry and wet season 2008. Values for the total profile, within the ML (ECMWF), and for 1500–2500 m are presented. \mathring{a} = Ångström exponent, α = particle extinction coefficient, β = particle backscatter coefficient.

Chapter 8

Summary, conclusion, and outlook

Continuous lidar measurements were performed in the Amazon rain forest for almost one year in 2008. The results of the lidar observations were presented in this dissertation. These measurements are the first long-term observations of the vertical aerosol structure ever made in the Amazon Basin. The advanced lidar observations were conducted 60 km north of Manaus in the central northern part of Amazonia. The area is widely covered with pristine rain forest. A HYSPLIT backward-trajectory analysis showed that the observations were representative on a regional scale for the central northern part of the Amazon rain forest. The general weather conditions in this region are characterized by a wet (December–June) and a dry season (July–November). During the dry season, a high fire activity occurs in Amazonia, which heavily influences the atmospheric conditions.

The lidar measurements were conducted with the automated multiwavelength-Raman-polarization lidar Polly^{XT}. With this instrument, vertical profiles of the particle backscatter coefficient at 355, 532, and 1064 nm, of the particle extinction coefficient at 355 and 532 nm, and of the particle linear depolarization ratio at 355 nm can be determined. Lidar observations near Manaus could be performed on 211 days from January to November 2008. A data coverage of 72% could thus be achieved. Nevertheless, instrumental problems and unfavorable weather conditions during the campaign were the reason that the full data set (all Polly^{XT} products) was available for 60 days only (mostly in the dry season).

As part of this thesis, several efforts were undertaken for Polly^{XT} to meet hardware and software standards of EARLINET. Calibration procedures were performed and correction schemes (e.g., overlap correction and polarization correction) were applied to assure a high quality of the determined aerosol properties. These efforts as well

as comparisons to other lidars during the EARLI09 campaign showed that the newly constructed Polly^{XT} was well designed and set up so that the measured signal profiles and derived aerosol properties were of high quality.

The results from the long-term lidar observations performed in Brazil contain a lot of new information about the aerosol conditions in the central northern Amazon Basin and corroborate certain findings from former aerosol measurements in Amazonia. It was shown for the first time that advection of Saharan dust together with BBA from Africa occurred regularly throughout the wet season. In about one third (32%) of all lidar observations during the wet season, African aerosol was dominating the optical aerosol properties in Amazonia. The analysis of the vertical aerosol structure during such events revealed that the African aerosol arriving in the central northern Amazon Basin was usually trapped in the lowermost 3–3.5 km of the troposphere. To quantify the amount of Saharan dust and African smoke transported towards the lidar site, the dust contribution to the measured optical aerosol properties was separated by means of the measured particle depolarization ratio. This study led to the result that in about one half of the cases with African aerosol advection, smoke particles contributed to more than 50% to the total AOD. The smoke transport from Africa towards Amazonia occurred predominantly between January and April when the fire activity in Central Africa was highest. BBA is thus a major constituent of the aerosol plumes that are regularly transported from Africa towards Amazonia. This is a key finding of the presented study. However, the transport mechanisms are not fully understood in terms of cloud processing and wet deposition. Furthermore, consequences of the transport of mixed aerosol on radiation transfer and cloud formation in the Amazon Basin but also on the Atlantic Ocean remain to be clarified by means of, e.g., atmospheric modeling.

From former experiments in Amazonia, it was reported that the aerosol load during the wet season is very low and probably free of anthropogenic influence (*Pöschl et al.*, 2010; *Martin et al.*, 2010a; *Rissler et al.*, 2004). These findings were partly confirmed by the lidar measurements. During clean conditions, an AOD (532 nm) of less than 0.05 was observed and the aerosol was trapped in the lowermost 2 km of the troposphere. However, the analysis of the long-term data set revealed that these clean atmospheric conditions occurred in only 48% of all wet-season cases. One example for such background conditions was intensively discussed and it was shown that a major meso-scale rain event occurred in the Amazon region at the same time.

This precipitation event was possibly partly responsible for the very low aerosol load. Thus, further investigations on the role of precipitation events on background aerosol conditions are needed.

Two case studies from the dry season were presented for which BBA dominated the optical properties. In the first case, a comparable high aerosol load (AOD of 0.41) prevailed while in the second one, a medium aerosol load (AOD of 0.15) was observed. Aged BBA advected from regions south of the lidar site were identified to be the dominant aerosol species for both cases. However, very different geometrical, optical and microphysical properties of BBA (e.g., vertical layering, lidar ratio, Ångström exponent, effective radius, SSA) were observed on both days. In the first case, aerosol was present up to about 4.5 km. Extinction-related Ångström exponents of about 1 and lidar ratios between 70 and 90 sr were found at different heights for the smoke aerosol. Effective particle radii ranged from 0.21 to 0.34 μm . The BBA was highly absorbing (SSA of 0.81) at heights of the highest RH (85%), whereas above under dry conditions (RH=50%) only moderate absorption (SSA of 0.93) was detected.

In the second case, smoke was detected up to 4.5 km, and Ångström exponents of about 2 and lidar ratios of 45–55 sr were measured in the aerosol layers. Effective particle radii of about 0.13 μm revealed that smaller particles were observed. The BBA was only moderately absorbing indicated by SSA values between 0.92 and 0.94. The reason for the differences in the smoke properties could be the shorter travel time to the lidar site (<24 h), different aging processes (e.g., cloud/rain processing), or different burning conditions. In both cases, no depolarizing effects of the BBA could be observed.

The effect of hygroscopic growth on the optical aerosol properties was explained for smoke aerosol in a third case study. The extensive optical properties increased by a factor up to 7.5 due to hygroscopic growth. The intensive optical properties (lidar ratio, Ångström exponent), however, did not show any significant change in dependence of the relative humidity. The hygroscopic growth of BBA observed by lidar was stronger than the one found in previous studies concerning Amazonian BBA (*Kotchenruther and Hobbs, 1998*) but weaker than hygroscopic growth of urban aerosol (*Skupin et al., 2010*). However, further investigations are needed to study the hygroscopic growth behavior under conditions of high RH (close to 100%), ideally with aerosol and humidity profiling at the same location. Nevertheless, this study showed that humidification effects of BBA cannot be neglected and has to be kept in mind when interpreting aerosol observations.

The strong contrast between the aerosol conditions in the dry season and the wet season were confirmed by the statistical analysis of all lidar observations in 2008. Due to the high BBA concentration in the atmosphere, the mean AOD of the dry season was found to be a factor of 3 higher than the mean AOD of the wet season (0.26 compared to 0.08 at 532 nm). Maximum AOD values were less than 0.55 (at 532 nm) and hence show that the lidar location was not in the direct vicinity of fire events. In only 7% of all cases in the dry season 2008, an AOD below 0.1 was observed. Also the maximum extinction and backscatter coefficient values in the dry season 2008 were 2–3 times higher than during the wet season of this year.

The vertical aerosol distributions differ also significantly between the two seasons. In the wet season, the aerosol was mostly trapped in the lowermost 2.5 km, while in the dry season aerosol typically reached up to 4.5 km. Aerosol was occasionally detected up to 6.14 km in the dry season. The majority of the aerosol (95% of the AOD), however, was found to be on average below 2.3 km in the wet season and below 3 km in the dry season. During the wet season, lofted aerosol layers and multiple aerosol stratification was less frequent than in the dry season. The extent of BBA plumes during the dry season showed no correlation to the ML top height. Virtually uniform smoke haze layers were observed up to the AL top. Thus, pyro-convection and/or cloud-related mixing seem to be the major processes for the vertical distribution of BBA.

The statistical analysis of the intensive aerosol properties corroborates the different aerosol conditions in the different seasons. Highly variable backscatter-related Ångström exponents (0.3–2.5) in the wet season revealed that different aerosol types, i.e., Saharan dust, aged BBA from Africa, and background aerosol dominated the Amazonian aerosol population. In contrast, a relatively narrow frequency distribution of the backscatter-related Ångström exponent in the dry season (mostly between 1 and 1.5) showed that only one aerosol species, namely BBA, was dominant during this season. This result validates findings from *Guyon et al.* (2003). However, optical and microphysical properties of BBA were comparably variable in the dry season 2008 as a result of different burning types, different transport times, different aging processes etc. For example, typical lidar ratios at 532 nm ranged between 60 and 80 sr. The analysis of the extinction-related Ångström exponent revealed that the smoke which arrived at the lidar site was usually aged by more than one day. This result corroborates findings from sun photometer measurements made in Brazil during

the dry season in the 1990s (*Holben et al.*, 1996b).

The results of the first long-term observations of height-resolved aerosol properties in the entire Amazon Basin presented here are promising and valuable for the understanding of aerosol effects on climate. Nevertheless, more long-term measurements at several locations are needed in this area which is half as large as Europe. For example, there is still a lack of knowledge how far African aerosol is advected into the Amazon Basin and how the smoke of vegetation fires in South America is distributed in entire Amazonia. The effects of in-cloud processing and wet scavenging on the aerosol during such transport events are rather unknown. Thus, investigations of the effectiveness of cloud and precipitation events on particle removal from the atmosphere should be one main focus of future research in Amazonia.

The Amazon Basin is one of a few continental regions in the world where warm precipitation (rain without ice phase) can occur. The strong contrast in the aerosol conditions between the wet and dry season – as was shown in this thesis – under similar meteorological conditions (compared to the mid-latitudes) thus favors future investigations of the effect of aerosol on clouds and precipitation (indirect aerosol effect) in this part of the world. Furthermore, the pronounced regional differences in the aerosol load during the dry season allow the study of microphysical cloud properties in a disturbed and undisturbed atmosphere under the same meteorological conditions. The Amazon Basin is thus an exquisite laboratory for future investigations of aerosol-cloud-climate interactions.

Appendix

A Optical properties of atmospheric molecules

For the determination of the molecular backscatter and extinction coefficient, the vertical profiles of pressure and temperature are needed. If no radiosonde data is available, these profiles are calculated according to the US standard atmosphere (*Eltermann*, 1968). For the cases shown in this work, a sounding from Manaus airport was always available, but for completeness the formulae are given in the following.

The temperature T at the height z is given by

$$T = T_0 - 0.0065H, \quad (8.1)$$

where H is the geopotential height

$$H = \frac{6356766z}{6356766 + z}. \quad (8.2)$$

This allows the calculation of the pressure p by

$$p = p_0 \exp \left(\frac{9.80665}{287.05072 (-0.0065)} \ln \frac{T_0}{T} \right). \quad (8.3)$$

Here T_0 and p_0 are the temperature and pressure at surface level.

Having vertical profiles of T and p , the calculation of optical properties follows (*Bucholtz*, 1995). First, the refractive index of air n_s is calculated by

$$(n_s - 1) 10^8 = \frac{5791817}{238.0185 - \lambda^{-2}} + \frac{167909}{57.362 - \lambda^{-2}}, \quad (8.4)$$

where λ is given in μm . The Rayleigh cross section σ is then determined by

$$\sigma = \left(\frac{24\pi^3 (n_s^2 - 1)^2}{\lambda^4 N_s^2 (n_s^2 + 2)^2} \right) \left(\frac{6 + 3d_{\text{mol}}}{6 - 7d_{\text{mol}}} \right). \quad (8.5)$$

Here, λ is given in cm. d_{mol} is the wavelength-dependent molecular depolarization factor of air, and N_s is the molecular number density for standard conditions at $p_s = 1013.25$ hPa and $T_s = 288$ K. For d_{mol} , values as listed in *Bucholtz (1995)* are used. This yields to the molecular extinction coefficient

$$\alpha_{\lambda}^{\text{mol}}(z) = \sigma N(z) = \sigma N_s \frac{T_s p(z)}{T(z) p_s}. \quad (8.6)$$

$N(z)$ is the number density of molecules at the height z . The molecular backscatter coefficient is finally calculated by

$$\beta_{\lambda}^{\text{mol}}(z) = \alpha_{\lambda}^{\text{mol}}(z) S^{\text{mol}}, \quad (8.7)$$

with the molecular lidar ratio (*Miles et al., 2001*)

$$S^{\text{mol}} = \frac{8\pi}{3} \left(1 + \frac{d_{\text{mol}}}{2} \right) \text{sr}. \quad (8.8)$$

B Dark measurement test

Correct photon counting and correct background subtraction are essential for the determination of high-quality aerosol properties from lidar measurements. Figure 8.1 illustrates the setup for photon counting in Polly^{XT} from the optical detection to the electronic counting. First, the PMT converts the detected photons to electronic



Figure 8.1: Schematic illustration of electronic devices for photon detection in Polly^{XT}.

pulses. These pulses are amplified by a preamplifier (Model: Philips Scientific Fast Pulse Preamplifier 6954), before they are counted by the DAQ (Model: Fast ComTec 7882). In the 1064 nm channel, photon counting is performed without a preamplifier. Hence, the counting of backscattered photons is not only an optical issue (i.e., the adjustment of the optical units) but also an electronic one.

During the operation of Polly^{XT}, it was found that this counting setup is sensible to laser-induced electromagnetic pulses. To assure correct counting by the DAQ, the discriminator (threshold) levels of the DAQ have to be set in such a way that almost no noise but all photon-induced pulses are counted. These levels are threshold voltages

that have to be exceeded before a single pulse is counted.

Therefore, several so-called dark measurement tests were performed in Brazil. For these tests, the laser beam is dumped so that no light is emitted into the atmosphere and only background light is measured. The data is recorded under usual atmospheric conditions by the DAQ. For an ideal system, the counting of the range-independent background light should give a straight line at a certain background value in the vertical profile of the raw signal. Example results from such a dark measurement test with Polly^{XT} for different discriminator levels are shown in Fig. 8.2. Obviously, in some channels the achieved straight line could not be observed for all discriminator levels, e.g., in the UV channels for a threshold of -5 mV or in the 607 nm channel for -10 mV. Hence, no height-independent background is measured during real measurements when these wrong discriminator levels are used. This causes problems in the data retrieval due to wrong background subtraction.

During the campaign in Brazil, several background tests were performed until the final adjustments were found. Discriminator levels of -15 , -15 , -20 , -55 , -20 , and -32 mV for the 355, 355s, 387, 532, 607, and 1064 channel, respectively, have been used to minimize these electronic problems.

The dark measurements for these levels are shown in the lower right panel in Fig. 8.2. A straight line and thus height-independent background was observed for all channels. The increased signal in the lowermost profile of the 1064 channel is most obviously caused by an incomplete laser beam dumping and thus is caused by reflected light. Hence, height-independent background is also measured for the this channel.

C Laser polarization characterization

The manufacturer of the laser used in Polly^{XT} states that the emitted light is completely linear-polarized. Nevertheless, a test was performed to check this issue. Since we use several optical elements until the laser beam is emitted into the atmosphere, it is necessary to characterize the laser beam after it has passed all optical units. Therefore, the apparatus to measure the polarization properties was installed behind the quartz plate on the roof of the lidar (see Fig. 3.4).

Figure 8.3 shows a photo of the measurement setup. The polarization characteristics of the emitted light were measured as follows: First, the laser beam (already expanded to 55 mm diameter) was attenuated by a neutral-density filter to protect the optical elements in the apparatus. Afterwards, the light beam passed an adjustable polariza-

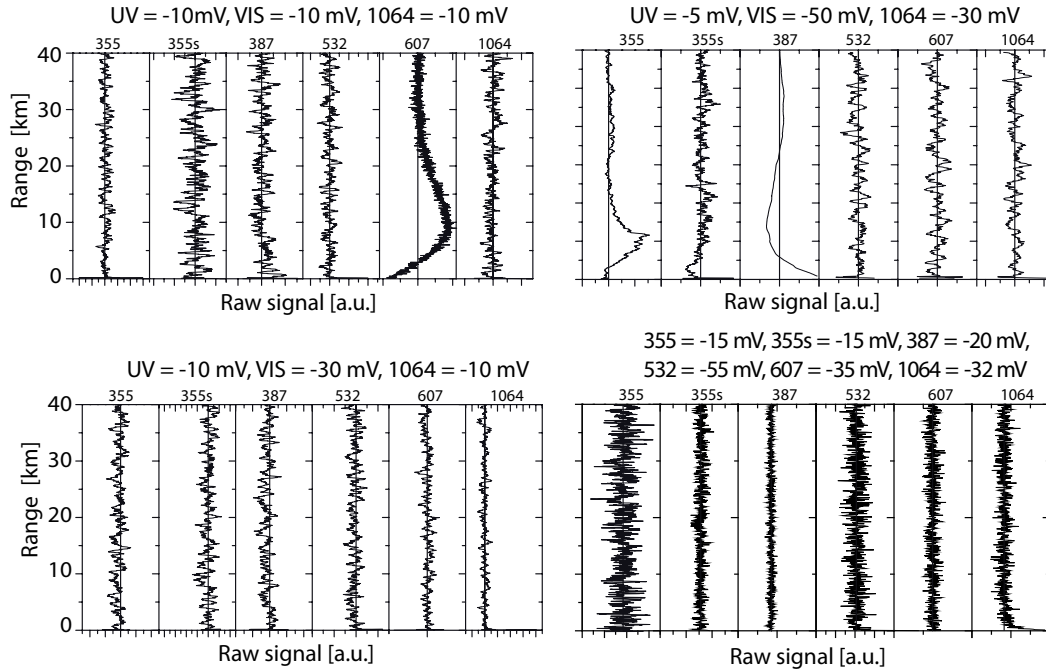


Figure 8.2: Dark measurement performed with Polly^{XT} in Brazil on 26 and 29 February and 28 July 2008. Vertical profiles of raw signals for the six photon-counting channels are shown. The discriminator levels for the channels are given at the top of each plot. UV: 355, 355s, and 387 channel. VIS: 532 and 607 channel.

tion filter that allows only light of one certain polarization plane to pass. The filter is rotatable via a remotely controlled motor so that all possible polarization planes could be set. Behind this filter, the beam had to pass an interference filter to measure only the investigated wavelength (either 355 or 532 nm). The laser power for the different polarization angles was then measured with a commercial power meter. The interference filter had to be changed for the measurement at a different wavelength. Hence, the apparatus had to be removed for filter changing. During this procedure, no focus was put on identical replacements of the apparatus since this is not necessary for data analysis. Consequently, the measured polarization-plane angle (with respect to the motor control) is shifted between the two wavelengths. For the experiment, the polarization plane of the polarization filter was changed from 0° to 350° . The received laser power was then measured for several angles.

Figure 8.4 shows the result of the performed test for both wavelengths. A very clear dependence of the laser power to the polarization plane was observed. Thus, a high purity of polarization of the emitted laser beam can be expected. To retrieve the polarization purity of the laser for the different wavelengths, a \sin^2 function was fitted

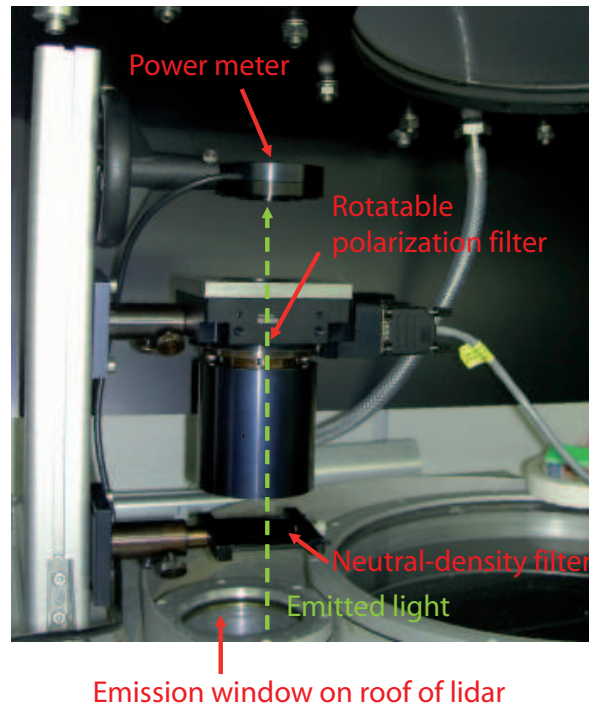


Figure 8.3: Apparatus for the determination of the polarization characteristics of the emitted laser light. The apparatus was installed on the roof of the Polly^{XT}.

to the determined curves. If one considers measurement errors of the power-meter of the order of 0.5 mW, a polarization purity of the emitted light of better than 95% is resulting from the measurements at both wavelengths. Most probably, the purity is even better, but the high measurement errors at very low light power (when the polarization plane of the apparatus is perpendicular to the laser polarization plane) made it impossible to specify values better than 95%. However, a purity of 100% is most probably not achieved as the calibration to cirrus clouds showed (cf. Sec. 5.2).

D NMMB/BSC-Dust

The dust load in Amazonia was analyzed by using data from NMMB/BSC-Dust (Pérez *et al.*, 2011; Haustein *et al.*, 2011). NMMB/BSC-Dust is a new multi-scale online dust model for regional and global simulations. The dust model is embedded into the dynamical Non-hydrostatic Multiscale Model NMMB (Janjic, 2003; Janjic and Black, 2006; Janjic *et al.*, 2011). NMMB/BSC-Dust can be regarded as the follow-up model of BSC-DREAM (Nickovic *et al.*, 2001; Pérez *et al.*, 2006) which is already well

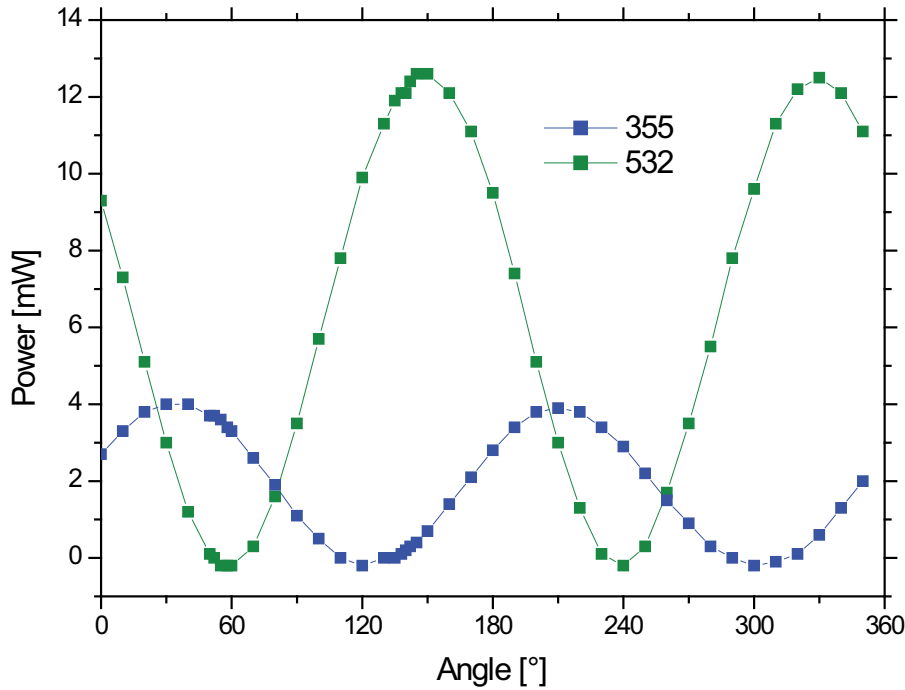


Figure 8.4: Results from the polarization test of the emitted laser light at 355 (blue) and 532 nm (green). The dependence of the laser power on the polarization plane is shown. Shifts in phase between 355 and 532 nm are due to different positions of the apparatus during the experiment.

established in the scientific community (e.g., *Haustein et al.*, 2009). For the global simulation used here, the horizontal and vertical resolution is $1^\circ \times 1.4^\circ$ and 40 levels, respectively.

NMMB/BSC-Dust takes into account the following processes (*Pérez et al.*, 2011):

1. dust generation by surface wind and turbulence,
2. horizontal and vertical advection,
3. horizontal diffusion and vertical transport by turbulence and convection,
4. dry deposition and gravitational settling,
5. wet removal which includes in-cloud and below-cloud scavenging by convective and stratiform clouds.

For the emission of dust, input data of surface wind speed, land-use type, vegetation cover, source erodibility (topographic preferential sources after *Ginoux et al.*, 2001), aerodynamic surface roughness, soil texture, and soil moisture are required (*Pérez*

et al., 2011). For dust transport, eight transport size bins with time-invariant, sub-bin log-normal distribution are applied in the model (*Zender et al.*, 2003). The model covers a dust particle size range (radius) from 0.1–10 μm . The dust radiative feedback can be interactively simulated. Wet deposition and precipitation-related mixing of dust is computed separately for convective and stratiform precipitation. In addition, below-cloud scavenging is taken into account.

All NMMB/BSC-Dust computations for this work were provided by the Barcelona Supercomputing Center¹. The global model NMMB was initialized with meteorological fields of the NCEP/NCAR global reanalysis ($2.5^\circ \times 2.5^\circ$ resolution), updated every 24 hours and with 12 hours spin-up. Results are shown in Sec. 6.1.

¹data kindly provided by Karsten Haustein, Barcelona Supercomputing Center, Spain (Email: karsten.haustein@bsc.es)

Bibliography

- Ångström, A. (1964), The parameters of atmospheric turbidity, *Tellus*, *16*, 64–75.
- Ahlm, L., E. D. Nilsson, R. Krejci, E. M. Mårtensson, M. Vogt, and P. Artaxo (2009), Aerosol number fluxes over the Amazon rain forest during the wet season, *Atmospheric Chemistry and Physics*, *9*, 9381–9400, doi:10.5194/acp-9-9381-2009.
- Althausen, D., R. Engelmann, H. Baars, B. Heese, A. Ansmann, D. Müller, and M. Komppula (2009), Portable Raman lidar PollyXT for automated profiling of aerosol backscatter, extinction, and depolarization, *Journal of Atmospheric and Oceanic Technology*, *26*, 2366–2378, doi:10.1175/2009JTECHA1304.1.
- Andreae, M. O., E. V. Browell, G. L. Gregory, R. C. Harriss, G. F. Hill, G. W. Sachse, R. W. Talbot, M. Garstang, D. J. Jacob, and A. L. Torres (1988), Biomass-burning emissions and associated haze layers over Amazonia, *Journal of Geophysical Research*, *93*, 1509–1527, doi:10.1029/JD093iD02p01509.
- Andreae, M. O. (1991), Biomass burning – Its history, use, and distribution and its impact on environmental quality and global climate, in *Global Biomass Burning, Atmospheric, Climatic, and Biospheric Implications*, edited by J. S. Levine, pp. 403–411, MIT Press, Cambridge, Mass.
- Andreae, M. O., P. Artaxo, H. Fischer, S. R. Freitas, J. Grégoire, A. Hansel, P. Hoor, R. Kormann, R. Krejci, L. Lange, J. Lelieveld, W. Lindinger, K. Longo, W. Peters, M. de Reus, B. Scheeren, M. A. F. Silva Dias, J. Ström, P. F. J. van Velthoven, and J. Williams (2001), Transport of biomass burning smoke to the upper troposphere by deep convection in the equatorial region, *Geophysical Research Letters*, *28*, 951–954, doi:10.1029/2000GL012391.
- Andreae, M. O., P. Artaxo, C. Brandão, F. E. Carswell, P. Ciccioli, A. L. da Costa, A. D. Culf, J. L. Esteves, J. H. C. Gash, J. Grace, P. Kabat, J. Lelieveld, Y. Malhi,
-

- A. O. Manzi, F. X. Meixner, A. D. Nobre, C. Nobre, M. d. L. P. Ruivo, M. A. Silva-Dias, P. Stefani, R. Valentini, J. von Jouanne, and M. J. Waterloo (2002), Biogeochemical cycling of carbon, water, energy, trace gases, and aerosols in Amazonia: The LBA-EUSTACH experiments, *Journal of Geophysical Research*, *107*, 8066, doi:10.1029/2001JD000524.
- Andreae, M. O., D. Rosenfeld, P. Artaxo, A. A. Costa, G. P. Frank, K. M. Longo, and M. A. F. Silva-Dias (2004), Smoking rain clouds over the Amazon, *Science*, *303*, 1337–1342.
- Ansmann, A., M. Riebesell, and C. Weitkamp (1990), Measurement of atmospheric aerosol extinction profiles with a Raman lidar, *Optics Letters*, *15*, 746–748.
- Ansmann, A., U. Wandinger, M. Riebesell, C. Weitkamp, and W. Michaelis (1992), Independent measurement of extinction and backscatter profiles in cirrus clouds by using a combined Raman elastic-backscatter lidar, *Applied Optics*, *31*, 7113–7131, doi:10.1364/AO.31.007113.
- Ansmann, A., F. Wagner, D. Althausen, D. Müller, A. Herber, and U. Wandinger (2001), European pollution outbreaks during ACE 2: Lofted aerosol plumes observed with Raman lidar at the Portuguese coast, *Journal of Geophysical Research*, *106*, 20725–20734, doi:10.1029/2000JD000091.
- Ansmann, A., F. Wagner, D. Müller, D. Althausen, A. Herber, W. von Hoyningen-Huene, and U. Wandinger (2002), European pollution outbreaks during ACE 2: Optical particle properties inferred from multiwavelength lidar and star-sun photometry, *Journal of Geophysical Research*, *107*, 4259, doi:10.1029/2001JD001109.
- Ansmann, A., and D. Müller (2005), Lidar and Atmospheric Aerosol Particles, in *Lidar – Range-Resolved Optical Remote Sensing of the Atmosphere*, Springer Series in Optical Sciences, vol. 102, edited by C. Weitkamp, pp. 105–141, Springer Berlin/Heidelberg.
- Ansmann, A., H. Baars, M. Tesche, D. Müller, D. Althausen, R. Engelmann, T. Pauliquevis, and P. Artaxo (2009), Dust and smoke transport from Africa to South America: Lidar profiling over Cape Verde and the Amazon rainforest, *Geophysical Research Letters*, *36*, L11802, doi:10.1029/2009GL037923.
-

- Ansmann, A., A. Petzold, K. Kandler, I. Tegen, M. Wendisch, D. Müller, B. Weinzierl, T. Müller, and J. Heintzenberg (2011), Saharan Mineral Dust Experiments SAMUM-1 and SAMUM-2: What have we learned?, *Tellus B*, *63*, 403–429, doi:10.1111/j.1600-0889.2011.00555.x.
- Araújo, A. C., A. D. Nobre, B. Kruijt, J. A. Elbers, R. Dallarosa, P. Stefani, C. von Randow, A. O. Manzi, A. D. Culf, J. H. C. Gash, R. Valentini, and P. Kabat (2002), Comparative measurements of carbon dioxide fluxes from two nearby towers in a central Amazonian rainforest: The Manaus LBA site, *Journal of Geophysical Research*, *107*, 8090, doi:10.1029/2001JD000676.
- Artaxo, P., and C. Orsini (1987), PIXE and receptor models applied to remote aerosol source apportionment in Brazil, *Nuclear Instruments and Methods in Physics Research B*, *22*, 259–263, doi:10.1016/0168-583X(87)90339-9.
- Artaxo, P., H. Storms, F. Bruynseels, R. van Grieken, and W. Maenhaut (1988), Composition and sources of aerosols from the Amazon Basin, *Journal of Geophysical Research*, *93*, 1605–1615, doi:10.1029/JD093iD02p01605.
- Artaxo, P., W. Maenhaut, H. Storms, and R. van Grieken (1990), Aerosol characteristics and sources for the Amazon Basin during the wet season, *Journal of Geophysical Research*, *95*, 16971–16985, doi:10.1029/JD095iD10p16971.
- Artaxo, P., and W. Maenhaut (1990), Trace element concentrations and size distribution of biogenic aerosols from the Amazon Basin during the wet season, *Nuclear Instruments and Methods in Physics Research B*, *49*, 366–371, doi:10.1016/0168-583X(90)90277-2.
- Artaxo, P., M. Yamasoe, J. V. Martins, S. Kocinas, S. Carvalho, and W. Maenhaut (1993), Case study of atmospheric measurements in Brazil: Aerosol emissions from Amazon Basin fires, in *Fire in the Environment: The Ecological, Atmospheric, and Climatic Importance of Vegetation Fires*, edited by P. J. Crutzen and J. G. Goldammer, pp. 139–158, John Wiley, New York.
- Artaxo, P., F. Gerab, M. Yamasoe, and J. Martins (1994), Fine mode aerosol composition at three long-term atmospheric monitoring sites in the Amazon Basin, *Journal of Geophysical Research*, *99*, 22857.
- Artaxo, P., and H. Hansson (1995), Size distribution of biogenic aerosol particles from the Amazon Basin, *Atmospheric Environment*, *29*, 393–402.
-

- Artaxo, P., J. V. Martins, M. A. Yamasoe, A. S. Procopio, T. M. Pauliquevis, M. O. Andreae, P. Guyon, L. V. Gatti, and A. M. C. Leal (2002), Physical and chemical properties of aerosols in the wet and dry seasons in Rondônia, Amazonia, *Journal of Geophysical Research*, *107*, 8081, doi:10.1029/2001JD000666.
- Artaxo, P., L. Rizzo, M. Paixo, K. Wiedemann, F. Morais, A. C. Ribeiro, A. L. Loureiro, A. Wiedensohler, E. Swietlicki, E. Vignati, S. Gilardoni, H. Baars, A. Andreae, and S. Martin (2010), Aerosols in the Amazon Basin: Results from EU-CAARI, in *EUCAARI Final meeting, Helsinki, 23 Nov. 2010*.
- Baars, H. (2007), Continuous monitoring of the planetary-boundary-layer depth with lidar, Diploma thesis, pp. 63, University of Leipzig.
- Baars, H., A. Ansmann, R. Engelmann, and D. Althausen (2008), Continuous monitoring of the boundary-layer top with lidar, *Atmospheric Chemistry and Physics*, *8*, 7281–7296.
- Baars, H., D. Althausen, R. Engelmann, A. Ansmann, D. Müller, P. Artaxo, T. Pauliquevis, R. Souza, and S. T. Martin (2009), Automated Raman lidar measurements in the Amazon rain forest during the wet and dry season 2008, in *Proceedings of the eighth edition of the International Symposium on Tropospheric Profiling*, S04–O02, Delft, The Netherlands, 18–23 October 2009, ISBN 978-90-6960-233-2.
- Baars, H., A. Ansmann, D. Althausen, R. Engelmann, P. Artaxo, T. Pauliquevis, and R. Souza (2011), Further evidence for significant smoke transport from Africa to Amazonia, *Geophysical Research Letters*, *38*, L20802, doi:10.1029/2011GL049200.
- Barthem, R. B., P. Charvet-Almeida, L. F. A. Montag, and A. Lanna (2004), *Amazon Basin, GIWA Regional assessment 40b*, UNEP, University of Kalmar, Kalmar, Sweden, ISSN 1651-9402.
- Behrendt, A., and T. Nakamura (2002), Calculation of the calibration constant of polarization lidar and its dependency on atmospheric temperature, *Optics Express*, *10*, 805–817.
- Ben-Ami, Y., I. Koren, Y. Rudich, P. Artaxo, S. T. Martin, and M. O. Andreae (2010), Transport of North African dust from the Bodélé depression to the Amazon Basin: a case study, *Atmospheric Chemistry and Physics*, *10*, 7533–7544, doi:10.5194/acp-10-7533-2010.
-

- Böckmann, C., U. Wandinger, A. Ansmann, J. Bösenberg, V. Amiridis, A. Boselli, A. Delaval, F. de Tomasi, M. Frioud, I. V. Grigorov, A. Hågård, M. Horvat, M. Iarlori, L. Komguem, S. Kreipl, G. Larchevêque, V. Matthias, A. Papayannis, G. Pappalardo, F. Rocadenbosch, J. A. Rodrigues, J. Schneider, V. Shcherbakov, and M. Wiegner (2004), Aerosol lidar intercomparison in the framework of the EARLINET project. 2. Aerosol backscatter algorithms, *Applied Optics*, *43*, 977–989, doi:10.1364/AO.43.000977.
- Böckmann, C., and G. Pappalardo (2007), Report on the inter-comparison of algorithms for new stations, *Tech. Rep. Contract number: RICA-CT-2006-025991 Deliverable D3.2*, EARLINET ASOS (European Aerosol Research Lidar Network: Advanced Sustainable Observation System).
- Bohren, C. F., and D. R. Huffman (1983), *Absorption and Scattering of Light by Small Particles*, 530 pp., John Wiley.
- Bowman, D. M. J. S., J. K. Balch, P. Artaxo, W. J. Bond, J. M. Carlson, M. A. Cochrane, C. M. D’Antonio, R. S. DeFries, J. C. Doyle, S. P. Harrison, F. H. Johnston, J. E. Keeley, M. A. Krawchuk, C. A. Kull, J. B. Marston, M. A. Moritz, I. C. Prentice, C. I. Roos, A. C. Scott, T. W. Swetnam, G. R. van der Werf, and S. J. Pyne (2009), Fire in the Earth System, *Science*, *324*, 481–484, doi:10.1126/science.1163886.
- Bristow, C. S., K. A. Hudson-Edwards, and A. Chappell (2010), Fertilizing the Amazon and equatorial Atlantic with West African dust, *Geophysical Research Letters*, *37*, L14807, doi:10.1029/2010GL043486.
- Browell, E. V., A. F. Carter, S. T. Shipley, R. J. Allen, C. F. Butler, M. N. Mayo, J. H. Siviter, Jr., and W. M. Hall (1983), NASA multipurpose airborne DIAL system and measurements of ozone and aerosol profiles, *Applied Optics*, *22*, 522–534, doi:10.1364/AO.22.000522.
- Browell, E. V., G. L. Gregory, R. C. Harriss, and V. W. J. H. Kirchhoff (1988), Tropospheric ozone and aerosol distributions across the Amazon Basin, *Journal of Geophysical Research*, *93*, 1431–1451, doi:10.1029/JD093iD02p01431.
- Bucholtz, A. (1995), Rayleigh-scattering calculations for the terrestrial atmosphere, *Applied Optics*, *34*, 2765–2773.
-

- Butler, C., E. Browell, R. Ferrare, J. Hair, S. Ismail, V. Brackett, M. Fenn, A. Notari, S. Kooi, and S. Burton (2003), Aerosol types and characteristics measured with airborne lidar during INTEX-NA, in *23th International Laser Radar Conference (ILRC)*, Nara, Japan, 24–28 July 2003.
- Cairo, F., G. di Donfrancesco, A. Adriani, L. Pulvirenti, and F. Fierli (1999), Comparison of various linear depolarization parameters measured by lidar, *Applied Optics*, *38*, 4425–4432, doi:10.1364/AO.38.004425.
- Chand, D., P. Guyon, P. Artaxo, O. Schmid, G. P. Frank, L. V. Rizzo, O. L. Mayol-Bracero, L. V. Gatti, and M. O. Andreae (2006), Optical and physical properties of aerosols in the boundary layer and free troposphere over the Amazon Basin during the biomass burning season, *Atmospheric Chemistry and Physics*, *6*, 2911–2925.
- Chen, Q., D. K. Farmer, J. Schneider, S. R. Zorn, C. L. Heald, T. G. Karl, A. Guenther, J. D. Allan, N. Robinson, H. Coe, J. R. Kimmel, T. Pauliquevis, S. Borrmann, U. Pöschl, M. O. Andreae, P. Artaxo, J. L. Jimenez, and S. T. Martin (2009), Mass spectral characterization of submicron biogenic organic particles in the Amazon Basin, *Geophysical Research Letters*, *36*, L20806, doi:10.1029/2009GL039880.
- Davies, D. K., S. Ilavajhala, M. M. Wong, and C. O. Justice (2009), Fire Information for Resource Management System: Archiving and distributing MODIS active fire data, *IEEE Transactions on Geoscience and Remote Sensing*, *47*, 72–79, doi:10.1109/TGRS.2008.2002076.
- Donovan, D., J. Whiteway, and A. Carswell (1993), Correction for nonlinear photon-counting effects in lidar systems, *Applied Optics*, *32*, 6742–6753.
- Draxler, R. R., and G. D. Hess (1998), An overview of the HYSPLIT4 modelling system for trajectories, dispersion, and deposition, *Australian Meteorological Magazine*, *47*, 295–308.
- Draxler, R. R., B. Stunder, G. D. Rolph, A. Stein, and A. Taylor (2009), HYSPLIT4 user’s guide. Access via NOAA ARL READY Website (<http://www.arl.noaa.gov/ready/hysplit4.html>), *NOAA Air Resources Laboratory, Silver Spring, MD*.
- Draxler, R. R., and G. D. Rolph (2011), HYSPLIT (HYbrid Single-Particle Lagrangian Integrated Trajectory) Model access via NOAA ARL READY Website
-

- (<http://ready.arl.noaa.gov/HYSPLIT.php>), *NOAA Air Resources Laboratory, Silver Spring, MD*.
- Dubovik, O., B. N. Holben, Y. J. Kaufman, M. Yamasoe, A. Smirnov, D. Tanré, and I. Slutsker (1998), Single-scattering albedo of smoke retrieved from the sky radiance and solar transmittance measured from ground, *Journal of Geophysical Research*, *103*, 31903–31923.
- Dubovik, O., B. Holben, T. F. Eck, A. Smirnov, Y. J. Kaufman, M. D. King, D. Tanré, and I. Slutsker (2002), Variability of absorption and optical properties of key aerosol types observed in worldwide locations, *Journal of Atmospheric Sciences*, *59*, 590–608, doi:10.1175/1520-0469(2002)059.
- Eck, T. F., B. N. Holben, I. Slutsker, and A. Setzer (1998), Measurements of irradiance attenuation and estimation of aerosol single scattering albedo for biomass burning aerosols in Amazonia, *Journal of Geophysical Research*, *103*, 31865–31878, doi:10.1029/98JD00399.
- Eck, T. F., B. N. Holben, J. S. Reid, N. T. O'Neill, J. S. Schafer, O. Dubovik, A. Smirnov, M. A. Yamasoe, and P. Artaxo (2003), High aerosol optical depth biomass burning events: A comparison of optical properties for different source regions, *Geophysical Research Letters*, *30*, 2035, doi:10.1029/2003GL017861.
- Eltermann, L. (1968), UV, visible, and IR attenuation for altitudes to 50 km, *Environmental Research Papers No. 285*, pp. 49, Air Force Cambridge Research Laboratories.
- Ferek, R. J., J. S. Reid, P. V. Hobbs, D. R. Blake, and C. Liou (1998), Emission factors of hydrocarbons, halocarbons, trace gases and particles from biomass burning in Brazil, *Journal of Geophysical Research*, *103*, 32107–32118, doi:10.1029/98JD00692.
- Fernald, F. G. (1984), Analysis of atmospheric lidar observations: some comments, *Applied Optics*, *23*, 652–653.
- Fiebig, M., A. Stohl, M. Wendisch, S. Eckhardt, and A. Petzold (2003), Dependence of solar radiative forcing of forest fire aerosol on ageing and state of mixture, *Atmospheric Chemistry and Physics*, *3*, 881–891.
- Fisch, G., J. Tota, L. A. T. Machado, M. A. F. Silva Dias, R. F. da F. Lyra, C. A. Nobre, A. J. Dolman, and J. H. C. Gash (2004), The convective boundary layer
-

- over pasture and forest in Amazonia, *Theoretical and Applied Climatology*, *78*, 47–59, doi:10.1007/s00704-004-0043-x.
- Fishman, J., J. M. Hoell, R. D. Bendura, R. J. McNeal, and V. W. J. H. Kirchhoff (1996), NASA GTE TRACE A Experiment (September–October 1992): Overview, *Journal of Geophysical Research*, *101*, 23865–23880, doi:10.1029/96JD00123.
- Formenti, P., M. O. Andreae, L. Lange, G. Roberts, J. Cafmeyer, I. Rajta, W. Maenhaut, B. N. Holben, P. Artaxo, and J. Lelieveld (2001), Saharan dust in Brazil and Suriname during the Large-Scale Biosphere-Atmosphere Experiment in Amazonia (LBA)–Cooperative LBA Regional Experiment (CLAIRE) in March 1998, *Journal of Geophysical Research*, *106*, 14919–14934, doi:10.1029/2000JD900827.
- Freitas, S. R., K. M. Longo, and M. O. Andreae (2006), Impact of including the plume rise of vegetation fires in numerical simulations of associated atmospheric pollutants, *Geophysical Research Letters*, *33*, L17808, doi:10.1029/2006GL026608.
- Freitas, S. R., K. M. Longo, R. Chatfield, D. Latham, M. A. F. Silva Dias, M. O. Andreae, E. Prins, J. C. Santos, R. Gielow, and J. A. Carvalho Jr. (2007), Including the sub-grid scale plume rise of vegetation fires in low resolution atmospheric transport models, *Atmospheric Chemistry and Physics*, *7*, 3385–3398.
- Freitas, S. R., K. M. Longo, M. A. F. Silva Dias, R. Chatfield, P. Silva Dias, P. Artaxo, M. O. Andreae, G. Grell, L. F. Rodrigues, A. Fazenda, and J. Panetta (2009), The Coupled Aerosol and Tracer Transport model to the Brazilian developments on the Regional Atmospheric Modeling System (CATT-BRAMS) Part 1: Model description and evaluation, *Atmospheric Chemistry and Physics*, *9*, 2843–2861.
- Freud, E., D. Rosenfeld, M. O. Andreae, A. A. Costa, and P. Artaxo (2008), Robust relations between CCN and the vertical evolution of cloud drop size distribution in deep convective clouds, *Atmospheric Chemistry and Physics*, *8*, 1661–1675.
- Freudenthaler, V. (2008), The Telecover Test: A quality assurance tool for the optical part of a lidar system, in *24th International Laser Radar Conference (ILRC)*, 145–146, Boulder, CO, USA, 23–27 June 2008.
- Freudenthaler, V., M. Esselborn, M. Wiegner, B. Heese, M. Tesche, A. Ansmann, D. Müller, D. Althausen, M. Wirth, A. Fix, G. Ehret, P. Knippertz, C. Toledano,
-

- J. Gasteiger, M. Garhammer, and M. Seefeldner (2009), Depolarization ratio profiling at several wavelengths in pure Saharan dust during SAMUM 2006, *Tellus Series B*, *61*, 165–179, doi:10.1111/j.1600-0889.2008.00396.x.
- Freudenthaler, V., S. Gross, R. Engelmann, I. Mattis, U. Wandinger, G. Pappalardo, A. Amodeo, A. Giunta, G. D'Amico, A. Chaikovsky, F. Osipenko, A. Slesar, D. Nicolaie, L. Belegante, C. Talianu, I. Serikov, H. Linné, F. Jansen, K. Wilson, M. de Graaf, A. Apituley, T. Trickl, H. Giehl, and M. Adam (2010), EARLI09 - Direct inter-comparison of eleven EARLINET lidar systems, in *25th International Laser Radar Conference (ILRC)*, 891–894, St. Petersburg, Russia, 5–9 July 2010.
- Garstang, M., S. Greco, J. Scala, R. Swap, S. Ulanski, D. Fitzjarrald, D. Martin, E. Browell, M. Shipman, V. Connors, R. Harriss, and R. Talbot (1990), The Amazon Boundary-Layer Experiment (ABLE 2B): A meteorological perspective., *Bulletin of the American Meteorological Society*, *71*, 19–32.
- Giglio, L., J. Descloitres, C. O. Justice, and Y. J. Kaufman (2003), An enhanced contextual fire detection algorithm for MODIS, *Remote Sensing of Environment*, *87*, 273–282, doi:10.1016/S0034-4257(03)00184-6.
- Ginoux, P., M. Chin, I. Tegen, J. M. Prospero, B. Holben, O. Dubovik, and S. Lin (2001), Sources and distributions of dust aerosols simulated with the GO-CART model, *Journal of Geophysical Research*, *106*, 20255–20274, doi:10.1029/2000JD000053.
- Grein, M. (2006), Charakterisierung und Erweiterung der Empfängeroptik des IfT-Ramanlidars MARTHA für kombinierte Aerosol- und Wolkenmessungen, Diploma thesis, pp. 78, University of Leipzig.
- Groß, S., V. Freudenthaler, C. Toledano, M. Seefeldner, and M. Wiegner (2008), Mini-lidar measurements of particle depolarization and Raman scattering of Saharan dust and biomass burning at 355 nm during SAMUM 2, in *24th International Laser Radar Conference (ILRC)*, S04P–10, Boulder, CO, USA, 23–27 June 2008.
- Groß, S., M. Tesche, V. Freudenthaler, C. Toledano, M. Wiegner, A. Ansmann, D. Althausen, and M. Seefeldner (2011), Characterization of Saharan dust, marine aerosols and mixtures of biomass burning aerosols and dust by means of multi-wavelength depolarization and Raman measurements during SAMUM 2, *Tellus Series B*, *63*, 706–724, doi:10.1111/j.1600-0889.2011.00556.x.
-

- Gunthe, S. S., S. M. King, D. Rose, Q. Chen, P. Roldin, D. K. Farmer, J. L. Jimenez, P. Artaxo, M. O. Andreae, S. T. Martin, and U. Pöschl (2009), Cloud condensation nuclei in pristine tropical rainforest air of Amazonia: size-resolved measurements and modeling of atmospheric aerosol composition and CCN activity, *Atmospheric Chemistry and Physics*, *9*, 7551–7575.
- Guyon, P., B. Graham, J. Beck, O. Boucher, E. Gerasopoulos, O. L. Mayol-Bracero, G. C. Roberts, P. Artaxo, and M. O. Andreae (2003), Physical properties and concentration of aerosol particles over the Amazon tropical forest during background and biomass burning conditions, *Atmospheric Chemistry and Physics*, *3*, 951–967.
- Guyon, P., G. P. Frank, M. Welling, D. Chand, P. Artaxo, L. Rizzo, G. Nishioka, O. Kolle, H. Fritsch, M. A. F. Silva Dias, L. V. Gatti, A. M. Cordova, and M. O. Andreae (2005), Airborne measurements of trace gas and aerosol particle emissions from biomass burning in Amazonia, *Atmospheric Chemistry and Physics*, *5*, 2989–3002.
- Harriss, R. C., S. C. Wofsy, M. Garstang, E. V. Browell, L. C. B. Molion, R. J. McNeal, J. M. Hoell, R. J. Bendura, S. M. Beck, R. L. Navarro, J. T. Riley, and R. L. Snell (1988), The Amazon Boundary Layer Experiment (ABLE 2A): Dry season 1985, *Journal of Geophysical Research*, *93*, 1351–1360, doi:10.1029/JD093iD02p01351.
- Harriss, R. C., M. Garstang, S. C. Wofsy, S. M. Beck, R. J. Bendura, J. R. B. Coelho, J. W. Drewry, J. M. Hoell, P. A. Matson, R. J. McNeal, L. C. B. Molion, R. L. Navarro, V. Rabine, and R. L. Snell (1990), The Amazon Boundary Layer Experiment: Wet season 1987, *Journal of Geophysical Research*, *95*, 16721–16736, doi:10.1029/JD095iD10p16721.
- Haustein, K., C. Pérez, J. M. Baldasano, D. Müller, M. Tesche, A. Schladitz, M. Esselborn, B. Weinzierl, K. Kandler, and W. von Hoyningen-Huene (2009), Regional dust model performance during SAMUM 2006, *Geophysical Research Letters*, *36*, L03812, doi:10.1029/2008GL036463.
- Haustein, K., C. Pérez, J. M. Baldasano, O. Jorba, S. Basart, R. L. Miller, Z. Janjic, T. Black, S. Nickovic, M. C. Todd, and R. Washington (2011), Atmospheric dust modeling from meso to global scales with the online NMMB/BSC-Dust model – Part 2: Experimental campaigns in Northern Africa, *Atmospheric Chemistry and Physics Discussions*, *11*, 30273–30331, doi:10.5194/acpd-11-30273-2011.
-

- Haywood, J. M., and K. P. Shine (1997), Multi-spectral calculations of the direct radiative forcing of tropospheric sulphate and soot aerosols using a column model, *Quarterly Journal of the Royal Meteorological Society*, *123*, 1907–1930, doi:10.1002/qj.49712354307.
- Haywood, J. M., J. Pelon, P. Formenti, N. Bharmal, M. Brooks, G. Capes, P. Chazette, C. Chou, S. Christopher, H. Coe, J. Cuesta, Y. Derimian, K. Desboeufs, G. Greed, M. Harrison, B. Heese, E. J. Highwood, B. Johnson, M. Mallet, B. Marticorena, J. Marsham, S. Milton, G. Myhre, S. R. Osborne, D. J. Parker, J.-L. Rajot, M. Schulz, A. Slingo, D. Tanré, and P. Tulet (2008), Overview of the Dust and Biomass-burning Experiment and African Monsoon Multidisciplinary Analysis Special Observing Period-0, *Journal of Geophysical Research*, *113*, D00C17, doi:10.1029/2008JD010077.
- Heese, B., V. Freudenthaler, M. Seefeldner, and M. Wiegner (2002), POLIS - A new POrtable LIdar System for ground-based and airborne measurements of aerosols and clouds, in *Proceedings of the 21th International Laser Radar Conference (ILRC)*, pp. 71–74, Quebec, Canada, 8–12 July 2002.
- Heese, B., and M. Wiegner (2008), Vertical aerosol profiles from Raman polarization lidar observations during the dry season AMMA field campaign, *Journal of Geophysical Research*, *113*, D00C11, doi:10.1029/2007JD009487.
- Heintzenberg, J. (2009), The SAMUM-1 experiment over Southern Morocco: Overview and introduction, *Tellus Series B*, *61*, 2–11, doi:10.1111/j.1600-0889.2008.00403.x.
- Hinds, W. C. (1999), *Aerosol technology: Properties, behavior, and measurement of airborne particles*, 2nd ed., 483 pp., Wiley, New York.
- Holben, B. N., T. F. Eck, A. Setzer, I. Slutsker, A. Pereira, B. Markham, and J. V. Castle (1996a), Temporal and Spatial Variability of Aerosol Loading and Properties during the Amazon, North American Temperate, and Boreal Forest Burning Seasons, in *Biomass Burning and Global Change*, vol. 2, edited by J. S. Levine, pp. 618–636, The MIT Press.
- Holben, B. N., A. Setzer, T. F. Eck, A. Pereira, and I. Slutsker (1996b), Effect of dry-season biomass burning on Amazon basin aerosol concentrations and optical properties, 1992–1994, *Journal of Geophysical Research*, *101*, 19465–19482, doi:10.1029/96JD01114.
-

- Holben, B. N., D. Tanré, A. Smirnov, T. F. Eck, I. Slutsker, N. Abuhassan, W. W. Newcomb, J. S. Schafer, B. Chatenet, F. Lavenu, Y. J. Kaufman, J. V. Castle, A. Setzer, B. Markham, D. Clark, R. Frouin, R. Halthore, A. Karneli, N. T. O'Neill, C. Pietras, R. T. Pinker, K. Voss, and G. Zibordi (2001), An emerging ground-based aerosol climatology: Aerosol optical depth from AERONET, *Journal of Geophysical Research*, *106*, 12067–12098, doi:10.1029/2001JD900014.
- Hunt, W. H., D. M. Winker, M. A. Vaughan, K. A. Powell, P. L. Lucker, and C. Weimer (2009), CALIPSO lidar description and performance assessment, *Journal of Atmospheric and Oceanic Technology*, *26*, 1214–1228, doi:10.1175/2009JTECHA1223.1.
- IPCC (2007), *Climate Change 2007: The Physical Science Basis. Contribution of Working Group I to the Fourth Assessment Report of the Intergovernmental Panel on Climate Change*, 153–188, Cambridge University Press, Cambridge, United Kingdom and New York, NY, USA.
- Janjic, Z. I. (2003), A nonhydrostatic model based on a new approach, *Meteorology and Atmospheric Physics*, 271–285.
- Janjic, Z. I., and T. Black (2006), From global to mesoscales with a unified model, *Tech. rep.*, National Centers for Environmental Prediction (NCEP), ams.confex.com/ams/pdfpapers/93731.pdf, 30278.
- Janjic, Z., T. Janjic, and R. Vasic (2011), A class of conservative fourth-order advection schemes and impact of enhanced formal accuracy on extended-range forecasts, *Monthly Weather Review*, *139*, 1556–1568, doi:10.1175/2010MWR3448.1.
- Johnson, B. T., B. Heese, S. A. McFarlane, P. Chazette, A. Jones, and N. Bellouin (2008), Vertical distribution and radiative effects of mineral dust and biomass burning aerosol over West Africa during DABEX, *Journal of Geophysical Research*, *113*, D00C12, doi:10.1029/2008JD009848.
- Justice, C. O., L. Giglio, S. Korontzi, J. Owens, J. T. Morisette, D. Roy, J. Descloitres, S. Alleaume, F. Petitcolin, and Y. Kaufman (2002), The MODIS fire products, *Remote Sensing of Environment*, *83*, 244–262, doi:DOI:10.1016/S0034-4257(02)00076-7.
- Kanitz, T. (2011), personal communication.
-

- Kaufman, Y. J., A. Setzer, D. Ward, D. Tanré, B. N. Holben, P. Menzel, M. C. Pereira, and R. Rasmussen (1992), Biomass Burning Airborne and Spaceborne Experiment in the Amazonas (BASE-A), *Journal of Geophysical Research*, *97*, 14581–14599.
- Kaufman, Y. J., P. V. Hobbs, V. W. J. H. Kirchhoff, P. Artaxo, L. A. Remer, B. N. Holben, M. D. King, D. E. Ward, E. M. Prins, K. M. Longo, L. F. Mattos, C. A. Nobre, J. D. Spinhirne, Q. Ji, A. M. Thompson, J. F. Gleason, S. A. Christopher, and S. Tsay (1998a), Smoke, Clouds, and Radiation-Brazil (SCAR-B) experiment, *Journal of Geophysical Research*, *103*, 31783–31808, doi:10.1029/98JD02281.
- Kaufman, Y. J., R. G. Kleidman, and M. D. King (1998b), SCAR-B fires in the tropics: Properties and remote sensing from EOS-MODIS, *Journal of Geophysical Research*, *103*, 31955–31968, doi:10.1029/98JD02460.
- Kaufman, Y. J., I. Koren, L. A. Remer, D. Tanré, P. Ginoux, and S. Fan (2005), Dust transport and deposition observed from the Terra – Moderate Resolution Imaging Spectroradiometer (MODIS) spacecraft over the Atlantic Ocean, *Journal of Geophysical Research*, *110*, D10S12, doi:10.1029/2003JD004436.
- King, M. D., S. Tsay, S. A. Ackerman, and N. F. Larsen (1998), Discriminating heavy aerosol, clouds, and fires during SCAR-B: Application of airborne multispectral MAS data, *Journal of Geophysical Research*, *103*, 31989–32000, doi:10.1029/98JD01043.
- Klett, J. (1981), Stable analytical inversion solution for processing lidar returns, *Applied Optics*, *20*, 211–220.
- Koren, I., Y. J. Kaufman, L. A. Remer, and J. V. Martins (2004), Measurement of the effect of Amazon smoke on inhibition of cloud formation, *Science*, *303*, 1342–1345, doi:10.1126/science.1089424.
- Koren, I., Y. J. Kaufman, R. Washington, M. C. Todd, Y. Rudich, J. V. Martins, and D. Rosenfeld (2006), The Bodélé depression: a single spot in the Sahara that provides most of the mineral dust to the Amazon forest, *Environmental Research Letters*, *1*, 014005.
- Koren, I., J. V. Martins, L. A. Remer, and H. Afargan (2008), Smoke invigoration versus inhibition of clouds over the Amazon, *Science*, *321*, 946–949, doi:10.1126/science.1159185.
-

- Kotchenruther, R. A., and P. V. Hobbs (1998), Humidification factors of aerosols from biomass burning in Brazil, *Journal of Geophysical Research*, *103*, 32081–32090, doi:10.1029/98JD00340.
- Krejci, R., J. Ström, M. de Reus, P. Hoor, J. Williams, H. Fischer, and H. Hansson (2003), Evolution of aerosol properties over the rain forest in Surinam, South America, observed from aircraft during the LBA-CLAIRE 98 experiment, *Journal of Geophysical Research*, *108*, 4561, doi:10.1029/2001JD001375.
- Kuhn, U., L. Ganzeveld, A. Thielmann, T. Dindorf, G. Schebeske, M. Welling, J. Sciare, G. Roberts, F. X. Meixner, J. Kesselmeier, J. Lelieveld, O. Kolle, P. Ciccioli, J. Lloyd, J. Trentmann, P. Artaxo, and M. O. Andreae (2010), Impact of Manaus City on the Amazon Green Ocean atmosphere: ozone production, precursor sensitivity and aerosol load, *Atmospheric Chemistry and Physics*, *10*, 9251–9282, doi:10.5194/acp-10-9251-2010.
- Kulmala, M., A. Asmi, H. K. Lappalainen, K. S. Carslaw, U. Pöschl, U. Baltensperger, Ø. Hov, J.-L. Brenguier, S. N. Pandis, M. C. Facchini, H.-C. Hansson, A. Wiedensohler, and C. D. O’Dowd (2009), Introduction: European Integrated Project on Aerosol Cloud Climate and Air Quality interactions (EUCAARI) integrating aerosol research from nano to global scales, *Atmospheric Chemistry and Physics*, *9*, 2825–2841, doi:10.5194/acp-9-2825-2009.
- Kulmala, M., A. Asmi, H. K. Lappalainen, U. Baltensperger, J.-L. Brenguier, M. C. Facchini, H.-C. Hansson, Ø. Hov, C. D. O’Dowd, U. Pöschl, A. Wiedensohler, R. Boers, O. Boucher, G. de Leeuw, H. Denier van den Gon, J. Feichter, R. Krejci, P. Laj, H. Lihavainen, U. Lohmann, G. McFiggans, T. Mentel, C. Pilinis, I. Ripinen, M. Schulz, A. Stohl, E. Swietlicki, E. Vignati, M. Amann, M. Amann, C. Alves, S. Arabas, P. Artaxo, D. C. S. Beddows, R. Bergström, J. P. Beukes, M. Bilde, J. F. Burkhardt, F. Canonaco, S. Clegg, H. Coe, S. Crumeyrolle, B. D’Anna, S. Decesari, S. Gilardoni, M. Fischer, A. M. Fjæraa, C. Fountoukis, C. George, L. Gomes, P. Halloran, T. Hamburger, R. M. Harrison, H. Herrmann, T. Hoffmann, C. Hoose, M. Hu, U. Hörrak, Y. Iinuma, T. Iversen, M. Josipovic, M. Kanakidou, A. Kiendler-Scharr, A. Kirkevåg, G. Kiss, Z. Klimont, P. Kolmonen, M. Komppula, J.-E. Kristjánsson, L. Laakso, A. Laaksonen, L. Labonnote, V. A. Lanz, K. E. J. Lehtinen, R. Makkonen, G. McMeeking, J. Merikanto, A. Minikin, S. Mirme, W. T. Morgan, E. Nemitz, D. O’Donnell, T. S. Panwar, H. Pawlowska, A. Petzold,
-

- J. J. Pienaar, C. Pio, C. Plass-Duelmer, A. S. H. Prévôt, S. Pryor, C. L. Reddington, G. Roberts, D. Rosenfeld, J. Schwarz, Ø. Seland, K. Sellegri, X. J. Shen, M. Shiraiwa, H. Siebert, B. Sierau, D. Simpson, J. Y. Sun, D. Topping, P. Tunved, P. Vaattovaara, V. Vakkari, J. P. Veefkind, A. Visschedijk, H. Vuollekoski, R. Vuolo, B. Wehner, J. Wildt, S. Woodward, D. R. Worsnop, G.-J. van Zadelhoff, A. A. Zardini, K. Zhang, P. G. van Zyl, V.-M. Kerminen, K. S. Carslaw, and S. N. Pandis (2011), General overview: European Integrated project on Aerosol Cloud Climate and Air Quality interactions (EUCAARI) integrating aerosol research from nano to global scales, *Atmospheric Chemistry and Physics Discussions*, *11*, 17941–18160, doi:10.5194/acpd-11-17941-2011.
- Lenton, T. M., H. Held, E. Kriegler, J. W. Hall, W. Lucht, S. Rahmstorf, and H. J. Schellnhuber (2008), Inaugural Article: Tipping elements in the Earth's climate system, *Proceedings of the National Academy of Science*, *105*, 1786–1793, doi:10.1073/pnas.0705414105.
- Léon, J.-F., Y. Derimian, I. Chiapello, D. Tanré, T. Podvin, B. Chatenet, A. Diallo, and C. Deroo (2009), Aerosol vertical distribution and optical properties over M'Bour (16.96W; 14.39N), Senegal from 2006 to 2008, *Atmospheric Chemistry and Physics*, *9*, 9249–9261, doi:10.5194/acp-9-9249-2009.
- Longo, K. M., S. R. Freitas, M. O. Andreae, R. Yokelson, and P. Artaxo (2009), Biomass burning in Amazonia: emissions, long-range transport of smoke and its regional and remote impacts, in *Amazonia and Global Change, Geophysical Monograph Series*, vol. 186, edited by M. Keller, M. Bustamante, J. Gash, and P. S. Dias, 207–232, American Geophysical Union.
- Longo, K. M., S. R. Freitas, M. O. Andreae, A. Setzer, E. Prins, and P. Artaxo (2010), The Coupled Aerosol and Tracer Transport model to the Brazilian developments on the Regional Atmospheric Modeling System (CATT-BRAMS); Part 2: Model sensitivity to the biomass burning inventories, *Atmospheric Chemistry and Physics*, *10*, 5785–5795, doi:10.5194/acp-10-5785-2010.
- Lutgens, F. K., and E. J. Tarbuck (2010), *The Atmosphere – An Introduction to Meteorology*, 11th ed., 201 pp., Pearson Education.
- Martin, S. T., M. O. Andreae, P. Artaxo, D. Baumgardner, Q. Chen, A. H. Goldstein, A. Guenther, C. L. Heald, O. L. Mayol-Bracero, P. H. McMurry, T. Pauliquevis,
-

- U. Pöschl, K. A. Prather, G. C. Roberts, S. R. Saleska, M. A. Silva Dias, D. V. Spracklen, E. Swietlicki, and I. Trebs (2010a), Sources and properties of Amazonian aerosol particles, *Reviews of Geophysics*, *48*, doi:10.1029/2008RG000280.
- Martin, S. T., M. O. Andreae, D. Althausen, P. Artaxo, H. Baars, S. Borrmann, Q. Chen, D. K. Farmer, A. Guenther, S. S. Gunthe, J. L. Jimenez, T. Karl, K. Longo, A. Manzi, T. Müller, T. Pauliquevis, M. D. Petters, A. J. Prenni, U. Pöschl, L. V. Rizzo, J. Schneider, J. N. Smith, E. Swietlicki, J. Tota, J. Wang, A. Wiedensohler, and S. R. Zorn (2010b), An overview of the Amazonian Aerosol Characterization Experiment 2008 (AMAZE-08), *Atmospheric Chemistry and Physics*, *10*, 11415–11438, doi:10.5194/acp-10-11415-2010.
- Martins, J. V., P. V. Hobbs, R. E. Weiss, and P. Artaxo (1998), Sphericity and morphology of smoke particles from biomass burning in Brazil, *Journal of Geophysical Research*, *103*, 32051–32058, doi:10.1029/98JD01153.
- Mattis, I. (2002), Aufbau eines Feuchte-Temperatur-Aerosol-Ramanlidars und Methodenentwicklung zur kombinierten Analyse von Trajektorien und Aerosolprofilen., Ph.D. thesis, pp. 130, University of Leipzig.
- Mattis, I., A. Ansmann, D. Müller, U. Wandinger, and D. Althausen (2004), Multiyear aerosol observations with dual-wavelength Raman lidar in the framework of EARLINET, *Journal of Geophysical Research*, *109*, D13203, doi:10.1029/2004JD004600.
- Mattis, I., M. Tesche, M. Grein, V. Freudenthaler, and D. Müller (2009), Systematic error of lidar profiles caused by a polarization-dependent receiver transmission: Quantification and error correction scheme, *Applied Optics*, *48*, 2742–2751.
- Miles, R. B., W. R. Lempert, and J. N. Forkey (2001), Laser Rayleigh scattering, *Measurement Science and Technology*, *12*, 33–51, doi:10.1088/0957-0233/12/5/201.
- Müller, D., U. Wandinger, and A. Ansmann (1999a), Microphysical particle parameters from extinction and backscatter lidar data by inversion with regularization: Simulation, *Applied Optics*, *38*, 2358–2368, doi:10.1364/AO.38.002358.
- Müller, D., U. Wandinger, and A. Ansmann (1999b), Microphysical particle parameters from extinction and backscatter lidar data by inversion with regularization: Theory, *Applied Optics*, *38*, 2346–2357, doi:10.1364/AO.38.002346.
-

- Müller, D., U. Wandinger, D. Althausen, and M. Fiebig (2001), Comprehensive particle characterization from three-wavelength Raman-lidar observations: Case study, *Applied Optics*, *40*, 4863–4869.
- Müller, D., I. Mattis, U. Wandinger, A. Ansmann, D. Althausen, and A. Stohl (2005), Raman lidar observations of aged Siberian and Canadian forest fire smoke in the free troposphere over Germany in 2003: Microphysical particle characterization, *Journal of Geophysical Research*, *110*, D17201, doi:10.1029/2004JD005756.
- Müller, D., I. Mattis, A. Ansmann, U. Wandinger, C. Ritter, and D. Kaiser (2007a), Multiwavelength Raman lidar observations of particle growth during long-range transport of forest-fire smoke in the free troposphere, *Geophysical Research Letters*, *34*, L05803, doi:10.1029/2006GL027936.
- Müller, D., A. Ansmann, I. Mattis, M. Tesche, U. Wandinger, D. Althausen, and G. Pisani (2007b), Aerosol-type-dependent lidar ratios observed with Raman lidar, *Journal of Geophysical Research*, *112*, D16202, doi:10.1029/2006JD008292.
- Murayama, T., H. Okamoto, N. Kaneyasu, H. Kamataki, and K. Miura (1999), Application of lidar depolarization measurement in the atmospheric boundary layer: Effects of dust and sea-salt particles, *Journal of Geophysical Research*, *104*, 31781–31792, doi:10.1029/1999JD900503.
- Murayama, T., D. Müller, K. Wada, A. Shimizu, M. Sekiguchi, and T. Tsukamoto (2004), Characterization of Asian dust and Siberian smoke with multi-wavelength Raman lidar over Tokyo, Japan in spring 2003, *Geophysical Research Letters*, *31*, L23103, doi:10.1029/2004GL021105.
- Nepstad, D. C., C. M. Stickler, B. S. Soares-Filho, and Merry, F. (2008), Interactions among Amazon land use, forests and climate: prospects for a near-term forest tipping point, *Philosophical Transactions of the Royal Society B: Biological Sciences*, *363*, 1737–1746, doi:10.1098/rstb.2007.0036.
- Nickovic, S., G. Kallos, A. Papadopoulos, and O. Kakaliagou (2001), A model for prediction of desert dust cycle in the atmosphere, *Journal of Geophysical Research*, *106*, 18113–18130, doi:10.1029/2000JD900794.
- Nobre, C., G. Fisch, H. da Rocha, R. Lyra, E. da Rocha, and V. Ubarana (1996), Observations of the atmospheric boundary layer in Rondônia, in *Amazonian De-*
-

- forestation and Climate*, edited by J. Gash, C. Nobre, J. Roberts, and R. Victoria, 413–423, John Wiley, Chichester.
- Nobre, C. A., M. A. Silva Dias, A. Culf, J. Polcher, J. H. C. Gash, J. Marengo, and R. Avissar (2004), The Amazonian climate, in *Vegetation, Water, Humans and the Climate: A New Perspective on an Interactive System*, edited by P. Kabat, pp. 79–92, Springer, Berlin.
- Oke, T. (1973), City size and the urban heat island, *Atmospheric Environment*, *7*, 769–779, doi:10.1016/0004-6981(73)90140-6.
- Oliveira, A. P., and D. R. Fitzjarrald (1993), The Amazon river breeze and the local boundary layer: I. Observations, *Boundary-Layer Meteorology*, *63*, 141–162, 10.1007/BF00705380.
- Oliveira, P. H. F., P. Artaxo, C. Pires, S. de Lucca, A. Procópio, B. Holben, J. Schafer, L. F. Cardoso, S. C. Wofsy, and H. R. Rocha (2007), The effects of biomass burning aerosols and clouds on the CO₂ flux in Amazonia, *Tellus Series B*, *59*, 338–349, doi:10.1111/j.1600-0889.2007.00270.x.
- Pappalardo, G., A. Amodeo, M. Pandolfi, U. Wandinger, A. Ansmann, J. Bösenberg, V. Matthias, V. Amiridis, F. de Tomasi, M. Frioud, M. Iarlori, L. Komguem, A. Papayannis, F. Rocadenbosch, and X. Wang (2004), Aerosol lidar intercomparison in the framework of the EARLINET project. 3. Raman lidar algorithm for aerosol extinction, backscatter, and lidar ratio, *Applied Optics*, *43*, 5370–5385, doi:10.1364/AO.43.005370.
- Pereira, E. B., A. W. Setzer, F. Gerab, P. E. Artaxo, M. C. Pereira, and G. Monroe (1996), Airborne measurements of aerosols from burning biomass in Brazil related to the TRACE A experiment, *Journal of Geophysical Research*, *101*, 23983–23992, doi:10.1029/96JD00098.
- Pérez, C., S. Nickovic, J. M. Baldasano, M. Sicard, F. Rocadenbosch, and V. E. Cachorro (2006), A long Saharan dust event over the western Mediterranean: Lidar, Sun photometer observations, and regional dust modeling, *Journal of Geophysical Research*, *111*, D15214, doi:10.1029/2005JD006579.
- Pérez, C., K. Haustein, Z. Janjic, O. Jorba, N. Huneus, J. M. Baldasano, T. Black, S. Basart, S. Nickovic, R. L. Miller, J. P. Perlwitz, M. Schulz, and M. Thom-
-

- son (2011), Atmospheric dust modeling from meso to global scales with the on-line NMMB/BSC-Dust model Part 1: Model description, annual simulations and evaluation, *Atmospheric Chemistry and Physics Discussions*, *11*, 17551–17620, doi:10.5194/acpd-11-17551-2011.
- Pöschl, U., S. T. Martin, B. Sinha, Q. Chen, S. S. Gunthe, J. A. Huffman, S. Borrmann, D. K. Farmer, R. M. Garland, G. Helas, J. L. Jimenez, S. M. King, A. Manzi, E. Mikhailov, T. Pauliquevis, M. D. Petters, A. J. Prenni, P. Roldin, D. Rose, J. Schneider, H. Su, S. R. Zorn, P. Artaxo, and M. O. Andreae (2010), Rainforest aerosols as biogenic nuclei of clouds and precipitation in the Amazon, *Science*, *329*, 1513–1516, doi:10.1126/science.1191056.
- Powell, K. A., C. A. Hostetler, Z. Liu, M. A. Vaughan, R. E. Kuehn, W. H. Hunt, K.-P. Lee, C. R. Trepte, R. R. Rogers, S. A. Young, and D. M. Winker (2009), CALIPSO lidar calibration algorithms. Part I: Nighttime 532-nm parallel channel and 532-nm perpendicular channel, *Journal of Atmospheric and Oceanic Technology*, *26*, 2015–2033, doi:10.1175/2009JTECHA1242.1.
- Prenni, A. J., M. D. Petters, S. M. Kreidenweis, C. L. Heald, S. T. Martin, P. Artaxo, R. M. Garland, A. G. Wollny, and U. Pöschl (2009), Relative roles of biogenic emissions and Saharan dust as ice nuclei in the Amazon basin, *Nature Geoscience*, *2*, 402–405, doi:10.1038/ngeo517.
- Prins, E. M., J. M. Feltz, W. P. Menzel, and D. E. Ward (1998), An overview of GOES-8 diurnal fire and smoke results for SCAR-B and 1995 fire season in South America, *Journal of Geophysical Research*, *103*, 31821–31836, doi:10.1029/98JD01720.
- Procopio, A. S., L. A. Remer, P. Artaxo, Y. J. Kaufman, and B. N. Holben (2003), Modeled spectral optical properties for smoke aerosols in Amazonia, *Geophysical Research Letters*, *30*, 2265, doi:10.1029/2003GL018063.
- Prospero, J. M., R. A. Glaccum, and R. T. Nees (1981), Atmospheric transport of soil dust from Africa to South America, *Nature*, *289*, 570–572, doi:10.1038/289570a0.
- Prospero, J. M. (2011), personal communication.
- Rasmusson, E. M., and J. M. Wallace (1983), Meteorological aspects of the El Niño/Southern Oscillation, *Science*, *222*, 1195–1202, doi:10.1126/science.222.4629.1195.
-

- Redelsperger, J.-L., C. D. Thorncroft, A. Diedhiou, T. Lebel, D. J. Parker, and J. Polcher (2006), African Monsoon Multidisciplinary Analysis: An international research project and field campaign, *Bulletin of the American Meteorological Society*, *87*, 1739–1746, doi:10.1175/BAMS-87-12-1739.
- Reichholf, J. H. (1986), Is Saharan dust a major source of nutrients for the Amazonian rain forest?, *Studies on Neotropical Fauna and Environment*, *21*, 251–255.
- Reid, J. S., and P. V. Hobbs (1998), Physical and optical properties of young smoke from individual biomass fires in Brazil, *Journal of Geophysical Research*, *103*, 32013–32030, doi:10.1029/98JD00159.
- Reid, J. S., P. V. Hobbs, R. J. Ferek, D. R. Blake, J. V. Martins, M. R. Dunlap, and C. Liousse (1998), Physical, chemical, and optical properties of regional hazes dominated by smoke in Brazil, *Journal of Geophysical Research*, *103*, 32059–32080, doi:10.1029/98JD00458.
- Reid, J. S., P. V. Hobbs, A. L. Rangno, and D. A. Hegg (1999), Relationships between cloud droplet effective radius, liquid water content, and droplet concentration for warm clouds in Brazil embedded in biomass smoke, *Journal of Geophysical Research*, *104*, 6145–6154, doi:10.1029/1998JD200119.
- Remer, L. A. (2009), Atmospheric science: Smoke above clouds, *Nature Geoscience*, *2*, 167–168, doi:10.1038/ngeo456.
- Rissler, J., E. Swietlicki, J. Zhou, G. Roberts, M. O. Andreae, L. V. Gatti, and P. Artaxo (2004), Physical properties of the sub-micrometer aerosol over the Amazon rain forest during the wet-to-dry season transition – comparison of modeled and measured CCN concentrations, *Atmospheric Chemistry and Physics*, *4*, 2119–2143, doi:10.5194/acp-4-2119-2004.
- Rizzo, L. (2010), personal communication.
- Roberts, G. C., M. O. Andreae, J. Zhou, and P. Artaxo (2001), Cloud condensation nuclei in the Amazon Basin: “Marine” conditions over a continent?, *Geophysical Research Letters*, *28*, 2807–2810, doi:10.1029/2000GL012585.
- Rosenfeld, D., U. Lohmann, G. B. Raga, C. D. O’Dowd, M. Kulmala, S. Fuzzi, A. Reissell, and M. O. Andreae (2008), Flood or drought: How do aerosols affect precipitation?, *Science*, *321*, 1309–1313, doi:10.1126/science.1160606.
-

- Ross, J. L., P. V. Hobbs, and B. Holben (1998), Radiative characteristics of regional hazes dominated by smoke from biomass burning in Brazil: Closure tests and direct radiative forcing, *Journal of Geophysical Research*, *103*, 31925–31942.
- Sassen, K., and S. Benson (2001), A midlatitude cirrus cloud climatology from the Facility for Atmospheric Remote Sensing. Part II: Microphysical properties derived from lidar depolarization, *Journal of Atmospheric Sciences*, *58*, 2103–2112.
- Schafer, J. S., T. F. Eck, B. N. Holben, P. Artaxo, and A. F. Duarte (2008), Characterization of the optical properties of atmospheric aerosols in Amazônia from long-term AERONET monitoring (1993–1995 and 1999–2006), *Journal of Geophysical Research*, *113*, D04204, doi:10.1029/2007JD009319.
- Skupin, A., A. Ansmann, and J. Heintzenberg (2010), Spectral particle extinction coefficient at high relative humidity measured with DOAS at Leipzig, in *International Aerosol Conference*, P1D75, Helsinki, Finland, 29 Aug. – 3 Sep. 2010.
- Skupin, A. (2011), personal communication.
- Smirnov, A., B. N. Holben, S. M. Sakerin, D. M. Kabanov, I. Slutsker, M. Chin, T. L. Diehl, L. A. Remer, R. Kahn, A. Ignatov, L. Liu, M. Mishchenko, T. F. Eck, T. L. Kucsera, D. Giles, and O. V. Kopelevich (2006), Ship-based aerosol optical depth measurements in the Atlantic Ocean: Comparison with satellite retrievals and GOCART model, *Geophysical Research Letters*, *331*, L14817, doi:10.1029/2006GL026051.
- Smirnov, A., B. N. Holben, I. Slutsker, D. M. Giles, C. R. McClain, T. F. Eck, S. M. Sakerin, A. Macke, P. Croot, G. Zibordi, P. K. Quinn, J. Sciare, S. Kinne, M. Harvey, T. J. Smyth, S. Piketh, T. Zielinski, A. Proshutinsky, J. I. Goes, N. B. Nelson, P. Larouche, V. F. Radionov, P. Goloub, K. Krishna Moorthy, R. Matarrese, E. J. Robertson, and F. Jourdin (2009), Maritime Aerosol Network as a component of Aerosol Robotic Network, *Journal of Geophysical Research*, *114*, D06204, doi:10.1029/2008JD011257.
- Soares-Filho, B. S., D. C. Nepstad, L. M. Curran, G. C. Cerqueira, R. A. Garcia, C. A. Ramos, E. Voll, A. McDonald, P. Lefebvre, and P. Schlesinger (2006), Modelling conservation in the Amazon basin, *Nature*, *440*, 520–523, doi:10.1038/nature04389.
-

- Swap, R., M. Garstang, S. Greco, R. Talbot, and P. Källberg (1992), Saharan dust in the Amazon Basin, *Tellus Series B*, *44*, 133–149, doi:10.1034/j.1600-0889.1992.t01-1-00005.x.
- Talbot, R. W., M. O. Andreae, H. Berresheim, P. Artaxo, M. Garstang, R. C. Harriss, and K. M. Beecher (1990), Aerosol chemistry during the wet season in Central Amazonia: The influence of long-range transport, *Journal of Geophysical Research*, *95*, 16955–16969, doi:10.1029/JD095iD10p16955.
- Tesche, M., A. Ansmann, D. Müller, D. Althausen, R. Engelmann, M. Hu, and Y. Zhang (2007), Particle backscatter, extinction, and lidar ratio profiling with Raman lidar in south and north China, *Applied Optics*, *46*, 6302–6308, doi:10.1364/AO.46.006302.
- Tesche, M., A. Ansmann, D. Müller, D. Althausen, R. Engelmann, V. Freudenthaler, and S. Groß (2009), Vertically resolved separation of dust and smoke over Cape Verde using multiwavelength Raman and polarization lidars during Saharan Mineral Dust Experiment 2008, *Journal of Geophysical Research*, *114*, D13202, doi:10.1029/2009JD011862.
- Tesche, M. (2011), Vertical profiling of aerosol optical properties with multiwavelength aerosol lidar during the Saharan Mineral Dust Experiments, Ph.D. thesis, pp. 163, University of Leipzig.
- Tesche, M., D. Müller, S. Groß, A. Ansmann, D. Althausen, V. Freudenthaler, B. Weinzierl, A. Veira, and Petzold (2011a), Optical and microphysical properties of smoke over Cape Verde inferred from multiwavelength lidar measurements, *Tellus B*, *63*, 677–694, doi:10.1111/j.1600-0889.2011.00549.x.
- Tesche, M., S. Groß, A. Ansmann, D. Müller, D. Althausen, V. Freudenthaler, and M. Esselborn (2011b), Profiling of Saharan dust and biomass-burning smoke with multiwavelength polarization Raman lidar at Cape Verde, *Tellus B*, *63*, 649–676, doi:10.1111/j.1600-0889.2011.00548.x.
- Turner, D. D., R. A. Ferrare, and L. A. Brasseur (2001), Average aerosol extinction and water vapor profiles over the Southern Great Plains, *Geophysical Research Letters*, *28*, 4441–4444, doi:10.1029/2001GL013691.
- UNEP (2008), *Environment Outlook in the Amazonia – GEO Amazonia*, United Nations Environment Programme, ISBN 978-92-807-2945-0.
-

- Vaughan, M., D. Winker, and K. Powell (2005), CALIOP Algorithm Theoretical Basis Document Part 2: Feature Detection and Layer Properties Algorithms, *PC-SCI-202.01*, available at http://www-calipso.larc.nasa.gov/resources/project_documentation.php.
- Veselovskii, I., A. Kolgotin, V. Griaznov, D. Müller, U. Wandinger, and D. N. Whiteman (2002), Inversion with regularization for the retrieval of tropospheric aerosol parameters from multiwavelength lidar sounding, *Applied Optics*, *41*, 3685–3699, doi:10.1364/AO.41.003685.
- Veselovskii, I., A. Kolgotin, V. Griaznov, D. Müller, K. Franke, and D. N. Whiteman (2004), Inversion of multiwavelength Raman lidar data for retrieval of bimodal aerosol size distribution, *Applied Optics*, *43*, 1180–1195, doi:10.1364/AO.43.001180.
- Wandinger, U. (2005a), Raman Lidar, in *Lidar – Range-Resolved Optical Remote Sensing of the Atmosphere*, *Springer Series in Optical Sciences*, vol. 102, edited by C. Weitkamp, pp. 241–267, Springer Berlin / Heidelberg.
- Wandinger, U. (2005b), Introduction to Lidar, in *Lidar – Range-Resolved Optical Remote Sensing of the Atmosphere*, *Springer Series in Optical Sciences*, vol. 102, edited by C. Weitkamp, pp. 1–18, Springer Berlin / Heidelberg.
- Wandinger, U., and A. Ansmann (2002), Experimental determination of the lidar overlap profile with Raman lidar, *Applied Optics*, *41*, 511–514.
- Ward, D. E., R. A. Susott, J. B. Kauffman, R. E. Babbitt, D. L. Cummings, B. Dias, B. N. Holden, Y. J. Kaufman, R. A. Rasmussen, and A. W. Setzer (1992), Smoke and fire characteristics for Cerrado and deforestation burns in Brazil: BASE-B experiment, *Journal of Geophysical Research*, *97*, 14601–14619.
- Williams, E., D. Rosenfeld, N. Madden, J. Gerlach, N. Gears, L. Atkinson, N. Dunne-mann, G. Frostrom, M. Antonio, B. Biazon, R. Camargo, H. Franca, A. Gomes, M. Lima, R. Machado, S. Manhaes, L. Nachtigall, H. Piva, W. Quintiliano, L. Machado, P. Artaxo, G. Roberts, N. Renno, R. Blakeslee, J. Bailey, D. Boccippio, A. Betts, D. Wolff, B. Roy, J. Halverson, T. Rickenbach, J. Fuentes, and E. Avelino (2002), Contrasting convective regimes over the Amazon: Implications for cloud electrification, *Journal of Geophysical Research*, *107*, 8082, doi:10.1029/2001JD000380.
-

- Wilson, S. R., and B. W. Forgan (2002), Aerosol optical depth at Cape Grim, Tasmania, 1986–1999, *Journal of Geophysical Research*, *107*, 4068, doi:10.1029/2001JD000398.
- Zender, C. S., H. Bian, and D. Newman (2003), Mineral Dust Entrainment and Deposition (DEAD) model: Description and 1990s dust climatology, *Journal of Geophysical Research*, *108*, 4416, doi:10.1029/2002JD002775.
- Zhou, J., E. Swietlicki, H. C. Hansson, and P. Artaxo (2002), Submicrometer aerosol particle size distribution and hygroscopic growth measured in the Amazon rain forest during the wet season, *Journal of Geophysical Research*, *107*, 8055, doi:10.1029/2000JD000203.
-

List of Abbreviations

ABLE	The Amazon Boundary Layer Experiment
AERONET	AERosol RObotic NETwork
agl	above ground level
asl	above sea level
AL	Aerosol layer
AMAZE-08	AMAZonian aerosol characterization Experiment 2008
AMMA	African Monsoon Multidisciplinary Analyses
AOD	Aerosol Optical Depth
AVHRR	Advanced Very High Resolution Radiometer
BASE-A & B	Biomass Burning Airborne and Spaceborne Experiment -Amazonas & -Brazil
BBA	Biomass Burning Aerosol
CATT-BRAMS	Coupled Aerosol and Tracer Transport model to the Brazilian developments on the Regional Atmospheric Modeling System
CALIOP	Cloud-Aerosol Lidar with Orthogonal Polarization
CAM	CAMera
CCL	Cloud Convective Layer
CCN	Cloud Condensation Nuclei
CLAIRE	Cooperative LBA Airborne Regional Experiment
DABEX	Dust And Biomass-burning Experiment
DAQ	Data AcQuisition
DIAL	Differential Absorption Lidar
EARLINET	European Aerosol Research LIdar NETwork
EARLI09	EARlinet Reference Lidar Intercomparison 2009
ECMWF	European Centre for Medium-Range Weather Forecasts
EUCAARI	European Integrated Project on Aerosol, Cloud, Climate, Air Quality Interactions
EUSTACH	EUropean Studies on Trace gases and Atmospheric CHemistry
INPE	Brazilian National Institute for Space Research (Instituto Nacional de Pesquisas Espaciais)
FIRMS	Fire Information for Resource Management System
FMI	Finish Meteorological Institute
FT	Free Troposphere
HYSPLIT	HYbrid Single Particle Lagrangian Integrated Trajectory Model
IN	Ice Nuclei
Ift	Leibniz Institute for Tropospheric Research
INPA	National Institute for Amazonia Research (Instituto Nacional de Pesquisas da Amazônia)
IPCC	Intergovernmental Panel on Climate Change
ITCZ	InterTropical Convergence Zone
LBA	The Large-Scale Biosphere-Atmosphere Experiment in Amazonia

MARTHA	Multiwavelength Atmospheric Raman lidar for Temperature, Humidity, and Aerosol profiling
ML	Mixing Layer
MODIS	Moderate Resolution Imaging Spectroradiometer
NOAA	National Oceanic and Atmospheric Administration
Nd:YAG	Neodymium-doped Yttrium Aluminum Garnet
NCEP	National Centers for Environmental Prediction
NetCDF	Network Common Data Form
PIXE	Particle-Induced X-ray Emission
PM	Particulate Matter
PMT	Photo Multiplier Tube
Polly	Portable lidar system
PSD	Particle Size Distribution
RH	Relative Humidity
RL	Residual Layer
SAMUM	Saharan Mineral Dust Experiment
SCAR-B	Smoke, Clouds, And Radiation - Brazil
SMOCC	Smoke, Aerosols, Clouds, Rainfall, and Climate
SSA	Single Scattering Albedo
TRACE-A	TRansport and Atmospheric Chemistry near the Equator – Atlantic
TWI	Trade Wind Inversion
UTC	Universal Time Coordinated
UV	Ultra Violet
VIS	VISible
VMD	Volume Mean Diameter
XT	eXTended

Acknowledgment

I would like to thank all people who supported this work during the last years and made this dissertation possible.

First of all I would like to express my gratitude to Prof. Dr. Jost Heintzenberg and Prof. Dr. Paulo Artaxo for reviewing this thesis. I also thank my advisory committee at the Leibniz Institute for Tropospheric Research (IfT), Dr. Dietrich Althausen, Dr. Albert Ansmann, and Dr. Ina Tegen. They kept me on track and gave me valuable scientific support during my PhD work.

Dietrich Althausen attracted me for lidar measurements several years ago and since that time he has continuously supported my work. He showed me how to work with Polly and pushed me to keep the “red line”. Albert Ansmann supported very much the interpretation of the lidar data. His critical comments on data evaluation and the first versions of this thesis were always very helpful and constructive, as well as his numerous ideas what else could be done.

The basis of this work are the lidar measurements performed overseas. Participating in the field campaigns in Brazil and also in China was a great experience for me. However, many people were involved in the lidar measurements. Ronny Engelmann accompanied me some time in the jungle. He solved every technical problem – and we had a lot of them in the beginning – and his skill for improvising is still incredible to me. Unfortunately, he also shared the bad sides of the jungle with me, only to mention stomach upsets and several insect bites. Dietrich Althausen was also several times in Brazil, preparing the lidar campaign and performing maintenance at the lidar together with Birgit Heese. These people spent a lot of time to travel between Germany, Cape Verde, and Amazonia to keep the system running.

I also thank my Brazilian colleagues for the continuous support and help. Paulo Artaxo, Theo Pauliquevis, and Rodrigo Souza did an indispensable contribution to the successful lidar campaign. Many “Skype” sessions were performed to repair the lidar during which I could sit in the office while they had to sweat in the jungle.

Melina Paixao and Scot T. Martin gave very valuable support in the beginning of the campaign. They organized a lot of things and introduced me into the Amazonian way of work. We also got great logistical support from many people at INPA. They helped whenever they could and gave us always a very warm welcome.

Karsten Hausteин performed a lot of additional model runs at the Barcelona Supercomputing Center to give me further evidence that Saharan dust reached our lidar site. He also introduced me to the secrets of NMMB/BSC-dust. Detlef Müller provided me with his inversion algorithm and taught me how to handle it. He never has been tired of answering all my questions. I also would like to thank Karla Longo for providing the CATT-BRAMS data. Ulla Wandinger shared her Fortran code for molecular scattering with me and gave me also a lot of useful hints concerning academic English. FMI (Mika Komppula) delivered the ML tops as derived from ECMWF.

I especially thank Albert Ansmann, Birgit Heese, Marcus Radlach, and Ulla Wandinger for the proofreading of this dissertation and for the many useful comments how to improve this work.

Patric Seifert and Matthias Tesche shared with me their experience in writing a PhD thesis and helped me with many software problems during the last years.

I also thank the whole lidar group at IfT for the pleasant working atmosphere and the convenient coffee breaks, which often brought up new ideas.

Last but not least, I really thank my family and Tina for the patience and support during the last years. They always back my plans and gave me the freedom to make my own choice.

Curriculum Vitae

Holger Baars

born 16 May 1981 in Meerane, Germany

Leibniz Institute for Tropospheric Research (IfT)

Permoserstr. 15

04318 Leipzig

Germany

Phone: +49 341 235 2411

E-mail: baars@tropos.de

Academic Education:

- Since 05/2007 PhD thesis at the IfT:
Aerosol profiling with lidar in the Amazon Basin during the wet and dry season 2008
- 05/2006 – 04/2007 Diploma thesis at the IfT:
Continuous monitoring of the planetary-boundary-layer depth with lidar
- 10/2000 – 04/2007 Studies of meteorology at the Meteorological Institute of the University of Leipzig, degree: Diploma

Measurement campaigns:

- 10/2009 – 12/2009 MEGACITY campaign,
Sun photometer and lidar observations, Pearl River Delta, China
- 04/2009 – 03/2010 EUCAARI China,
Lidar observations near Beijing
- 05/2009 EARLI09,
EARLINET Lidar Intercomparison 2009, Leipzig, Germany
- 01/2008 – 11/2008 EUCAARI Brazil,
Lidar observations in the Amazon rain forest, Manaus, Brazil
- 02/2008 – 03/2008 The Amazonian Aerosol Characterization Experiment
AMAZE-08, Lidar observation near Manaus, Brazil
- 06/2007 – 05/2009 EUSAAR JRA1,
Lidar and MAX-DOAS comparison measurements
in Melpitz and Leipzig, Germany
- since 2006 Automated Raman lidar measurements in Leipzig, Germany

Publications:

- **H. Baars**, A. Ansmann, D. Althausen, R. Engelmann, P. Artaxo, T. Pauliquevis, and R. Souza (2011), Further evidence for significant smoke transport from Africa to Amazonia, *Geophysical Research Letters*, *38*, L20802, doi:10.1029/2011GL049200.
- S. T. Martin, M. O. Andreae, D. Althausen, P. Artaxo, **H. Baars**, S. Borrmann, Q. Chen, D. K. Farmer, A. Guenther, S. S. Gunthe, J. L. Jimenez, T. Karl, K. Longo, A. Manzi, T. Pauliquevis, M. D. Petters, A. J. Prenni, U. Pöschl, L. V. Rizzo, J. Schneider, J. N. Smith, E. Swietlicki, J. Tota, J. Wang, A. Wiedensohler, and S. R. Zorn (2010), An overview of the Amazonian Aerosol Characterization Experiment 2008 (AMAZE-08), *Atmospheric Chemistry and Physics*, *10*, 11415–11438, doi:10.5194/acp-10-11415-2010.
- M. Komppula, T. Mielonen, A. Arola, K. Korhonen, H. Lihavainen, A.-P. Hyvärinen, **H. Baars**, R. Engelmann, D. Althausen, A. Ansmann, D. Müller, T. S. Panwar, R. K. Hooda, V. P. Sharma, V.-M. Kerminen, K. E. J. Lehtinen, and Y. Viisanen (2010), One year of Raman-lidar measurements in Gual Pahari EUCAARI site close to New Delhi in India: Seasonal characteristics of the aerosol vertical structure, *Atmospheric Chemistry and Physics Discussions*, *10*, 31123–31151, doi:10.5194/acpd-10-31123-2010.
- A. Ansmann, **H. Baars**, M. Tesche, D. Müller, D. Althausen, R. Engelmann, T. Pauliquevis, and P. Artaxo (2009), Dust and smoke transport from Africa to South America: Lidar profiling over Cape Verde and the Amazon rainforest, *Geophysical Research Letters*, *36*, L11802, doi:10.1029/2009GL037923.
- D. Althausen, R. Engelmann, **H. Baars**, B. Heese, A. Ansmann, D. Müller, and M. Komppula (2009), Portable Raman Lidar PollyXT for Automated Profiling of Aerosol Backscatter, Extinction, and Depolarization, *Journal of Atmospheric and Oceanic Technology*, *26*, 2366–2378.
- **H. Baars**, A. Ansmann, R. Engelmann, and D. Althausen (2008), Continuous monitoring of the boundary-layer top with lidar. *Atmospheric Chemistry and Physics*, *8*, 7281–7296, doi:10.5194/acp-8-7281-2008.

Selected conference contributions:

- **H. Baars**, D. Althausen, R. Engelmann, A. Ansmann, D. Müller, P. Artaxo, T. Pauliquevis, R. Souza, and S. Martin (2011), Long-range transport of dust and smoke towards and over the Amazon rain forest observed with lidar during the wet and dry season, *The EGU General Assembly 2011*, Vienna, Austria, 3 – 8 April 2011.
- **H. Baars**, D. Althausen, A. Ansmann, R. Engelmann, B. Heese, A. Hiebsch, I. Mattis, J. Schmidt, P. Seifert, M. Tesche, and U. Wandinger (2010), Lidar-beobachtungen der Vulkanasche des Eyjafjallajökull im April 2010 in Leipzig, *DACH Meteorologentagung*, Bonn, Germany, 20 – 24 September 2010.
- **H. Baars**, D. Althausen, R. Engelmann, A. Ansmann, D. Müller, P. Artaxo, T. Pauliquevis, R. Souza, and S. T. Martin (2010), Automated Raman lidar measurements in the Amazon rain forest during the wet and dry season 2008, *International Aerosol Conference 2010*, Helsinki, Finland, 29 August – 3 September 2010.
- **H. Baars**, D. Althausen, R. Engelmann, A. Ansmann, D. Müller, P. Artaxo, T. Pauliquevis, R. Souza, and S. T. Martin (2009), Automated Raman lidar measurements in the Amazon rain forest during the wet and dry season 2008, *8th International Symposium on Tropospheric Profiling: Integration of Needs, Technologies and Applications*, Delft, The Netherlands, 19 – 23 October 2009.
- **H. Baars**, R. Engelmann, D. Althausen, A. Ansmann, P. Artaxo, T. Pauliquevis, and R. Souza (2008), Vertical profiles of aerosol properties over Amazonia observed with lidar, *International Scientific Conference: Amazon in Perspective - Integrated Science for a Sustainable Future*, Manaus, Amazonas, Brazil, 17 – 20 November 2008.
- **H. Baars**, D. Althausen, R. Engelmann, T. Pauliquevis, and P. Artaxo (2008), Multiwavelength aerosol observations over the Amazonian tropical rain forest with the compact, automated seven-channel polarization Raman lidar PollyXT, *24th International Laser Radar Conference (ILRC)*, Boulder, CO, USA, 23 – 27 June, 2008.
- **H. Baars**, D. Althausen, A. Ansmann, and R. Engelmann (2007), Kontinuierliche Langzeitmessungen der Grenzschichtdicke und Grenzschichtwachstumsraten mit einem Lidar, *DACH Meteorologentagung*, Hamburg, Germany, 10 – 14 September 2007.